REDUCED MIXED METAL OXIDES FOR THE HYDROGENATION, HYDROGENOLYSIS, AND RING-OPENING OF FURANICS

A Dissertation
Presented to
The Academic Faculty

by

Taylor Phillip Sulmonetti

In Partial Fulfillment
of the Requirements for the Degree
Doctor of Philosophy in the
School of Chemical & Biomolecular Engineering

Georgia Institute of Technology
December 2017

REDUCED MIXED METAL OXIDES FOR THE HYDROGENATION, HYDROGENOLYSIS, AND RING-OPENING OF FURANICS

Approved by:

Dr. Christopher W. Jones, Advisor
School of Biomolecular & Chemical Engineering
Georgia Institute of Technology

Dr. Angus Wilkinson
School of Chemistry & Biochemistry
Georgia Institute of Technology

Dr. Pradeep K. Agrawal
School of Biomolecular & Chemical Engineering
Georgia Institute of Technology

Dr. Faisal Alamgir
School of Material Science and Engineering
Georgia Institute of Technology

Dr. Carsten Sievers
School of Biomolecular & Chemical Engineering
Georgia Institute of Technology

Date Approved: October 18, 2017

To My Family and My Father

ACKNOWLEDGEMENTS

There are so many people that have made this journey a possibility and have helped me grow both technically and professionally. I first want to start by thanking my adviser, Prof. Christopher Jones, for his endless support. Not only did he give me the financial needs and resources, but more importantly he consistently provided me with advice that spanned more than just research. Prof. Jones, I really appreciated the ability to travel to various conferences and present my work to a wide variety of audiences, while also interacting with other academics. With that I must thank my funding source throughout my PhD that Prof. Jones obtained for me: The Catalysis Center for Energy Innovation (CCEI), an Energy Frontier Research Center funded by the U.S. Department of Energy, Office of Science under grant DE-SC0001004.

Along with Prof. Jones, Prof. Pradeep Agrawal became my pseudo co-adviser a year into my PhD, and I greatly appreciate him taking the time to also meet with me to discuss all science aspects. I would also like to thank my committee members, including Prof. Carsten Sievers, Prof. Faisal Alamgir, and Prof. Angus Wilkinson, for being a part of my project. More specifically, I would like to thank Prof. Alamgir for additional discussions with regards to XAS.

Next, I would like to thank many of my colleges throughout my PhD tenure. This includes many current and past Jones group member. Though everyone in the Jones group has contributed in some way, I would like to specifically mention Simon Pang, Caroline Hoyt, Miles Sakwa-Novak, Bo Hu, Nathan Ellebracht, and Mica Taborga Claure for their invaluable advice. More specifically, I would like to thank Steph Didas for dealing with all

my "1st year" questions. There are many people outside of the Jones group including Brian Pimentel, Brandon Plaisance, Bunger-Henry crew, David Cullen (STEM), and Sungsik Lee (XAS), that have helped broaden my research knowledge. Outside of research there were so many others that helped motivate me throughout my PhD including my life-long friends from Atlanta and Lehigh.

I would like to extend a heart-filled appreciation to Rachael Porter who has been my rock throughout this whole process. She has encouraged me to pursue my dreams both inside academics and outside academics. She has always been engaged when I talk about my research, and she has patiently listened to me vent about reactor problems and more. I am so happy that I get to share this accomplishment with her.

Finally, I would like to show my greatest appreciation and love to my family. My mom and twin brother have been there every step of the way, and they have constantly pushed me to strive for the best. Also, I would not be here without my father. His guidance and love helped me get through the hard times in life. Even though he is not physically present for this moment, I will always feel his presence, and I know that he is cheering me on now and always: I love you dad.

TABLE OF CONTENTS

ACKNOWLEDGEMENTS **IV**

LIST OF TABLES **XI**

LIST OF FIGURES **XIII**

LIST OF COMMON ABBREVIATIONS **XX**

SUMMARY **XXI**

CHAPTER 1 INTRODUCTION **1**

1.1 Motivation 1

1.2 Catalysis for Furanic Conversion 2

1.2.1 Single Metal Catalysts for Furanic Conversion 4

1.2.2 Multi-Metal and Multi-Functional Catalysts for Furanic Conversion 7

1.2.2.1 Hydrogenation 8

1.2.2.2 Side Chain Hydrogenolysis 10

1.2.2.3 Ring-Opening 14

1.3 Layered Double Hydroxides Derived Catalysis 19

1.3.1 LDH Materials 20

1.3.2 LDH Derived Catalysts for Biomass Conversion 23

1.4 Research Gaps and Dissertation Objectives 25

1.4.1 Research Gaps and Outlook 25

1.4.2 Vapor Phase Hydrogenation of Furfural (Chapter 2) 26

1.4.3 Vapor Phase Hydrogenolysis of Furfuryl Alcohol (Chapter 3) 26

1.4.4 Liquid Phase Ring-Opening of Furanics (Chapter 4) 27

1.4.5 Well-Defined Multi-Metal Catalysts for Furanic Conversion (Chapter 5) 27

1.5 References 28

CHAPTER 2 VAPOR PHASE HYDROGENATION OF FURFURAL UTILIZING NI BASED MMO CATALYSTS 39
2.1 Introduction 39
2.2 Experimental Procedures 41
2.2.1 Materials and Chemicals 41
2.2.2 Catalyst Synthesis 42
2.2.3 Reaction Studies 42
2.2.4 Catalyst Characterization 43
2.2.4.1 Adsorption Characterization: N_2 Physisorption and Chemisorption 43
2.2.4.2 XRD, XPS, ICP Analysis, and STEM Characterization 44
2.2.4.3 X-ray Absorption Spectroscopy 45
2.3 Results and Discussion 45
2.3.1 Materials Synthesis and Initial Characterization 46
2.3.2 Vapor Phase Flow Reactions 52
2.3.3 Spectroscopic Characterization 57
2.4 Conclusions 65
2.5 References 66

CHAPTER 3 PRODUCTION OF 2-METHYLFURAN UTILIZING REDUCED CO-FE-AL MMO CATALYSTS 72
3.1 Introduction 72
3.2 Experimental Section 74
3.2.1 Materials and Chemicals 75
3.2.2 Catalyst Synthesis 75
3.2.3 Reaction Studies 76
3.2.4 Characterization Techniques 76
3.2.4.1 Physical Characterization and XRD 76
3.2.4.2 Spectroscopic Experiments 77
3.3 Results and Discussion 78
3.3.1 Initial MMOs Characterization 78
3.3.2 Vapor Phase Flow Reactions 82

3.3.3 In situ Spectroscopic Experiments 87
3.4 Conclusion 94
3.5 References 95

CHAPTER 4 REDUCED CU-CO-AL MMO CATALYSTS FOR THE PRODUCTION OF RENEWABLE DIOLS 100
4.1 Introduction 100
4.2 Experimental Section 103
4.2.1 Materials and Chemicals 103
4.2.2 Catalysts Synthesis 104
4.2.3 Reaction Studies 105
4.2.4 Characterization 106
4.2.4.1 N_2 Physisorption, Chemisorption, XRD, and ICP 106
4.2.4.2 Spectroscopic Experiments 106
4.3 Results and Discussion 108
4.3.1 Physical Characterization 108
4.3.2 Reaction Analysis 110
4.3.3 XRD and TPR Experiments 116
4.3.4 Spectroscopic Experiments 119
4.4 Conclusions 130
4.5 References 131

CHAPTER 5 WELL-DEFINED MULTI-METAL CATALYSTS FOR FURANIC RING-OPENING: SCREENING AND ALD EQUIPMENT DESIGN 137
5.1 Introduction 137
5.2 Experimental Procedure 142
5.2.1 Materials and Chemicals 142
5.2.2 Catalysts Synthesis 143
5.2.2.1 Oxide Support Synthesis 143
5.2.2.2 Wetness Impregnation on Various Supports 144
5.2.2.3 ALD Prepared Catalysts 145

5.2.3 Reaction Studies 145
5.3 Results and Discussion 146
5.3.1 ALD Design and Construction 146
5.3.2 Screening of Various Supports 148
5.4 Conclusion 151
5.5 References 151

CHAPTER 6 SUMMARY AND FUTURE DIRECTION 155
6.1 Summary 155
6.1.1 Chapter 1: Introduction and Motivation 155
6.1.2 Chapter 2: Hydrogenation Utilizing Ni Based MMOs 155
6.1.3 Chapter 3: Hydrogenolysis Utilizing Co-Fe Based MMOs 156
6.1.4 Chapter 4: Ring-Opening Utilizing Cu-Co Based MMOs 157
6.1.5 Chapter 5: Development of ALD Equipment for Furanic Conversion 157
6.2 Future Directions 158
6.2.1 Screening ALD Prepared Multi-Metal Catalysts for Ring-Opening 158
6.2.2 Ring-Opening of HMF Utilizing Reduced MMOs 159
6.2.3 Tandem Reaction: Coupled Furanics and Subsequent HDO 160
6.2.4 MOF-derived Catalysts for Furanic Conversion 161
6.3 References 163

APPENDIX A SUPPORTING INFORMATION FOR CHAPTER 2 165
A.1 Additional XRD Patterns 165
A.2 Temperature Programmed Reduction 166
A.3 Reaction Data 168
A.4 Post-reaction TGA 170
A.5 CO Adsorption Data 171
A.6 Derivatives of XAS Data Ni k-edge 172
A.7 Additional XPS Spectra 173
A.8 Additional STEM Images 176
A.9 References 178

APPENDIX B SUPPORTING INFORMATION FOR CHAPTER 3 179
B.1 Additional Physical Characterizations 179
B.2 Additional Reaction Data 180
B.3 Additional Spectroscopic Experiments and Data 186
B.3.1 XPS data 186
B.3.2 XAS Data 186
B.4 Post-reaction TGA 191
B.5 References 192

APPENDIX C SUPPORTING INFORMATION FOR CHAPTER 4 193
C.1 Additional Physical Characterizations 193
C.2 Additional Reaction Data 195
C.3 Additional XPS Data 200
C.4 Additional Co XAS Data 202
C.5 Additional Cu XAS Data 209
C.6 References 211

LIST OF TABLES

Table 2.1	Physical properties of the catalysts utilized for FUR hydrogenation.	47
Table 2.2	Selectivities and activities for each catalyst under reaction conditions yielding nearly complete conversion of FUR.	52
Table 2.3	Activity and selectivity at low FUR conversion for selected catalysts.	55
Table 2.4	Activity and selectivity of the 1.1Ni-0.8Co-Al catalyst at various temperatures.	55
Table 3.1	Physical properties of multiple Co based MMO catalysts.	80
Table 3.2	Reaction data of FUR over 3Co-0.25Fe-0.75Al at 180 °C at various W/F.	87
Table 3.3	EXAFS results for the analysis of Co k-edge post-reduction.	89
Table 3.4	EXAFS results for the analysis of Fe k-edge post-reduction.	92
Table 4.1	Physical properties of multiple Co and/or Cu based MMOs.	109
Table 4.2	FAL batch reactions conducted over various xCu-yCo-Al catalysts.	111
Table 4.3	Kinetic analysis of the 0.25Cu-2.75Co-Al catalyst prepared using various reduction temperatures during the 1st pretreatment step.	114
Table 4.4	EXAFS fitting of the 0.25Cu-2.75Co-Al material after pretreatment at various reduction temperatures and a passivation step.	123
Table 4.5	Quantitative XPS analysis of Co species from various spectra displayed in Figure 4.8.	127
Table 5.1	N_2 physisorption results for each support prior to metal impregnation.	149
Table A.1	Hydrogen uptake and peak temperatures obtained by temperature programmed reduction.	167
Table A.2	CO pulse chemisorption results conducted at 30 °C.	171

Table A.3	Co XPS peak fitting parameters for the 1.1Ni-0.8Co-Al sample, both pre- and post-reduction (Refer to Figure 2.8).	174
Table A.4	Ni XPS peak fitting parameters for the 1.1Ni-0.8Co-Al sample, both pre- and post-reduction (Refer to Figure A.6).	175
Table A.5	Ni peak fitting parameters for the 1.4Ni-1.4Mg-Al sample, both pre- and post-reduction (Refer to Figure A.7).	175
Table B.1	Conversion and selectivity of products of various catalysts tested in Figure 3.3.	183
Table B.2	Conversion and selectivity of products of various catalysts tested in Figure 3.5.	184
Table B.3	XANES analysis of Co k-edge for each catalysts and standard.	188
Table C.1	Conversion and selectivity to products of various catalysts tested in Table 4.2.	196
Table C.2	Reaction conditions, conversion, and selectivity of additional reactions with FAL.	197
Table C.3	Reaction conditions, conversion, and selectivity utilizing other substrates.	197
Table C.4	Peak fitting data for Figure C.7 for various reduction temperatures conducted after fully pretreatment (Flow reduction, passivation, and batch reactor reduction).	202
Table C.5	EXAFS results for the analysis of the Co k-edge post-reduction.	207
Table C.6	Edge Energy of the Cu k-edge from Figure C.17.	209
Table C.7	Edge Energy of Cu k-edge from Figure C.18.	210

LIST OF FIGURES

Figure 1.1	Example acid dehydration pathway to create furanic compounds from lignocellulosic biomass.	3
Figure 1.2	Major proposed pathways of FUR to value added products. Pink: 1st objective target molecules; Blue: 2nd objective target molecule; Maroon: 3rd objective target molecules.	4
Figure 1.3	Proposed mechanism of FUR adsorption over metals.	5
Figure 1.4	The reaction of FAL over a bimetallic catalyst containing M_1 (noble metal) and M_2 (oxophilic metal) to produce 2-MF.	11
Figure 1.5	Proposed pathways of the ring-opening of furanic compounds: a) Ring-opening of THFA through hydride pathway.[85] b) THFA ring-opening through acidic H.[89] c) FAL ring-opening over reduced MMO catalysts.[37,90]	16
Figure 1.6	General depiction of LDH materials exposed to various post-synthesis thermal treatment.	21
Figure 1.7	(Left) Example XRD pattern of LDH material; (center): TGA and DSC plot during thermal treatment in air; (right) Example XRD pattern of MMO material post-calcination at 400 °C.	22
Figure 2.1	XRD patterns of post-calcined Ni-Co-Al MMO materials.	47
Figure 2.2	XRD patterns of post-calcined Ni-Mg-Al MMO materials.	48
Figure 2.3	TPR profiles of Ni-Co-Al catalysts.	50
Figure 2.4	TPR profiles of Ni-Mg-Al catalysts	51
Figure 2.5	Reaction pathways of the major products from FUR conversion of Ni based catalysts.	53
Figure 2.6	XANES spectra at the Ni k-edge of the catalysts at RT both before and after reduction at 500 ºC with 4% H_2 balance He and 10 mL/min. Inset graphs show Fourier Transformed EXAFS data for each catalyst; a) 1.1Ni-0.8Co-Al b) 1.4Ni-1.4Mg-Al.	58
Figure 2.7	*In situ* XANES of Co k-edge of the 1.1Ni-0.8Co-Al catalyst at RT both before and after reduction with 4% H_2 balance He and	60

10 mL/min. Inset graph shows Fourier transformed EXAFS data of the same sample.

Figure 2.8 XPS spectra of 1.1Ni-0.8Co-Al catalysts in the Co binding energy region. a) Pre-reduction; b) Post-reduction, after passivation. 63

Figure 2.9 HRSTEM image and diffraction of reduced 1.1Ni-0.8Co-Al catalysts at 500 °C for 1 hour and then passivated at RT for 1 hour in 1% O_2 balance N_2. 64

Figure 3.1 a) XRD patterns of Co-xFe-yAl catalysts after calcination at 400 °C; b) Enlarged section of major Bragg peak between 35-40°. 79

Figure 3.2 TPR profile of each Co-xFe-yAl catalyst in a 10% H_2 (balance Ar) atmosphere with a 5 °C/min ramp rate. 81

Figure 3.3 Time on stream data of FAL conversion and 2-MF selectivity over various 3Co-xFe-yAl catalysts at W/F (g_{cat}*h*mol^{-1}) = 3.63, 180 °C, 1 atm, and FAL conc = 0.0015 mmol/mL; Black lines represent conversion and red lines represent 2-methylfuran selectivity. a) 3Co-0.25Fe-0.75Al; b) 3Co-0.5Fe-0.5Al; c) 3Co-0.75Fe-0.25Al; d) 3Co-Al; e) 3Co-xFe-yAl; f) 3Co-Al. 83

Figure 3.4 Recycle tests of 3Co-0.25Fe-0.75Al displaying conversion and selectivity towards 2-MF at W/F (g_{cat}*h*mol^{-1}) = 3.63 with FAL as a substrate. Data point taken at approximately 40 min on stream. 84

Figure 3.5 Varying W/F of the 3Co-0.25Fe-0.75Al catalyst at 180 °C and 1 atm with a FA flow rate varying between 5.5-12 mmol/h and H_2 flow rate varying between 60-130 mL/min while keeping the FAL concentration at 0.0015 mmol/mL. Inset graph displays the selectivity of significant minor products over varying W/F. Values taken at approximately 40 min on stream. 86

Figure 3.6 Fourier transformed EXAFS of Co k-edge post-reduction at 500 ºC. Scans were taken at room temperature, and the k range displayed is 2.7-12 $Å^{-1}$ with a k weight of k^2. 89

Figure 3.7 Fourier transformed EXAFS of Fe k-edge post-reduction at 500 ºC. Scans were taken at room temperature, and the k range displayed is 2.7-10.5 $Å^{-1}$ at a k weight of k^2. 91

Figure 4.1	N_2 physisorption isotherms of each catalyst synthesized and were conducted after calcination and before reduction. The data for each plot were offset for clarity.	110
Figure 4.2	Conversion of FUR over 0.25Cu-2.75Co-Al at 140 °C and 4 MPa of H_2.	115
Figure 4.3	Proposed reaction pathways for the conversion of furfural to the ring-opening products and ring saturated product.	116
Figure 4.4	Powder XRD patterns of each xCu-yCo-Al catalyst synthesized and were conducted after calcination and before reduction.	117
Figure 4.5	TPR profile of each MMO material utilized in this study.	117
Figure 4.6	XANES spectra of Co k-edge of known standards and the 0.25Cu-2.75Co-Al catalyst after H_2 pretreatment at 300 °C, 400 °C, and 500 °C, and subsequent passivation for 1 h in 1% O_2/N_2.	121
Figure 4.7	XANES linear combinations of the 0.25Cu-2.75Co-Al material after various pretreatment conditions.	122
Figure 4.8	Co 2p XPS spectra of the 0.25Cu-2.75Co-Al material after reduction in the flow reactor at various temperatures, passivation, and re-reduction in the batch reactor to 180 °C and 500 psi of H_2. A) No Reduction; b) 300 °C reduction; c) 400 °C reduction; d) 500 °C reduction.	125
Figure 4.9	Cu 2p XP spectra of the 0.25Cu-2.75Co-Al material after reduction in the flow reactor at various temperatures, passivation, and re-reduction in the batch reactor to 180 °C and 500 psi of H_2. A) No reduction; b) 300 °C reduction; c) 400 °C reduction; d) 500 °C reduction.	127
Figure 5.1	Generalized deposition concept displaying growth rate vs substrate temperature.	139
Figure 5.2	Schematic of ALD equipment containing two precursor zones for multi-metal catalyst synthesis.	147
Figure 5.3	Conversion and selectivity of FAL reaction over various 5 wt% Cu_1Co_4/Support. Temperature: 150 °C, H_2 pressure: 4 MPa, Time: 3 hours, Catalyst: 50 mg, FAL: 500 mg, ethanol: 50 mL.	149
Figure A.1	XRD Patterns of filtered and dried LDH materials.	165

Figure A.2	XRD Patterns of known references to compare.	166
Figure A.3	Conversion and major product selectivities vs time on stream for multiple runs of each catalyst.	169
Figure A.4	Ramp rate 10 °C/min. a) 1.1Ni-0.8Co-Al post-reaction mass change and DSC vs temperature. b) Co-Al post-reaction mass change and DSC vs temperature. c) 1.4Ni-0.4Mg-Al post-reaction mass change and DSC vs temperature.	170
Figure A.5	Derivative of norm(E) of XANES data from Figure 2.6. a) 1.1Ni-0.8Co-Al pre-and post-reduction compared to Ni foil. b) 1.4Ni-1.4Mg-Al pre-and post-reduction compared to Ni foil.	172
Figure A.6	XPS spectra in the Ni 2p binding energy region of pre- and post-reduction samples of 1.1Ni-0.8Co-Al. a) pre-reduction; b) post-reduction.	173
Figure A.7	XPS spectra in the Ni 2p binding energy region of pre- and post-reduction samples of 1.4Ni-1.4Mg-Al. a) pre-reduction; b) post-reduction.	173
Figure A.8	Electron Energy Loss Spectrum of Figure 2.9 STEM image.	176
Figure A.9	STEM image and EDS spectra of each species present in the unreduced 1.1Ni-0.8Co-Al catalysts. The inset table displays the quantification of each species from EDS analysis.	177
Figure A.10	STEM image and EDS spectra of each species present in the reduced 1.1Ni-0.8Co-Al catalysts. The inset table displays the quantification of each species from EDS analysis.	177
Figure B.1	N_2 physisorption isotherms of the catalytic materials post-calcination utilized in this study. The catalysts are arbitrarily offset from 0 to display clearly. The $P/P_0 = 0$ offset of each catalysts were 100 cm^3/g.	179
Figure B.2	XRD patterns of each catalyst after filtration and drying and before calcination. The patterns have a y-axis offset to display each clearly.	180
Figure B.3	Conversion of FAL vs. time on stream for 3Co-0.25Fe-0.75Al with various particle sizes.	181
Figure B.4	Conversion and selectivity (2-MF and FAL) vs. time on stream for furfural reaction displayed in Table 2; Reaction conditions: 180 °C and 1 atm, W/F ($g_{cat}*h*mol^{-1}$) = 3.63, substrate: FUR.	185

Figure B.5	X-ray photoelectron spectroscopy (XPS) of the 3Co-0.25Fe-0.75 sample before and after reduction/passivation. Co species of the reduced and unreduced sample (right). Fe species of the reduced and unreduced sample (left).	186
Figure B.6	X-ray absorption near edge spectrum of Co k-edge for various Co-Fe-Al oxides before reduction and post-calcination; Also displayed are some standards used.	187
Figure B.7	Normalized XANES spectrum of Co k-edge of each 3Co-xFe-yAl after reduction at 500 °C; Also displayed with some standards used.	187
Figure B.8	Normalized XANES spectrum of Fe k-edge collected before reduction for each catalyst before reduction and post-calcination; Also displayed with some standards used.	189
Figure B.9	Normalized XANES spectrum of Fe k-edge of each 3Co-xFe-yAl after reduction at 500 °C; Also displayed with some standards used.	189
Figure B.10	Fourier transformed EXAFS of Co k-edge of 500 °C reduced 3Co-0.25Fe-0.75Al catalysts at k weight, k^2. This demonstrates an example fit conducted on the catalysts.	190
Figure B.11	Fourier transformed EXAFS of Fe k-edge of 500 °C reduced 3Co-0.25Fe-0.75Al catalysts at k weight, k^2. This demonstrates an example fit conducted on the catalysts.	190
Figure B.12	TGA/DSC profiles of catalysts post-reaction when FAL is fed for approximately 180 min. Top-left: 3Co-Al, Top-right: 3Co-0.25Fe-0.75Al, Bottom-left: 3Co-0.5Fe-0.5Al, Bottom-right: 3Co-0.75Fe-0.25Al.	191
Figure C.1	XRD patterns of each catalyst after filtration and drying and before calcination. The patterns have a y-axis offset to display each clearly.	193
Figure C.2	TPR profile of the catalysts after reduction and passivation. The reduction temperature is indicated after the catalyst name.	194
Figure C.3	Temperature: 140 °C, Pressure: 4 MPa of H_2, Reaction time: 1 h, 0.25Cu-2.75Co-Al/Furfuryl Alcohol/Solvent: 25 mg/500 mg/ 50 mL.	195
Figure C.4	Conversion of FAL time on stream data for 0.25Cu-2.75Co-Al after different pretreatment temperatures. The data displayed	199

include conversion and selectivity towards to the two major products (THFA and 1,5-PD).

Figure C.5 Co XPS spectra, 2p, of 0.25Cu-2.75Co-Al after reduction in a flow reactor and passivation. A) No reduction; b) 300 °C reduction; c) 400 °C reduction; d) 500 °C reduction. 200

Figure C.6 Cu XP spectra, 2p, of 0.25Cu-2.75Co-Al after reduction in flow reactor and passivation. A) No reduction; b) 300 °C reduction; c) 400 °C reduction; d) 500 °C reduction. 200

Figure C.7 Deconvolution of XPS Spectra of Co species for 0.25Cu-2.75Co-Al catalyst displayed in Figure 4.8. These catalysts have been reduced at their respective temperature for 1 h, passivated at room temperature for 1 h in 1% O_2, and re-reduced in the batch reactor to 180 °C. a) 300 °C reduction; b) 400 °C reduction; c) 500 °C reduction. 201

Figure C.8 XANES spectra of the Co K-edge after calcination and prior to any reduction. 203

Figure C.9 XANES spectra of the Co k-edge for various Cu-Co-Al oxides; Also displayed are some standards used. Post-reduction and prior to passivation. 203

Figure C.10 XANES spectra of the Co k-edge for various Cu-Co-Al oxides; Also displayed are some standards used. Post-passivation. 204

Figure C.11 Fourier transformed EXAFS spectra of the Co k-edge collected before reduction for each catalyst; displayed with some standards used. Post-reduction and prior to passivation. 204

Figure C.12 Fourier transformed EXAFS spectra of the Co k-edge collected before reduction for each catalyst; Also displayed with some standards used. Post-passivation. 205

Figure C.13 Fourier transformed EXAFS of the Co k-edge of reduced (300 °C) 0.25Cu-2.75Co-0.75Al catalysts at k weight of k^2. This demonstrates an example fit conducted on the catalysts. Post-passivation. 205

Figure C.14 Fourier transformed EXAFS of the Co k-edge of reduced (400 °C) 0.25Cu-2.75Co-0.75Al catalysts at k weight of k^2. This demonstrates an example fit conducted on the catalysts. Post-passivation. 206

Figure C.15 Fourier transformed EXAFS of the Co k-edge of reduced (500 °C) 0.25Cu-2.75Co-0.75Al catalysts at k weight of k^2. This 206

demonstrates an example fit conducted on the catalysts. Post-passivation.

Figure C.16 XANES linear combinations of the catalysts after pretreatment (reduction at 400 °C for an h and passivation for 1 h). Related to Figure C.10. 208

Figure C.17 XANES of the Cu K-edge post-calcination and prior to any reduction. 209

Figure C.18 XANES spectra of the Cu k-edge for 0.25Cu-2.75Co-Al oxides pretreated at different reduction temperatures and with a room temperature passivation for 1 h; Also displayed are some standards used. 210

LIST OF COMMON ABBREVIATIONS

FUR	Furfural
FAL	Furfuryl Alcohol
HMF	Hydroxymethylfurfural
THFA	Tetrahydrofurfuryl Alcohol
2-MF	2-Methylfuran
2-MTHF	2-Methyltetrahydrofuran
1-POH	1-Pentanol
2-POH	2-Pentanol
THF	Tetrahydrofuran
1,2-PD	1,2-Pentanediol
1,5-PD	1,5-Pentanediol
CPO	Cyclopentanone
GVL	γ-Valerolactone
LA	Levulinic Acid
MMO(s)	Mixed Metal Oxide(s)
LDH(s)	Layered Double Hydroxide(s)
XAS	X-ray Absorption Spectroscopy
XRD	X-ray Diffraction
XPS	X-ray photoelectron spectroscopy
ALD	Atomic Layer Deposition
HDO	Hydrodeoxygenation

SUMMARY

The demand for energy and chemicals derived from petroleum continues to increase due to the rise in the global population and quality of life. As a result, it is important to find new alternatives to supplement petroleum resources to increase sustainability and reduce risk in the energy and chemical markets. Lignocellulosic biomass (2^{nd} generation biomass) has been identified as a promising renewable resource since it is inedible, more abundant, and cheaper component of biomass. Significant progress in the field of catalysis has been made regarding upstream lignocellulose processing (breaking down the oligomeric molecules to platform chemicals), while downstream catalytic processing to create value-added products requires improvements. Consequently, more fundamental research needs to be conducted on converting biomass platform molecules into fuel additives and specialty chemicals utilizing heterogeneous catalysis.

The aim of this dissertation was to investigate the conversion of furanics (mainly furfural), which have been identified as a top platform molecule derived from hemicellulose, into value-added products. Additionally, it was sought to develop heterogeneous multi-metal catalysts without precious metal additions to selectively and actively produce products to reduce downstream separation and reaction costs to create a more economical process. It was identified that tuneable, versatile, thermally stable, and porous multi-metal catalysts could be easily synthesized through the thermal treatment of layered double hydroxides (LDHs). Generally, the studies in this dissertation focused on changing the metal combinations in the LDH precursor to create active mixed metal oxide (MMO) after reduction for various furanic chemistries.

The first aim focused on studying the effects of different metal additions in a Ni based MMO catalyst for the vapor phase hydrogenation of furfural. Ni-Mg-Al and Ni-Co-Al with varying metal ratios were reduced under H_2 atmosphere and subsequently, tested for the conversion of furfural into furfuryl alcohol and tetrahydrofurfuryl alcohol at multiple conversions. It was determined that the yields towards hydrogenation products did not vary significantly, but it was observed that the Ni-Co-Al catalysts had a higher activity on a per site basis compared to Ni-Mg-Al. Multiple characterization techniques including microscopy and spectroscopy suggested that the materials were highly dispersed before and after reduction and that Ni-Co may form an alloy post-reduction.

Building off the Ni based studies, Co-Al based MMOs were shown to have promising yields towards 2-methylfuran, a potential fuel additive. Further studies were done to investigate the effects of adding in an oxophilic promoter such as Fe in an aim to increase the selectivity and activity towards 2-methylfuran. In tandem with reactivity studies that demonstrated the enhancement when Fe was doped in the Co-Al matrix, spectroscopic experiments were conducted that suggested that upon reduction the Fe was well incorporated into Co metallic particles.

The third objective of this thesis was to evaluate the activity of MMO materials on the ring-opening of furanic compounds into renewable diols. By exploiting the tunability of the MMO synthesis, Cu-Co-Al was identified as a promising multi-metal catalyst that displayed high yields towards 1,5-pentanediol, a potential poly(ester) precursor, in liquid phase batch under H_2 pressures. Pathway experiments were conducted to suggest that an unsaturated or partially saturated ring was the active species; however, a full saturated compound was inactive under these conditions. Multiple characterization techniques

probed the electronic environment of the catalysts and suggested that both CoO and Co^0/Cu^0 species were located on the surface prior to reaction.

Though the above objectives displayed the promising aspects of various MMO materials for furanic chemistries, the complexity of the materials made it difficult to full understand reaction mechanisms and active sites. Consequently, the final objective was to stray away from LDH based materials, and develop a method to create well-defined multi-metal catalysts. The aim of the last project was to design and construct an atomic layer deposition instrument to control metal deposition on an oxide support in an effort to move towards more well-defined catalysts for furanic conversion. This transition was done with the outlook that future projects will utilize this equipment to develop materials for not only catalysis, but also separations.

CHAPTER 1 INTRODUCTION

1.1 Motivation

Rising population levels and increasing economic development in the world has intensified energy demands, consumer chemicals demands, and resource diversification demands. One outcome has been a surge in shale gas production, and this rise in production of fossil resources will continue for the foreseeable future.[1] However, it has become ever more important to not rely solely on one energy and/or chemical resource, especially due to the recent volatility in the petroleum market. Additionally, fossil fuels release significant amounts of greenhouse gases into the atmosphere, which has driven researchers and industries to seek cleaner sources of fuel and chemicals. Not only do petroleum resources make up a large portion of our energy consumption, but also petroleum resources are traditionally used to produce commodity chemicals such as adhesives, cosmetics, inks, paints, polymers, surfactants, etc. Therefore, both academia and industry have begun to increase focus on creating processes to derive both fuel additives and consumer products from renewable resources to create a more sustainable future.

Biomass is one such renewable source of carbon that can supplement petroleum because unlike wind and solar, biomass is a renewable resource that can be used as a feedstock to create both fuels and value-added chemicals.[2–4] Ideally, biomass feedstocks that do not compete with food sources would be used to supplement the fuel and chemical industry; therefore, breaking down 2nd generation biomass (i.e. crop and tree residues) instead of 1st generation biomass would be chosen as the starting material. Fortunately, lignocellulosic biomass is also cheaper and more abundant, making it a superior feedstock

over 1st generation biomass for both fuel and chemical production.[1,5] For these reasons, researchers have been developing methods to selectively break down lignocellulosic biomass into platform molecules, which can then be further converted into fuel additives and specialty chemicals using heterogeneous catalysis, homogeneous catalysis, or bio-catalysis. Various advances in upstream biorefining including fermentation, gasification pyrolysis, acid hydrolysis, enzymatic hydrolysis of lignocellulose have made the downstream processing of platform molecules, such as furanics, more attractive.[5–10] Therefore, the interest in developing more economic processes for converting bioderived molecules has gained significant traction in the scientific community, especially in the field of heterogeneous catalysis.[11] The work presented in this thesis investigates utilizing non-precious metals to covert furanic compounds into specialty chemicals and fuel additives and utilizing various characterization techniques to understand the catalytic materials.

1.2 Catalysis for Furanic Conversion

As mentioned above, this work is motivated by the desire to reduce the world's dependence on petroleum resources by developing more economic processes for biomass conversion. More specifically, developing lower cost catalysts with higher activities and selectivities to desired value-added products would significantly reduce separation costs in the downstream biomass processing. One class of downstream biomass derivatives is furanic compounds such as furfural (FUR) and hydroxymethylfurfural (HMF). These molecules have been identified as top biorefinery platform chemicals, and they are the major components of bio-oil derived from pyrolysis of lignocellulose.[8,12–14] Current commercial production relies on acid-catalyzed dehydration of sugars that come from

agricultural waste. Furthermore, FUR was being produced on the scale of 10^5 tons/year in 2013.[14]

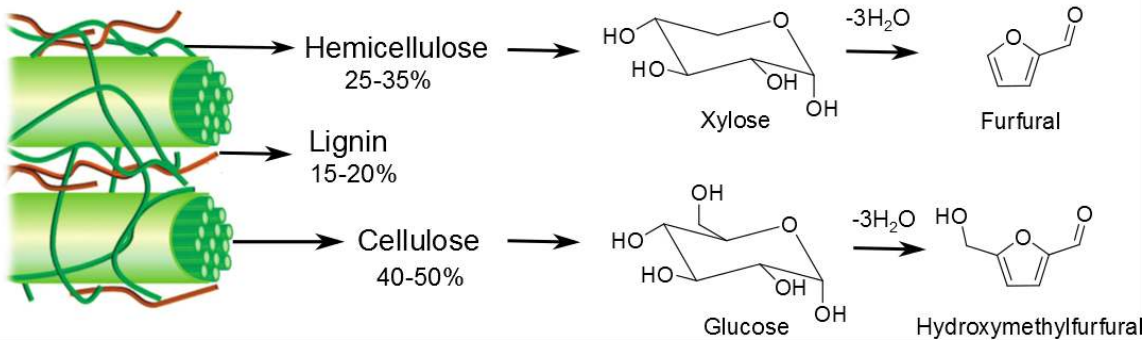

Figure 1.1 – Example acid dehydration pathway to create furanic compounds from lignocellulosic biomass. Modified with permission from The Royal Society of Chemistry.[1]

FUR is a critical bioderived platform molecule, and it is a unique compound due to the wide variety of reaction pathways towards value-added products that are possible. This makes FUR a good model compound to investigate how selective a catalyst is towards a specific product and can a catalyst be tuned to choose a desired pathway. The major products to which FUR can be converted using heterogenous catalysis, typically in the presence of H_2, are shown in Figure 1.2 (note the colored molecules are associated with the different target molecules for each objective). These pathways include hydrogenation, hydrogenolysis, decarbonylation, coupling, etc. Although Figure 1.2 displays a wide variety of pathways, there are significantly more reaction pathways that have been investigated that are not relevant to this thesis.[12]

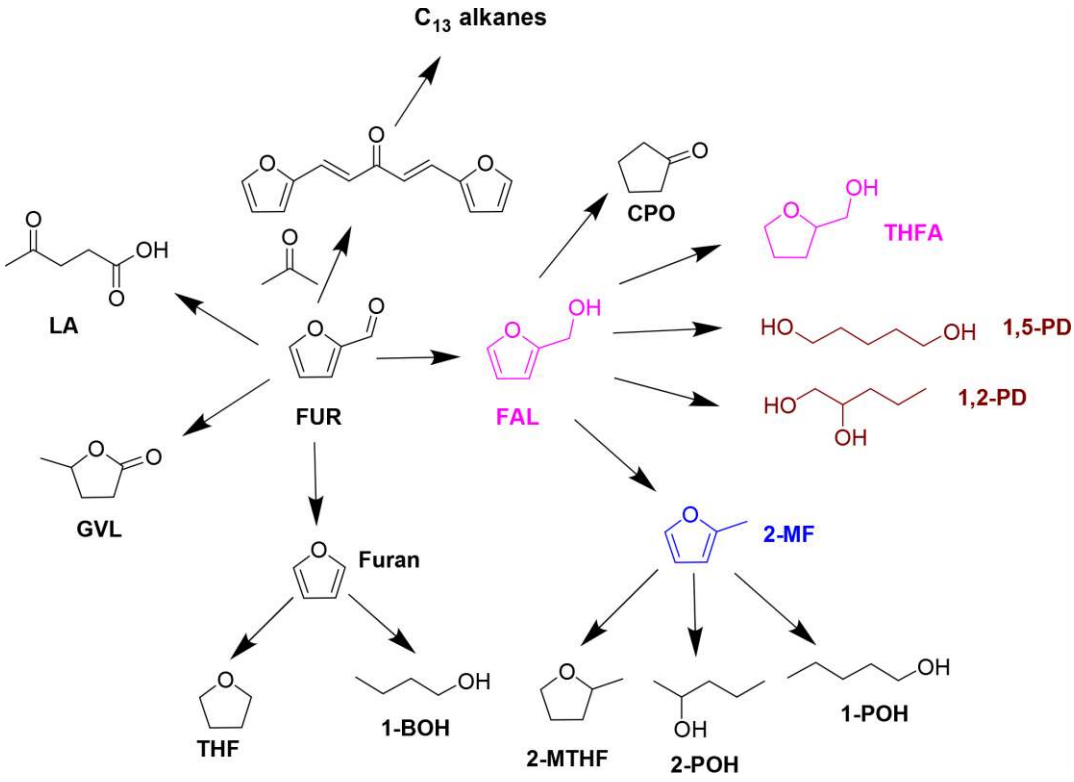

Figure 1.2 - Major proposed pathways of FUR to value added products. Pink: 1st objective target molecules; Blue: 2nd objective target molecule; Maroon: 3rd objective target molecules.

1.2.1 Single Metal Catalysts for Furanic Conversion

Early studies on furanic conversion through heterogeneous catalysts have been conducted both under vapor phase and liquid phase conditions, and these studies provide the benchmarks for this thesis. Industrially, copper-chromite catalysts have been used for hydrogenation of FUR, but due to the potential environmental hazards of some chromite species, continued research has sought to develop other transition metal catalysts.[14,15] Regarding single metal catalysts (one fully reduced metal), most of the transition metals supported on inert oxides or carbon have been studied for the conversion of furanic compounds. The most common routes of FUR conversion with single metal catalysts are the hydrogenation of the aldehyde to furfuryl alcohol (FAL), full saturation to

tetrahydrofurfuryl alcohol (THFA), or decarbonylation towards furan. Each of these bio-based products can be used as solvents, resins, or polymer precursors, but further conversion can result in other value-added chemicals as well.[12,13] One of the pioneering studies in FUR conversion was from Resasco et al., in which a comparative study was conducted between Cu, Ni, and Pd supported on SiO_2 for the vapor phase hydrogenation of FUR under high H_2 concentrations.[16] Through various temperature studies (210 °C – 250 °C) and a range of conversions, three proposed mechanisms for FUR hydrogenation are discussed that tailor to each metal (depicted in Figure 1.3).

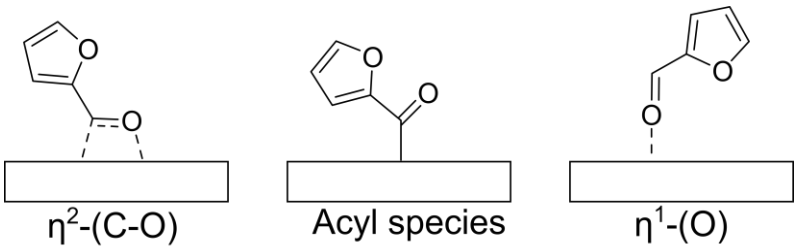

Figure 1.3 - Proposed mechanism of FUR adsorption over metals.

In regards to Cu/SiO_2, only FAL and 2-methylfuran (2-MF) are observed over a wide range of temperatures and conversions, which supports a few other studies with Cu metal.[17–20] More recent studies also have shown that Cu supported on oxides other than SiO_2, such as ZnO and CeO_2, demonstrate promising aldehyde hydrogenation yields in the gas phase.[21,22] This suggests that the adsorption of FUR primarily proceeded through η^1-(O) due to the repulsive interactions of the satisfied 3d band and the anti-bonding orbital of the aromatic furan ring.[16] These results are also further supported by Density Functional Theory (DFT) calculations performed of a Cu(111) surface that has demonstrated that the furan ring is repelled from the surface.[23] Unlike Cu/SiO_2, Pd and Ni (Group VIII metals) supported on SiO_2 have demonstrated that not only is FAL formed, but also THFA and

decarbonylation products (furan and tetrahydrofuran, THF), which suggests that both metals can adsorb FUR through a η^2-(C,O) or acyl species. Furthermore, Ni and Pd have increased interaction with the furan ring, resulting in higher ring-saturated products.[16] Lastly, it is observed that the activity (turnover frequency, TOF) proceeded as follows: Pd > Ni > Cu. An in depth adsorption study including temperature programmed desorption (TPD) and DFT on the Pd(111) surface complemented reaction studies by elucidating the FUR and FAL pathways towards furan, 2-MF, and full decomposition.[28,29] Pt, another Group VIII metal, monometallic catalysts have also been thoroughly investigated for the hydrogenation of FUR.[24–27] Like Ni and Pd, Pt has been reported to produce both FAL and furan in the vapor phase (~200 °C) over various supports, suggesting that the η^2-(C,O) or acyl species are preferential. Further work has shown that Pt particle sizes and surface facets are major factors in the selectivity of FAL and furan; the general trend is smaller Pt nanoparticles prefer furan (~1-2 nm) while larger particles produce more FAL, when converting FUR.[25,26] Finally, studies in the liquid phase have investigated single metal catalysts for the hydrogenation of FUR to FAL such as Co/SiO_2,[30] Ru/UiO-66,[31] Pt/C,[32,33] Cu/Al_2O_3,[34] and Pd/SiO_2,[35] but there are limitations to these studies such as high hydrogen pressures, side reactions, and use of costly metals.

Further hydrogenation of FUR/FAL to THFA has also been studied utilizing single metal catalysts. Ni metal supported on silica have been studied in the vapor phase and display high yields towards THFA, the fully saturated compound (~94% yield at 140 °C).[36] This pathway requires FAL to adsorb flat onto the surface where the ring is subsequently hydrogenated to THFA. Consequently, single metal Cu catalysts are generally unable to produce THFA in vapor or liquid phase due to the repulsion effect upon the aromatic ring.

This repulsion is absent with a majority of Group VIII metals, which allows the ability to adsorb the furanic ring and hydrogenate it.[12] Other precious metal catalysts have been investigated mainly through liquid phase studies on complete saturation of FUR. For example Ru supported on various metal oxides including $MgAl_2O_4$, MnO_x, NaY, and TiO_2 all demonstrate high yields towards THFA at mild temperatures.[37,38]

In general, single metal catalyst studies provide a great deal of information on how FUR and FAL adsorbs onto the surface of the metal species. However, single metal catalysts tend to lack either in activity or selectivity compared to other catalysts such as those based on multi-metals. Though much of the pioneering work has been conducted on single-metal catalysts for furanic conversion, the more recent and promising routes involve synthesizing multi-metal or multi-functional catalysts to investigate not only hydrogenation pathways, but also, hydrogenoylsis, ring-opening, coupling, etc.

1.2.2 Multi-Metal and Multi-Functional Catalysts for Furanic Conversion

As mentioned above, the current focus in biomass conversion has shifted towards designing and synthesizing more complex catalysts to selectively target a product. This can be done in several ways such as introducing an additional metal, additional metal oxide, a non-metal promoter, or changing the synthesis method. All of these possibilities try to target one or more aspects: improved activity, improved selectivity, and/or improved stability.[1] The most common way to achieve one of the goals above is to introduce a secondary or tertiary metal or metal oxide to either create a bimetallic or bifunctional catalyst. Though it can be difficult to discern during experimentation, it is important to differentiate between bimetallic and bifunctional in this discussion. Bimetallic catalysts

refer to a system with two fully reduced metals that can have geometric effects, electronic effects, stabilizing effects, and/or synergistic effects.[1,39] On the contrary, bifunctional catalysts typically do not contain two fully reduced metals, instead two metals have separate characteristics that cooperate in the reaction mechanism such as metal – acid, metal – base, or metal – metal oxide. Both types of catalysts can be effective in furanic conversion due to the ability to more selectively choose a reaction pathway. In the rest of this sub-chapter, multiple examples of bimetallic and bifunctional catalysts for furanic chemistries including hydrogenation, hydrogenoylsis, and ring-opening will be presented. Additionally, some pertinent examples will be presented that do not have multi-metal systems, but through synthesis methods have created unique bifunctionalities. Finally, reaction pathways including rearrangement, coupling, oxidation, and hydrolysis are not outlined below, but the reader can refer to other comprehensive reviews of furanic conversion.[5,12–14]

1.2.2.1 Hydrogenation

As mentioned above the most well-studied pathway is the hydrogenation of FUR to FAL and/or THFA, which again are potential solvents, resin precursors, or intermediates to other chemicals. In regard to multi-metal systems, few studies have focused on the vapor phase hydrogenation of FUR to FAL or THFA. Most of these vapor phase studies have looked into adding metals besides Cr to Cu such as Pd,[40] Co,[41] and Ca,[42] which all have shown high yields towards FAL from FUR, and had comparable if not better yields than single metal Cu. However, these catalysts display minimal affinity towards THFA, which suggests Cu still had a major electronic impact in the bimetallic matrix.

Though there are few vapor phase studies with bimetallics, many other studies have investigated bimetallics for liquid phase hydrogenation of furanics. The most notable bimetallic mixture was the addition of Sn to Pt or Ni, which have shown promising results in the hydrogenation of FUR to FAL due to the high selectivity.[43,44] Due to the oxophilicity of Sn when reduced, the Sn selectively adsorbs the C=O, which then is subsequently hydrogenated by the adjacent noble metal that dissociates H_2.[14,44,45] Further advancements utilizing Sn as an oxophilic promoter for FUR hydrogenation have been studied, such as creating encapsulated Pt-Sn bimetallic nanoparticles to increase Pt-Sn interactions.[46] Recently, a few other bimetallic systems have been studied for the liquid phase hydrogenation of FUR to FAL including Cu-Co/SBA-15[47] and Pd-Cu/MgO,[48] which have obtained yields of FAL greater than 80% with operating temperatures of 170 ºC and 110 ºC, respectively.

Investigations into the series reaction of FUR to FAL to THFA have been thoroughly studied with multi-metal systems; however, these studies mainly focus on utilizing high H_2 pressure batch reactors instead of plug flow reactors. For example, Pd was mixed with Ni to create a more active catalyst than the monometallic, and it has displayed about a 96% yield at mild temperatures and 8 MPa of H_2.[49] In that study, it has been demonstrated that other furanics such as HMF could be converted into their fully ring-saturated product as well. This same bimetallic combination has been tested utilizing another support, TiO_2-ZrO_2 instead of SiO_2, and it has demonstrated similar results.[50] Lastly, Tomishige has provided evidence that a Pd-Ir/SiO_2 had superior performance for the total hydrogenation of FUR compared to other precious metal combinations (Pd-Pt, Pd-Rh, and Pd-Ru) at room temperature and 8 MPa of H_2 pressure.[51]

Though some metal combinations have been studied for the hydrogenation of FUR in both the vapor phase and liquid phase, most of the studies consist of catalysts based on expensive precious metals or are conducted under high H_2 pressures and low throughput. Consequently, more multi-metal systems need to be investigated to better understand how such catalysts interact with the highly-oxygenated biomass molecules.

1.2.2.2 Side Chain Hydrogenolysis

Another crucial reaction pathway for creating value-added products from furanics is hydrogenoylsis, which typically removes oxygen from the oxygenated compounds. Generally, hydrogenolysis is the breaking of a C-C or C-heteroatom bond, mainly C-O, C-N, or C-S, by hydrogen, but C-O bond cleavage is the most common chemistry in biomass conversion. In regards to furanic hydrogenolysis, the focus is on breaking the C-O bond located on the methyloxy side chain without going through a decarbonylation pathway. For FUR and HMF, side-chain hydrogenolysis results in the production of 2-MF or 2,5-dimethylfuran (2,5-DMF), respectively, which are promising fuel additives due to their higher research octane numbers than ethanol and lower water solubility than ethanol.[52] Also, these molecules are precursors in forming toluene and *p*-xylene through the Diels-Alder mechanism.[53,54] For these reactions, it is crucial to avoid C-C bond breakage that creates products such as furan; therefore, designing catalysts to selectivity cleave the C-O would help create an economic process that can supplement petroleum in the fuel sector.

Most of the catalysts that have been studied for this reaction involve multi-metal systems or single metal catalysts that through synthesis or pre-treatment methods have created bifunctionalities. Typically, single metal catalysts have low selectivities towards 2-

MF or 2,5-DMF, which requires additional promoters and metals to drive the reaction towards breaking the C-O bond. A few notable vapor phase studies have been conducted on both precious and non-precious metals. Very early works on FUR or FAL to 2-MF have been conducted in the vapor phase with Cu-Cr catalysts and Cu-Fe catalysts, which both display high yields (≥ 80%) in the vapor phase at temperatures above 200 °C; however, these studies do not investigate the mechanism or deactivation of the catalysts.[55,56] Additionally, TPD and high resolution electron energy loss spectroscopy (HREELS) experiments have demonstrated a higher affinity towards 2-MF on Ni(111)-Cu(111) bimetallic surfaces.[57] In one of the most recent influential works, Resasco et al. conducted investigations into the bimetallic Ni-Fe supported on silica for the vapor phase hydrogenolysis of FUR and FAL to 2-MF.[58] When FAL is utilized as the feed, a yield of about 78% towards 2-MF is achieved (5wt% Ni – 2 wt.% Fe/SiO_2 at 250 ºC), which is attributed to the oxophilic nature of the Fe addition. According to their DFT calculations, the Fe addition stabilizes the η^2(C,O) bonding more than the pure Ni surface, and suppresses the acyl species formation to decrease decarbonylation products.[58]

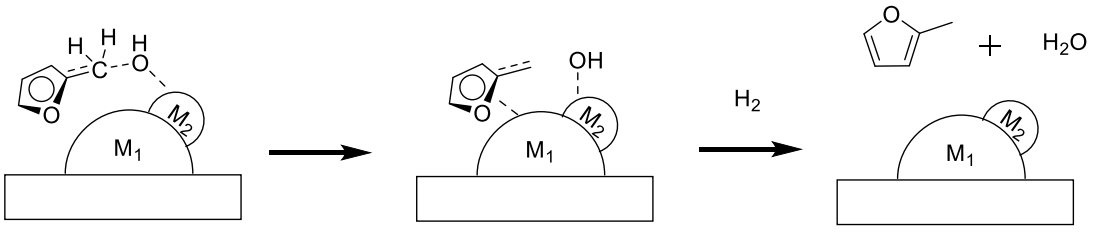

Figure 1.4 – The reaction of FAL over a bimetallic catalyst containing M_1 (noble metal) and M_2 (oxophilic metal) to produce 2-MF.[58]

Another bimetallic combination, Pt-Zn, has been explored utilizing TPD and HREELS, which also suggests that the oxopholicity of the metallic Zn particle allowed for

higher affinity towards side-chain hydrogenoylsis of FAL.[59] This study inspired other works that exploit the oxophilicity of metallic Fe such as Ni-Fe/Al_2O_3 investigating hydrodeoxygenation in the vapor phase of many bio-oil model compounds including FAL.[60] Additional studies with Fe as a promoter have been investigated including Cu-Fe/SiO_2[61] and reduced Co-Fe-Al mixed metal oxide (MMO) materials,[62] which will be discussed further in Chapter 3. Lastly, Pd-Fe/SiO_2[63] and Ni-Fe/C[64] have been investigated for the liquid phase and vapor phase hydrogenolysis of FUR and FAL and have shown to obtain optimum yields of ~80% towards 2-MF.

The above-mentioned catalysts mainly focus on exploiting the oxopholicity of one metallic species in the system; however, other catalysts without a second metal have been studied for the hydrogenolysis of FUR and FAL. Unlike systems containing an oxophilic and noble bimetallic combination, these catalysts have bifunctionalities (i.e. metallic-acid) that can selectively produce 2-MF. For example, through a co-precipitation method Cu based catalysts were embedded in oxide supports such as SiO_2, Al_2O_3, and ZnO, and utilized in a vapor phase flow reactor.[20,65] The screening studies have indicated that the Cu/SiO_2 catalyst is superior due to the formation of a copper phyllosilicate phase along with metallic copper, which results in a significant increase in acid sites, as determined by NH_3 TPD. This additional acidic functionality results in high yields towards 2-MF (~95%) at 200 °C when FUR is fed.[65] Another bifunctional catalyst that has been explored for the hydrodeoxygenation (HDO) of FUR was Mo_2C, which has achieved a 55% yield towards 2-MF at 150 °C. Interestingly, kinetic analysis suggests there was a “metal-like site” along with an additional site, either carbidic, oxycarbidic, or oxide site.[66,67] Further DFT studies

on a Mo_2C (101) slab also supports the hypothesis that the Mo_2C contained two sites in which one adsorbed the furanic compound while the other site dissociated H_2.[68]

Most of the above examples focus on vapor phase reactions of FUR or FAL, but some prior literature has observed 2-MF production in liquid phase reactions. Thorough work has been conducted on Ru based catalysts mainly on transfer hydrogenation to produce 2-MF from FUR in the liquid phase between 120 – 200 ºC and has achieved approximately 61%-76% yield.[69,70] Vlachos et al. claims that the Ru species is partial reduced resulting in a Ru/RuO_2 bifunctional combination that could conduct transfer hydrogenation between 2-propanol and FUR to produce 2-MF and acetone. This Meerwein-Ponndork-Verley reaction is further supported by a DFT study and a deuterium labelled study that shows that H_2 can readily occupy Ru_{cus} sites on an RuO_2 surface adjacent to a Lewis acid site. This results in C-O bond cleavage to produce 2-MF.[71,72]

Though this thesis focuses on the conversion of FUR and its derivatives, it is important to identify catalysts utilized in the conversion of HMF to help design better materials. HMF contains both an alcohol and aldehyde functional group attached to the furan ring, and this molecule can be converted into 2,5-DMF, which has similar promising fuel additive characteristics as 2-MF. This requires the breaking of two C-O bonds, which creates additional pathways and complexity; however, some catalysts have been used for both FUR and HMF hydrogenolysis such as Ru/C.[70,73] Since HMF has a high boiling point and can decompose at high temperatures, reactions are typically conducted in liquid phase batch reactions between 130 °C – 220 °C. Many catalysts including Ni/Co_3O_4,[74] Ru/Co_3O_4,[75] Ru/Mg-Al,[76] Ni-W_2C/C,[77] Cu-Mg-Al MMO,[78] Ni/SiO_2 (phyllosilicate),[79] and PtCo/C nanospheres[80] have displayed yields towards 2,5-DMF between 58% - 98% in

liquid phase batch reactions under H_2 pressure. Lastly, Dumesic et al. has demonstrated that yields of 76% of 2,5-DMF can be produced starting from fructose in a biphasic reactor with a dehydration step and then a subsequent hydrogenoylsis step utilizing a Cu-Ru/C catalyst.[52]

1.2.2.3 Ring-Opening

Other than hydrogenation and side-chain hydrogenolysis, an interesting reaction pathway for furanic conversion is ring-opening to produce diols. This reaction can be categorized as a hydrogenoylsis reaction since it requires the breaking of the C-O bond of the cyclic ether using H_2. The two major products of FUR ring-opening are 1,5-pentanediol (1,5-PD) and 1,2-pentanediol (1,2-PD), which could be used as potential monomers in resins and poly(ester)s, resulting in rapid developments in this area.[81] In general, these reactions must be conducted in the liquid phase in the presence of H_2 due to the high boiling points of the diol products (>205°C), and the likelihood of unwanted side-reactions above these temperatures in the vapor phase. Most of the prior art presented below was conducted in liquid phase batch or flow reactors under high hydrogen pressures. The first study on ring-opening of FUR to 1,5-PD and 1,2-PD has been conducted over a Cu-Cr catalyst at temperatures above 175 °C and very high hydrogen pressures (10-15 MPa), and has demonstrated yields of approximately 40% towards 1,2-PD and 30% towards 1,5-PD.[15]

After the initial Cu-Cr work, no reports to my knowledge regarding ring-opening of furanics were presented until Tomishige et al. demonstrated the ring-opening of THFA to 1,5-PD over a Rh-ReO_x/SiO_2 in liquid phase batch conditions.[82] This communication claims that Rh is in a fully reduced state while Re was partially oxidized, which results in

a bifunctional catalyst. They have achieved approximately 80% yield towards 1,5-PD after a 24 h reaction at 120 °C, water as a solvent, and 8 MPa of H_2.[82] After this discovery, many papers have followed to screen other bifunctional combinations and elucidate the mechanism THFA ring-opening. For example, other bifunctional catalysts including Rh-MoO_x/SiO_2, Rh-WoO_x/SiO_2, Ir-ReO_x/SiO_2, Ir-MoO_x/SiO_2, and Ir-WO_x/SiO_2 have been utilized for the ring-opening of THFA.[82–86] Another group has investigated effects of different noble metals (Pt, Pd, Ir, Ru, and Rh) with MoO_x supported on SiO_2 and conclude that the Ir-MoO_x and Rh-MoO_x catalysts are most efficient at 1,5-PD production.[87] Various spectroscopic experiments (X-ray absorption spectroscopy, XAS), CO chemisorption, and kinetic analysis suggest the oxophilic metal species (Mo, Re, and W) are decorated around the noble metal nanoparticles (Ir and Rh) in a partially oxidized state. It is important to note that the supports chosen were relatively inert (SiO_2 and C), which results in high interactions between the multi-metal systems.[81,88]

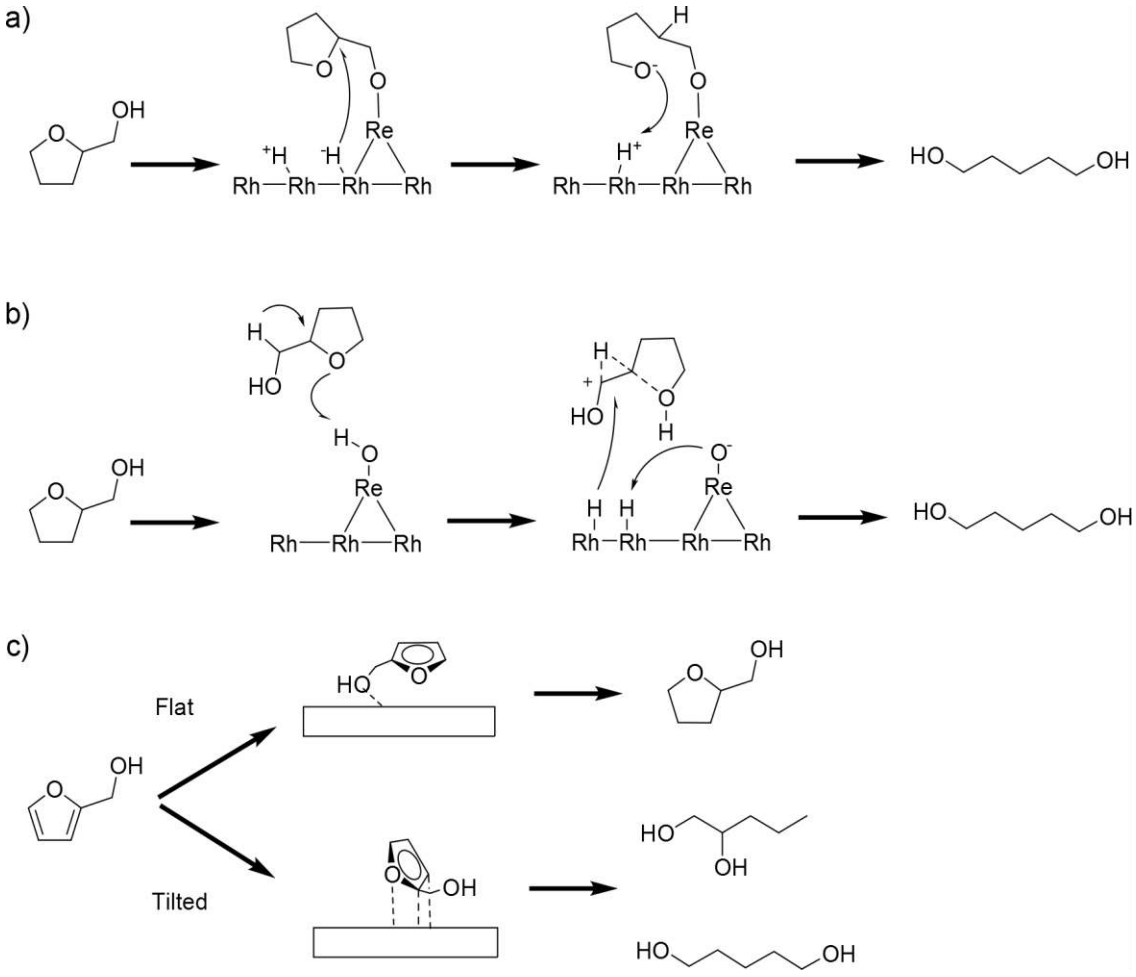

Figure 1.5 – Proposed pathways of the ring-opening of furanic compounds: a) Ring-opening of THFA through hydride pathway.[85] b) THFA ring-opening through acidic H.[89] c) FAL ring-opening over reduced MMO catalysts.[37,90] Figure a) and b) were modified with permission from [14]. Copyright 2013 American Chemical Society.

Further investigations of the mechanism have been conducted using kinetic analysis, deuterium-labelled experiments, and reactions of other cyclic ethers, which have resulted in the proposed mechanism displayed in Figure 1.5a.[85,86] It suggests that the oxophilic Re species readily adsorbs the alcohol, and the H_2 undergoes heterolytic activation on the adjacent noble metal species (Rh or Ir) forming a hydride species. This hydride species then attacks the 2-position of the alkoxide species, and undergoes a S_N2 reaction to break the C-O bond.[14]

In parallel to Tomishige's work, Dumesic et al. was also investigating the ring-opening of cyclic ethers including THFA utilizing Rh-MoO_x/C and Rh-ReO_x/C at 120 °C and 3.4 MPa of H_2 in water.[89] A wide range of cyclic ethers including tetrahydropyran, tetrahydrofuran, and 2-(hydroxymethyl) tetrahydropyran along with other diols and triols (i.e. glycerol, pentanediols, and 1,2,6-hexanetriols) have been utilized as substrates to determine the reaction mechanism. Additional DFT calculations have been conducted to determine the stabilization of possible intermediates. From these studies, the proposed mechanism (Figure 1.5b) involves an acidic proton located on the Re hydroxide species, resulting in the formation of a stable carbenium ion intermediate after reacting with the acidic proton.[89] Both mechanisms have been well studied and have their merit; however, it is also possible that more than one mechanism may be involved due to the complexity of these reactions.

Though the above examples describe the ring-opening of THFA, it is important to investigate the possibility of deriving 1,5-PD from the fully unsaturated furanic compound, FUR. Various multi-metal catalysts were screened in one study to determine the feasibility of deriving 1,5-PD starting from FUR in a one-pot synthesis. This has resulted in an optimized reaction procedure including a two-step process where a low temperature ring-saturation step (50 ºC) is employed followed by a high temperature ring-opening step (120 ºC).[91,92] For this one-pot reaction, a tri-metal catalyst has been utilized, Pd-Ir-ReO_x/SiO_2 or Rh-Ir-ReO_x/SiO_2, which seems to incorporate multiple active sites specific for each step. XAS data supported the hypothesis that there are negligible strong interactions between the two reducible metals or no bimetallic formation (Pd-Ir or Rh-Ir); however, the ReO_x particles decorated both metallic species.[91,92] It has been suggested that the Pd-ReO_x

particles perform the total hydrogenation, while the Ir-ReO_x particles perform the ring-opening. Although these studies provide evidence that 1,5-PD could be produced at high yields (max 78%) from FUR, they require the usage of three precious metals, long reaction times, and high H_2 pressures, making it a significantly less attractive route.

Ring-opening of other furanic compounds has been attempted utilizing the bifunctional catalysts containing expensive precious metals. Heeres et al. investigated the pathways into making 1,6-hexanediol, an important precursor in producing renewable nylon products, from HMF over Rh-ReO_x/SiO_2 combined with a solid acid catalyst.[93,94] For these catalysts, the pathway still requires the full saturation of HMF to 2,5-bishydroxymethyl tetrahydrofuran (BHMTF), which then can be ring-opened.[95] Also, another study has demonstrated that a series reactor with a dual zone catalyst bed that includes Pd/SiO_2 for hydrogenation and Ir-ReO_x/SiO_2 for the ring-opening reaction can convert HMF to 1,6-HD in one process.[96] In that work, 58% yield towards 1,6-hexanediol have been achieved, but the process still requires expensive metals and high H_2 pressures (7 MPa).

The above examples give a detailed outline of previous work conducted on the ring-opening of the fully saturated compound, either THFA or BHMTF, to renewable diols. Some accounts display the ability to convert FUR into 1,5-PD, but this requires the addition of multiple expensive metals and a two phase reaction process.[91] Though there has been significant advancement in THFA ring-opening, recent attention has been given to the conversion of the unsaturated furanic compounds such as FAL using other bifunctional catalysts. This allows for a one-step reaction process where both hydrogenation and ring-opening occur. A majority of these catalysts are derived from MMO materials or reduced

metals on highly active supports. Some of these catalysts are derived from layered double hydroxide (LDH) materials including Ni-Co-Al MMO,[90] Cu-Mg-Al MMO,[97] and Pt/Co-Al[98] and these are discussed in more detail in chapter 1.3. Outside of the LDH derived materials, Ru/MnO_x has demonstrated the ability to ring-open FAL to 1,2-PD with an optimum yield of 42% at 150 ºC and 1.5MPa of H_2 pressure.[37] The proposed mechanism is that FAL adsorbs on the surface and either partially hydrogenated and ring-opened or fully hydrogenated to yield THFA. This suggests that there are three parallel pathways to THFA, 1,2-PD, and 1,5-PD and giving rise to the general pathway proposed in Figure 1.5c.[37,90] More recently, Cu/Al_2O_3 and Ru/Al_2O_3 have shown relatively high selectivities towards 1,2-PD in the liquid phase ring-opening of FAL, 50% and 32%, respectively.[99,100] Finally, Co/TiO_2 has been used in the aqueous phase hydrogenation of FAL and has demonstrated about 30% yield towards 1,5-PD, which is mainly due to the strong-metal-support-interaction (SMSI).[101] All the catalysts described in this paragraph have shown their ability to ring-open the unsaturated furanic compound (FAL, 2-MF, or THF), but there are still many limitations including the use of expensive metals, low yields towards 1,5-PD, and little spectroscopic experiments to understand the structure of the bifunctional catalysts.

1.3 Layered Double Hydroxides Derived Catalysis

The above section describes how multi-metal catalysts have been utilized for various furanic chemistries either in the form of bifunctional, bimetallic, or catalysts combining both types of domains. Though there are many ways to synthesize multi-metal catalysts, a majority of the catalysts above are synthesized through traditional wetness impregnation on high surface area supports. However, this traditional method can lead to poor interaction

with the oxide support resulting in leaching and sintering of the metallic particles, especially when investigating base metals for liquid phase biomass processes and high temperatures.[101–103] Due to the possible irreversible deactivation pathways and potentially poor metal mixing, it is necessary to investigate other multi-metal catalysts for biomass processing. Consequently, the work in this dissertation involves investigating tunable and versatile multi-metal catalysts derived from LDH materials for the conversion of furanic compounds. Thermal treatment of LDH materials can yield catalytic materials with relatively high surface areas, high dispersion, and high thermal stability. In this section, a detailed introduction about LDH materials and their beneficial properties in catalysis is presented.

1.3.1 LDH Materials

LDH materials are hydrotalcite-like compounds and have become increasing useful in catalysis, adsorption, and medicine.[104] A hydrotalcite is a mineral found in nature with the formula $Mg_6Al_2(OH)_{16}CO_3 \cdot 4H_2O$, where the hydroxide and carbonate species balance the cationic charge formed by the Mg-Al complex. Therefore, hydrotalcite-like materials consist of metal cations counterbalanced with interlayer anions with a chemical formula of $[M^{2+}_{1-x}M^{3+}_x(OH)_2]^{x+}$ $(A^{n-}_{x/n}) \cdot mH_2O$. One benefit of these materials is their versatility: many different multi-metal systems can form the LDH structure including M^{2+} (Fe, Co, Ni, Mg, Cu, and Zn) and M^{3+} (Al, Co, Fe, Mn, and Cr).[104,105] These types of materials are synthesized through a simple co-precipitation method at a controlled pH (typically above pH 9), and must contain a M^{2+}/M^{3+} ratio between 1.5 – 4 to create the layered structure.[104–107] Without the creation of the layered structure there may be significant loss in surface area and /or poor dispersion. The experimental sections in future chapters will give more

detail of the preparation methods for materials in this dissertation. Varying synthesis methods, such as anion intercalation, nanocomposite assembly, or post-treatments methods, can allow for unique catalytic properties.[105] Of the post-treatment methods, calcination at high temperatures creates MMOs, which can be useful multi-metal materials. Including a reduction step post-calcination can result in supported metal catalysts containing bimetallic or bifunctional moieties depicted in Figure 1.6. Typically, upon reduction, these metal species are highly embedded in the matrix, which may result in increased stability and/or increased interaction between other metals/metal oxides in the system.

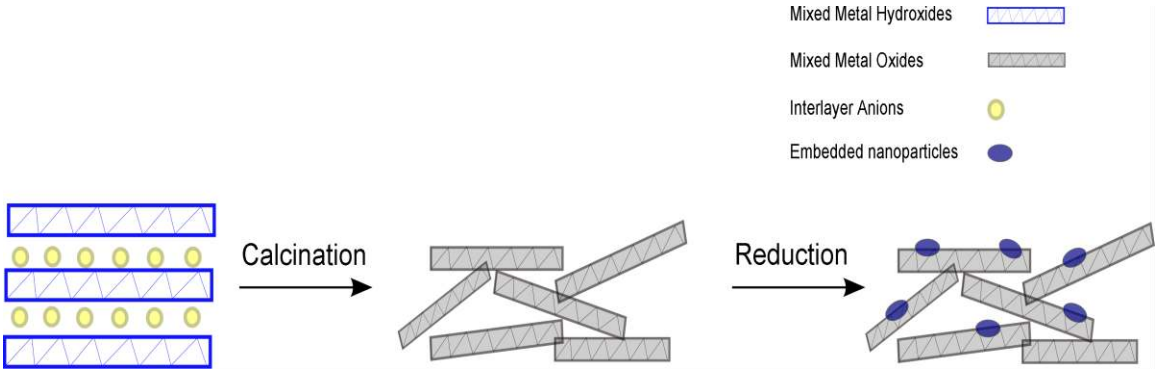

Figure 1.6 – General depiction of LDH materials exposed to various post-synthesis thermal treatments.

After filtering and drying the LDH material, X-ray diffraction (XRD) is an easy method to determine if the layered structure has been created. The sharp (003) and (006) peaks indicate that a crystalline layered structure with intercalated anions (CO_3^{2-}) in between each layer. After calcination, the organic layers and water are removed, which is observed by thermogravimetric analysis (TGA) and differential scanning calorimetry (DSC). Once the thermal treatment in air is complete, the resulting material is a less crystalline material with small, well-dispersed MMOs, possibly a solid-solution.[105] Since

the organic anions and water are removed during calcination, pockets are created within the material, increasing pore volume and accessible surface area. Along with tunability, the post-calcination MMO materials derived from LDHs can give enhanced catalytic properties, especially when multi-metal systems are included. Again, these materials can then be reduced in hydrogen, which can result in small embedded nanoparticles within an oxide "binder" or support.

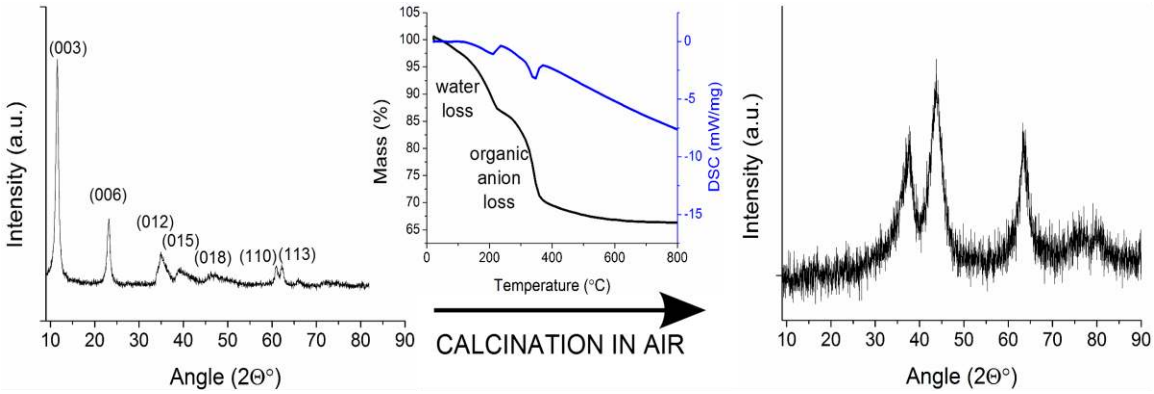

Figure 1.7 – (Left) Example XRD pattern of LDH material; (center): TGA and DSC plot during thermal treatment in air; (right) Example XRD pattern of MMO materials post-calcination at 400 °C.

Reduction of these MMO materials in H_2 allows for much greater tunability of these catalysts post-synthesis. Due to the high dispersity of each metal oxide post-calcination, there is high interaction among each oxide in the matrix, creating unique reduction profiles compared to traditional impregnation techniques.[108] Behrens et al. has conducted thermoanalytical analysis on a Cu-Zn-Al LDH material to determine how different reduction parameters affect the species evolution.[109] Transmission electron microscopy (TEM) and chemisorption analysis shows that after reduction the metallic Cu surface area (determined through N_2O chemisorption) is less than expected from calculated surface areas from TEM particle sizes. This suggests that due to the high dispersity of the LDH

matrix, the Cu particles are embedded into the oxide matrix, exposing less surface area. Although there may be less accessible sites, the TOF is much greater than catalysts made by traditional impregnation, suggesting the strong interaction with the oxides (possibly creating bifunctionalities) in the matrix.[109] Additionally, if multiple reducible metals are incorporated into the LDH matrix, it is possible to create small bimetallic nanoparticles even at high loadings of reducible metals.[108,110] Especially due to the high dispersity, this can allow for greater electronic changes within the MMO matrix upon reduction, and can be exploited for different furanic chemistries.

1.3.2 LDH Derived Catalysts for Biomass Conversion

Due to the recent developments in the LDH platform, very few investigations have been conducted on furanic compound conversion; however, some investigations mainly on Cu based LDH materials for the conversion of FUR to FAL have been attempted. For example, LDH derived Cu-Mg-Al and Cu-Zn-Al MMOs have been utilized for the liquid phase conversion of FUR to FAL, and it has been determined that the TOF for Cu-Mg-Al is twice that of Cu-Cr and five times greater than Cu/SiO_2.[111] Further work has also demonstrated the ability to use the Cu-Mg-Al for liquid phase transfer hydrogenation instead of relying on high H_2 pressures.[112] These studies suggest that there is a strong interaction between the Mg-Al oxide matrix and the embedded Cu particles which may have led to the observed increased activity, and it is possible that FUR is able to be activated by both the oxophilic Mg-Al oxide and metallic Cu.

Other hydrogenation studies include the use of a bimetallic Cu-Ni catalysts within a Cu-Ni-Mg-Al MMO matrix derived from LDH materials.[113,114] It has been demonstrated

that the bimetallic catalyst is more active than the reduced Ni-Mg-Al and Cu-Mg-Al catalysts for FUR hydrogenation to FAL. This is then followed up by another research group that has demonstrated that varying the Cu-Ni ratio along with reduction temperature results in different hydrogenation selectivities (FAL vs THFA) in the liquid phase hydrogenation of FUR.[115] These few investigations show the promise of utilizing catalysts derived from LDH materials for hydrogenation of furanic compounds due to the high dispersity and tunability of the metal species.

The other major reaction pathway that has gained recent attraction for LDH derived catalysts is ring-opening. In subchapter 1.2.2.3, a variety of catalysts are discussed about the ring-opening of furanics utilizing bifunctional catalysts (metallic – oxide), most of them containing precious metals. Due to the versatility of LDH materials, similar bifunctionalities can arise after careful reduction treatments, possibly resulting in active catalysts for ring-opening. To my knowledge, four different MMO catalysts derived from LDH materials have been tested for the ring-opening of unsaturated furanic compounds including Ni-Co-Al,[90] Pt/$CoAl_2O_4$,[98] Cu-Mg-Al,[97] and Pt/Mg-Al.[116]

The first of these works involves impregnating Pt on a Co-Al MMO material derived from LDHs to investigate the ring-opening of FAL in the liquid phase. An optimum 1,5-PD yield was obtained when Li was doped into the matrix to create a more basic catalyst. Ultimately, a yield of approximately 31% was achieved after 24 hours at 140 ºC, 1.5 MPa of H_2, with ethanol as a solvent and FUR as a reactant. They claim that the Co^{3+} species located on the surface may have allowed for a tilted adsorption confirmation and subsequent hydrogenation; however, little characterization has been done to determine the surface species.[98] After reduction, the Cu-Mg-Al and Pt/Mg-Al MMO catalysts have

displayed high yields towards 1,2-PD (>70%), but very low yields towards 1,5-PD, which is a more desired product.[97,116] Lastly, Ni-Co-Al MMOs derived from LDH materials have demonstrated the ability to conduct ring-opening of HMF to 1,2,6-hexanetriol through a very similar mechanism as proposed in Figure 1.5c.[90] This demonstrates the possibility to have similar mechanisms for ring-opening for the related unsaturated furanic compounds HMF or FUR.

The above reactions mentioned from LDH derived materials highlight important pathways relevant to this dissertation; however, LDH materials have been used for a wide-variety of other biomass conversions including oxidation, aldol condensation, isomerization, dehydration, etc., and there is a very recent comprehensive review on this subject.[117]

1.4 Research Gaps and Dissertation Objectives

1.4.1 Research Gaps and Outlook

From the examples above, multi-metal systems have improved the activity and/or the selectivity when it comes to the conversion of biomass oxygenates. However, many of the studies utilize reactions with high H_2 pressures, low throughput, and/or expensive metals. Along with those concerns, improvements in activity and selectivity are still needed to increase the viability of producing fuels and chemicals from biomass. Consequently, it is crucial to continue to explore new multi-metal catalysts for the conversion of furanic compounds, especially without the use of precious metals. Along with screening various metal combinations, conducting spectroscopic experiments will help explore how each metal interacts with the catalyst, and correlate that to structure-reactivity properties. The

overall goal of this project was to provide evidence of the tunability of MMOs derived from LDH materials for different furanic reaction pathways, all while using non-precious metals.

1.4.2 Vapor Phase Hydrogenation of Furfural (Chapter 2)

The objective of this chapter is to investigate the effects on vapor phase hydrogenation of FUR to FAL and THFA when different metal dopants are added into a Ni-Al MMO matrix. This study is aimed to determine how Ni interacts with other metal additives and screen various metal ratios. Additionally, it is important to utilize various characterization techniques to shed light on how the electronic environment of the metals and morphology of the catalysts change after being introduced to a reducing environment. Something that has been infrequently studied with MMO materials based off LDHs.

Hypothesis: Ni has been shown to be an active metal in catalysts for hydrogenation of FUR to both THFA and FAL; therefore, including additional promoters such as Co and/or Mg may enhance the hydrogenation activity of FUR. The reducibility of Co and irreducibility of Mg under the pre-treatment conditions employed will result in electronic changes to the Ni metal that could vary activity and/or selectivity.

1.4.3 Vapor Phase Hydrogenolysis of Furfuryl Alcohol (Chapter 3)

As mentioned in the introduction, 2-MF production has become of interest due to its potential in supplementing petroleum fuels; therefore, it is of interest to develop catalytic processes that can effectively produce 2-MF from FUR/FAL. From knowledge gained in

Chapter 2, it became evident that Co based MMO materials have promise in producing 2-MF.

Hypothesis: Instead of incorporating Ni into the MMO matrix, incorporating small amounts of a more oxophilic, yet still reducible, metal, Fe, into the Co-Al matrix will facilitate the hydrogenoylsis reaction of FAL to 2-MF in the vapor phase flow reaction.

1.4.4 Liquid Phase Ring-Opening of Furanics (Chapter 4)

Ring-Opening of FUR, FAL, or THFA to diol products is a crucial pathway in creating renewable plastic precursors. Over the past few years, interest in this field has grown, and most of the catalysts active for this pathway involve bifunctionalities (metallic – oxide domains). Still, many concerns remain including low 1,5-PD yields and use of precious metals; however, tuning the MMO matrix may create unique bifunctionalities that are more active for ring-opening.

Hypothesis: Exploiting the tunability characteristic of LDH derived MMO catalysts, incorporating Cu in the Co-Al matrix will result in increased activity for the liquid phase ring-opening of FAL under a H_2 atmosphere. Cu will help facilitate reduction of the Co oxide species, but the catalyst will still contain both oxide and metallic species to allow for ring-opening.

1.4.5 Well-Defined Multi-Metal Catalysts for Furanic Conversion (Chapter 5)

From the knowledge gained in Chapters 2-4, it is apparent there are some limitations in characterizing the structure of the active domains in MMO materials, especially after reduction. This made it difficult conduct mechanistic studies on furanic hydrogenation and

hydrogenolysis; however, I was still able to determine effective multi-metal combinations, and gain a broad understanding of the electronic environment of the key metals. Consequently, I sought to move away from MMO materials and create well-defined catalyst structures, while still incorporating ideas gained from the MMO investigations. Recent developments in atomic layer deposition (ALD) experiments have made it a highly attractive catalyst synthesis method, which may allow for greater control and tuning of metal additions on an oxide support.[118]

Hypothesis: Synthesizing well-defined multi-metal catalysts (Cu-Co) through ALD will enhance the ring-opening activity, due to the ability of tuning particle size, metal placement, and oxidation state. This is the overall hypothesis of the research directions introduced in this chapter; however, this work is still underway, and will be completed by others in the group. There is an intermediate hypothesis that was more fully investigated within this chapter: Designing and building a controlled vacuum adsorption system will allow for volatile metal precursors to be adsorbed onto oxide supports, thus providing a home built ALD apparatus.

1.5 References

(1) Alonso, D. M.; Wettstein, S. G.; Dumesic, J. A. Bimetallic catalysts for upgrading of biomass to fuels and chemicals. *Chem. Soc. Rev.* **2012**, *41*, 8075–8098.

(2) Zhou, C.-H.; Xia, X.; Lin, C.-X.; Tong, D.-S.; Beltramini, J. Catalytic conversion of lignocellulosic biomass to fine chemicals and fuels. *Chem. Soc. Rev.* **2011**, *40*, 5588.

(3) Gallezot, P. Conversion of biomass to selected chemical products. *Chem. Soc. Rev.* **2012**, *41*, 1538–1558.

(4) Alonso, D. M.; Bond, J. Q.; Dumesic, J. A. Catalytic conversion of biomass to biofuels. *Green Chem.* **2010**, *12*, 1493–1513.

(5) Lange, J.-P.; van der Heide, E.; van Buijtenen, J.; Price, R. Furfural-a promising platform for lignocellulosic biofuels. *ChemSusChem* **2012**, *5*, 150–166.

(6) Sheldon, R. A. Green and sustainable manufacture of chemicals from biomass: state of the art. *Green Chem.* **2014**, *16*, 950.

(7) De, S.; Dutta, S.; Saha, B. One-pot conversions of lignocellulosic and algal biomass into liquid fuels. *ChemSusChem* **2012**, *5*, 1826–1833.

(8) Liu, C.; Wang, H.; Karim, A. M.; Sun, J.; Wang, Y. Catalytic fast pyrolysis of lignocellulosic biomass. *Chem. Soc. Rev.* **2014**, *43*, 7594–7623.

(9) Zhang, K.; Pei, Z.; Wang, D. Organic solvent pretreatment of lignocellulosic biomass for biofuels and biochemicals: A review. *Bioresour. Technol.* **2016**, *199*, 21–33.

(10) Singh, R.; Shukla, A.; Tiwari, S.; Srivastava, M. A review on delignification of lignocellulosic biomass for enhancement of ethanol production potential. *Renew. Sustain. Energy Rev.* **2014**, *32*, 713–728.

(11) Rinaldi, R.; Schüth, F. Design of solid catalysts for the conversion of biomass. *Energy Environ. Sci.* **2009**, *2*, 610–626.

(12) Mariscal, R.; Maireles-Torres, P.; Ojeda, M.; Sádaba, I.; López Granados, M. Furfural: a renewable and versatile platform molecule for the synthesis of chemicals and fuels. *Energy Environ. Sci.* **2016**, *9*, 1144–1189.

(13) Li, X.; Jia, P.; Wang, T. Furfural: a promising platform compound for sustainable production of C_4 and C_5 chemicals. *ACS Catal.* **2016**, *6*, 7621–7640.

(14) Nakagawa, Y.; Tamura, M.; Tomishige, K. Catalytic reduction of biomass-derived furanic compounds with hydrogen. *ACS Catal.* **2013**, *3*, 2655–2668.

(15) Adkins, H.; Connor, R. The catalytic hydrogenation of organic compounds over copper chromite. *J. Am. Chem. Soc.* **1931**, *53*, 1091–1095.

(16) Sitthisa, S.; Resasco, D. E. Hydrodeoxygenation of furfural over supported metal catalysts: A comparative study of Cu, Pd and Ni. *Catal. Letters* **2011**, *141*, 784–791.

(17) Nagaraja, B. M.; Siva Kumar, V.; Shasikala, V.; Padmasri, A. H.; Sreedhar, B.; David Raju, B.; Rama Rao, K. S. A highly efficient Cu/MgO catalyst for vapour phase hydrogenation of furfural to furfuryl alcohol. *Catal. Commun.* **2003**, *4*, 287–293.

(18) Nagaraja, B. M.; Padmasri, A. H.; David Raju, B.; Rama Rao, K. S. Vapor phase selective hydrogenation of furfural to furfuryl alcohol over Cu–MgO coprecipitated catalysts. *J. Mol. Catal. A Chem.* **2007**, *265*, 90–97.

(19) Rao, R.; Dandekar, A.; Baker, R. T. K.; Vannice, M. A. Properties of copper chromite catalysts in hydrogenation reactions. *J. Catal.* **1997**, *171*, 406–419.

(20) Dong, F.; Zhu, Y.; Zheng, H.; Zhu, Y.; Li, X.; Li, Y. Cr-free Cu-catalysts for the selective hydrogenation of biomass-derived furfural to 2-methylfuran: The synergistic effect of metal and acid sites. *J. Mol. Catal. A Chem.* **2015**, *398*, 140–148.

(21) Jiménez-Gómez, C. P.; Cecilia, J. A.; Durán-Martín, D.; Moreno-Tost, R.; Santamaría-González, J.; Mérida-Robles, J.; Mariscal, R.; Maireles-Torres, P. Gas-phase hydrogenation of furfural to furfuryl alcohol over Cu/ZnO catalysts. *J. Catal.* **2016**, *336*, 107–115.

(22) Jiménez-Gómez, C. P.; Cecilia, J. A.; Márquez-Rodríguez, I.; Moreno-Tost, R.; Santamaría-González, J.; Mérida-Robles, J.; Maireles-Torres, P. Gas-phase hydrogenation of furfural over Cu/CeO2 catalysts. *Catal. Today* **2017**, *279*, 327–338.

(23) Sitthisa, S.; Sooknoi, T.; Ma, Y.; Balbuena, P. B.; Resasco, D. E. Kinetics and mechanism of hydrogenation of furfural on Cu/SiO_2 catalysts. *J. Catal.* **2011**, *277*, 1–13.

(24) Pang, S. H.; Medlin, J. W. Adsorption and reaction of furfural and furfuryl alcohol on Pd(111): Unique reaction pathways for multifunctional reagents. *ACS Catal.* **2011**, No. 111, 1272–1283.

(25) Wang, S.; Vorotnikov, V.; Vlachos, D. G. Coverage-induced conformational effects on activity and selectivity: Hydrogenation and decarbonylation of furfural on Pd(111). *ACS Catal.* **2015**, *5*, 104–112.

(26) Kije, J.; Winiarek, P.; Paryjczak, T.; Lewicki, A.; Mikołajska, A. Platinum deposited on monolayer supports in selective hydrogenation of furfural to furfuryl alcohol. *Appl. Catal. A Gen.* **2002**, *233*, 171–182.

(27) An, K.; Musselwhite, N.; Kennedy, G.; Pushkarev, V. V.; Baker, L. R.; Somorjai, G. A. Preparation of mesoporous oxides and their support effects on Pt nanoparticle catalysts in catalytic hydrogenation of furfural. *J. Colloid Interface Sci.* **2013**, *392*, 122–128.

(28) Baker, L. R.; Kennedy, G.; Van Spronsen, M.; Hervier, A.; Cai, X.; Chen, S.; Wang, L.-W.; Somorjai, G. A. Furfuraldehyde hydrogenation on titanium oxide-supported platinum nanoparticles studied by sum frequency generation vibrational spectroscopy: acid-base catalysis explains the molecular origin of strong metal-support interactions. *J. Am. Chem. Soc.* **2012**, *134*, 14208–14216.

(29) Pushkarev, V. V; Musselwhite, N.; An, K.; Alayoglu, S.; Somorjai, G. A. High structure sensitivity of vapor-phase furfural decarbonylation/hydrogenation reaction network as a function of size and shape of Pt nanoparticles. *Nano Lett.* **2012**, *12*,

5196–5201.

(30) Audemar, M.; Ciotonea, C.; De Oliveira Vigier, K.; Royer, S.; Ungureanu, A.; Dragoi, B.; Dumitriu, E.; Jérôme, F. Selective hydrogenation of furfural to furfuryl alcohol in the presence of a recyclable cobalt/SBA-15 catalyst. *ChemSusChem* **2015**, *8*, 1885–1891.

(31) Yuan, Q.; Zhang, D.; Haandel, L. Van; Ye, F.; Xue, T.; Hensen, E. J. .; Guan, Y. Selective liquid phase hydrogenation of furfural to furfuryl alcohol by Ru/Zr-MOFs. *J. Mol. Catal. A Chem.* **2015**, *406*, 58–64.

(32) Taylor, M. J.; Durndell, L. J.; Isaacs, M. A.; Parlett, C. M. A.; Wilson, K.; Lee, A. F.; Kyriakou, G. Highly selective hydrogenation of furfural over supported Pt nanoparticles under mild conditions. *Appl. Catal. B Environ.* **2016**, *180*, 580–585.

(33) Vaidya, P. D.; Mahajani, V. V. Kinetics of liquid-phase hydrogenation of furfuraldehyde to furfuryl alcohol over a Pt/C catalyst. *Ind. Eng. Chem. Res.* **2003**, *42*, 3881–3885.

(34) Lesiak, M.; Binczarski, M.; Karski, S.; Maniukiewicz, W.; Rogowski, J.; Szubiakiewicz, E.; Berlowska, J.; Dziugan, P.; Witońska, I. Hydrogenation of furfural over Pd-Cu/Al_2O_3 catalysts. The role of interaction between palladium and copper on determining catalytic properties. *J. Mol. Catal. A Chem.* **2014**, *395*, 337–348.

(35) Zhao, Y. Facile synthesis of Pd nanoparticles on SiO2 for hydrogenation of biomass-derived furfural. *Environ. Chem. Lett.* **2014**, *12*, 185–190.

(36) Nakagawa, Y.; Nakazawa, H.; Watanabe, H.; Tomishige, K. Total hydrogenation of furfural over a silica-supported nickel catalyst prepared by the reduction of a nickel nitrate precursor. *ChemCatChem* **2012**, *4*, 1791–1797.

(37) Zhang, B.; Zhu, Y.; Ding, G.; Zheng, H.; Li, Y. Selective conversion of furfuryl alcohol to 1,2-pentanediol over a Ru/MnO_x catalyst in aqueous phase. *Green Chem.* **2012**, *14*, 3402–3409.

(38) Tike, M. A.; Mahajani, V. V. Kinetics of liquid-phase hydrogenation of furfuryl alcohol to tetrahydrofurfuryl alcohol over a Ru/TiO_2 Catalyst. *Ind. Eng. Chem. Res.* **2007**, *46*, 3275–3282.

(39) Sankar, M.; Dimitratos, N.; Miedziak, P. J.; Wells, P. P.; Kiely, C. J.; Hutchings, G. J. Designing bimetallic catalysts for a green and sustainable future. *Chem. Soc. Rev.* **2012**, *41*, 8099–8139.

(40) Seo, G.; Chon, H. Hydrogenation of furfural over copper-containing catalysts. *J. Catal.* **1981**, *67*, 424–429.

(41) Reddy, B. M.; Reddy, G. K.; Rao, K. N.; Khan, A.; Ganesh, I. Silica supported

transition metal-based bimetallic catalysts for vapour phase selective hydrogenation of furfuraldehyde. *J. Mol. Catal. A Chem.* **2007**, *265*, 276–282.

(42) Wu, J.; Shen, Y.; Liu, C.; Wang, H.; Geng, C.; Zhang, Z. Vapor phase hydrogenation of furfural to furfuryl alcohol over environmentally friendly Cu-Ca/SiO_2 catalyst. *Catal. Commun.* **2005**, *6*, 633–637.

(43) Rodiansono; Khairi, S.; Hara, T.; Ichikuni, N.; Shimazu, S. Highly efficient and selective hydrogenation of unsaturated carbonyl compounds using Ni–Sn alloy catalysts. *Catal. Sci. Technol.* **2012**, *2*, 2139.

(44) Merlo, A. B.; Vetere, V.; Ruggera, J. F.; Casella, M. L. Bimetallic PtSn catalyst for the selective hydrogenation of furfural to furfuryl alcohol in liquid-phase. *Catal. Commun.* **2009**, *10*, 1665–1669.

(45) Vicente, A.; Lafaye, G.; Especel, C.; Marécot, P.; Williams, C. T. The relationship between the structural properties of bimetallic Pd-Sn/SiO_2 catalysts and their performance for selective citral hydrogenation. *J. Catal.* **2011**, *283*, 133–142.

(46) Maligal-Ganesh, R. V.; Xiao, C.; Goh, T. W.; Wang, L. L.; Gustafson, J.; Pei, Y.; Qi, Z.; Johnson, D. D.; Zhang, S.; Tao, F.; et al. A ship-in-a-bottle strategy to synthesize encapsulated intermetallic nanoparticle catalysts: Exemplified for furfural hydrogenation. *ACS Catal.* **2016**, *6*, 1754–1763.

(47) Srivastava, S.; Solanki, N.; Mohanty, P.; Shah, K. a.; Parikh, J. K.; Dalai, A. K. Optimization and kinetic studies on hydrogenation of furfural to furfuryl alcohol over SBA-15 supported bimetallic copper–cobalt catalyst. *Catal. Letters* **2015**, *145*, 816–823.

(48) Fulajtárova, K.; Soták, T.; Hronec, M.; Vávra, I.; Dobročka, E.; Omastová, M. Aqueous phase hydrogenation of furfural to furfuryl alcohol over Pd-Cu catalysts. *Appl. Catal. A Gen.* **2015**, *502*, 78–85.

(49) Nakagawa, Y.; Tomishige, K. Total hydrogenation of furan derivatives over silica-supported Ni–Pd alloy catalyst. *Catal. Commun.* **2010**, *12*, 154–156.

(50) Chen, B.; Li, F.; Huang, Z.; Yuan, G. Tuning catalytic selectivity of liquid-phase hydrogenation of furfural via synergistic effects of supported bimetallic catalysts. *Appl. Catal. A Gen.* **2015**, *500*, 23–29.

(51) Nakagawa, Y.; Takada, K.; Tamura, M.; Tomishige, K. Total hydrogenation of furfural and 5‑hydroxymethylfurfural over supported Pd−Ir alloy catalyst. *ACS Catal.* **2014**, *4*, 2718–2726.

(52) Román-Leshkov, Y.; Barrett, C. J.; Liu, Z. Y.; Dumesic, J. A. Production of dimethylfuran for liquid fuels from biomass-derived carbohydrates. *Nature* **2007**, *447*, 982–985.

(53) Patet, R. E.; Nikbin, N.; Williams, C. L.; Green, S. K.; Chang, C. C.; Fan, W.; Caratzoulas, S.; Dauenhauer, P. J.; Vlachos, D. G. Kinetic regime change in the tandem dehydrative aromatization of furan Diels-Alder products. *ACS Catal.* **2015**, *5*, 2367–2375.

(54) Green, S. K.; Patet, R. E.; Nikbin, N.; Williams, C. L.; Chang, C. C.; Yu, J.; Gorte, R. J.; Caratzoulas, S.; Fan, W.; Vlachos, D. G.; et al. Diels-Alder cycloaddition of 2-methylfuran and ethylene for renewable toluene. *Appl. Catal. B Environ.* **2016**, *180*, 487–496.

(55) Burnett, L. W.; Johns, I. B.; Holdren, R. F.; Hixon, R. M. Production of 2-methylfuran by vapor-phase hydrogenation of furfural. *Ind. Eng. Chem.* **1948**, *40*, 502–505.

(56) Wilson, C. L.; Lukes, R. M. Reactions of furan compounds. XI. Side chain reactions of furfural and furfuryl alcohol over nickel-copper and iron-copper catalysts. *J. Am. Chem. Soc.* **1951**, *9*, 3–7.

(57) Xiong, K.; Wan, W.; Chen, J. G. Reaction pathways of furfural, furfuryl alcohol and 2-methylfuran on Cu(111) and NiCu bimetallic surfaces. *Surf. Sci.* **2016**, *652*, 91–97.

(58) Sitthisa, S.; An, W.; Resasco, D. E. Selective conversion of furfural to methylfuran over silica-supported NiFe bimetallic catalysts. *J. Catal.* **2011**, *284*, 90–101.

(59) Shi, D.; Vohs, J. M. Deoxygenation of biomass-derived oxygenates: reaction of furfural on Zn-modified Pt(111). *ACS Catal.* **2015**, *5*, 2177–2183.

(60) Leng, S.; Wang, X.; He, X.; Liu, L.; Liu, Y.; Zhong, X.; Zhuang, G.; Wang, J. G. NiFe/γ-Al_2O_3: A universal catalyst for the hydrodeoxygenation of bio-oil and its model compounds. *Catal. Commun.* **2013**, *41*, 34–37.

(61) Sheng, H.; Lobo, R. F. Iron-promotion of silica-supported copper catalysts for furfural hydrodeoxygenation. *ChemCatChem* **2016**, *8*, 3402–3408.

(62) Sulmonetti, T. P.; Hu, B.; Ifkovits, Z.; Lee, S.; Agrawal, P. K.; Jones, C. W. Vapor phase hydrogenolysis of furanics utilizing reduced cobalt mixed metal oxide catalysts. *ChemCatChem* **2017**, *9*, 1815–1823.

(63) Pino, N.; Sitthisa, S.; Tan, Q.; Souza, T.; López, D.; Resasco, D. E. Structure, activity, and selectivity of bimetallic Pd-Fe/SiO_2 and Pd-Fe/γ-Al_2O_3 catalysts for the conversion of furfural. *J. Catal.* **2017**, *350*, 30–40.

(64) Wang, C.; Luo, J.; Liao, V.; Lee, J. D.; Onn, T. M.; Murray, C. B.; Gorte, R. J. A comparison of furfural hydrodeoxygenation over Pt-Co and Ni-Fe catalysts at high and low H_2 pressures. *Catal. Today* **2017**, In Press.

(65) Dong, F.; Ding, G.; Zheng, H.; Xiang, X.; Chen, L.; Zhu, Y.; Li, Y. Highly dispersed

Cu nanoparticles as an efficient catalyst for the synthesis of the biofuel 2-methylfuran. *Catal. Sci. Technol.* **2016**, *6*, 767–779.

(66) Lee, W.-S.; Wang, Z.; Zheng, W.; Vlachos, D. G.; Bhan, A. Vapor phase hydrodeoxygenation of furfural to 2-methylfuran on molybdenum carbide catalysts. *Catal. Sci. Technol.* **2014**, *4*, 2340–2352.

(67) Xiong, K.; Lee, W.-S.; Bhan, A.; Chen, J. G. Molybdenum carbide as a highly selective deoxygenation catalyst for converting furfural to 2-methylfuran. *ChemSusChem* **2014**, *7*, 2146–2149.

(68) Shi, Y.; Yang, Y.; Li, Y.-W.; Jiao, H. Mechanisms of $Mo_2C(101)$-catalyzed furfural selective hydrodeoxygenation to 2-methylfuran from computation. *ACS Catal.* **2016**, *6*, 6790–6803.

(69) Panagiotopoulou, P.; Martin, N.; Vlachos, D. G. Effect of hydrogen donor on liquid phase catalytic transfer hydrogenation of furfural over a $Ru/RuO_2/C$ catalyst. *J. Mol. Catal. A Chem.* **2014**, *392*, 223–228.

(70) Panagiotopoulou, P.; Vlachos, D. G. Liquid phase catalytic transfer hydrogenation of furfural over a Ru/C catalyst. *Appl. Catal. A Gen.* **2014**, *480*, 17–24.

(71) Jenness, G. R.; Vlachos, D. G. DFT study of the conversion of furfuryl alcohol to 2-methylfuran on RuO_2 (110). *J. Phys. Chem. C* **2015**, *2*, 5938–5945.

(72) Gilkey, M. J.; Panagiotopoulou, P.; Mironenko, A. V.; Jenness, G. R.; Vlachos, D. G.; Xu, B. Mechanistic insights into metal lewis acid-mediated catalytic transfer hydrogenation of furfural to 2-methylfuran. *ACS Catal.* **2015**, *5*, 3988–3994.

(73) Jae, J.; Zheng, W.; Lobo, R. F.; Vlachos, D. G. Production of dimethylfuran from hydroxymethylfurfural through catalytic transfer hydrogenation with ruthenium supported on carbon. *ChemSusChem* **2013**, *6*, 1158–1162.

(74) Yang, P.; Cui, Q.; Zu, Y.; Liu, X.; Lu, G.; Wang, Y. Catalytic production of 2,5-dimethylfuran from 5-hydroxymethylfurfural over Ni/Co_3O_4. *Catal. Commun.* **2015**, *66*, 55–59.

(75) Zu, Y.; Yang, P.; Wang, J.; Liu, X.; Ren, J.; Lu, G.; Wang, Y. Efficient production of the liquid fuel 2,5-dimethylfuran from 5-hydroxymethylfurfural over Ru/Co_3O_4 catalyst. *Appl. Catal. B Environ.* **2014**, *146*, 244–248.

(76) Nagpure, A. S.; Venugopal, A. K.; Lucas, N.; Manikandan, M.; Thirumalaiswamy, R.; Chilukuri, S. Renewable fuels from biomass-derived compounds: Ru-containing hydrotalcites as catalysts for conversion of HMF to 2,5-dimethylfuran. *Catal. Sci. Technol.* **2014**, *2*.

(77) Huang, Y.-B.; Chen, M.-Y.; Yan, L.; Guo, Q.-X.; Fu, Y. Nickel-tungsten carbide catalysts for the production of 2,5-dimethylfuran from biomass-derived molecules.

ChemSusChem **2014**, *7*, 1068–1072.

(78) Kumalaputri, A. J.; Bottari, G.; Erne, P. M.; Heeres, H. J.; Barta, K. Tunable and selective conversion of 5-HMF to 2,5-furandimethanol and 2,5-dimethylfuran over copper-doped porous metal oxides. *ChemSusChem* **2014**, *7*, 2266–2275.

(79) Kong, X.; Zhu, Y.; Zheng, H.; Li, X.; Zhu, Y.; Li, Y. W. Ni nanoparticles inlaid nickel phyllosilicate as a metal-acid bifunctional catalyst for low-temperature hydrogenolysis reactions. *ACS Catal.* **2015**, *5*, 5914–5920.

(80) Wang, G.; Hilgert, J.; Richter, F. H.; Wang, F.; Bongard, H.; Spliethо, B.; Weidenthaler, C.; Schüth, F. Platinum–cobalt bimetallic nanoparticles in hollow carbon nanospheres for hydrogenolysis of 5-hydroxymethylfurfural. *Nat. Mater.* **2014**, *13*, 293–300.

(81) Nakagawa, Y.; Tamura, M.; Tomishige, K. Catalytic conversions of furfural to pentanediols. *Catal. Surv. from Asia* **2015**, *19*, 249–256.

(82) Koso, S.; Furikado, I.; Shimao, A.; Miyazawa, T.; Kunimori, K.; Tomishige, K. Chemoselective hydrogenolysis of tetrahydrofurfuryl alcohol to 1,5-pentanediol. *Chem. Commun.* **2009**, *0*, 2035–2037.

(83) Koso, S.; Ueda, N.; Shinmi, Y.; Okumura, K.; Kizuka, T.; Tomishige, K. Promoting effect of Mo on the hydrogenolysis of tetrahydrofurfuryl alcohol to 1,5-pentanediol over Rh/SiO_2. *J. Catal.* **2009**, *267*, 89–92.

(84) Chen, K.; Koso, S.; Kubota, T.; Nakagawa, Y.; Tomishige, K. Chemoselective hydrogenolysis of tetrahydropyran-2-methanol to 1,6-hexanediol over rhenium-modified carbon-supported rhodium catalysts. *ChemCatChem* **2010**, *2*, 547–555.

(85) Chen, K.; Mori, K.; Watanabe, H.; Nakagawa, Y.; Tomishige, K. C–O bond hydrogenolysis of cyclic ethers with OH groups over rhenium-modified supported iridium catalysts. *J. Catal.* **2012**, *294*, 171–183.

(86) Nakagawa, Y.; Tomishige, K. Production of 1,5-pentanediol from biomass via furfural and tetrahydrofurfuryl alcohol. *Catal. Today* **2012**, *195*, 136–143.

(87) Wang, Z.; Pholjaroen, B.; Li, M.; Dong, W.; Li, N.; Wang, A.; Wang, X.; Cong, Y.; Zhang, T. Chemoselective hydrogenolysis of tetrahydrofurfuryl alcohol to 1, 5-pentanediol over Ir-MoO_x/SiO_2 catalyst. *J. Energy Chem.* **2014**, *23*, 427–434.

(88) Tomishige, K.; Nakagawa, Y.; Tamura, M. Selective hydrogenolysis and hydrogenation using metal catalysts directly modified with metal oxide species. *Green Chem.* **2017**, *19*, 2876–2924.

(89) Chia, M.; Pagán-Torres, Y. J.; Hibbitts, D.; Tan, Q.; Pham, H. N.; Datye, A. K.; Neurock, M.; Davis, R. J.; Dumesic, J. A. Selective hydrogenolysis of polyols and cyclic ethers over bifunctional surface sites on rhodium-rhenium catalysts. *J. Am.*

Chem. Soc. **2011**, *133*, 12675–12689.

(90) Yao, S.; Wang, X.; Jiang, Y.; Wu, F.; Chen, X.; Mu, X. One-Step conversion of biomass-derived 5-hydroxymethylfurfural to 1,2,6-hexanetriol over Ni–Co–Al mixed oxide catalysts under mild conditions. *ACS Sustain. Chem. Eng.* **2014**, *2*, 173–180.

(91) Liu, S.; Amada, Y.; Tamura, M.; Nakagawa, Y.; Tomishige, K. One-pot selective conversion of furfural into 1,5-pentanediol over a Pd-added Ir–ReO_x/SiO2 bifunctional catalyst. *Green Chem.* **2014**, *16*, 617–626.

(92) Liu, S.; Amada, Y.; Tamura, M.; Nakagawa, Y.; Tomishige, K. Performance and characterization of rhenium-modified Rh–Ir alloy catalyst for one-pot conversion of furfural into 1,5-pentanediol. *Catal. Sci. Technol.* **2014**, *4*, 2535–2349.

(93) Buntara, T.; Noel, S.; Phua, P. H.; Melián-Cabrera, I.; de Vries, J. G.; Heeres, H. J. Caprolactam from renewable resources: catalytic conversion of 5-hydroxymethylfurfural into caprolactone. *Angew. Chem.* **2011**, *50*, 7083–7087.

(94) Buntara, T.; Noel, S.; Phua, P. H.; Melián-Cabrera, I.; Vries, J. G.; Heeres, H. J. From 5-hydroxymethylfurfural (HMF) to polymer precursors: Catalyst screening studies on the conversion of 1,2,6-hexanetriol to 1,6-hexanediol. *Top. Catal.* **2012**, *55*, 612–619.

(95) Tang, X.; Wei, J.; Ding, N.; Sun, Y.; Zeng, X.; Hu, L.; Liu, S.; Lei, T.; Lin, L. Chemoselective hydrogenation of biomass derived 5-hydroxymethylfurfural to diols: Key intermediates for sustainable chemicals, materials and fuels. *Renew. Sustain. Energy Rev.* **2017**, *77*, 287–296.

(96) Xiao, B.; Zheng, M.; Li, X.; Pang, J.; Sun, R.; Wang, H.; Pan, X.; Wang, A.-Q.; Wang, X.; Zhang, T. Synthesis of 1,6-hexanediol from HMF over double-layered catalysts of Pd/SiO_2+Ir-ReO_x/SiO2 in a fixed-bed reactor. *Green Chem.* **2015**.

(97) Liu, H.; Huang, Z.; Zhao, F.; Cui, F.; Li, X.; Xia, C.; Chen, J. Efficient hydrogenolysis of biomass-derived furfuryl alcohol to 1,2- and 1,5-pentanediols over a non-precious Cu–$Mg_3AlO_{4.5}$ bifunctional catalyst. *Catal. Sci. Technol.* **2015**, *6*, 668–671.

(98) Xu, W.; Wang, H.; Liu, X.; Ren, J.; Wang, Y.; Lu, G. Direct catalytic conversion of furfural to 1,5-pentanediol by hydrogenolysis of the furan ring under mild conditions over Pt/Co_2AlO_4 catalyst. *Chem. Commun.* **2011**, *47*, 3924–3926.

(99) Liu, H.; Huang, Z.; Kang, H.; Xia, C.; Chen, J. Selective hydrogenolysis of biomass-derived furfuryl alcohol into 1,2- and 1,5-pentanediol over highly dispersed Cu-Al_2O_3 catalysts. *Chinese J. Catal.* **2016**, *37*, 700–710.

(100) Götz, D.; Lucas, M.; Claus, P. C–O bond hydrogenolysis vs. C=C group hydrogenation of furfuryl alcohol: towards sustainable synthesis of 1,2-pentanediol.

React. Chem. Eng. **2016**, *1*, 161–164.

(101) Lee, J.; Burt, S. P.; Carrero, C. A.; Alba-Rubio, A. C.; Ro, I.; O'Neill, B. J.; Kim, H. J.; Jackson, D. H. K.; Kuech, T. F.; Hermans, I.; et al. Stabilizing cobalt catalysts for aqueous-phase reactions by strong metal-support interaction. *J. Catal.* **2015**, *330*, 19–27.

(102) O'Neill, B. J.; Jackson, D. H. K.; Crisci, A. J.; Farberow, C. A.; Shi, F.; Alba-Rubio, A. C.; Lu, J.; Dietrich, P. J.; Gu, X.; Marshall, C. L.; et al. Stabilization of copper catalysts for liquid-phase reactions by atomic layer deposition. *Angew. Chem.* **2013**, *52*, 13808–13812.

(103) O'Neill, B. J.; Miller, J. T.; Dietrich, P. J.; Sollberger, F. G.; Ribeiro, F. H.; Dumesic, J. a. Operando X-ray absorption spectroscopy studies of sintering for supported copper catalysts during liquid-phase reaction. *ChemCatChem* **2014**, *60563*, 2493–2496.

(104) Cavani, F.; Trifirò, F.; Vaccari, A. Hydrotalcite-type anionic clays: preparation, properties and applications. *Catal. Today* **1991**, *11*, 173–301.

(105) Fan, G.; Li, F.; Evans, D. G.; Duan, X. Catalytic applications of layered double hydroxides: recent advances and perspectives. *Chem. Soc. Rev.* **2014**, *43*, 7040–7066.

(106) Nishimura, S.; Takagaki, A.; Ebitani, K. Characterization, synthesis and catalysis of hydrotalcite-related materials for highly efficient materials transformations. *Green Chem.* **2013**, *15*, 2026–2042.

(107) Sels, B. F.; De Vos, D. E.; Jacobs, P. A. Hydrotalcite-like anionic clays in catalytic organic reactions. *Catal. Rev.* **2001**, *43*, 443–488.

(108) Xiang, J.; Wen, X.; Zhang, F. Supported Nickel–Cobalt Bimetallic Catalysts Derived from Layered Double Hydroxide Precursors for Selective Hydrogenation of Pyrolysis Gasoline. *Ind. Eng. Chem. Res.* **2014**, *53*, 15600–15610.

(109) Kühl, S.; Tarasov, A.; Zander, S.; Kasatkin, I.; Behrens, M. Cu-based catalyst resulting from a Cu,Zn,Al hydrotalcite-like compound: a microstructural, thermoanalytical, and in situ XAS study. *Chem. Eur. J.* **2014**, *20*, 3782–3792.

(110) Coq, B.; Tichit, D.; Ribet, S. Co/Ni/Mg/Al layered double hydroxides as precursors of catalysts for the hydrogenation of nitriles: hydrogenation of acetonitrile. *J. Catal.* **2000**, *189*, 117–128.

(111) Villaverde, M. M.; Bertero, N. M.; Garetto, T. F.; Marchi, a. J. Selective liquid-phase hydrogenation of furfural to furfuryl alcohol over Cu-based catalysts. *Catal. Today* **2013**, *213*, 87–92.

(112) Villaverde, M. M.; Garetto, T. F.; Marchi, A. J. Liquid-phase transfer hydrogenation

of furfural to furfuryl alcohol on Cu–Mg–Al catalysts. *Catal. Commun.* **2015**, *58*, 6–10.

(113) Xu, C.; Zheng, L.; Deng, D.; Liu, J.; Liu, S. Effect of activation temperature on the surface copper particles and catalytic properties of Cu–Ni–Mg–Al oxides from hydrotalcite-like precursors. *Catal. Commun.* **2011**, *12*, 996–999.

(114) Xu, C.; Liu, J.; Zheng, L.; Huang, Z. Furfural hydrogenation on nickel-promoted Cu-containing catalysts prepared from hydrotalcite-like precursors. *Chinese J. Chem.* **2011**, *29*, 691–697.

(115) Wu, J.; Gao, G.; Li, J.; Sun, P.; Long, X.; Li, F. Efficient and versatile CuNi alloy nanocatalysts for the highly selective hydrogenation of furfural. *Appl. Catal. B Environ.* **2017**, *203*, 227–236.

(116) Mizugaki, T.; Yamakawa, T.; Nagatsu, Y.; Maeno, Z.; Mitsudome, T.; Jitsukawa, K.; Kaneda, K. Direct transformation of furfural to 1,2-pentanediol using a hydrotalcite-supported platinum nanoparticle catalyst. *ACS Sustain. Chem. Eng.* **2014**, *2*, 2243–2247.

(117) Yan, K.; Liu, Y.; Lu, Y.; Chai, J.; Sun, L. Catalytic application of layered double hydroxide-derived catalysts for the conversion of biomass-derived molecules. *Catal. Sci. Technol.* **2017**, *7*, 1622–1645.

(118) Van Bui, H.; Grillo, F.; van Ommen, R. Atomic and molecular layer deposition: Off the beaten track. *Chem. Commun.* **2017**, *53*, 45–71.

CHAPTER 2 VAPOR PHASE HYDROGENATION OF FURFURAL UTILIZING NI BASED MMO CATALYSTS

This chapter and Appendix A are adapted from the published article, Sulmonetti, T. P.; Pang, S. H.; Taborga Claure, M.; Lee, S.; Cullen, D. A.; Agrawal, P. K.; Jones, C. W. Vapor phase hydrogenation of furfural over nickel mixed metal oxide catalysts derived from layered double hydroxides. *Appl. Catal. A Gen.* **2016**, *517*, 187–195, with permission from Elsevier. DOI: 10.1016/j.apcata.2016.03.005.[1]

2.1 Introduction

In an effort to reduce society's dependency on oil as a feedstock, conversion of biomass into chemicals and fuels continues to be a promising route towards feedstock sustainability.[2] Different challenges emerge in biomass refining compared to petroleum refining due to the over-functionalized and highly oxygenated compounds derived from common forms of biomass such as lignocellulose.[3,4] FUR, which can be produced through the dehydration of xylose or via fast pyrolysis of biomass, is a lignocellulose derivative that can be converted into a wide variety of chemicals and fuels.[5,6] Some of the important chemicals include FAL, THFA, 2-MF, furan, and 1,5-PD. Typically, FUR conversion utilizes heterogeneous catalysts due to the higher stabilities and ease of separation of these materials compared to homogeneous catalysts.[7]

Industrially, chromium based catalysts have been heavily used for conversion of FUR to various chemicals. However, due to the environmentally hazardous nature of many oxidized chromium species, other metals may be preferred.[8–12] To date, many studies

utilizing catalysts derived from a single metal species supported on a relatively inert material such as silica have been reported for FUR reduction. Specific examples include reports utilizing a variety of different transition metals, including Pt, Pd, Ir, Ni, and Cu.[13–21] Unfortunately, many monometallic catalysts suffer from lack of selectivity and therefore, the addition of a secondary metal has been used to greatly improve the properties of the first metal. One particularly successful approach has been to combine a reducible metal with a more oxophilic metal to create catalytic domains that offer the potential for multi-point interactions with the oxygenated FUR molecule.[22–26] The degree of reduction of the metal(s) plays a key role in creating a bifunctional catalyst surface with the reducible and oxophilic metal pair.[3]

Among the array of bimetallic/bifunctional catalysts used for FUR hydrogenation, Ir-ReO_x catalysts have demonstrated high selectivity towards FAL, with some authors proposing that the ReO_x orients FUR on the surface, while Ir subsequently hydrogenates the aldehyde.[27,28] Since typically these bifunctional catalysts contain precious metals that may not be economically attractive for large scale use, we sought to utilize non-precious metals to create MMO domains similar to those mentioned above. More specifically, Ni has previously been shown to be a good hydrogenation catalyst for FUR.[15] To this end, Ni was chosen as the reducible metal, and other oxophilic metals were included into the support matrix. Most studies conducted with two metal systems for FUR conversion containing Ni have focused on bimetallics or alloyed catalysts including NiFe, NiPd, and NiSn systems.[13,29,30] Two recent reports have shown the promise of Ni bifunctional catalysts by demonstrating that both Ni phyllosilicates and Ni-Al MMOs conduct C-O hydrogenolysis of HMF due to acid sites adjacent to Ni nanoparticles[25,26] In this work,

nickel-containing LDH similar to hydrotalcites have been used to create highly dispersed, porous, and thermally stable MMOs. LDH derived MMOs provide useful characteristics in the field of catalysis due to their wide versatility.[31–34] LDH materials derived from hydrotalcite structures have a balance of M^{3+} and M^{2+} cations, which allows for a variety of metals to be incorporated into the structure while maintaining high metal dispersity, high thermal stability, and sufficient porosity. Few studies have been conducted to investigate furanic compound hydrogenation utilizing LDH derived catalysts, and no in-depth spectroscopy has been reported.[24,26,35] In this study, two other metals, Co and Mg, were mixed with Ni and Al through a co-precipitation method. A couple of recent studies have been conducted with Co in the metallic phase, which have shown promise in the hydrogenation of FUR to FAL in liquid phase batch.[36,37] Thermodynamically, Co and Mg oxides have vastly different reduction energies, Co oxide being more reducible than Mg oxide, which causes varying interactions with Ni during the reduction phase of catalyst synthesis. An in-depth investigation was conducted on the metallic and oxide species present after reduction, which gave insight into the catalytic behavior of the materials in the gas phase hydrogenation of FUR.

2.2 Experimental Procedures

2.2.1 Materials and Chemicals

Furfural (99% purity, ACS Grade) was purchased from Sigma Aldrich and stored in inert N_2 atmosphere to limit its polymerization. $Co(NO_3)_2 \cdot 6H_2O$ (99% purity), Na_2CO_3 (99.5% purity), and ethylene glycol diethyl ether (98% purity) were purchased from Sigma Aldrich. $Ni(NO_3)_2 \cdot 6H_2O$, $Al(NO_3)_3 \cdot 9H_2O$, and $Mg(NO_3)_2 \cdot 6H_2O$ were purchased from Alfa

Aesar (98%-102%). NaOH (97% purity) was purchased from EMD. Lastly, all chemicals were used as received without any further purification.

2.2.2 Catalyst Synthesis

Ni-M-Al (M- Co, Mg) mixed metal oxides with varying Ni:M ratios of 1:2, 1:1, 2:1, while trying to maintain (Ni+M)/Al=0.25, were prepared in the following manner. Solution A contained 0.6 M of the metal nitrates corresponding to the molar ratio of metal cations. Solution B contained 1 M solution of NaOH, and solution C contained 0.3 M solution of Na_2CO_3. Using a peristaltic pump Solution A and Solution B were added dropwise into Solution C, contained in a flat-bottom flask, at approximately 5 mL/min under vigorous stirring and room temperature. A pH meter was placed in the solution, and a Labview program maintained the pH at approximately 10 by adjusting the flow of Solution B. Once Solution A was empty, the mixture was heated to 60°C, and it was aged under vigorous stirring for 48 hours. After, the precipitant was filtered and washed with distilled water until the wash solution was at about pH of 7. The recovered solid was dried in an oven at 100°C overnight, and then it was calcined at 400°C with 50 mL/min flow of air with a ramp rate of 10°C/min and a hold time of 4 hours.

2.2.3 Reaction Studies

Vapor phase reactions were performed in a ¼" tubular stainless steel reactor located inside a furnace. The catalyst was pelletized (120-170 mesh) diluted with SiC (200-400 mesh) and loaded into the reactor between layers of SiC (46 mesh) and quartz wool. The catalyst was reduced *in situ* under 60 mL/min H_2 (Airgas, UHP) to 500 ˚C at 5 °C/min and held for one hour. Once the reduction was completed, the bed was cooled under N_2 (Airgas,

UHP) to reaction temperature. Unless stated otherwise, reactions were conducted in a flow of 60 mL/min of H_2. FUR was pumped into the vaporization zone at a rate of 5.5 mmol/h (~2.5 mol% ethylene glycol diethyl ether as internal standard). The FUR flow met heated H_2 (H_2/FUR approximately 25) in the vaporization zone, which was heated to approximately 165 °C. The vapor flowed through the catalyst bed at temperatures fixed in the range of 155 °C-175 °C, and then it flowed into an online Agilent 7890A GC through lines heated to approximately 180 °C to minimize condensation. Selectivity and conversion were determined by the internal standard method, and carbon balances closed within 5% unless stated otherwise. After the reaction or reduction was completed, the catalyst was passivated for one hour at room temperature under 1% O_2/N_2 (Airgas) before removal from the reactor, separated form SiC, and stored under argon for further characterization studies.

2.2.4 Catalyst Characterization

2.2.4.1 Adsorption Characterization: N_2 Physisorption and Chemisorption

Nitrogen physisorption was performed in a Micromeritics Tristar II at -196°C after the samples were pretreated at 200°C (150°C for uncalcined LDH materials) under vacuum for 12 hours. Chemisorption experiments including temperature programmed reduction (TPR) and pulse CO chemisorption were conducted in Micromeritics AutoChem II 2920. For each TPR experiment, approximately 50 mg of sample was placed on top of a small bed of quartz wool in a quartz U-tube. In regards to the TPR experiment, the MMO was pretreated in 20 mL/min of He (Airgas, UHP) at 200°C for 2 hours to remove preadsorbed species. The sample was then cooled to 50°C and 20 mL/min of 10% H_2 balance He was flown over the sample. The furnace was heated to 800°C at 5°C/min while under the flow

of 10% H_2/He. The outlet gas passed through a liquid acetone/nitrogen trap, and then passed through a thermal conductivity detector (TCD). Pulse CO experiments were conducted in a similar fashion with a few minor changes. Approximately 20 mg catalyst sample was diluted with 80 mg of SiC, and placed in the quartz tube held in place by quartz wool. During the reduction step the sample was heated to 500°C at 5°C/min and held for 1 hour. The sample was then cooled to 400°C where He began to flow for 30 min to remove all adsorbed species. Afterwards the sample was cooled down to 30°C to begin pulse CO testing. Doses of 10% CO/He (Airgas) were passed over the sample and analyzed in the TCD. Once saturation was reached, He was flowed over the sample for 60 min to remove physisorbed species. Finally, a second round of pulses was conducted to verify if there were any physisorbed species adsorbed, which was taken into consideration when calculating the active metallic surface area.

2.2.4.2 XRD, XPS, ICP Analysis, and STEM Characterization

Powder XRD were collected using a Philips X-pert diffractometer using Cu Kα radiation. X-ray Photoemission Spectroscopy (XPS) analysis was conducted using a Thermo K-Alpha spectrometer employing a monochromatic Al Kα. The pressure inside the analytical chamber was approximately $5x10^{-8}$ Torr. The binding energies (BE) of all elements were tuned to the Ag 3d peak (368.2 eV) with an uncertainty of ± 0.2eV. Catalysts for scanning transmission electron microscopy (STEM) imaging were prepared by dropping a methanol-catalyst mixture on a lacy carbon-coated Cu grid and allowing the methanol to evaporate. Images were collected on an aberration-corrected-Nion UltraSTEM100 at 100 kV and aberration corrected JEOL 2200FS STEM at 200 kV.

Electron energy loss spectroscopy (EELS) was performed on the Nion while energy-dispersive X-ray spectroscopy (EDS) was performed on the JEOL. Elemental analysis was conducted at Georgia Tech Renewable Bioproducts Institute utilizing inductively coupled plasma optical emission spectroscopy (ICP-OES) by Perkin Elmer OPTIMA 7300 DV after dissolving the metal oxides by caustic fusion and acid digestion.

2.2.4.3 X-ray Absorption Spectroscopy

In situ X-ray absorption spectroscopy (X-ray absorption near edge structure, XANES and extended X-ray absorption fine structure, EXAFS) was conducted at the Advanced Photon Sources (APS), Argonne National Lab (ANL) at beamline 12-BM. The data were obtained in transmission mode at the Ni k-edge (8333 eV) in the range of 8130-9190 eV, and the Co k-edge (7712 eV) in the range of 7510-8260 eV, both with a spot size of 0.5mm x 1.2mm. To perform the *in situ* reduction XAS experiments, the catalyst sample was diluted and ground with boron nitride, and then ~1 mg sample was loaded into a 1/16" quartz tube held in place by quartz wool. The quartz tube was secured in a sample holder with a gas inlet and outlet, and a coil heater was centered along the catalyst. An XAS scan was taken before reduction at room temperature. Next the catalyst was heated to 500°C at 5°C/min and held for 1 h, all while under a 10 mL/min flow of 4% H_2/He. Transient scans were collected during the reduction. After the reduction was complete, the sample was cooled in He, and a final scan was collected at room temperature. The XAS data were processed and analyzed with Athena software including background removal, edge-step normalization, and Fourier transform.

2.3 Results and Discussion

2.3.1 Materials Synthesis and Initial Characterization

LDH materials were synthesized as the precursors to the MMO catalysts due to the large variability of metal cations that can be introduced during synthesis. LDH precursors allow for synthesis of materials with consistent physical properties even when various metals and metal ratios are used. Once these materials are calcined there is an emergence of high porosity and surface area, and additionally, high dispersion of metal oxides can be achieved. This suggests the potential for high interaction of the metallic species with oxide species once the MMOs are partially reduced compared to catalysts prepared by traditional wetness impregnation techniques. The physical properties of the catalysts are summarized in Table 2.1. The catalysts are named according to their metal molar ratio determined through ICP-OES, normalized to Al content.

As shown in Table 2.1, the LDH derived synthesis yielded porous MMOs with relatively high BET surface areas ranging from 150 m^2/g – 300 m^2/g. In general, calcined Co samples had lower surface areas than Mg samples, and Co-Al had the lowest surface area of all the catalysts, which may be due to the larger ionic radius of Co^{2+} over Mg^{2+} and the potential for Co^{2+} to oxidize to Co^{3+}.[31,38] According to ICP-OES results, the synthesized Co catalysts did not reach the target molar ratios. Since Co has the ability to oxidize to the 3+ oxidation state, the presence of large amounts of Co may have caused a charge imbalance that did not allow its full incorporation into the precursor hydrotalcite structure.[39]

Table 2.1 – Physical properties of the catalysts utilized for FUR hydrogenation.

Catalyst	ICP-Analysis	Uncalcined			Calcined at 400°C		
	Ni:M:Al ratio	BET Surface Area (m^2/g)	Pore Volume (cm^3/g)	Average Pore Diameter (nm)	BET Surface Area (m^2/g)	Pore Volume (cm^3/g)	Average Pore Diameter (nm)
2Ni-Al	2.0:0:1	129	0.47	14.6	239	0.61	12.8
1.3Ni-0.5Co-Al	1.3:0.5:1	113	0.54	19.4	196	0.67	16.5
1.9Ni-Mg-Al	1.9:1:1	137	0.45	9.3	288	0.5	8.9
1.1Ni-0.8Co-Al	1.1:0.8:1	108	0.57	21.4	175	0.59	16.3
1.4Ni-1.4Mg-Al	1.4:1.4:1	128	0.51	15.6	236	0.39	10.6
0.7Ni-1.1Co-Al	0.7:1.1:1	93	0.41	21.1	163	0.46	12.0
0.9Ni-1.9Mg-Al	0.9:1.9:1	148	0.41	10.9	236	0.51	10.3
Co-Al	0:1:1	62	0.33	28	160	0.32	8.5

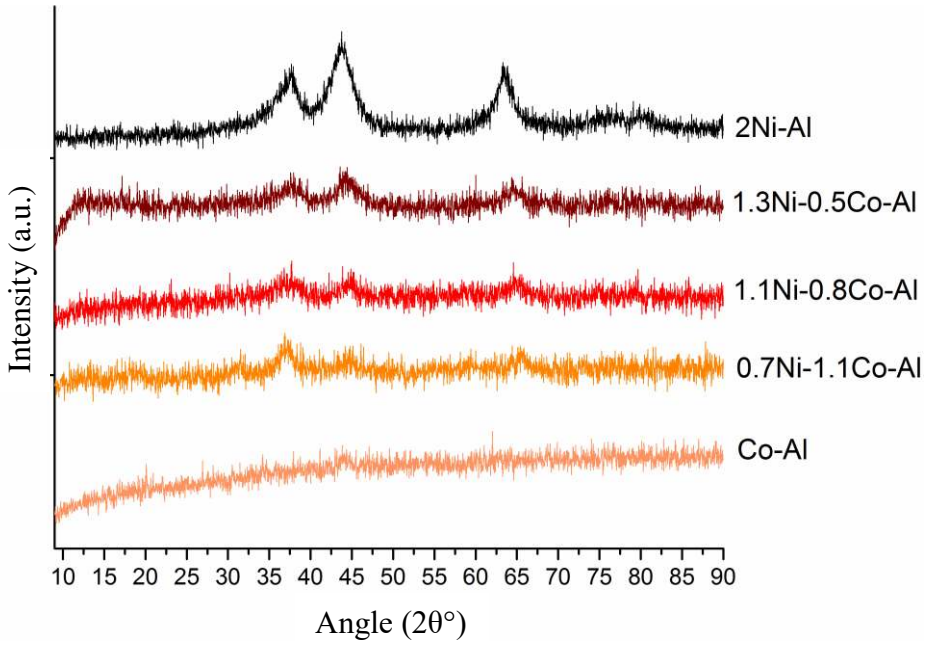

Figure 2.1 – XRD patterns of post-calcined Ni-Co-Al MMO materials.

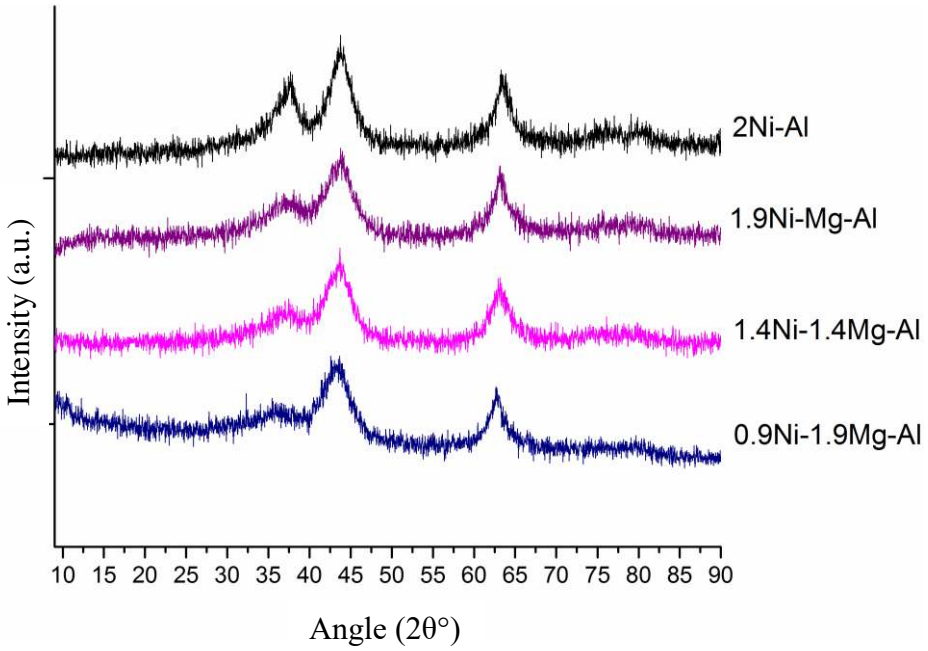

Figure 2.2 – XRD patterns of post-calcined Ni-Mg-Al MMO materials.

XRD patterns obtained for the uncalcined samples showed characteristic layered structures such as the (003) and (006) peaks (Figure A.1), whereas the XRD patterns of the calcined catalysts shown in Figure 2.1 and 2.2 above, lack such sharp crystalline peaks. Interestingly, as the Co content increased, the intensity of the peaks decreased, which is similar to the phenomenon observed upon incorporation of Co into Mg-Al LDH materials.[38] Once the samples were calcined in air, the crystalline layered structures vanished and the XRD patterns contained only small, moderately broad peaks. The lack of sharp peaks in Figure 2.1 and 2.2 suggested the absence of large crystalline domains or clusters of metal oxides, which may have helped promote metal dispersion when reducing the catalysts.

The three diffraction lines approximately at 37.5°, 42.5°, and 62.5° were difficult to conclusively assign since various metal oxides and spinels in the compositional system

have reflections that overlap with the broad peaks (Figure A.2). The intensities of the Co sample peaks were severely diminished compared to the Mg samples, suggesting smaller domain sizes or a more amorphous structure. The absence of specific metal oxide domains may be explained by the homogeneous mixing of oxides that created a solid solution.[24,40,41] These solid solutions caused reduction of nickel to be significantly more difficult than for samples containing large nickel oxide domains, such as those often prepared by impregnation methods, due to the dispersion of the NiO domains and intermixing with other oxide species. Therefore, H_2-TPR was a useful tool in determining the reduction profiles of the MMOs. The reduction behavior of each MMO is displayed in Figure 2.3 and 2.4, and the total hydrogen uptake is in Table A.1.

The TPR profiles contained many different features due to the compositional complexity of the MMOs. Under these conditions, MgO and Al_2O_3 are unreducible, but Ni^{2+}, Co^{3+}, and Co^{2+} are reducible. Starting with the more complex TPR profiles, the Ni-Co-Al catalysts displayed large hydrogen uptakes as the temperature increased. The addition of Co resulted in the emergence of a peak at lower temperatures (~250°C). This suggested that during calcination in air, Co_3O_4 domains evolved, and at lower temperatures, Co_3O_4 was reduced to CoO.[42] The very broad uptake could result from a mixture of many different oxide species being reduced, including Ni^{2+} and Co^{2+}. According to prior literature, the low temperature shoulder is due to the reduction of surface Ni^{2+} to Ni^0, which is followed by the reduction of bulk Ni^{2+} to metallic Ni.[24,26,43] Although XRD does not provide evidence for any spinel structures ($NiAl_2O_4$ or $NiCo_2O_4$), as the temperatures rise above 600 °C, the reduction of more recalcitrant (perhaps highly embedded) Ni or Co species clearly occurred.[44,45] As the Ni content was increased, the apex of the broad peak

shifted slightly to lower temperatures, confirming that Ni oxide species required less thermal energy to reduce. Along with the shift in the broad peak, the Co_3O_4 peak shifted towards lower temperatures as well, which alludes to the potential of Ni assisting in the reduction of Co. Similar to the addition of Pt to Co/Al_2O_3, the more easily reducible Ni may assist in the reduction of cobalt oxide through H_2 dissociation and spillover.[42] Therefore, not only does NiO reduce to metallic Ni, but it was possible that CoO was reduced to metallic Co under specific reduction conditions. Unfortunately, these TPR profiles cannot give a detailed depiction of the reduced species. Consequently, spectroscopic studies were conducted to probe this, as discussed further below.

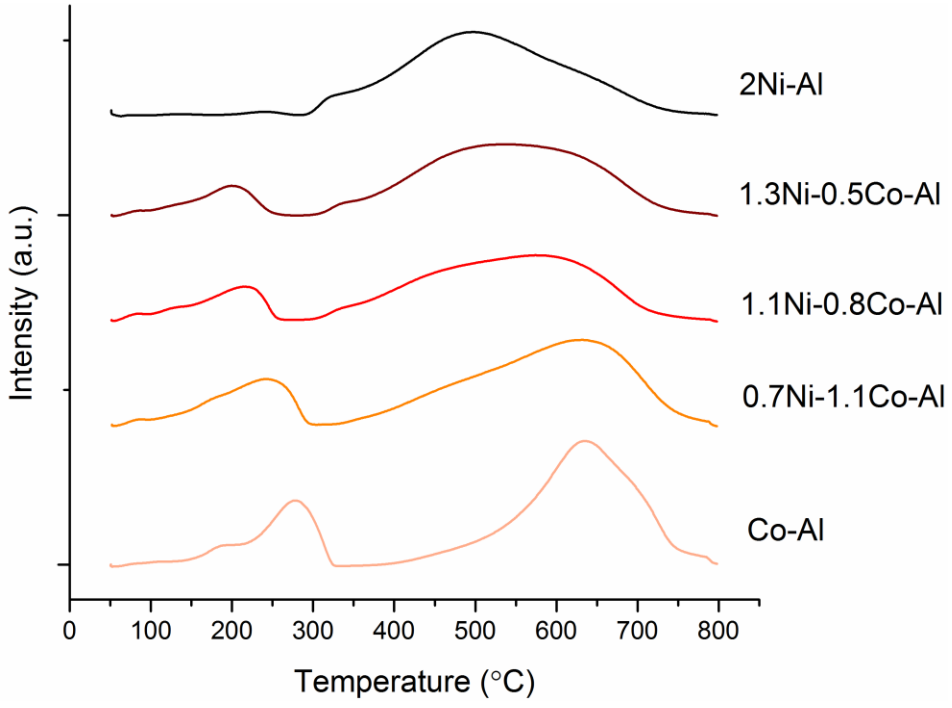

Figure 2.3 – TPR profiles of Ni-Co-Al catalysts.

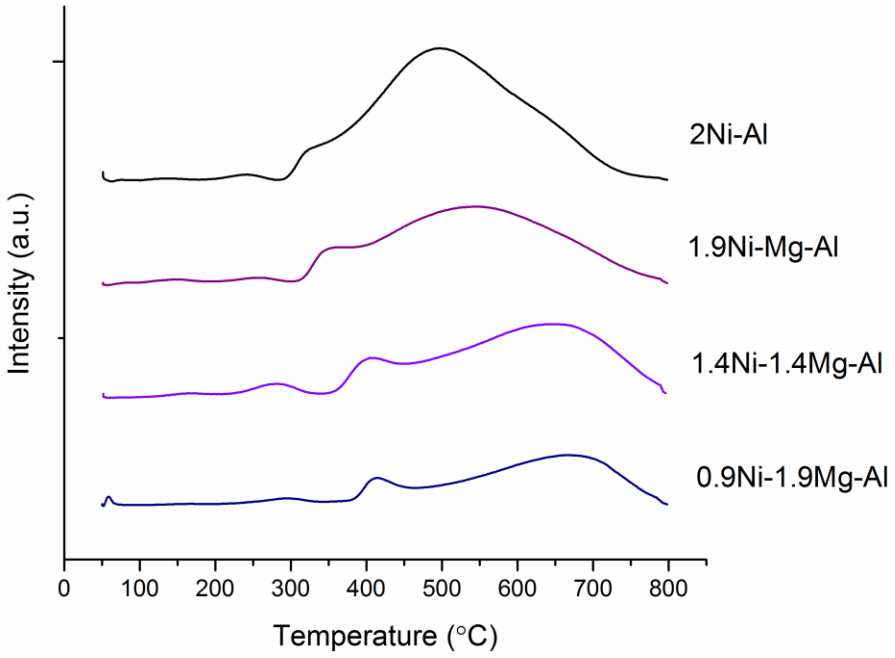

Figure 2.4 – TPR profiles of Ni-Mg-Al catalysts.

Unlike the Co samples, the Ni-Mg-Al catalysts showed significantly less hydrogen uptake due to the unreducible (under these conditions) MgO. Like the Co samples, there was a shift of the main peak to lower temperatures as there was an increase of Ni in the system. The Ni-Mg-Al profiles displayed a prominent lower temperature shoulder, alluding to more surface NiO species segregated from embedded NiO species. The potential for more segregated surface species allowed for production of larger Ni domains during reduction (see below). Overall, these MMOs derived from LDH precursors create highly embedded oxide species, which yields higher reduction temperatures compared to samples prepared by wetness impregnation. For the vapor phase reaction studies, 500 °C was chosen as the pre-reduction temperature to create a bifunctional catalyst with the partial reduction of the reducible oxide species. Metallic Ni or Co was expected to act as the hydrogenation site, while the hydrophilic oxide support would facilitate adsorption of the highly-oxygenated FUR molecule.

2.3.2 Vapor Phase Flow Reactions

Initial high FUR conversion testing (90%-99.5%) was completed using all the catalysts to compare selectivities and activities at similar reactions conditions and conversions. Reactions were conducted at 155°C, a pressure of about 1 atm, and a H_2/FUR molar ratio of ~25. The major pathway for all reactions was hydrogenation of the aldehyde to produce FAL, followed by side or sequential products yielding products such as THFA, furan, and 2-MF.

Table 2.2 – Selectivities and activities for each catalyst under reaction conditions yielding nearly complete conversion of FUR.

Catalyst[1]	Conversion	Activity	Selectivity (%)						
	%	$\frac{mol_{prod}}{hr * g_{cat}}$	FAL	THFA	Furan	2-MF	1-BOH	1,2-PD	Others[2]
2Ni-Al	94	0.098 ± 0.002	58.2	21.1	11.7	5.6	1.2	1.4	0.8
1.9Ni-Mg-Al	95	0.124 ± 0.002	65.0	13.1	18.2	1.1	2.0	0.6	0.0
1.3Ni-0.5Co-Al	99	0.100 ± 0.001	70.0	11.8	11.0	4.1	1.8	1.3	0.0
1.4Ni-1.4Mg-Al	94	0.081 ± 0.007	68.6	10.2	19.0	0.4	1.3	0.0	0.5
1.1Ni-0.8Co-Al	98	0.140 ± 0.002	71.8	9.9	8.9	5.3	2.2	0.9	1.0
0.9Ni-1.9Mg-Al	92	0.037 ± 0.003	66.7	13.1	16.9	0.7	1.6	0.4	0.6
0.7Ni-1.1Co-Al	91	0.124 ± 0.003	75.6	6.6	6.8	6.4	2.2	1.2	1.2
Co-Al[3]	98	0.086 ± 0.003	48.0	0.8	2.3	42.3	3.4	0.6	2.6

[1]Reactions Conditions: 155 °C and 1 atm with a FUR flow rate of 5.5 mmol/hr and H_2/FUR = 25. Values obtained after approximately 1 hour on stream. [2]Others include 1-pentanol, 2-pentanol, and 1-butanal. [3]Carbon balance was within 10%.; 1-BOH- 1-butanol.

The major product obtained for each catalyst was FAL, which resulted from the hydrogenation of the aldehyde of FUR to an alcohol. In prior literature, it has been established that bifunctional catalysts that contain a reduced metal and an oxide such as Ir-ReO_x/SiO_2 are highly active and selective towards unsaturated aldehyde hydrogenation.[27] The oxide is suggested to adsorb the oxygen of the aldehyde and the zero valent metal hydrogenates the carbonyl over the "bifunctional" catalyst. The Ni MMOs reduced *in situ* may create similar bifunctionalities due to the formation of Ni and/or Co metallic phases embedded in a solid solution metal oxide support. The oxide support may allow for strong interaction of the aldehyde with the catalyst, while the reduced metal hydrogenates the carbonyl species. Furthermore, the LDH synthesis method allowed for strong interactions between the oxide and the reduced metal due to the relative homogeneity of the starting MMO. In general, the Ni-Co-Al catalysts produced slightly more FAL than the Ni-Mg-Al materials, and the major outliers were 2Ni-Al and Co-Al due to the large amounts of side products or sequential products formed.

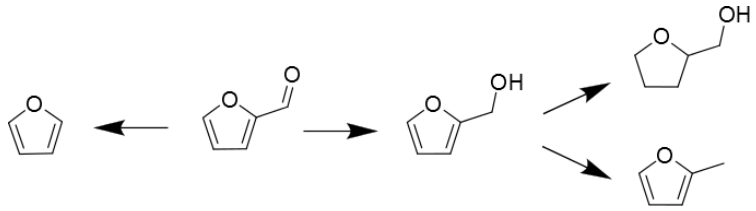

Figure 2.5 – Reaction pathways of the major products from FUR conversion of Ni based catalysts.

Other products were formed through hydrogenation, decarbonylation, and hydrogenolysis pathways. Further hydrogenation through ring saturation occurred in all catalysts except Co-Al, potentially due to reduced Ni allowing for flat adsorption of FAL at low temperatures, leading to reduction of the olefinic bonds.[15] The second major side

product was furan, resulting from decarbonylation of FUR, which has been shown to form over Ni catalysts at high temperatures.[14] Prior studies revealed that furan production is due to the strong η^2(C,O) adsorption of the aldehyde, which seems to be more predominant over the Mg catalysts.[14] When Co was incorporated into the Ni MMOs, 2-MF production increased slightly; moreover, Co-Al, which contained no Ni species, produced a significant amount of 2-MF. Additional, minor ring-opening products were formed, including 1-BOH and 1,2-PD, but were in insignificant amounts.

Activities per gram of catalyst are displayed in Table 2.2, and it can be seen that the 1.1Ni-0.8Co-Al catalyst showed the highest activity per gram. However, further investigation at lower FUR conversions of 1.9Ni-Mg-Al, 1.4Ni-1.4Mg-Al, 1.1Ni-0.8Co-Al, 0.7Ni-1.1Co-Al, and 2Ni-Al were conducted to compare catalysts with various metal ratios under conditions that minimized side reactions and sequential reactions. Table 2.3 displays the activity per gram and per active site, as estimated by CO chemisorption (for chemisorption data, see Table A.2). Due to the potential for multiple CO species forming on the metallic surfaces, including monodentate and bidendate CO, it was assumed that each adsorbed CO corresponded to 1.5 active sites.[46–50] The active site estimation by CO chemisorption may be slightly overstated for each catalyst due to potential titration of Lewis acid sites with CO, but previous literature has used CO adsorption to estimate metallic sites on similar catalysts based on LDH derived MMOs.[31,51,52] The 1.4Ni-1.4Mg-Al catalyst gave slightly higher CO adsorption than both the 1.1Ni-0.8Co-Al and 2Ni-Al materials. Even though the dispersion and estimated particle size ranged between approximately 2.5%-5.5% and 18 nm-38 nm, respectively, these values are likely not a good representation of the morphology (Table A.2) of the metal species. MMOs derived

from LDH precursors yield highly embedded metallic species after reduction, which can yield lower exposed metallic surface areas.[53] Consequently dispersion will be understated in such materials, while particle diameter will be overstated.

Table 2.3 – Activity and selectivity at low FUR conversion for selected catalysts.

Catalyst[1]	Conversion	Activity		Selectivity (%)			
	%	$\frac{mol_{conv}}{h * g_{cat}}$	$\frac{mol_{conv}}{hr * mol_{site}}$	FAL	THFA	Furan	2-MF
1.4Ni-1.4Mg-Al	14	0.20	550±10	80.7	3.5	15.8	-
1.1Ni-0.8Co-Al	25	0.44	1690±160	78.6	7.2	11.0	3.2
0.7Ni-1.1Co-Al	15	0.25	1020±100	79.1	7.8	8.6	4.4
1.9Ni-Mg-Al	17	0.29	550±10	76.0	10.5	13.5	-
2Ni-Al	16	0.29	1050±80	77.8	9.1	11.9	1.2

[1]Reactions Conditions: 155 °C and 1 atm with a FUR flow rate of 12 mmol/hr and H_2/FUR = 20. Values obtained after approximately 1 hour on stream. Assuming 1.5 sites per CO adsorbed.

Table 2.4 – Activity and selectivity of the 1.1Ni-0.8Co-Al catalyst at various temperatures.

Catalyst[1]	Conversion	Activity	Selectivity (%)				
1.1Ni-0.8Co-Al	%	$\frac{mol_{prod}}{hr * g_{cat}}$	FAL	THFA	Furan	2-MF	Others[2]
155 °C	24	0.44	78.6	7.2	11.0	3.2	-
165 °C	26	0.57	75.8	7.1	11.3	3.3	2.5
175 °C	27	0.61	74.3	6.5	11.8	4.6	2.8

[1]Reactions Conditions: 1 atm with a FUR flow rate of 12 mmol/hr and H_2/FUR = 20. Values obtained after approximately 1 hour on stream. [2]Others includes 1-BOH and butanal.

Others have reported the use of base metal catalysts for FUR hydrogenation as well. Reduced Cu impregnated on SiO_2 has been employed for vapor phase hydrogenation of FUR and displayed high selectivity towards FAL (99%). Similarly, Ni impregnated on

SiO_2 has shown high selectivity towards THFA at a low temperature of 130 °C (94%).[15,16,54] For FUR conversion to FAL, Tomishige et al. reported a TOF of 130 h^{-1} at 130 °C using a 10 wt% Ni/SiO_2 catalyst, and Mérida-Robles et al. reported a TOF of 9.6 h^{-1} for an 8 wt% Cu/SiO_2 catalyst at 170 °C. Although these studies were conducted at different temperatures, the site-time-yields (STYs) of both 1.1Ni-0.8Co-Al and 2Ni-Al demonstrated these materials to have promising activity for FUR hydrogenation (Table 2.3); however, improvements in selectivity by lowering decarbonylation products are needed to compete with the best catalysts.

Low conversion testing also supported the observation at higher FUR conversions of higher activity (per gram catalyst) associated with the 1.1Ni-0.8Co-Al, compared to all other catalysts tested at low conversion. Also, both Co catalysts showed higher activity per site compared to both Mg samples. The activity per site, as measured by CO chemisorption, showed an almost three times higher activity of the 1.1Ni-0.8Co-Al catalyst compared to 1.4Ni-1.4Mg-Al and 1.9Ni-Mg-Al sample. The 1.1Ni-0.8Co-Al catalyst had more than a 50% higher turnover frequency than 2Ni-Al, suggesting the addition of Co had a positive effect on activity, unlike Mg addition. In terms of selectivity very little difference was observed compared to high conversion tests except slightly higher FAL selectivites due to reduced sequential reactions. The 1.1Ni-0.8Co-Al catalyst was used at low conversion to investigate the effects of temperature on the reaction rate, with the results displayed in Table 2.4. Increasing the temperature increased the activity, as expected, while also changing the product distribution. Slightly greater amounts of furan and 2-MF were produced with the increase in temperature, which has been noted in a previous report utilizing Ni catalysts.[14]

2.3.3 Spectroscopic Characterization

The use of TPR and XRD together did not allow for sufficient insight into the nature of the reduced metallic species. To this end, XAS and XPS were applied to further elucidate the states of Ni and Co. *In situ* XAS under reduction conditions similar to the reaction pretreatment was utilized to give insight into the bulk characteristics of the 1.4:1.4 Ni:Mg and 1.1:0.8 Ni:Co catalysts. XAS was conducted in a quartz tube that was heated to 500 °C at 5˚C/min and held for 1 hour, all while under 10 mL/min 4% H_2 (balance He). Scans were taken throughout the reduction process, but only pre-and post-reduction conditions are presented here. The quality of the EXAFS spectrum can significantly diminish as temperature rises, especially temperatures above 600K, due to significant changes in the Debye-Waller factor, which adjusts for the thermal vibration effects.[55–57] For this reason, room temperature spectra were used to allow for ease of EXAFS processing and comparison. Both the Ni K-edge and the Co K-edge were interrogated to determine if Co also reduced under the pretreatment conditions employed in this work. Figure 2.6 displays the Ni k-edge XAS results for both the 1.4Ni-1.4Mg-Al and 1.1Ni-0.8Co-Al samples at room temperature before and after reduction at 500 °C.

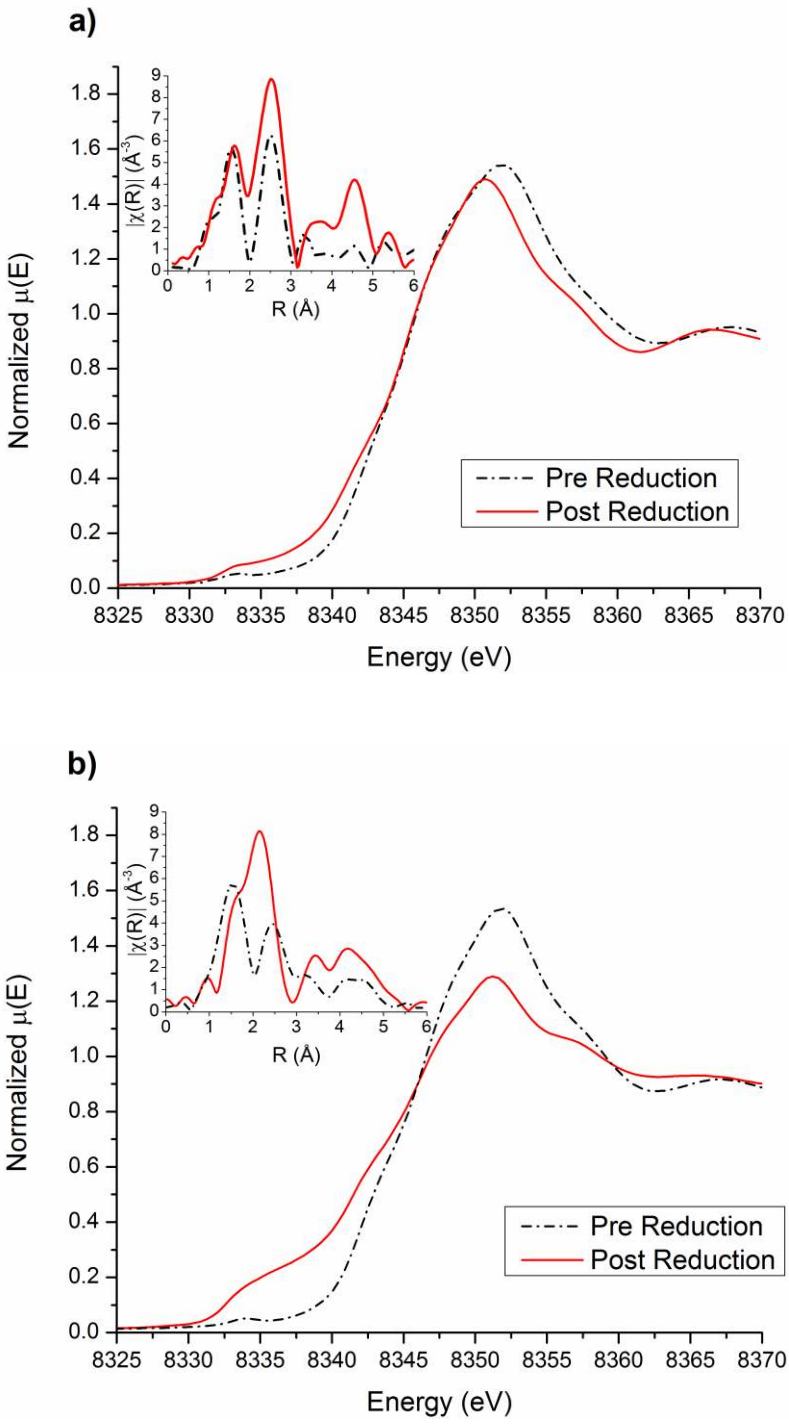

Figure 2.6 – XANES spectra at the Ni k-edge of the catalysts at RT both before and after reduction at 500 ºC with 4% H_2 balance He and 10 mL/min. Inset graphs show Fourier Transformed EXAFS data for each catalyst; a) 1.1Ni-0.8Co-Al b) 1.4Ni-1.4Mg-Al.

Qualitatively, both XANES spectra showed a shift in the white line to lower energies as well as a decrease in the intensity; however, the Mg catalyst showed a much more significant shift and reduction in intensity, suggesting larger amounts of NiO reduced to Ni^0 in this catalyst.[53,58] The pre-reduction spectra for both the Co and Mg containing samples mimicked the NiO spectrum due to the presence of the pre-edge feature at 8333 eV and the major peak at 8352 eV. After reduction for an hour at 500 °C, the pre-edge feature disappeared for the Mg catalyst and the appearance of a second edge started, similar to that of Ni foil.[59,60] Moreover, when examining the derivative norm(E) (Figure A.5) there was an increase in the peak at 8333 eV and a decrease in peaks at 8342 eV and 8346 eV, which was more characteristic of Ni foil reference. The Co catalyst displayed a smaller shift in the white line of the Ni k-edge, suggesting a simultaneous reduction of both Ni and Co. The Mg samples do not have that reduction competition since MgO and Al_2O_3 are not reducible under these conditions, allowing for significantly more reduction of the NiO species. In terms of the Co catalyst, there were still strong characteristic NiO features after reduction, including the small pre-edge feature at 8333 eV; therefore, there was clearly less reduction of Ni in the Ni-Co-Al catalyst, relative to the Ni-Mg-Al catalyst. Overall, both catalysts did not have 100% reduction of Ni^{2+} to Ni^0, possibly due to the large amount of imbedded Ni^{2+} species in the well-mixed oxide as well as strong interactions with the oxide support, as supported by TPR results, unlike traditional impregnated Ni catalysts.[15]

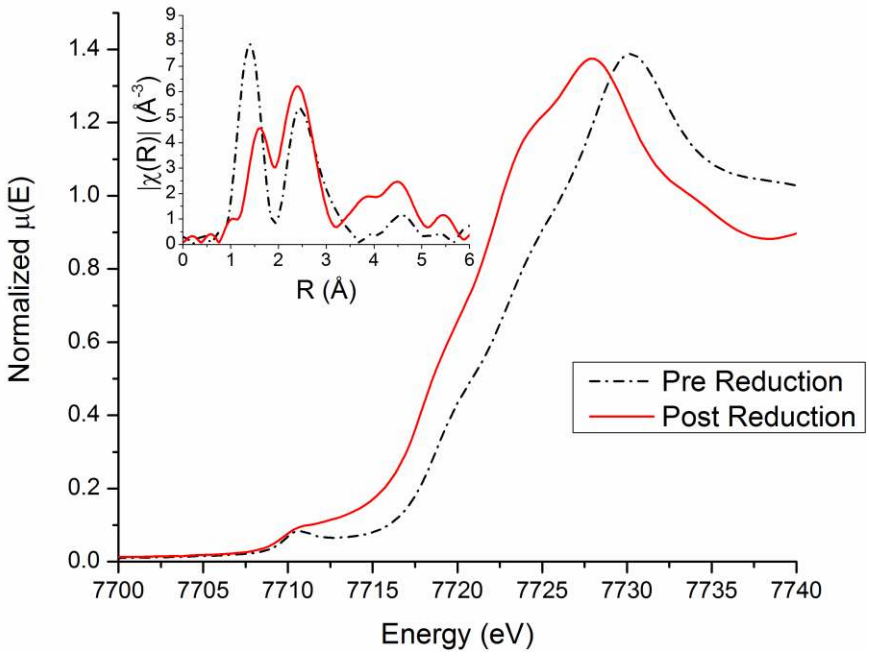

Figure 2.7 – In situ XANES of Co k-edge of the 1.1Ni-0.8Co-Al catalyst at RT both before and after reduction with 4% H_2 balance He and 10 mL/min. Inset graph shows Fourier transformed EXAFS data of the same sample.

EXAFS spectra displayed significant changes between the pre-and post-reduction catalyst samples, especially with the first two major scattering peaks. For both pre-reduction samples, two major peaks were present: a first peak at ~1.5 Å and a second peak at ~2.5 Å, corresponding to Ni-O and Ni-Ni (or Ni-Co) scattering, respectively.[61,62] After pretreatment, each catalyst showed a large increase in the Ni-Ni (Ni-Co) peak, which suggested an increase in the coordination number and formation of metallic Ni particles or Ni-Co alloys. Although both samples showed an increase of the metal-metal peaks after reduction, the Mg sample also showed a slight shift to lower atomic scattering distances, suggesting a larger degree of agglomeration of the Ni atoms. This larger agglomeration was potentially due to the larger amount of Ni atoms present on the surface of the mixed oxide, as shown by the larger shoulder at lower reduction temperatures in the TPR data.

Even though there was a large increase in the magnitude of the second peak of the Co sample, there was no shift in the second peak, which suggested less Ni agglomeration due to the Co addition. From TPR, it was suggested that Co begins mainly as a Co_3O_4 that was reduced to CoO at low temperatures. However, from the TPR data over these samples, at higher temperatures it was uncertain when CoO reduction began. The *in situ* XAS spectra of the Co-containing sample at the Co k-edge before and after reduction, as shown in Figure 2.7, do not display characteristics of significant metallic Co, as the post-reduction white line mimics CoO from prior literature.[63] However, the EXAFS spectrum showed a small increase in the second scattering peak corresponding to Co-Co (Co-Ni), suggesting a slight increase in the coordination number, which could result from total reduction of some Co oxide species to metallic Co or development of alloyed, metallic CoNi domains.[64]

XPS spectra of the catalysts before and after reduction in hydrogen further support the hypothesis that some Co oxide species were reduced to metallic Co, which may contribute to increased activity (Table 2.3) of the catalyst. XPS spectra shown in Figure 2.8 demonstrated the partial reduction of CoO to metallic cobalt. Peak deconvolution of the spectra, including multiplet splitting and Auger peaks, was conducted similar to prior literature using standard references analyzed on the same instrument.[65–68] The experimental conditions were slightly different than those for the XAS experiments, since post-reduction XPS was conducted after the catalysts were passivated in 1% O_2 (balance N_2) for one hour, which was necessary to transfer the sample from the reactor to the XPS instrument. Deconvolution of the Co region revealed that the main species present before reduction was Co_3O_4, which was reduced to Co^{2+} and Co^0 after reduction. This was noticeable mainly through the increase in the $2p_{3/2}$ satellite peak (786.7 eV), since many of the Co_3O_4 and

Co^{2+} $2p_{3/2}$ peaks were similar. After reduction at 500 °C and passivation at room temperature, the major species present was CoO, with a quantifiable amount of Co^0 that caused the shoulder at lower binding energies. Even after passivation, by analyzing the $2p_{3/2}$ deconvolution approximately 15% Co^0 species remained on the surface of the catalysts, hence adding to the metallic surface area of the catalyst.

XPS conducted around the Ni binding energy region displayed reduction results that were consistent with those gleaned from the previously mentioned characterization techniques (TPR, XAS). After passivation of the 1.1Ni-0.8Co-Al sample, the amount of Ni^0 on the surface was approximately 19% compared to the 1.4Ni-1.4Mg-Al sample, which had 14% Ni^0. Although this may at first glance appear to differ with the results from XAS, which showed more extensive reduction, the post-reduction XPS results were from a sample that experienced a passivation step, which re-oxidizes some of the reduced metal in the catalysts. When considering the combined results, the XPS and XAS of the 1.4Ni-1.4Mg-Al catalyst gave evidence of significant agglomeration of Ni, likely due to the presence of more Ni species on the surface after calcination compared to the 1.1Ni-0.8Co-Al sample. This would yield more accessible Ni^0 species, which after passivation yielded less Ni^0, as observed in the XPS results.

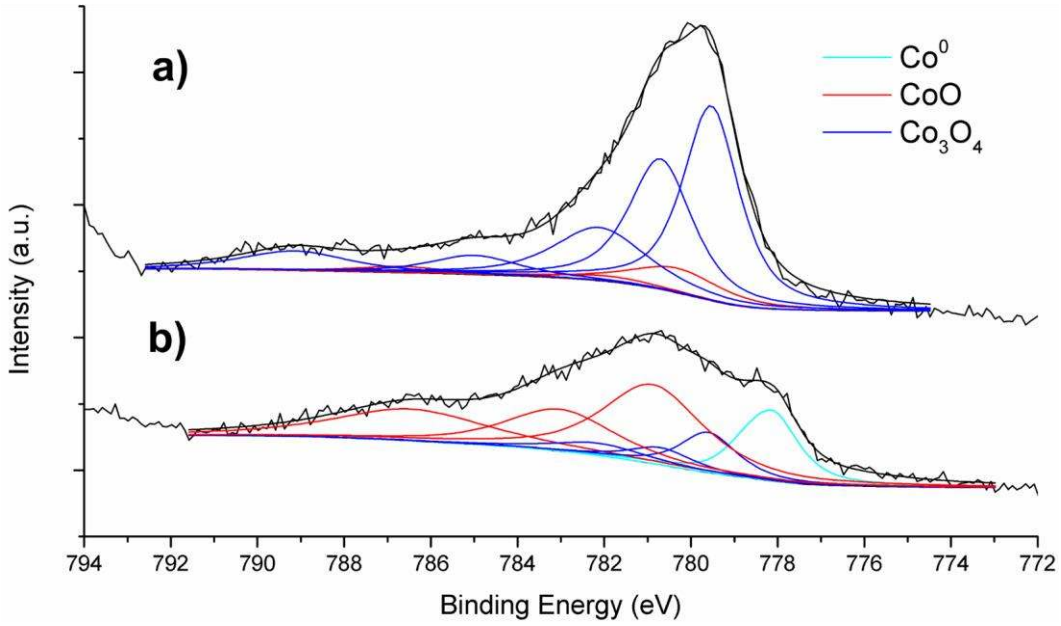

Figure 2.8 – XPS spectra of 1.1Ni-0.8Co-Al catalysts in the Co binding energy region. a) Pre-reduction; b) Post-reduction, after passivation.

The combined spectroscopic studies demonstrated that there was the emergence of metallic Ni in the Ni-Mg-Al catalyst and both metallic Ni and Co species in the Ni-Co-Al sample. However, these techniques were unable to determine the interactions between the two metallic species in the Ni-Co-Al catalyst. High angle annular dark field (HAADF) STEM allowed the morphology of both the reduced and unreduced catalysts to be probed, and EDS and EELS were conducted to complement the imaging. Figure 2.9 displays a HAADF-STEM image of a nanoparticle approximately 5 nm in size on the reduced 1.1Ni-0.8Co-Al sample, which had been reduced at similar conditions and then passivated for 1 hour in 1% O_2 (balance N_2) for sample transfer to the microscope. Two major domains can be distinguished in the nanoparticle through fast Fourier transform (FFT) analysis: the center domain contains either Ni and/or Co and the outer edge contains either NiO and/or CoO. Lattice analysis cannot discern if the particle is a mixture of Ni and Co or just an individual species; therefore, EELS and EDS were used to probe the compositions (Figure

A.8, A.9, and A.10). Both methods provide evidence that suggests a random mixture of Ni and Co species, which hints that upon reduction, NiCo alloys were produced when both metals were present in the sample. This EELS and EDS certainly support the emergence of NiCo alloys previously observed by the other techniques.

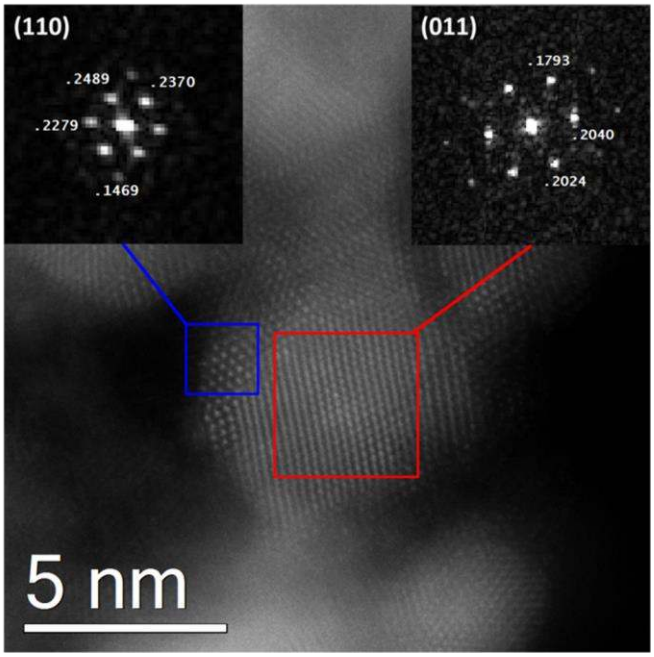

Figure 2.9 – HRSTEM image and diffraction of reduced 1.1Ni-0.8Co-Al catalysts at 500 °C for 1 hour and then passivated at RT for 1 hour in 1% O_2 balance N_2.

The hypothesis that bimetallic nanoparticle emerge after reduction may offer an explanation for the enhanced catalytic activity in the 1.1Ni-0.8Co-Al compared to both 2Ni-Al and 1.4Ni-1.4Mg-Al, where no bimetallic particles can be formed under the reduction conditions employed. The intimate mixing of each metal species may facilitate hydrogen spillover to CoO, which may allow CoO to reduce simultaneously, ultimately being a factor in the increase in activity. From XAS, XPS, and STEM results, the oxide species present after reduction were a mixture of NiO, CoO, and Al_2O_3, which may have been a more useful combination than NiO, MgO, and Al_2O_3. Lastly, it is interesting to note

that the metallic species do not seem to significantly change the overall FAL selectivity, but the nature of the oxide species does produce changes in the nature of the different side products observed.

2.4 Conclusions

Porous nickel MMO catalysts were synthesized by calcination of LDH derived materials to investigate the effects of various oxophilic metal additions to the structure and reactivity of the Ni metal particles. LDH derived MMOs allowed for the comparison of various metal additions to Ni based catalysts on the conversion of FUR under vapor phase hydrogenation conditions. In the calcined mixed oxide materials, a homogeneous solid solution was formed with no observed separation of oxide domains as shown by XRD, suggesting close interactions between the Ni and other metals. TPR profiles suggested complex reduction behavior in the materials due to the various reducible species present in the MMOs including surface NiO, bulk NiO, Co_3O_4, and CoO species. Under the reduction conditions employed, neither Ni nor Co were fully reduced, which is attributed to metallic particles embedded in an oxide structure, likely with strong metal-support interactions. At high FUR conversion in a flow reactor, FAL was the major product produced. The inclusion of different oxophilic metals (Co vs. Mg) in varied amounts influenced the product distribution (mildly) and activity (more significantly) of the catalysts. In general, Mg catalysts showed less activity per site and slightly higher furan production, while the Co catalysts showed higher activity per site and slightly higher 2-MF production. At low conversions, the STY of the 1.1Ni-0.8Co-Al was more than three times that of the 1.4Ni-1.4Mg-Al catalyst and 50% greater than the catalyst with no metal addition (2Ni-Al). Through extensive spectroscopic characterization by XAS and XPS, the increase in activity

was attributed to the increased homogeneity of the Ni-Co catalysts, which gave metallic domains associated with both Ni^0 and Co^0. STEM and EELS characterization supported the hypothesis that NiCo alloys may have formed in the catalysts containing both metals. Further studies varying the calcination temperature and reduction temperature could potentially allow for tuning of the nature of the reduced species in the NiCo catalyst, further influencing the activity and product distribution.

2.5 References

(1) Sulmonetti, T. P.; Pang, S. H.; Taborga Claure, M.; Lee, S.; Cullen, D. A.; Agrawal, P. K.; Jones, C. W. Vapor phase hydrogenation of furfural over nickel mixed metal oxide catalysts derived from layered double hydroxides. *Appl. Catal. A Gen.* **2016**, *517*, 187–195.

(2) Baños, R.; Manzano-Agugliaro, F.; Montoya, F. G.; Gil, C.; Alcayde, a.; Gómez, J. Optimization methods applied to renewable and sustainable energy: A review. *Renew. Sustain. Energy Rev.* **2011**, *15*, 1753–1766.

(3) Alonso, D. M.; Wettstein, S. G.; Dumesic, J. A. Bimetallic catalysts for upgrading of biomass to fuels and chemicals. *Chem. Soc. Rev.* **2012**, *41*, 8075–8098.

(4) Alonso, D. M.; Bond, J. Q.; Dumesic, J. A. Catalytic conversion of biomass to biofuels. *Green Chem.* **2010**, *12*, 1493–1513.

(5) Lange, J.-P.; van der Heide, E.; van Buijtenen, J.; Price, R. Furfural-a promising platform for lignocellulosic biofuels. *ChemSusChem* **2012**, *5*, 150–166.

(6) Gallezot, P. Conversion of biomass to selected chemical products. *Chem. Soc. Rev.* **2012**, *41*, 1538–1558.

(7) Rinaldi, R.; Schüth, F. Design of solid catalysts for the conversion of biomass. *Energy Environ. Sci.* **2009**, *2*, 610–626.

(8) Adkins, H.; Connor, R. The catalytic hydrogenation of organic compounds over copper chromite. *J. Am. Chem. Soc.* **1931**, *53*, 1091–1095.

(9) Rao, R.; Dandekar, A.; Baker, R. T. K.; Vannice, M. A. Properties of copper chromite catalysts in hydrogenation reactions. *J. Catal.* **1997**, *171*, 406–419.

(10) Frainer, L.; Fineberg, H. United States. 4,302,397, 1981.

(11) Vicente, A.; Lafaye, G.; Especel, C.; Marécot, P.; Williams, C. T. The relationship between the structural properties of bimetallic Pd-Sn/SiO_2 catalysts and their performance for selective citral hydrogenation. *J. Catal.* **2011**, *283*, 133–142.

(12) Merlo, A. B.; Vetere, V.; Ruggera, J. F.; Casella, M. L. Bimetallic PtSn catalyst for the selective hydrogenation of furfural to furfuryl alcohol in liquid-phase. *Catal. Commun.* **2009**, *10*, 1665–1669.

(13) Nakagawa, Y.; Tamura, M.; Tomishige, K. Catalytic reduction of biomass-derived furanic compounds with hydrogen. *ACS Catal.* **2013**, *3*, 2655–2668.

(14) Sitthisa, S.; Resasco, D. E. Hydrodeoxygenation of furfural over supported metal catalysts: A comparative study of Cu, Pd and Ni. *Catal. Letters* **2011**, *141*, 784–791.

(15) Nakagawa, Y.; Nakazawa, H.; Watanabe, H.; Tomishige, K. Total hydrogenation of furfural over a silica-supported nickel catalyst prepared by the reduction of a nickel nitrate precursor. *ChemCatChem* **2012**, *4*, 1791–1797.

(16) Sitthisa, S.; Sooknoi, T.; Ma, Y.; Balbuena, P. B.; Resasco, D. E. Kinetics and mechanism of hydrogenation of furfural on Cu/SiO_2 catalysts. *J. Catal.* **2011**, *277*, 1–13.

(17) Pushkarev, V. V; Musselwhite, N.; An, K.; Alayoglu, S.; Somorjai, G. A. High structure sensitivity of vapor-phase furfural decarbonylation/hydrogenation reaction network as a function of size and shape of Pt nanoparticles. *Nano Lett.* **2012**, *12*, 5196–5201.

(18) Baker, L. R.; Kennedy, G.; Van Spronsen, M.; Hervier, A.; Cai, X.; Chen, S.; Wang, L.-W.; Somorjai, G. A. Furfuraldehyde hydrogenation on titanium oxide-supported platinum nanoparticles studied by sum frequency generation vibrational spectroscopy: acid-base catalysis explains the molecular origin of strong metal-support interactions. *J. Am. Chem. Soc.* **2012**, *134*, 14208–14216.

(19) Pang, S. H.; Medlin, J. W. Adsorption and Reaction of Furfural and Furfuryl Alcohol on Pd(111): Unique Reaction Pathways for Multifunctional Reagents. *ACS Catal.* **2011**, No. 111, 1272–1283.

(20) Shi, Y.; Zhu, Y.; Yang, Y.; Li, Y.-W.; Jiao, H. Exploring Furfural Catalytic Conversion on Cu(111) from Computation. *ACS Catal.* **2015**, *5*, 4020–4032.

(21) Wang, S.; Vorotnikov, V.; Vlachos, D. G. Coverage-induced conformational effects on activity and selectivity: Hydrogenation and decarbonylation of furfural on Pd(111). *ACS Catal.* **2015**, *5*, 104–112.

(22) Xu, W.; Wang, H.; Liu, X.; Ren, J.; Wang, Y.; Lu, G. Direct catalytic conversion of furfural to 1,5-pentanediol by hydrogenolysis of the furan ring under mild conditions over Pt/Co_2AlO_4 catalyst. *Chem. Commun.* **2011**, *47*, 3924–3926.

(23) Zhang, B.; Zhu, Y.; Ding, G.; Zheng, H.; Li, Y. Selective conversion of furfuryl alcohol to 1,2-pentanediol over a Ru/MnO_x catalyst in aqueous phase. *Green Chem.* **2012**, *14*, 3402–3409.

(24) Yao, S.; Wang, X.; Jiang, Y.; Wu, F.; Chen, X.; Mu, X. One-Step conversion of biomass-derived 5-hydroxymethylfurfural to 1,2,6-hexanetriol over Ni–Co–Al mixed oxide catalysts under mild conditions. *ACS Sustain. Chem. Eng.* **2014**, *2*, 173–180.

(25) Kong, X.; Zhu, Y.; Zheng, H.; Li, X.; Zhu, Y.; Li, Y. W. Ni nanoparticles inlaid nickel phyllosilicate as a metal-acid bifunctional catalyst for low-temperature hydrogenolysis reactions. *ACS Catal.* **2015**, *5*, 5914–5920.

(26) Kong, X.; Zheng, R.; Zhu, Y.; Ding, G.; Zhu, Y.; Li, Y. Rational design of Ni-based catalysts derived from hydrotalcite for selective hydrogenation. *Green Chem.* **2015**, *17*, 2504–2514.

(27) Tamura, M.; Tokonami, K.; Nakagawa, Y.; Tomishige, K. Rapid synthesis of unsaturated alcohols under mild conditions by highly selective hydrogenation. *Chem. Commun.* **2013**, *49*, 7034–7036.

(28) Wu, S.-H.; Chen, D.-H. Synthesis and characterization of nickel nanoparticles by hydrazine reduction in ethylene glycol. *J. Colloid Interface Sci.* **2003**, *259*, 282–286.

(29) Sitthisa, S.; An, W.; Resasco, D. E. Selective conversion of furfural to methylfuran over silica-supported NiFe bimetallic catalysts. *J. Catal.* **2011**, *284*, 90–101.

(30) Nakagawa, Y.; Tomishige, K. Total hydrogenation of furan derivatives over silica-supported Ni–Pd alloy catalyst. *Catal. Commun.* **2010**, *12*, 154–156.

(31) Cavani, F.; Trifirò, F.; Vaccari, A. Hydrotalcite-type anionic clays: preparation, properties and applications. *Catal. Today* **1991**, *11*, 173–301.

(32) Xu, Z. P.; Zhang, J.; Adebajo, M. O.; Zhang, H.; Zhou, C. Catalytic applications of layered double hydroxides and derivatives. *Appl. Clay Sci.* **2011**, *53*, 139–150.

(33) Sels, B. F.; De Vos, D. E.; Jacobs, P. A. Hydrotalcite-like anionic clays in catalytic organic reactions. *Catal. Rev.* **2001**, *43*, 443–488.

(34) Feng, J.; He, Y.; Liu, Y.; Du, Y.; Li, D. Supported catalysts based on layered double hydroxides for catalytic oxidation and hydrogenation: general functionality and promising application prospects. *Chem. Soc. Rev.* **2015**, *44*, 5291–5319.

(35) Villaverde, M. M.; Garetto, T. F.; Marchi, A. J. Liquid-phase transfer hydrogenation of furfural to furfuryl alcohol on Cu–Mg–Al catalysts. *Catal. Commun.* **2015**, *58*, 6–10.

(36) Audemar, M.; Ciotonea, C.; De Oliveira Vigier, K.; Royer, S.; Ungureanu, A.;

Dragoi, B.; Dumitriu, E.; Jérôme, F. Selective hydrogenation of furfural to furfuryl alcohol in the presence of a recyclable cobalt/SBA-15 catalyst. *ChemSusChem* **2015**, *8*, 1885–1891.

(37) Srivastava, S.; Solanki, N.; Mohanty, P.; Shah, K. a.; Parikh, J. K.; Dalai, A. K. Optimization and kinetic studies on hydrogenation of furfural to furfuryl alcohol over SBA-15 supported bimetallic copper–cobalt catalyst. *Catal. Letters* **2015**, *145*, 816–823.

(38) Ribet, S.; Tichit, D.; Coq, B.; Ducourant, B.; Morato, F. Synthesis and activation of Co-Mg-Al layered double hydroxides. *J. Solid State Chem.* **1999**, *142*, 382–392.

(39) Fan, G.; Li, F.; Evans, D. G.; Duan, X. Catalytic applications of layered double hydroxides: recent advances and perspectives. *Chem. Soc. Rev.* **2014**, *43*, 7040–7066.

(40) Kuboon, S.; Hu, Y. H. Study of NiO - CoO and Co_3O_4 – Ni_3O_4 Solid Solutions in Multiphase Ni - Co - O Systems. *Ind. Eng. Chem. Res.* **2011**, *50*, 2015–2020.

(41) Li, M.; Wang, X.; Li, S.; Wang, S.; Ma, X. Hydrogen production from ethanol steam reforming over nickel based catalyst derived from Ni/Mg/Al hydrotalcite-like compounds. *Int. J. Hydrogen Energy* **2010**, *35*, 6699–6708.

(42) Jacobs, G.; Ji, Y.; Davis, B. H.; Cronauer, D.; Kropf, a. J.; Marshall, C. L. Fischer-Tropsch synthesis: Temperature programmed EXAFS/XANES investigation of the influence of support type, cobalt loading, and noble metal promoter addition to the reduction behavior of cobalt oxide particles. *Appl. Catal. A Gen.* **2007**, *333*, 177–191.

(43) Rudolf, C.; Dragoi, B.; Ungureanu, A.; Chirieac, A.; Royer, S.; Nastro, A.; Dumitriu, E. NiAl and CoAl materials derived from takovite-like LDHs and related structures as efficient chemoselective hydrogenation catalysts. *Catal. Sci. Technol.* **2014**.

(44) Busca, G.; Costantino, U.; Montanari, T.; Ramis, G.; Resini, C.; Sisani, M. Nickel versus cobalt catalysts for hydrogen production by ethanol steam reforming: Ni–Co–Zn–Al catalysts from hydrotalcite-like precursors. *Int. J. Hydrogen Energy* **2010**, *35*, 5356–5366.

(45) Salam, M. A.; Lwin, Y.; Sufian, S. Synthesis of nano-structured Ni-Co-Al hydrotalcites and derived mixed oxides. *Adv. Mater. Res.* **2012**, *626*, 173–177.

(46) Tada, S.; Yokoyama, M.; Kikuchi, R.; Haneda, T.; Kameyama, H. N_2O pulse titration of Ni/Al_2O_3 catalysts: A new technique applicable to nickel surface-area determination of nickel-based catalysts. *J. Phys. Chem. C* **2013**, *117*, 14652–14658.

(47) Chia, M.; Pagán-Torres, Y. J.; Hibbitts, D.; Tan, Q.; Pham, H. N.; Datye, A. K.; Neurock, M.; Davis, R. J.; Dumesic, J. A. Selective hydrogenolysis of polyols and

cyclic ethers over bifunctional surface sites on rhodium-rhenium catalysts. *J. Am. Chem. Soc.* **2011**, *133*, 12675–12689.

(48) Layman, K. a.; Bussell, M. E. Infrared spectroscopic investigation of CO adsorption on silica-supported nickel phosphide catalysts. *J. Phys. Chem. B* **2004**, *108*, 15791–15802.

(49) Shalvoy, R. B. Summary Abstract: Investigation of the metal-support interaction in coprecipitated nickel on alumina methanation catalysts using x-ray photoelectron spectroscopy. *J. Vac. Sci. Technol.* **1980**, *17*, 209.

(50) Khassin, A. a.; Yurieva, T. M.; Kustova, G. N.; Itenberg, I. S.; Demeshkina, M. P.; Krieger, T. a.; Plyasova, L. M.; Chermashentseva, G. K.; Parmon, V. N. Cobalt-aluminum co-precipitated catalysts and their performance in the Fischer-Tropsch synthesis. *J. Mol. Catal. A Chem.* **2001**, *168*, 193–207.

(51) Zhang, J.; Wang, H.; Dalai, A. K. Effects of metal content on activity and stability of Ni-Co bimetallic catalysts for CO_2 reforming of CH_4. *Appl. Catal. A Gen.* **2008**, *339*, 121–129.

(52) Tichit, D.; Coq, B. Catalysis by Hydrotalcites and Related Materials. *Cattech* **2003**, *7*, 206–217.

(53) Kühl, S.; Tarasov, A.; Zander, S.; Kasatkin, I.; Behrens, M. Cu-based catalyst resulting from a Cu,Zn,Al hydrotalcite-like compound: a microstructural, thermoanalytical, and in situ XAS study. *Chem. Eur. J.* **2014**, *20*, 3782–3792.

(54) Vargas-Hernández, D.; Rubio-Caballero, J. M.; Santamaría-González, J.; Moreno-Tost, R.; Mérida-Robles, J. M.; Pérez-Cruz, M. a.; Jiménez-López, a.; Hernández-Huesca, R.; Maireles-Torres, P. Furfuryl alcohol from furfural hydrogenation over copper supported on SBA-15 silica catalysts. *J. Mol. Catal. A Chem.* **2014**, *383–384*, 106–113.

(55) Gonzalez-delacruz, V. M.; Pere, R.; Ternero, F.; Holgado, J. P.; Caballero, A. In Situ XAS study of synergic effects on Ni-Co/ZrO_2 methane reforming catalysts. *J. Phys. Chem. C* **2012**, *116*, 2919–2926.

(56) Günter, M. M.; Ressler, T.; Jentoft, R. E.; Bems, B. Redox behavior of copper oxide/zinc oxide catalysts in the steam reforming of methanol studied by in situ X-ray diffraction and absorption spectroscopy. *J. Catal.* **2001**, *203*, 133–149.

(57) *X-ray Absorption Fine Structure for Catalysts and Surfaces*; Iwasawa, Y., Ed.; World Scientific Publisihing Co. Pte. Ltd.: Singapore, 1996.

(58) Sankar, G.; Thomas, J. M. In situ combined X-ray absorption spectroscopic and X-ray diffractometric studies of solid catalysts. *Top. Catal.* **1999**, *8*, 1–21.

(59) Gonzalez-Delacruz, V. M.; Pereñiguez, R.; Ternero, F.; Holgado, J. P.; Caballero,

A. Modifying the size of nickel metallic particles by H_2/CO treatment in Ni/ZrO_2 methane dry reforming catalysts. *ACS Catal.* **2011**, *1*, 82–88.

(60) Baudouin, D.; Rodemerck, U.; Krumeich, F.; Mallmann, A. De; Szeto, K. C.; Ménard, H.; Veyre, L.; Candy, J. P.; Webb, P. B.; Thieuleux, C.; et al. Particle size effect in the low temperature reforming of methane by carbon dioxide on silica-supported Ni nanoparticles. *J. Catal.* **2013**, *297*, 27–34.

(61) Marco, J. F.; Gancedo, J. R.; Gracia, M.; Gautier, J. L.; Rios, E.; Berry, F. J. Characterization of the nickel cobaltite, $NiCo_2O_4$ prepared by several methods: An XRD, XANES, EXAFS, and XPS study. *J. Solid State Chem.* **2000**, *153*, 74–81.

(62) Wang, L.; Li, D.; Koike, M.; Watanabe, H.; Xu, Y.; Nakagawa, Y.; Tomishige, K. Catalytic performance and characterization of Ni-Co catalysts for the steam reforming of biomass tar to synthesis gas. *Fuel* **2013**, *112*, 654–661.

(63) Castner, D. G.; Watson, P. R.; Chan, I. Y. X-ray absorption spectroscopy , X-ray photoelectron spectroscpy, and analytical electron microscopy studies of cobalt catalysts. 2. Hydrogen reduction properties. *J. Phys. Chem.* **1990**, *94*, 819–828.

(64) Tsakoumis, N. E.; Voronov, A.; Ronning, M.; Beek, W. Van; Borg, O.; Rytter, E.; Holmen, A. Fischer-Tropsch synthesis: An XAS/XRPD combined in situ study from catalyst activation to deactivation. *J. Catal.* **2012**, *291*, 138–148.

(65) Grosvenor, A. P.; Biesinger, M. C.; Smart, R. S. C.; McIntyre, N. S. New interpretations of XPS spectra of nickel metal and oxides. *Surf. Sci.* **2006**, *600*, 1771–1779.

(66) Biesinger, M. C.; Payne, B. P.; Grosvenor, A. P.; Lau, L. W. M.; Gerson, A. R.; Smart, R. S. C. Resolving surface chemical states in XPS analysis of first row transition metals, oxides and hydroxides: Cr, Mn, Fe, Co and Ni. *Appl. Surf. Sci.* **2011**, *257*, 2717–2730.

(67) Heracleous, E.; Lee, a; Wilson, K.; Lemonidou, a. Investigation of Ni-based alumina-supported catalysts for the oxidative dehydrogenation of ethane to ethylene: structural characterization and reactivity studies. *J. Catal.* **2005**, *231*, 159–171.

(68) Zhang, L.; Li, F.; Xiang, X.; Wei, M.; Evans, D. G. Ni-based supported catalysts from layered double hydroxides: Tunable microstructure and controlled property for the synthesis of carbon nanotubes. *Chem. Eng. J.* **2009**, *155*, 474–482.

CHAPTER 3 PRODUCTION OF 2-METHYLFURAN UTILIZING REDUCED CO-FE-AL MMO CATALYSTS

This chapter and Appendix B are adapted from the published article, Sulmonetti, T. P.; Hu, B.; Ifkovits, Z. P.; Lee, S.; Agrawal, P. K.; Jones, C. W. Vapor phase hydrogenolysis of furanics utilizing reduced cobalt mixed metal oxide catalysts. *ChemCatChem* **2017**, *9*, 1815–1823, with permission from Wiley. DOI: 10.1002/cctc.201700228.[1]

3.1 Introduction

Second generation lignocellulosic biomass, the inedible fraction of biomass, is a target for conversion into chemicals and fuel additives because of its perceived likelihood to not interrupt food supplies.[2,3] Lignocellulose can be broken down into various sugars that can be further processed through dehydration to create furanic compounds. FUR and FAL are major platform chemicals in biomass processing that can be catalytically converted into valuable products such as THFA, 2-MF, 1,2-PD, and 1,5-PD, among others.[4] Through the hydrogenolysis of FAL, 2-MF is produced, which is a valuable fuel additive. With a research octane number of 131 and low water solubility, 2-MF is an attractive replacement for bio-ethanol as a fuel additive.[5] Therefore, recent research has focused on catalytically converting FUR and/or FAL selectively towards 2-MF.

Industrially, Cu-Cr catalysts have shown versatility in FUR conversion, and at certain conditions, these catalysts give high yields towards 2-MF.[6] However, due to environmental concerns associated with Cr, development of alternative catalysts is

worthwhile. Many monometallic catalysts, typically supported on silica, have been investigated for hydrogenation of furanic compounds. However, these typically suffer from poor selectivities towards 2-MF.[7,8] Improvements in selectivity for catalytic conversion of furanics has often been achieved by the incorporation of multiple metals to form bimetallic or bifunctional catalysts. In this work, the term bimetallic catalyst will refer to a catalyst that contains two fully reduced metals forming an alloy, while the term bifunctional catalyst will refer to catalysts that combine a metallic species and metal oxide species, which may form acidic or basic sites.[9] In regards to 2-MF production, prior work involving Ni-Fe/SiO_2 has been conducted to investigate the enhancement in selectivity that occurs when a secondary metal is added.[10] Through DFT and kinetic studies, it has been suggested that the oxophilicity of Fe facilitated the adsorption of FAL through a η^2-(C,O) surface species, which drove the reaction towards hydrogenolysis of the C=O bond.[10,11] Additionally, very recent studies have been conducted with Cu-Fe supported on carbon and silica have also demonstrated a synergistic effect between the more oxophilic Fe species and the more reduced Cu species for hydrogenation and hydrogenolysis of FUR. TPD and HREELS experiments under ultra-high vacuum conducted on Pt-Zn catalysts have suggested a similar mechanism, where Zn acts as the oxophilic metal and allows for a tilted adsorption mode to be more prevalent on the catalyst surface.[14] Other vapor phase reactions have been conducted with multiple metal systems including Cu-Zn-Al and Cu-Zn-Al-Ca-Na.[15,16] Lastly, Mo_2C catalysts have been shown to be selective towards 2-MF due to the creation of two active sites (bifunctional), a "metal-like site" and a carbidic, oxycarbidic, or oxide site; however, the type of secondary site remains unknown based on the evidence presented to date.[17]

Many investigations involving liquid phase reactions, both flow and batch, for the hydrogenolysis of furanics including FUR to 2-MF and HMF to DMF have been performed, mainly involving multiple metal catalyst systems. In regards to HMF to DMF, Ni/Co_3O_4, Ru/Co_3O_4, Ni-W_2C/C, Cu-Ru/C, Pt-Co/C, Cu-Co/C and Cu-ZnO have been investigated, and in regards to FUR to 2-MF, Ru-RuO_2/C, Cu-Co/Al_2O_3, and Pd/TiO_2 have been utilized.[5,18–26] Unfortunately, many of these reactions require high H_2 pressures, have low product throughput, and/or use precious metals, which makes vapor phase flow reactions with non-precious metals a potentially attractive alternative. Consequently, in this work, we sought to create a non-precious, multi-metal system that would be selective towards hydrogenolysis of the C-O bond of FAL in vapor phase flow reactions.

A previous study involving Co-Al MMOs derived from LDH displayed elevated selectivities towards 2-MF in the vapor phase hydrogenation of FUR at 155 °C.[27] The use of LDH materials as precursors to synthesize MMOs is a well-known approach to create well-dispersed and relatively high porosity materials.[28] The LDH material allows for high interaction between the various metals in the matrix, and can lead to smaller metal domains upon reduction. To this end, Co was chosen as the base metal in the catalyst family explored here, while various Fe amounts were added into the matrix to tailor the activity and selectivity. Reduction with hydrogen allowed for the creation of active metallic species, and through TPR, XAS, and XPS, it was shown that the incorporation of Fe facilities reduction at lower temperatures, which in turn enhances both selectivity and activity towards 2-MF

3.2 Experimental Section

3.2.1 Materials and Chemicals

Furfural (99% purity, ACS Grade) and Furfuryl Alcohol (98% purity) were purchased from Sigma Aldrich, vacuum distilled, and then stored in inert atmosphere before use in reactions. $Co(NO_3)_2 \cdot 6H_2O$ (99% purity), Na_2CO_3 (99.5% purity), and ethylene glycol diethyl ether (98% purity) were purchased from Sigma Aldrich. $Fe(NO_3)_3 \cdot 9H_2O$, and $Al(NO_3)_3 \cdot 9H_2O$ were all purchased from Alfa Aesar (98%-102%). NaOH (97% purity) was purchased from EMD. Lastly, unless noted, all chemicals were used as is without any further purification.

3.2.2 Catalyst Synthesis

Co-Fe-Al mixed metal oxides with varying Co:Fe ratios of 12:1, 6:1, 4:1, 3:1, and no Fe addition (Co/(Fe+Al) always kept at 0.25) were prepared in the following manner, similar to prior LDH syntheses, with minor modifications.[27,29] A 0.6 M metal nitrate solution, Solution A, with corresponding metal cations ratios above, and a 1.0 M NaOH solution, Solution B, were created. A 0.3 M solution of Na_2CO_3, Solution C, was placed in a 3-neck, 1 L flask, and using a peristaltic pump Solution A and Solution B were added dropwise into Solution C at approximately 5 mL/min under vigorous stirring, at room temperature, with N_2 bubbling. The pH was maintained at 10 by adjusting Solution B. The pump was shut off once Solution A ran out, and the final solution was heated to 60 °C, and maintained under vigorous stirring and N_2 bubbling for 24 h. Once complete, the final solution was filtered and washed until the filtered solution had a pH of ~7 (about 1.5 L of DI water was used) to obtain the LDH precipitant. The recovered solid was dried in an oven at 105°C overnight. To create the MMO, the dried LDH material was calcined at

400°C with 50 mL/min flow of air with a ramp rate of 10°C/min, being held at 400°C for 4 hours.

3.2.3 Reaction Studies

Vapor phase reactions were performed in a ¼" tubular stainless steel reactor located inside a furnace. The catalyst was pelletized (>270 mesh), diluted with SiC (200-400 mesh), and loaded into the reactor between layers of SiC (46 mesh) and quartz wool. The catalysts were reduced in situ under 60 mL/min H_2 (Airgas, UHP) to 500˚C with a ramp rate of 5°C/min, then subsequently held for one hour. Once the reduction was completed, the bed was cooled under H_2 to reaction temperature, which was typically conducted at 180 °C. Unless stated otherwise, reactions were conducted in a flow of 60 mL/min of H_2, while FAL was pumped into the vaporization zone at a rate of 5.5 mmol/h (with ~4 mol% ethylene glycol diethyl ether as internal standard). The FAL flow met heated H_2 in the vaporization zone, which was heated to approximately 180 °C. The vapor flowed through the catalyst bed, and then it flowed into an online Agilent 7890A GC through lines heated to approximately 185 °C to mitigate reactant and product condensation. Selectivity and conversion were determined by the internal standard method, and carbon balances were within 95% typically due to small amounts of unknown products, unless stated otherwise. After the reaction or reduction was completed, the catalyst was passivated for one hour at room temperature under 1% O_2/N_2 (Airgas), separated form SiC, and stored under argon for further characterization studies.

3.2.4 Characterization Techniques

3.2.4.1 Physical Characterization and XRD

Nitrogen physisorption was performed in a Micromeritics Tristar II at -196°C after the samples were pretreated at 200°C under vacuum for 12 h. Chemisorption and TPR experiments were conducted in a Micromeritics AutoChem II 2920. For each experiment, approximately 50 mg of sample was placed on top of a small bed of quartz wool in a quartz U-tube. In regards to the TPR experiment, the MMO was pretreated in 20 mL/min of He (Airgas, UHP) at 200°C for 2 h to remove pre-adsorbed species. The sample was then cooled to 50°C and 20 mL/min of 10% H_2 (balance Ar) was passed through the sample. The furnace was heated to 800°C at 5°C/min while under the flow of 10% H_2/Ar. The outlet gas passed through a liquid acetone/nitrogen trap, and then was passed through a TCD. Elemental analysis for each catalyst was conducted at the Georgia Tech Renewable Bioproducts Institute on an ICP-OES instrument, a PerkinElmer OPTIMA 7300 DV, after dissolving the metal oxides in dilute H_2SO_4 solution.

Powder XRD were collected using a Philips X-pert diffractometer using Cu Kα radiation. XPS analysis was performed using a Thermo K-Alpha spectrometer employing a monochromatic Al Kα. The pressures inside the analytical chamber was approximately $1x10^{-7}$ Torr. The binding energies (BE) of all elements were tuned to the Ag 3d peak (368.2 eV) with an uncertainty of ± 0.2 eV.

3.2.4.2 Spectroscopic Experiments

In situ X-ray absorption spectroscopy (XANES and EXAFS) were conducted at the APS in ANL at beamline 12-BM. The data were obtained in transmission mode at the Fe K-edge (7112 eV) in the range of 6910-7910 eV, and the Co K-edge (7712 eV) in the range of 7510-8712 eV, both with a spot size of 0.5 mm x 1.2 mm. To perform the *in situ*

reduction XAS, the catalyst sample was diluted and ground with boron nitride (5:1 BN: catalyst), and then ~8 mg of the mixture was loaded and pressed into a "six shooter" holder (multiple samples could be pressed into the holder). This holder was then placed into a quartz tube with Kapton windows at each end to allow X-rays to pass through, and a gas line was attached to the tube. A scan was collected prior to reduction at room temperature. Next, the catalyst was heated to 500 °C at 5 °C/min and held for 1 h, all while under a 60 mL/min flow of pure H_2. After the reduction was complete, the sample was cooled down in H_2, and a final scan was collected at room temperature. Various standards were used to verify the species present in the catalyst sample. The XAS data were processed and analyzed with Athena software including background removal, edge-step normalization, and Fourier transform. Artemis software was utilized to fit the Fourier transformed EXAFS data with a model. Co-Co, Fe-Fe, Fe-O reference parameters were calculated using Co foil (FCC), Fe foil (BCC), and Fe(III) acetylacetonate as standards. Multiple scattering paths through crystallographic data including, Co-Co[30], Fe-Fe[31], Fe-O-Fe[32], Fe-O-Al[33], and Fe-Al[34], were calculated using FEFF8.[35] Due to the complexity of the matrix, various constraints were added on the Debye-Waller factor and bond distances for some of the catalysts, similar to previous bimetallic systems.[36,37]

3.3 Results and Discussion

3.3.1 Initial MMOs Characterization

Our main interest in LDH based materials was that the synthesis procedure allows for versatility in metal additions while maintaining similar physical properties. After calcination of these materials, the intercalated anions are removed, leaving a porous MMO

with high dispersion of metal oxide species. This high dispersion suggests intimate contact of various metal species, which could improve activity or selectivity of the catalyst. To that end, Co was chosen as the base metal in the system due to the unique selectivity properties previously determined in FUR reduction.[27] Along with Co, small amounts of Fe were added into MMO matrix to tune the activity and selectivity towards 2-MF. In Table 3.1, the physical properties are summarized for various Co/Fe ratio.

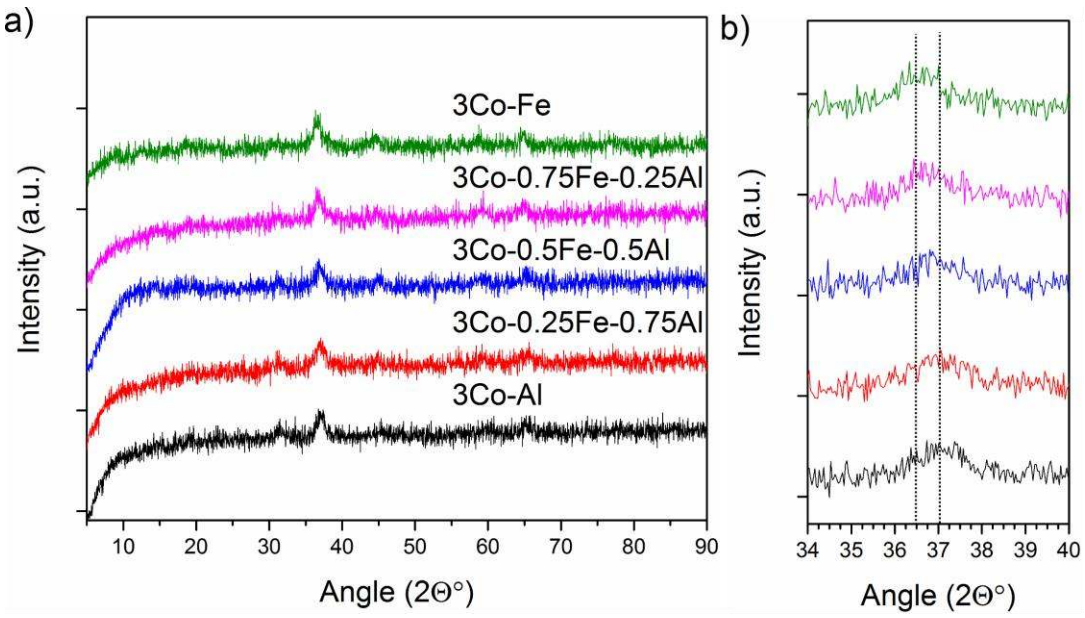

Figure 3.1 – a) XRD patterns of Co-xFe-yAl catalysts after calcination at 400 °C; b) Enlarged section of major Bragg peak between 35-40°.

The porosity of the post-calcined LDH materials is displayed in Table 3.1, which shows that the BET surface area for all materials, was within a narrow range (105 m^2/g-150 m^2/g), while the pore volumes were approximately 0.30 cm^3/g. ICP analyses were in good agreement with the targeted molar ratios, with slightly lower Co amounts than anticipated. For simplicity throughout the manuscript, the catalysts were labeled with their target molar ratios.

Table 3.1 – Physical properties of multiple Co based MMO catalysts

Catalyst	Elemental analysis (Co:Fe:Al)	BET Surface Area (m^2/g)	Pore Volume (cm^3/g)	Average Pore Diameter (nm)
3Co-Al	2.94:0:1.0	129	0.35	11.0
3Co-0.25Fe-0.75Al	2.83:0.25:0.75	150	0.32	8.6
3Co-0.5Fe-0.5Al	2.83:0.50:0.50	133	0.30	8.7
3Co-0.75Fe-0.25Al	2.92:0.74:0.26	115	0.31	10.4
3Co-Fe	2.93:1.0:0	107	0.33	12.1

After calcination at 400 °C, most LDH materials lose their layered structure to create a more homogeneous MMOs. Through XAS and XPS analysis, it was determined that the majority of the crystalline species present after calcination were Co_3O_4, Fe_2O_3, and Al_2O_3, and there was no indication of CoO, FeO, or significant metal aluminate species. The XRD patterns of the uncalcined material are shown in Figure B.2, which display prominent (003) and (006) peaks. These peaks represent the layered hydroxides with intercalating CO_3^{-2} and H_2O to balance framework charge. The XRD patterns post-calcination demonstrated that a non-crystalline structure was created, as evidenced by the lack of sharp peaks associated with the oxides present in Figure 3.1a. One broad peak is distinguishable between 35-40°, which correlates with the Co_3O_4 (311) peak at 37.0°. Additionally, when that section is enlarged in Figure 3.1b, there was a small yet noticeable shift to lower Bragg angles with the increased addition of Fe. The poor crystallinity along with the shift in the Co_3O_4 (311) peak towards the Fe_2O_3 (311) peak at 35.0° and no visible Al_2O_3 peaks, might have suggested good dispersion of the oxide species. Potentially the material formed a solid solution similar to Ni-Co-Al and Ni-Mg-Al MMOs reported in prior literature.[27,28,38]

The reduction profile of each catalyst was investigated through TPR to gather information about the catalyst under an H_2 atmosphere with varying temperature. Figure 3.2 shows the reduction profile of each catalyst in 10% H_2/Ar using a 5 °C/min ramp rate. All five profiles demonstrated a two-step reduction, one at a low temperature between 200 °C- 300 °C and one at high temperature between 400 °C - 750 °C. The low temperature peaks referred to Co_3O_4 and Fe_2O_3 phases reducing to CoO, and Fe_3O_4/FeO, while the broad, high temperature peak were associated with the reduction of cobalt and iron oxide species to metallic Co and Fe.[38,39] As expected, the addition of Fe slightly shifted the peak reduction temperature to lower temperatures since the reduction potential of Fe oxide was much greater than Al_2O_3. Without any Al_2O_3, the TPR profile became much sharper, and the H_2 uptake began to significantly decline around 500 °C. This indicated that the Al_2O_3 acts as a stabilizer, even at 6.6 wt% in the matrix, since it was unable to reduce under these conditions, and may have helped prevent complete aggregation of metallic species.

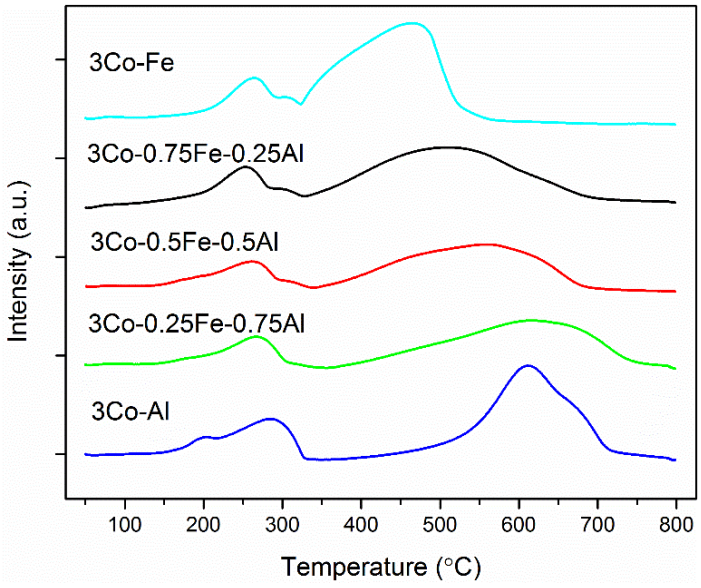

Figure 3.2 – TPR profile of each Co-xFe-yAl catalyst in a 10% H_2 (balance Ar) atmosphere with a 5 °C/min ramp rate.

3.3.2 Vapor Phase Flow Reactions

Initial reaction studies with FAL as the substrate were conducted at a common weight hourly space velocity (WHSV) to screen the various catalysts synthesized. Further studies were conducted on the 3Co-0.25Fe-0.75Al catalyst due to the observed high activity of this sample during the initial screening. When comparing the catalysts at similar WHSV, noticeable differences in conversion were observed. Initial testing helped distinguish the effects of Fe addition into the Co-Al matrix. It was clear that the addition of Fe significantly enhances the activity of the catalysts, while also increasing the selectivity towards the desired product. In all samples that contained Fe, the selectivity towards 2-MF hovered around 83% while 2-MF selectivity for the 3Co-Al was between 53%-57%. The 3Co-Fe catalyst is not displayed due to its inactivity under the conditions used for these reactions. A wide variety of other products were obtained due to the many side reactions and series reactions that are possible (Table B.1). Additional products include furan, 2-MTHF, 1-butanol (1-BOL), 2-pentanone (2-PONE), 1-pentanol (1-POH), 2-pentanol (2-POH), etc., the latter of which are a result of ring-saturation, decarbonylation, and ring-opening. Interestingly, some hydrocarbons were observed, such as propane and butane, which indicates minor hydrocracking pathways, similar to what was previously observed over a Cu/Cr/Ni/Zn/Fe catalyst in the vapor phase hydrogenation of 2-MF.[40] At similar WHSV, the Co catalysts with lowest Fe addition displayed the highest activity, followed by 3Co-0.5Fe-0.5Al and 3Co-0.75Fe-0.25Al. A catalytic test was performed on a lower Fe loaded catalyst (3Co-0.125Fe-0.875) which demonstrated an incremental increase in conversion (99% after 40 min on stream) with no variation in selectivity. This suggested that there may be an exact optimum in regards to activity at lower Fe loadings than 3Co-0.25Fe-

0.75Al. Since further characterization studies, such as XAS, at lower Fe loadings would have been difficult, only the higher loaded catalysts were chosen for further studies.

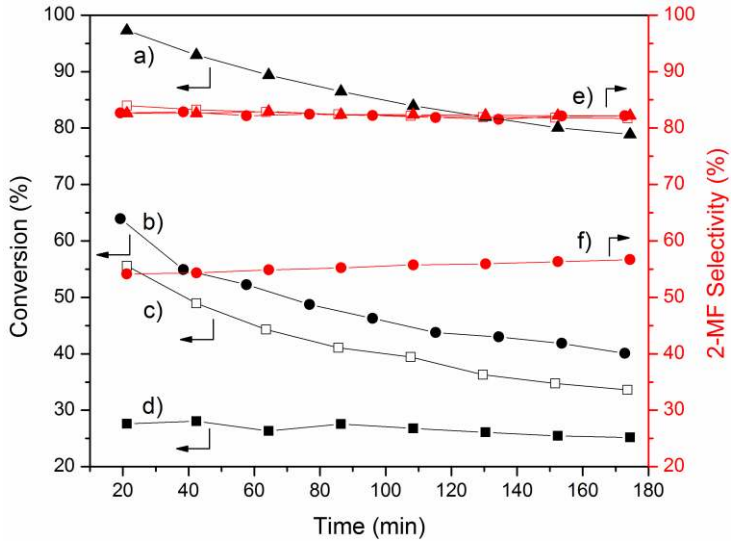

Figure 3.3 – Time on stream data of FAL conversion and 2-MF selectivity over various 3Co-xFe-yAl catalysts at W/F (g_{cat}*h*mol^{-1}) = 3.63, 180 °C, 1 atm, and FAL conc = 0.0015 mmol/mL; Black lines represent conversion and red lines represent 2-methylfuran selectivity. a) 3Co-0.25Fe-0.75Al; b) 3Co-0.5Fe-0.5Al; c) 3Co-0.75Fe-0.25Al; d) 3Co-Al; e) 3Co-xFe-yAl; f) 3Co-Al.

Time on stream data indicated deactivation of all the catalysts over time; however, little to no change in the selectivity occurred. Post-reaction TGA (Figure B.12) experiments displayed little to no carbon deposition, which may have suggested that the major deactivation mechanism was not blocking of sites from carbon deposits. Additionally, recycle tests were conducted on the 3Co-0.25Fe-0.75Al catalyst, which included a calcination step at 400 °C in air for 4 h followed by a reduction step outlined in the experimental section. Each of the catalysts in the recycle test was run for approximately 150 min. The recycle tests demonstrated the catalysts regained their initial activity upon reuse over 3 recycles, as shown in Figure 3.4. This indicated the MMO matrix prepared through the co-precipitation method does not facilitate irreversible sintering after reduction

and the mildly deactivated sample can be easily regenerated. A more likely deactivation mechanism could be through the oxidation of metallic sites, since 2-MF production creates H_2O, potentially causing surface oxidation similar to what Resasco et al. observed over Ni-Fe/SiO_2.[7] However, operando spectroscopic studies would need to be conducted to further verify the major deactivation mechanism.

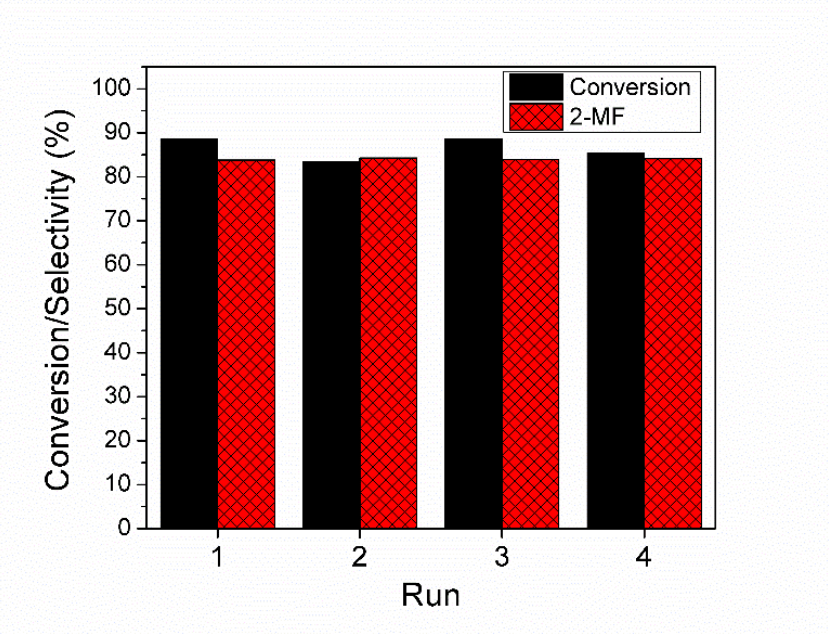

Figure 3.4 – Recycle tests of 3Co-0.25Fe-0.75Al displaying conversion and selectivity towards 2-MF at W/F (g_{cat}*h*mol^{-1}) = 3.63 with FAL as a substrate. Data point taken at approximately 40 min on stream.

Further investigations of the 3Co-0.25Fe-0.75Al catalyst were conducted as a function of the weight hourly space velocity, W/F. Figure 3.5 shows the conversion and selectivity of 2-MF along with significant minor products while the temperature and pressure remained constant at 180 °C and 1 atm. The values were obtained at approximately 40 min on stream after the system reached a pseudo steady-state.

As expected, conversion increased with an increase in residence time, but interestingly, at high W/F, there was noticeably little difference in the selectivity towards 2-MF (80-85%). On the contrary, when lower residence times were used there was an incremental decrease in 2-MF selectivity, and an increase in ring saturation products, THFA, and FUR. These results were reproducible yet unexpected since THFA and FUR are not intermediates to 2-MF. It was likely a result of differing surface coverages of various species, but more mechanistic studies and DFT would need to be conducted to determine the root cause of ring-saturation propensity to THFA only at lower conversions.

Investigations into the reactivity of FUR over the Co-Fe-Al catalysts were conducted to verify reaction pathways and to determine if additional side products emerged. Various weight hourly space velocities were tested utilizing the 3Co-0.25Fe-0.75Al catalyst due its greater activity for FAL conversion. As expected, the data for FUR conversion in Table 3.2 demonstrated an increase in conversion with an increase in catalysts loading, and an increase in 2-MF selectivity as the conversion increases. Similarly, the yield to FAL seemed to decrease linearly with the increase in 2-MF, confirming the series reaction of FUR to FAL to 2-MF observed in prior literature.[10]

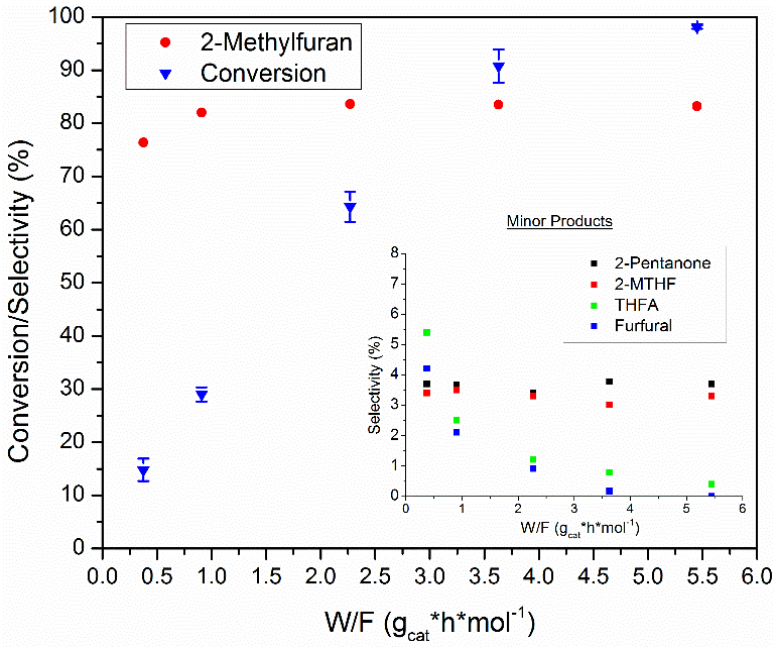

Figure 3.5 – Varying W/F of the 3Co-0.25Fe-0.75Al catalyst at 180 °C and 1 atm with a FAL flow rate varying between 5.5-12 mmol/h and H_2 flow rate varying between 60-130 mL/min while keeping the FAL concentration at 0.0015 mmol/mL. Inset graph displays the selectivity of significant minor products over varying W/F. Values taken at approximately 40 min on stream.

A combined selectivity towards 2-MF and FAL of 75-79% was achieved at a variety of conversion levels. An important distinction between reactions between FAL and FUR was the slight decrease in carbon balance when FUR was fed into the reactor, and significantly more unknown peaks were visible at high retention times, indicating more oligomer formation from FUR. Though the carbon balance closed within 91% for each FUR run, there was a clear indication of the increased propensity of FUR oligomerization with itself or other unidentifiable side products.[41,42] Deactivation was also observed during continuous flow like the deactivation with FAL as the substrate. Ultimately, a yield of 60% towards 2-MF was achieved when feeding FUR, which was equivalent to or better than most prior literature using vapor phase reactions.[10,16,17,43] Though a very recently study of

imbedded Cu in SiO_2 demonstrated higher yields towards 2-MF in the vapor phase when FUR was fed as the reactant, the reactions were conducted mainly above 220 °C.[44,45]

Table 3.2 – Reaction data of FUR over 3Co-0.25Fe-0.75Al at 180 °C at various W/F

W/F (g_{cat}*h*mol^{-1})	Conversion (%)	2-MF (%)	FAL (%)	Furan (%)	1-BOL (%)	2-PONE (%)	Others
3.63	45.0	43.7	35.0	3.9	2.6	1.4	13.4
7.27	83.0	57.1	19.2	4.5	3.8	1.5	13.9
10.91	90.0	66.6	8.5	4.0	3.9	2.4	14.6

Conversion and selectivities obtained at approximately 40 min on stream. 1-BOL, 2-PONE, and others include hydrocarbons, 2-MTHF, THFA, 1,2-PD, 1-POH, and 2-POH.

3.3.3 In situ Spectroscopic Experiments

Further characterizations of these complex MMOs were carried out to better understand the electronic environment of the catalyst before reaction. XPS was utilized to probe the catalytic surface after reduction; however, due to pyrophoric nature of the reduced catalyst, a 1 h passivation step at room temperature in 1% O_2 was conducted prior to employing the characterization technique. As shown in Figure B.5, there was a clear change in the Co species before and after reduction/passivation of the 3Co-0.25Fe-0.75Al sample. Prior to reaction, the spectrum mimics Co_3O_4 due to the lack of a $2p_{3/2}$ satellite peak and the peak maximum of $2p_{3/2}$ at approximately 780.5 eV.[27,46–48] The emergence of a shoulder after reduction at approximately at 778 eV, and the presences of a satellite peak, indicated the reduction of Co_3O_4 to CoO and Co^0.[46] With regards to the Fe species, very

little change was indicated before and after reduction/passivation, with the peak maximum around 712 eV. This maximum was located at higher eV than standard Fe oxides (FeO, Fe_3O_4, and Fe_2O_3), which may further support the strong interaction between Fe and Co, causing the Fe spectra to shift as a consequence of the more electronegative Co oxide.[49] XPS suggested that the Fe oxide species hardly reduced or that the passivation had enough of an impact to bring it close to its original state after initial reduction (most likely the latter).

To further probe the catalyst structure, *in situ* XAS was used to investigate the electronic environment of these materials before and after reduction without the need to passivate the catalyst. The same catalyst pretreatment conditions were implemented at ANL, and scans were taken at room temperature to reduce the effect of the Debye-Waller factor, a correction for thermal vibration effects.[50,51] After investigating the Co k-edge before reduction and matching each spectrum to standards, it was clear by XANES (Figure B.6) and EXAFS analysis that the major species was Co_3O_4, which matches XPS results (Figure B.5). There was no indication of additional spinel structures formed including $CoFe_2O_4$ or $CoAl_2O_4$, though there may still be strong interactions between the various oxide species. Once the samples were reduced for an hour in H_2, a clear change in the Co species was indicated by the major shift in the white line XANES of each catalyst and the emergence of a new peak in EXAFS analysis. Near edge analysis did indicate that the majority of the Co species were in a metallic state (Table B.3). EXAFS analysis of the catalyst post-reduction displayed one major feature at the 1st shell, which corresponds to Co-Co (Fe) scattering peak associated to a FCC structure, similar to that of Co foil and stable metallic Co.[52] Fitting of each catalyst using Co foil as a reference was conducted to

determine the coordination number or Co-Co (Fe) species, since the magnitude of the peaks are significantly lower than the foil. The parameters of the fit are given in Table 3.3, and example fits are shown in Figure B.10 and B.11.

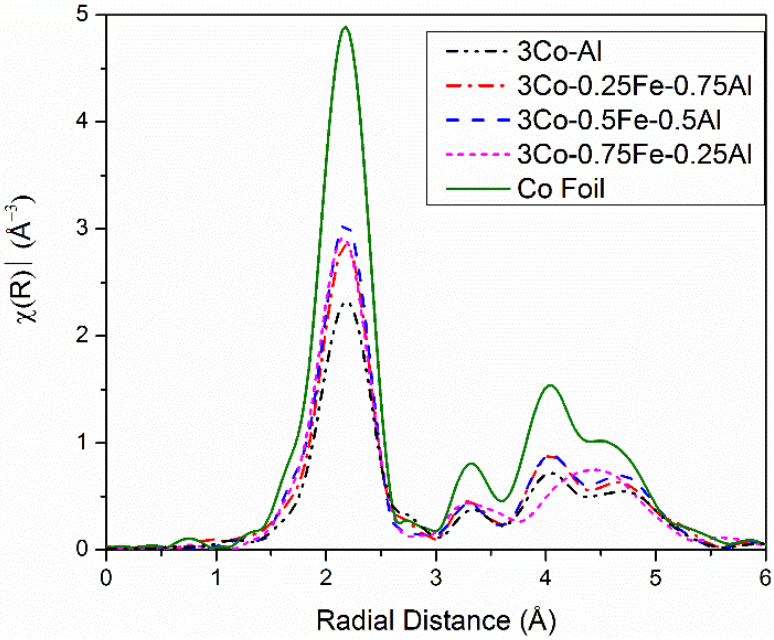

Figure 3.6 – Fourier transformed EXAFS of Co k-edge post-reduction at 500 ºC. Scans were taken at room temperature, and the k range displayed is 2.7-12 Å^{-1} with a k weight of k^2.

Table 3.3 – EXAFS results for the Analysis of Co k-edge post-reduction[a]

Sample	Shell	CN	r (Å)	Δσ (10^{-3} Å^2)	ΔE$_0$ (eV)	R factor
Co foil[b]	Co-Co	12	2.50 ± 0.01	6.4 ± 0.4	7.8 ± 0.5	0.008
3Co-Al	Co-Co	5.7 ± 0.6	2.49 ± 0.01	6.5 ± 0.9	8.6 ± 1.1	0.015
3Co-0.25Fe-0.75Al	Co-Co(Fe)	6.9 ± 0.6	2.49 ± 0.01	6.5 ± 0.7	7.7 ± 0.8	0.007
3Co-0.5Fe-0.5Al	Co-Co(Fe)	7.8 ± 0.4	2.49 ± 0.01	6.9 ± 0.4	7.1 ± 0.5	0.003
3Co-0.75Fe-0.25Al	Co-Co(Fe)	7.1 ± 0.3	2.47 ± 0.01	6.5[c]	7.3 ± 1.0	0.013

[a]Fitting parameters: Fourier transform range, Δk, 2.7-12 Å^{-1} with weighting k^2. [b]Fourier transform range, Δk, 2.7-14 Å^{-1} with weighting k^2. Coordination number assigned from standard FCC Co^0 structure; S$_0^2$ (Co-Co) = 0.806 determined from Co foil fitting. [c]The Debye-Waller factor was fixed to the average to keep consistency with the other samples/model.

All of the R factors are <0.03, indicating good agreement with the experimental data and the curve fits. Upon fitting of each spectrum, it became clear that there was no significant contribution of a Co-O scattering peak, indicating that the majority if not all the Co species were reduced to a metallic state. Additionally, even though there were Fe species most likely intercalated into the Co species, the Co-Co(Fe) bond distance was within error of the metallic standard. This may be due to the high amount of Co in the sample as well as Co and Fe atomic radius being very similar. The most notable difference between the standard and the fitted catalysts after treatment was the clear reduction in coordination number of each of the samples tested, indicating the formation of particles and not a bulk-like and significantly aggregated metallic structure. Compared to the 3Co-Al catalyst, all of the 3Co-xFe-yAl catalysts had a minor increase in coordination number, which may be due to the reduction of Fe that becomes coordinated with Co or increased ease of reduction, supported by TPR, causing increased aggregation. Further investigation of the Fe k-edge provided more evidence of a change in the electronic environment after reduction. The Fourier transformed EXAFS data are displayed in Figure 3.7, and they show a significant difference between each 3Co-xFe-yAl catalyst. After reduction, there was clear increase in the peak height of the 1st shell.

Fitting of the Fe EXAFS spectra proved to be more complicated than for the Co region since the Co k-edge is approximately 600 eV after Fe k-edge. This limits the EXAFS range of Fe, causing fewer independent variables available for the fitting. Additionally, the complexity and potential inhomogeneity of each species in the sample results in an increase in constraints. XANES analysis of the Fe k-edge in Figure B.9 indicates qualitatively that there may be a significant presence of FeO for a few samples, which may require a Fe-O

scattering peak within the EXAFS fit. Additionally, fits without the inclusion of Fe-O proved to be poor for the 3Co-0.25Fe-0.75Al and 3Co-0.5Fe-0.5Al samples. Furthermore, in both 3Co-0.25Fe-0.75Al and 3Co-0.5Fe-0.5Al, the Fe-Fe(Co) peaks for metallic Fe were modelled as a FCC structure while for 3Co-0.75Fe-0.25Al the Fe-Fe(Co) peak was modelled after a BCC crystal structure, similar to that of Fe foil.

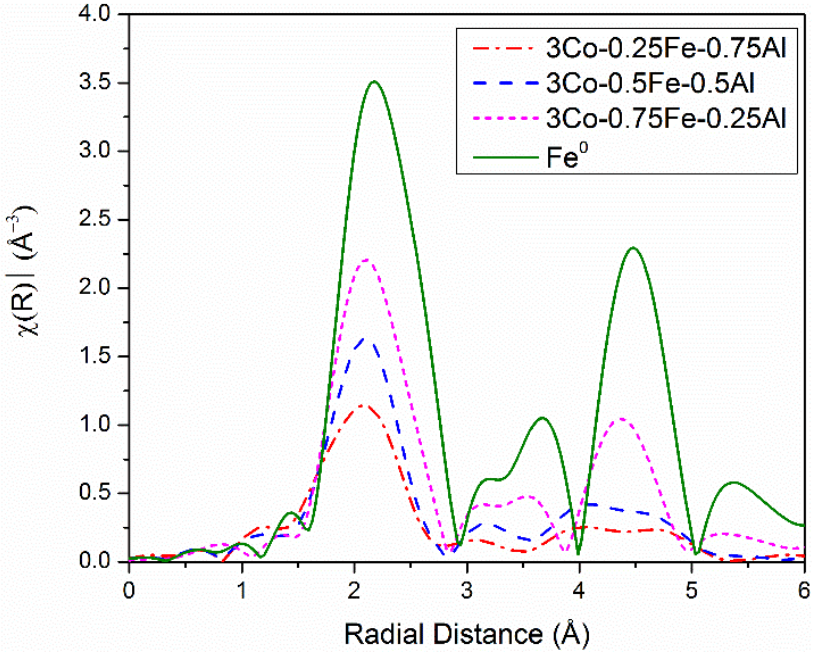

Figure 3.7 – Fourier transformed EXAFS of Fe k-edge post-reduction at 500 ºC. Scans were taken at room temperature, and the k range displayed is 2.7-10.5 Å^{-1} at a k weight of k^2.

This became necessary after attempts at fitting a BCC structure for all catalysts, and poor fits were obtained for the lower Fe loaded samples. Lastly, a qualitative evaluation of the 2nd shell (4-5 Å) shows the emergence of a major peak for 3Co-0.75Fe-0.25Al that mimics a BCC structure formation, while the other catalysts still mimic scattering peaks of the 2nd shell associated with FCC.[53] Therefore, for the two lower Fe loading catalysts, a model where Fe^0 atom is substituted into the FCC lattice of Co^0 and Fe-O scattering path

was more consistent with the data collected. As a side note, Fe-Al bonds were neglected since there was no evidence of alloying of Al species, and there was only existence of an Al^{3+} oxide structure. Table 3.4 displays the best fit and the structural parameters associated with each.

Table 3.4 – EXAFS results for the analysis of Fe k-edge post-reduction[a]

Sample	Shell	CN	r (Å)	Δσ (10^{-3} Å^2)	ΔE_0 (eV)	R factor
Fe Foil[b]	Fe-Fe_{edge} Fe-Fe_{center}	8 6	2.46 ± 0.01 2.85 ± 0.01	5.0 ± 0.5 7.5 ± 1.1	5.2 ± 1.3 5.2 ± 1.3	0.004
Fe(III)acac[c]	Fe-O	6	1.93 ± 0.01	10.3 ± 0.8	-0.5 ± 1.2	0.012
3Co-0.25Fe-0.75Al	Fe-O Fe-Co(Fe)[d]	2.1 ± 0.6 3.6 ± 0.3	2.01 ± 0.02 2.49[f]	9.5[e] 6.5[f]	-5.9 ± 1.0 -5.9 ± 1.0	0.027
3Co-0.5Fe-0.5Al	Fe-O Fe-Co(Fe)[d]	1.4 ± 0.5 5.1 ± 0.3	1.99 ± 0.03 2.49[f]	9.9[e] 6.9[f]	-3.6 ± 0.6 -3.6 ± 0.6	0.013
3Co-0.75Fe-0.25Al	Fe-Fe_{edge} (Co) Fe-Fe_{center} (Co)	5.6 ± 0.7 4.2 ± 0.5	2.44 ± 0.01 2.82 ± 0.01	5.3 ± 0.1 7.7 ± 0.2	-3.7 ± 2.7 -3.7 ± 2.7	0.006

[a]Fitting parameters: Fourier transform range, Δk, 2.7-10.5 Å^{-1} and R range, ΔR, of 1.2-3.0 Å with weighting k^2 unless stated otherwise. [b]Fourier transform range, Δk, 2.3-13 Å^{-1} with weighting k^2; Coordination number assigned from standard BCC Fe^0 structure; S_0^2 (Fe-Fe) = 0.733 determined from Fe foil fitting. [c]Coordination number assigned from standard Fe(III) acetylacetonate structure; R range, ΔR, of 1.1-2.2 Å and S_0^2 (Fe-O) = 0.721 determined from fitting. [d]Modelled after Co^0 FCC structure where Fe^0 replaces Co^0 atoms. [e]Manually optimized Debye-Waller factor. [f]Constrained values to corresponding Co-Co from Co EXAFS fitting since the model is Fe^0 replacing Co^0 in the lattice.

Analysis of the Fe k-edge proved to have a more significant difference than the Co k-edge for each catalyst. Even though the majority of the Co species were in metallic form, the Fe species still maintained some Fe oxide species in the lower Fe loaded samples. Additionally, through various model tests, EXAFS suggested that the 0.25 and 0.5 Fe loaded samples contained Fe^0 species that were substituted into the lattice of the FCC Co^0. This supports the hypothesis of good dispersity of each species resulting from the starting LDH precursor, and may suggest the formation of a bimetallic particle upon reduction. As the Fe loading increases, EXAFS analysis suggested a BCC structure similar to bulk

metallic Fe begins to emerge.[54] In regards to the Fe-O scattering path fitted in the two samples, the bond distance was determined to be approximately 2.00 Å, which is lower than a standard Fe-O in an FeO structure, 2.17 Å.[32] However, for an Fe-O bond incorporated into an $FeAl_2O_4$ matrix the bond distance is approximately 1.95 Å, which suggests that Al influences the Fe-O bond distance, decreasing the overall average bond distance.[33]

Unlike the Co EXAFS analysis, there is a clear trend in which there was an increase in metal-metal coordination as the amount of Fe increased. This correlated well with TPR, which indicated that the higher Fe loading materials were easier to reduce overall. The increase in metal-metal coordination was indicative of aggregation, which could result in larger particle sizes. This larger particle size and loss in metallic surface area supported the loss in activity per gram of catalyst for higher Fe loading materials, as shown in Figure 3.3. Additionally, at the higher Fe loading it may have be possible that the metallic Fe phases were beginning to separate from Co due to the formation of a BCC structure. Though reactivity studies showed there was no indication of a change in active sites since the selectivities do not vary, the loss in activity may be due to the loss in the amount of active sites due to metal aggregation. The highly dispersed Fe species for each catalyst may just be providing an electronic effect on the majority metallic Co species present in the catalysts leading to no significant change in selectivity over different Fe/Al ratios. Lastly, the small amount of Fe oxide present in the samples with lower Fe loadings may have facilitated the adsorption of the highly oxygenated compound allowing for an increase in activity per gram of catalyst, similar to what was observed with a partially reduced Fe species mixed in a Cu-Fe/SiO_2 catalyst.[12] Unfortunately, due to the complexity of these catalysts and the

highly oxophilic nature after reduction (discussed above with XPS characterization) it proved difficult to measure the active site density on the catalyst post-reduction, and thus TOFs are not reported.

3.4 Conclusion

Co based MMOs were derived from the calcination of LDH materials, yielding porous, thermally stable, non-precious metal catalysts for the hydrogenolysis of FAL to 2-MF, a promising biomass derived fuel additive. By utilizing the LDH synthesis method, a well-dispersed solid solution between each oxide domain was formed, which was supported by the weak/broad diffraction peaks in each XRD pattern. Additionally, the method allowed for the simple addition of other metal components such as Fe, which drastically impacted the electronic environment of the catalyst without significant deviations in physical properties (N_2 physisorption and XRD). An array of Co-Fe-Al catalysts with varying Co:Fe ratios were investigated in a vapor phase flow reactor, and prior to reaction the catalysts were reduced *in situ* in an H_2 atmosphere. Through XAS analysis, it was evident that the reduction parameters conducted allowed for the almost full reduction of Co_3O_4 for each catalyst, with varying degrees of reduction for the Fe species. As the loading of Fe increased, there was an increase in Fe reduction due to the ease of Fe oxide reduction over Al_2O_3, which may contribute to increased aggregation of metallic species and a loss in surface area. This was evident during reactivity studies, which showed that the activities for each Co-Fe-Al catalyst followed as such: 0.25Fe > 0.5Fe > 0.75Fe. Despite differences in activity among the Fe loaded samples, it was evident that the addition of Fe enhanced both the activity per gram and selectivity towards 2-MF compared to the 3Co-Al catalyst. Furthermore, the 3Co-0.25Fe-0.75Al catalyst exhibited high

selectivities towards 2-MF over a range of conversions (75%-84%). The ability to recycle these catalysts was shown after calcining and re-reducing the catalysts. Through this study, it is evident that MMOs derived from LDH materials can yield multi-metal systems where there is good interaction between each component, which can produce selective catalysts for FAL and FUR conversion. Further investigations on various additives into an LDH matrix may allow for additional tuning to reduce catalyst deactivation or enhance the yield to 2-MF even further.

3.5 References

(1) Sulmonetti, T. P.; Hu, B.; Ifkovits, Z. P.; Lee, S.; Agrawal, P. K.; Jones, C. W. Vapor Phase Hydrogenolysis of Furanics Utilizing Reduced Cobalt Mixed Metal Oxide Catalysts. *ChemCatChem* **2017**, *9*, 1815–1823.

(2) Gallezot, P. Conversion of biomass to selected chemical products. *Chem. Soc. Rev.* **2012**, *41*, 1538–1558.

(3) Alonso, D. M.; Bond, J. Q.; Dumesic, J. A. Catalytic conversion of biomass to biofuels. *Green Chem.* **2010**, *12*, 1493–1513.

(4) Li, X.; Jia, P.; Wang, T. Furfural: a promising platform compound for sustainable production of C_4 and C_5 chemicals. *ACS Catal.* **2016**, *6*, 7621–7640.

(5) Román-Leshkov, Y.; Barrett, C. J.; Liu, Z. Y.; Dumesic, J. A. Production of dimethylfuran for liquid fuels from biomass-derived carbohydrates. *Nature* **2007**, *447*, 982–985.

(6) Burnett, L. W.; Johns, I. B.; Holdren, R. F.; Hixon, R. M. Production of 2-Methylfuran by Vapor-Phase Hydrogenation of Furfural. *Ind. Eng. Chem.* **1948**, *40*, 502–505.

(7) Sitthisa, S.; Resasco, D. E. Hydrodeoxygenation of Furfural Over Supported Metal Catalysts: A Comparative Study of Cu, Pd and Ni. *Catal. Letters* **2011**, *141*, 784–791.

(8) Nakagawa, Y.; Nakazawa, H.; Watanabe, H.; Tomishige, K. Total Hydrogenation of Furfural over a Silica-Supported Nickel Catalyst Prepared by the Reduction of a Nickel Nitrate Precursor. *ChemCatChem* **2012**, *4*, 1791–1797.

(9) Alonso, D. M.; Wettstein, S. G.; Dumesic, J. A. Bimetallic catalysts for upgrading

of biomass to fuels and chemicals. *Chem. Soc. Rev.* **2012**, *41*, 8075–8098.

(10) Sitthisa, S.; An, W.; Resasco, D. E. Selective conversion of furfural to methylfuran over silica-supported NiFe bimetallic catalysts. *J. Catal.* **2011**, *284*, 90–101.

(11) Yu, W.; Xiong, K.; Ji, N.; Porosoff, M. D.; Chen, J. G. Theoretical and experimental studies of the adsorption geometry and reaction pathways of furfural over FeNi bimetallic model surfaces and supported catalysts. *J. Catal.* **2014**, *317*, 253–262.

(12) Sheng, H.; Lobo, R. F. Iron-promotion of silica-supported copper catalysts for furfural hydrodeoxygenation. *ChemCatChem* **2016**, *8*, 3402–3408.

(13) Manikandan, M.; Venugopal, A. K.; Nagpure, A. S.; Chilukuri, S.; Raja, T. Promotional effect of Fe on the performance of supported Cu catalyst for ambient pressure hydrogenation of furfural. *RSC Adv.* **2016**, *6*, 3888–3898.

(14) Shi, D.; Vohs, J. M. Deoxygenation of Biomass-Derived Oxygenates: Reaction of Furfural on Zn-Modified Pt(111). *ACS Catal.* **2015**, *5*, 2177–2183.

(15) Zheng, H.-Y.; Zhu, Y.-L.; Bai, Z.-Q.; Huang, L.; Xiang, H.-W.; Li, Y.-W. An environmentally benign process for the efficient synthesis of cyclohexanone and 2-methylfuran. *Green Chem.* **2006**, *8*, 107–109.

(16) Zheng, H.-Y.; Zhu, Y.-L.; Teng, B.-T.; Bai, Z.-Q.; Zhang, C.-H.; Xiang, H.-W.; Li, Y.-W. Towards understanding the reaction pathway in vapour phase hydrogenation of furfural to 2-methylfuran. *J. Mol. Catal. A Chem.* **2006**, *246*, 18–23.

(17) Lee, W.-S.; Wang, Z.; Zheng, W.; Vlachos, D. G.; Bhan, A. Vapor phase hydrodeoxygenation of furfural to 2-methylfuran on molybdenum carbide catalysts. *Catal. Sci. Technol.* **2014**, *4*, 2340–2352.

(18) Yang, P.; Cui, Q.; Zu, Y.; Liu, X.; Lu, G.; Wang, Y. Catalytic production of 2,5-dimethylfuran from 5-hydroxymethylfurfural over Ni/Co_3O_4. *Catal. Commun.* **2015**, *66*, 55–59.

(19) Zu, Y.; Yang, P.; Wang, J.; Liu, X.; Ren, J.; Lu, G.; Wang, Y. Efficient production of the liquid fuel 2,5-dimethylfuran from 5-hydroxymethylfurfural over Ru/Co_3O_4 catalyst. *Appl. Catal. B Environ.* **2014**, *146*, 244–248.

(20) Huang, Y.-B.; Chen, M.-Y.; Yan, L.; Guo, Q.-X.; Fu, Y. Nickel-tungsten carbide catalysts for the production of 2,5-dimethylfuran from biomass-derived molecules. *ChemSusChem* **2014**, *7*, 1068–1072.

(21) Wang, G.; Hilgert, J.; Richter, F. H.; Wang, F.; Bongard, H.; Spliethoff, B.; Weidenthaler, C.; Schüth, F. Platinum–cobalt bimetallic nanoparticles in hollow carbon nanospheres for hydrogenolysis of 5-hydroxymethylfurfural. *Nat. Mater.* **2014**, *13*, 293–300.

(22) Zhu, Y.; Kong, X.; Zheng, H.; Ding, G.; Zhu, Y.; Li, Y.-W. Efficient synthesis of 2,5-dihydroxymethylfuran and 2,5-dimethylfuran from 5-hydroxymethylfurfural using mineral-derived Cu catalysts as versatile catalysts. *Catal. Sci. Technol.* **2015**, *5*, 4208–4217.

(23) Panagiotopoulou, P.; Vlachos, D. G. Liquid phase catalytic transfer hydrogenation of furfural over a Ru/C catalyst. *Appl. Catal. A Gen.* **2014**, *480*, 17–24.

(24) Srivastava, S.; Jadeja, G. C.; Parikh, J. A versatile bi-metallic copper-cobalt catalyst for liquid phase hydrogenation of furfural to 2-methylfuran. *RSC Adv.* **2016**, *6*, 1649–1658.

(25) Iqbal, S.; Liu, X.; Aldosari, O. F.; Miedziak, P. J.; Edwards, J. K.; Brett, G. L.; Akram, A.; King, G. M.; Davies, T. E.; Morgan, D. J.; et al. Conversion of furfuryl alcohol into 2-methylfuran at room temperature using Pd/TiO_2 catalyst. *Catal. Sci. Technol.* **2014**, *4*, 2280–2286.

(26) Chen, B.; Li, F.; Huang, Z.; Yuan, G. Carbon-coated Cu-Co bimetallic nanoparticles as selective and recyclable catalysts for production of biofuel 2,5-dimethylfuran. *Appl. Catal. B Environ.* **2017**, *200*, 192–199.

(27) Sulmonetti, T. P.; Pang, S. H.; Taborga Claure, M.; Lee, S.; Cullen, D. A.; Agrawal, P. K.; Jones, C. W. Vapor phase hydrogenation of furfural over nickel mixed metal oxide catalysts derived from layered double hydroxides. *Appl. Catal. A Gen.* **2016**, *517*, 187–195.

(28) Nishimura, S.; Takagaki, A.; Ebitani, K. Characterization, synthesis and catalysis of hydrotalcite-related materials for highly efficient materials transformations. *Green Chem.* **2013**, *15*, 2026–2042.

(29) Taborga Claure, M.; Chai, S.-H.; Dai, S.; Unocic, K. A.; Alamgir, F. M.; Agrawal, P. K.; Jones, C. W. Tuning of higher alcohol selectivity and productivity in CO hydrogenation reactions over K/MoS_2 domains supported on mesoporous activated carbon and mixed MgAl oxide. *J. Catal.* **2015**, *324*, 88–97.

(30) Wyckoff, R. W. G. *Crystal Structures*, 2nd ed.; Interscience Publishers: New York, 1963.

(31) Woodward, P. M.; Suard, E.; Karen, P. Structural tuning of charge, orbital, and spin ordering in double-cell perovskite series between $NdBaFe_2O_5$ and $HoBaFe_2O_5$. *J. Am. Chem. Soc.* **2003**, *125*, 8889–8899.

(32) Jette, E. R.; Foote, F. An X-Ray Study of the Wüstite (FeO) Solid Solutions. *J. Chem. Phys.* **1933**, *1*, 29–36.

(33) Hill, R. J. X-ray powder diffraction profile refinement of synthetic hercynite. *Am. Mineral.* **1984**, *69*, 937–942.

(34) Ridley, N. Defect structures in binary and ternary alloys based on Co-Al. *J. Insitute Met.* **1966**, *94*, 255–258.

(35) Calvin, S.; Carpenter, E.; Ravel, B.; Harris, V.; Morrison, S. Multiedge refinement of extended X-ray-absorption fine structure of manganese zinc ferrite nanoparticles. *Phys. Rev. B* **2002**, *66*, 224405.

(36) Batista, J.; Pintar, A.; Gomilsek, J. P.; Kodre, A.; Bornette, F. On the structural characteristics of γ-supported Pd-Cu bimetallic catalysts. *Appl. Catal. A Gen.* **2001**, *217*, 55–68.

(37) Lee, A. F.; Baddeley, C. J.; Hardacre, C.; Ormerod, R. M.; Lambert, R. M.; Schmid, G.; West, H. Structural and catalytic properties of novel Au/Pd bimetallic colloid articles: EXAFS, XRD, and acetylene coupling. *J. Phys. Chem.* **1995**, *99*, 6096–6102.

(38) Khassin, A. a.; Yurieva, T. M.; Kustova, G. N.; Itenberg, I. S.; Demeshkina, M. P.; Krieger, T. a.; Plyasova, L. M.; Chermashentseva, G. K.; Parmon, V. N. Cobalt-aluminum co-precipitated catalysts and their performance in the Fischer-Tropsch synthesis. *J. Mol. Catal. A Chem.* **2001**, *168*, 193–207.

(39) Sun, J.; Karim, A. M.; Zhang, H.; Kovarik, L.; Li, X. S.; Hensley, A. J.; McEwen, J. S.; Wang, Y. Carbon-supported bimetallic Pd-Fe catalysts for vapor-phase hydrodeoxygenation of guaiacol. *J. Catal.* **2013**, *306*, 47–57.

(40) Biswas, P.; Lin, J.-H.; Kang, J.; Guliants, V. V. Vapor phase hydrogenation of 2-methylfuran over noble and base catalysts. *Appl. Catal. A Gen.* **2014**, *475*, 379–385.

(41) Nakagawa, Y.; Tamura, M.; Tomishige, K. Catalytic reduction of biomass-derived furanic compounds with hydrogen. *ACS Catal.* **2013**, *3*, 2655–2668.

(42) Yan, K.; Wu, G.; Lafleur, T.; Jarvis, C. Production, properties and catalytic hydrogenation of furfural to fuel additives and value-added chemicals. *Renew. Sustain. Energy Rev.* **2014**, *38*, 663–676.

(43) Luo, J.; Monai, M.; Yun, H.; Arroyo-Ramírez, L.; Wang, C.; Murray, C. B.; Fornasiero, P.; Gorte, R. J. The H_2 pressure dependence of hydrodeoxygenation selectivities for furfural over Pt/C catalysts. *Catal. Letters* **2016**, *146*, 711–717.

(44) Dong, F.; Zhu, Y.; Zheng, H.; Zhu, Y.; Li, X.; Li, Y. Cr-free Cu-catalysts for the selective hydrogenation of biomass-derived furfural to 2-methylfuran: The synergistic effect of metal and acid sites. *J. Mol. Catal. A Chem.* **2015**, *398*, 140–148.

(45) Dong, F.; Ding, G.; Zheng, H.; Xiang, X.; Chen, L.; Zhu, Y.; Li, Y. Highly dispersed Cu nanoparticles as an efficient catalyst for the synthesis of the biofuel 2-methylfuran. *Catal. Sci. Technol.* **2016**, *6*, 767–779.

(46) Biesinger, M. C.; Payne, B. P.; Grosvenor, A. P.; Lau, L. W. M.; Gerson, A. R.; Smart, R. S. C. Resolving surface chemical states in XPS analysis of first row transition metals, oxides and hydroxides: Cr, Mn, Fe, Co and Ni. *Appl. Surf. Sci.* **2011**, *257*, 2717–2730.

(47) Khassin, A. a.; Yurieva, T. M.; Kaichev, V. V.; Bukhtiyarov, V. I.; Budneva, A. a.; Paukshtis, E. a.; Parmon, V. N. Metal–support interactions in cobalt-aluminum co-precipitated catalysts: XPS and CO adsorption studies. *J. Mol. Catal. A Chem.* **2001**, *175*, 189–204.

(48) Yang, Q.; Choi, H.; Al-Abed, S. R.; Dionysiou, D. D. Iron-cobalt mixed oxide nanocatalysts: Heterogeneous peroxymonosulfate activation, cobalt leaching, and ferromagnetic properties for environmental applications. *Appl. Catal. B Environ.* **2009**, *88*, 462–469.

(49) Guittet, M. J.; Crocombette, J. P.; Gautier-Soyer, M. Bonding and XPS chemical shifts in $ZrSiO_4$ versus SiO_2 and ZrO_2: Charge transfer and electrostatic effects. *Phys. Rev. B* **2001**, *63*, 125117.

(50) Günter, M. M.; Ressler, T.; Jentoft, R. E.; Bems, B. Redox Behavior of Copper Oxide/Zinc Oxide Catalysts in the Steam Reforming of Methanol Studied by in Situ X-Ray Diffraction and Absorption Spectroscopy. *J. Catal.* **2001**, *203*, 133–149.

(51) Gonzalez-delacruz, V. M.; Pere, R.; Ternero, F.; Holgado, J. P.; Caballero, A. In Situ XAS Study of Synergic Effects on Ni-Co /ZrO_2 Methane Reforming Catalysts. *J. Phys. Chem. C* **2012**, *116*, 2919–2926.

(52) Tsakoumis, N. E.; Voronov, A.; Ronning, M.; Beek, W. Van; Borg, O.; Rytter, E.; Holmen, A. Fischer-Tropsch synthesis: An XAS/XRPD combined in situ study from catalyst activation to deactivation. *J. Catal.* **2012**, *291*, 138–148.

(53) Sekine, Y.; Nakazawa, Y.; Oyama, K.; Shimizu, T.; Ogo, S. Effect of small amount of Fe addition on ethanol steam reforming over Co/Al_2O_3 catalyst. *Appl. Catal. A Gen.* **2014**, *472*, 113–122.

(54) Hong, Y.; Zhang, H.; Sun, J.; Ayman, K. M.; Hensley, A. J. R.; Gu, M.; Engelhard, M. H.; McEwen, J.-S.; Wang, Y. Synergistic Catalysis between Pd and Fe in Gas Phase Hydrodeoxygenation of m -Cresol. *ACS Catal.* **2014**, *4*, 3335–3345.

CHAPTER 4 REDUCED CU-CO-AL MMO CATALYSTS FOR THE PRODUCTION OF RENEWABLE DIOLS

This chapter and Appendix C are adapted from the published article, Sulmonetti, T. P.; Hu, B.; Lee, S.; Agrawal, P. K.; Jones, C. W. Reduced Cu−Co−Al mixed metal oxides for the ring-opening of furfuryl alcohol to produce renewable diols. *ACS Sustain. Chem. Eng.* **2017**, 5, 8959-8969, with permission from American Chemical Society. DOI: 10.1021/acssuschemeng.7b01769.[1]

4.1 Introduction

Furanic compounds have become increasingly important substrates in the effort to synthesize commercial chemicals from renewable feedstocks. These molecules can be derived from second generation lignocellulosic biomass, an abundant and inedible part of biomass, creating an alternate route to the synthesis of products commonly made from petroleum.[2,3] Common furanic substrates include FUR and FAL, both of which can be catalytically converted into a variety of fuel additives, solvents, and polymer precursors.[4,5] Most notably, FAL can be converted into 1,5-PD through a variety of pathways, which shows promise in facilitating the synthesis of renewable poly(ester)s and poly(urethane)s using biomass.[6] Significant upstream investigations have been conducted to demonstrate the viability of converting raw or processed lignocellulose to furanics;[3,7–9] however, the study of ring-opening of FUR and FAL to 1,5-PD is relatively unexplored and a majority of studied catalysts utilize precious metals.[6,10–21]

A variety of catalysts based on metallic domains typically supported on an inert material have been widely studied in the literature for furanic conversion both in vapor phase and liquid phase; however, these catalysts tend to have limitations, either in activity, selectivity, or both.[5,22] Due to wide variety of pathways through which FAL and FUR can be catalytically converted, it is crucial to develop catalysts that can selectively steer the conversion towards the target compound. This has led to the emergence of multi-metal systems for furanic conversion, ultimately creating bifunctional and/or bimetallic catalysts for selective reactions. Initial work on furanic ring-opening has been independently conducted by Dumesic and Tomishige, who demonstrated the selective conversion of THFA to 1,5-PD at high yields by utilizing bifunctional catalysts.[10,12] These bifunctional catalysts included Rh-ReO_x,[12] Rh-MoO_x,[10,19] Ir-ReO_x,[13,23,24] Ir-MoO_x/SiO_2,[25] Rh-Ir-ReO_x[6] and Pd-Ir-ReO_x[13] supported on relatively inert materials such as SiO_2 and C, which have been able to achieve >90% yields in liquid phase batch reactions at high hydrogen pressures, ~120 °C, and with water as a solvent. Although there are differences in the proposed reaction pathways and mechanisms, in general, these catalysts create a bifunctional system where the oxophilic metal (Re or Mo) facilitates ring-opening and the metallic species (Ir, Rh, or Pd) facilitate hydrogenation.[23] This pioneering work has inspired attempts at creating similar bifunctional systems such as Ir-VO_x, but these catalysts still continue to contain expensive and rare metals.[17]

Additional studies have investigated the ring-opening of other cyclic ethers not including FUR, FAL, and THFA. For example the conversion of 2-hydroxymethyl-tetrahydropyran to 1,6-hexandiol has been observed over RhRe/C[26] and Rh-ReO_x/C.[10] The work conducted by Dumesic, et al. with Rh-ReO_x/C also included the ring-opening of 2-

methyltetrahydropyran, tetrahydropyran, and 2-methyltetrahydrofuran.[10] Furthermore, HREELS was utilized to study the ring-opening of 2(5H)-furanone on Pd(111) and Pt(111) single cyrstals.[27] Lastly, a recent study targeting the production of 1,5-pentanediol reported the tautomerization and subsequent ring-opening of furfural through a three step process containing Ni and Al_2O_3 catalysts.[11] Although this process requires a few additional steps, it was determined through economic analysis that the process can be carried out at lower cost due to the use of more economical catalysts.

The work above suggests the general utility of multi-metal systems in creating bifunctional catalysts for the selective ring-opening of furanics to produce diol products. Consequently, there have recently been several promising investigations in the utilization of bifunctional catalysts through the reduction of MMOs or metallic particles supported on active oxide supports. A variety of catalysts have been attempted including reduced Ni-Co-Al MMO,[28] Cu/Al_2O_3,[18] Cu-Mg-Al MMO,[14] $Pt/CoAl_2O_4$,[29] $Pt/MgO\text{-}Al_2O_3$,[16] Ru/MnO_x,[30] Co/TiO_2,[31] and Ru/Al_2O_3[32] all of which produced ring-opening products. These studies were conducted in the liquid phase under hydrogen pressure, typically with an alcohol solvent and temperatures above 100 °C. With these types of catalysts, it has been proposed that the active ring-opening species is FAL not THFA in the conversion to 1,5-PD, which is unique compared to the Ir-ReO_x studies mentioned above.[23] The proposed mechanism is that the oxide species in the catalysts facilitate adsorption in a tilted conformation for the saturated furanic, which ring-opens and subsequently hydrogenates through the metallic species.[28] Unfortunately, a majority of these catalysts utilize an expensive metal and/or have low yields towards 1,5-PD and higher yields towards 1,2-PD, a less desired product. Additionally, from the above-mentioned literature, few

spectroscopic experiments have been conducted to help understand the nature of the bifunctional surface domains.

Consequently, in this study, non-precious MMO catalysts were investigated for the liquid phase ring-opening of FAL to increase ring-opening yields and create a better understanding of the nature of the structural domains in these complex materials. In our prior work, MMO materials have been shown to be a promising catalyst for the selective conversion of FUR/FAL to other products, specifically 2-MF or THFA, excluding diol formation.[33,34] Reduction of the MMO catalysts was crucial in creating the bifunctionalities (metallic and oxide domains), and after different reduction procedures, we sought to determine the electronic environment of these compositionally complex catalysts. In this work, along with reactivity studies, XAS and XPS experiments were conducted to determine how the catalysts behaved under various reduction conditions. The collected results help further the understanding of how the electronic environment of these complex systems effect the conversion of FAL to ring-saturation and ring-opening products, while using more economically viable metals than most of the studies described above.

4.2 Experimental Section

4.2.1 Materials and Chemicals

Furfural (99% purity, ACS Grade) and furfuryl alcohol (98% purity) were purchased from Sigma Aldrich, vacuum distilled, and then stored in inert atmosphere before using in reactions. $Co(NO_3)_2 \cdot 6H_2O$ (99% purity), Na_2CO_3 (99.5% purity), ethanol (ACS Grade, 99.5%), and dodecane (99% purity) were purchased from Sigma Aldrich. $Cu(NO_3)_2 \cdot 3H_2O$, and $Al(NO_3)_3 \cdot 9H_2O$ were all purchased from Alfa Aesar (98%-102%). NaOH (97% purity)

was purchased from EMD. Lastly, all other chemicals were used as is without any further purification.

4.2.2 Catalysts Synthesis

Cu-Co-Al mixed metal oxides with varying target Co:Cu ratios of 29:1, 11:1, and 5:1 ((Co+Cu)/Al) always kept at 0.25) were prepared in the following manner, similar to prior LDH syntheses, with minor modifications.[33–35] Additionally, a catalyst with a 4:1 Co:Cu ratio and higher Al content (0.5Cu-2.0Co-Al) was prepared to investigate a composition with lower amounts of reducible metals in the system. A 0.6 M metal nitrate solution, Solution A, with corresponding metal cations ratios above, and a 1.0 M NaOH solution, Solution B, were created. A 0.3 M solution of Na_2CO_3 (in molar excess), Solution C, was placed in a flat-bottom flask, and using a peristaltic pump Solution A and Solution B were added dropwise into Solution C at approximately 5 mL/min under vigorous stirring, room temperature, and N_2 bubbling. The pH was maintained at 10 by adjusting Solution B flowrate. The pump was shut off once Solution A ran out, and the solution was heated to 60 °C, and maintained under vigorous stirring and N_2 bubbling for 24 h. Once complete, the final solution was filtered and washed until the filtered solution had a pH of ~7 (about 1.5 L of DI water) to obtain the LDH precipitant. The recovered solid was dried under vacuum overnight. To create the MMO, the dried LDH material was calcined at 400 °C with 50 mL/min flow of air with a ramp rate of 10 °C/min and held for 4 h.

4.2.3 Reaction Studies

Liquid phase batch reactions were performed in a 160 mL stainless steel Parr autoclave with a Teflon liner. The catalysts were reduced under 60 mL/min H_2 (Airgas, UHP) to 400˚C (unless stated otherwise) with a ramp rate of 5°C/min, then subsequently held for 1 h. Once the reduction was completed, the bed was cooled under H_2 to room temperature, where 1% O_2/N_2 was passed over the catalyst for 1 h. This passivation step was conducted due to the pyrophoric nature of the catalyst after reduction. For a typical reaction, the catalyst was then charged in the Parr autoclave with 25 mL of solvent, purged with N_2, then purged with H_2 5 times. A second reduction step occurred where a H_2 pressure of 500 psi was achieved, and the reactor was heated to 180 °C (approximately 45 min). Once 180 °C was achieved the reactor was immediately cooled down to room temperature. At room temperature, typically 0.5 g of furfuryl alcohol, ~ 0.125 g of dodecane (internal standard), and 25 mL of solvent were added into the reactor. The reactor was purged 5 times with N_2 and heated to reaction temperature under N_2 to avoid reactions during heat up. Once the reaction temperature (typically 140 °C) was achieved, the reactor was purged 5 times with H_2, and stirrer was turned to 800 RPM, which was determined to be free of external mass transfer limitations. As a general note, there was typically a 5 min period until the reactor temperature equilibrated at desired value. Samples were obtained through a sampling port, and less than 300 µL were acquired for each sample to minimize reaction volume loss. The aliquots were filtered and analyzed through an Agilent 7890A GC fitted with an auto sampler. Selectivity and conversion were determined by the internal standard method, and all carbon balances closed within 5%. Additionally, the catalysts that were

tested post-reduction were dried and stored under vacuum until further characterization to avoid oxygen exposure.

4.2.4 Characterization

4.2.4.1 N_2 Physisorption, Chemisorption, XRD, and ICP

Nitrogen physisorption was performed in a Micromeritics Tristar II at -196°C after the samples were pretreated for 12 h under vacuum at approximately 200 °C. TPR experiments were performed in a Micromeritics AutoChem II 2920. For each experiment, approximately 50 mg of sample was placed on a small bed of quartz wool in a quartz U-tube. First, the MMO was pretreated in 20 mL/min of He (Airgas, UHP) at 200°C for 2 h, and then the sample was cooled to 50 °C. Finally, 20 mL/min of 10% H_2 balance Ar was flown through the U-tube, and the sample was heated to 800 °C at 5 °C/min. The outlet gas passed through a liquid acetone/nitrogen trap, and H_2 consumption was recorded by a TCD. To investigate the composition, the MMO materials were dissolved in dilute H_2SO_4 solution heated at 120 °C, and elemental analysis was done at the Georgia Tech Renewable Bioproducts Institute utilizing ICP-OES a PerkinElmer OPTIMA 7300 DV. Powder X-ray diffraction patterns ranging from 5° - 90° (2θ°) were collected using a Philips X-pert diffractometer using Cu Kα radiation.

4.2.4.2 Spectroscopic Experiments

XPS analysis was collected using Thermo K-Alpha spectrometer employing monochromatic Al Kα radiation, and the pressures inside the analytical chamber was approximately $1x10^{-7}$ Torr. The samples were placed on carbon tape to mitigate charging

effects during testing. The binding energies (BE) of all elements were tuned to the carbon tape (284.8 eV) with an uncertainty of ± 0.2 eV. The samples that were tested in the through XPS were pretreated like the above steps before reaction. To avoid any oxygen exposure, the samples were placed under vacuum before loading into the XPS.

XAS was conducted at the APS beamline 12-BM in ANL. The data was obtained in transmission mode at the Cu K-edge (8988 eV) in the range of 8790-9930 eV, and the Co K-edge (7712 eV) in the range of 7510-8565 eV, both with spot size of 0.5mm x 1.2mm. To perform the catalyst pretreatment before XAS, the catalyst sample was diluted and ground with boron nitride (8:1 – BN:catal.), and then ~8 mg of this mixture was loaded and pressed into a "six shooter" holder (multiple samples could be pressed into the holder). This holder was then placed into a quartz tube with Kapton windows at each end to allow X-rays to pass through, and a gas line was attached to the tube. A scan was collected pre-reduction at room temperature. Next the catalyst was heated to various reduction temperatures at 5°C/min and held for 1 h all while under a 60 mL/min flow of pure H_2. After the reduction was complete, the samples were cooled down in H_2, and scans were collected at room temperature (RT). Finally, the samples were passivated in 1% O_2 balance in N_2 for 1 h at RT and subsequently analyzed. This pretreatment step mimicked the high temperature pretreatment step conducted in the flow reactor along with passivation. The XAS data were processed and analyzed with Athena software including background removal, edge-step normalization, and Fourier transform. Co foil, Cu foil, and Co(III) acetylacetonate (Co(III) acac) were used as standards, and scattering paths were calculated using FEFF8.[36] Artemis software was utilized to fit the Fourier transformed EXAFS data with a model.

4.3 Results and Discussion

4.3.1 Physical Characterization

A variety of LDH materials were synthesized as precursor materials to the MMOs utilized in the reactions. These materials consisted of 2+ and 3+ metal cations (Cu^{2+}, Co^{2+}, and Al^{3+}) in an octahedral configuration bonded to hydroxides that form sheet-like layers. The charge imbalance due to the mixture of cations was counterbalanced by an organic anion (CO_3^{2-} in this investigation) and H_2O. The synthesis was conducted through a co-precipitation method at a controlled pH, which typically allowed for increased dispersion among each metal cation, and minimizing metal clustering. Calcination of LDH materials at high temperatures under air yielded porous MMO. The calcination removed the water, CO_3^{-2}, and hydroxides, creating pockets within the layered structure, which enhanced the surface area compared to the LDH structure.[33,37] Additionally, the dispersity of each metal oxide species can remain, and the high temperature calcination increased the thermal stability of the material. MMOs derived from LDHs display promising textural properties that increase their potential as catalyst materials in biomass conversion.

As mentioned in the introduction, Cu-Co-Al materials with high Co fractions were studied for the ring-opening of furanics. The physical properties of each catalyst are shown in Table 4.1 and Figure 4.1.

Table 4.1 – Physical properties of multiple Co and/or Cu based MMOs.

Catalyst	Elemental analysis (Cu:Co:Al)	Cu:Co (Normalized by Cu)	BET Surface Area (m^2/g)	Pore Volume (cm^3/g)	Average Pore Diameter (nm)
3Co-Al	0.0:2.94:1.0	-	129	0.35	11.0
0.1Cu-2.9Co-Al	0.11:2.83:1.0	1:25.7	138	0.46	14.1
0.25Cu-2.75Co-Al	0.26:2.62:1.0	1:10.5	146	0.39	12.8
0.5Cu-2.5Co-Al	0.51:2.45:1.0	1:4.8	140	0.58	17.6
0.5Cu-2.0Co-Al	0.44:1.82:1.0	1:4.1	130	0.37	14.1

It was observed by N_2 physisorption that each MMO material had similar porosity and also displayed a hysteresis beginning at high relative pressures (~0.8 P/P_0), which indicated the formation of mesoporosity.[38] The surface areas of all five catalysts were between 125 m^2/g – 150 m^2/g, the similarity of which minimized surface area effects between each catalyst during reaction screening. Additionally, ICP analysis indicated the metal ratios closely matched that of the target ratios. For consistency and ease in the nomenclature, the catalysts were labeled with their target ratios throughout the manuscript.

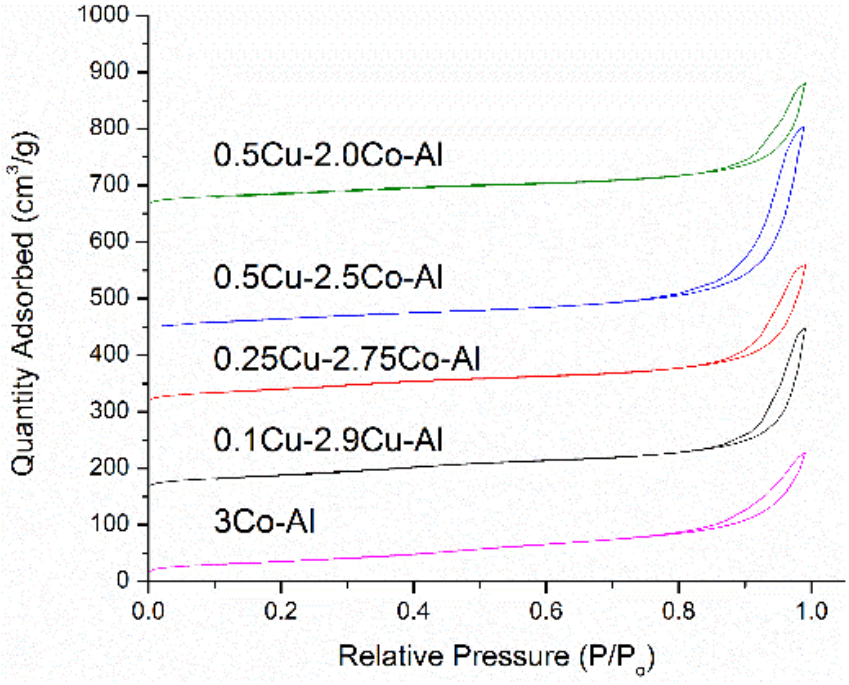

Figure 4.1 – N_2 physisorption isotherms of each catalyst synthesized and were conducted after calcination and before reduction. The data for each plot were offset for clarity

4.3.2 Reaction Analysis

For the initial reaction tests, a reduction of 400 °C was conducted, and a room temperature passivation post-reduction was done due to the pyrophoric nature in air. After reduction and passivation, the catalysts were charged into the reactor, and re-reduced to 180 °C to provide a common set of pretreatment conditions, as explained above. The variation in conditions tested is displayed below in Table 4.2.

Table 4.2 – FAL batch reactions conducted over various xCu-yCo-Al catalysts[a]

Entry	Catalyst	Solvent	Temp. (°C)	Pressure (MPa)	Conv. (%)	1,5-PD (%)	THFA (%)	1,2-PD (%)	Others (%)
1	3Co-Al	EtOH	140	4	10.3	30.6	39.4	9.1	20.9
2	0.1Cu-2.9Co-Al	EtOH	140	4	41.5	40.4	24.9	18.5	16.2
3	0.25Cu-2.75Co-Al	EtOH	140	4	66.8	36.6	29.7	14.4	19.3
4	0.5Cu-2.5Co-Al	EtOH	140	4	53.0	33.2	31.1	13.3	22.4
5	0.5Cu-2.0Co-Al	EtOH	140	4	16.1	30.4	29.6	22.2	17.8
6	0.25Cu-2.75Co-Al	2-POH	140	4	55.3	33.6	28.4	16.3	21.7
7	0.25Cu-2.75Co-Al	10% H_2O	140	4	47.5	37.7	38.3	10.9	13.1
8	0.25Cu-2.75Co-Al	EtOH	120	4	37.0	26.6	54.0	8.9	10.5
9	0.25Cu-2.75Co-Al	EtOH	160	4	98.8	41.6	15.0	16.1	27.3
10	0.25Cu-2.75Co-Al	EtOH	140	3	54.6	37.7	23.7	15.9	22.7
11	0.25Cu-2.75Co-Al	EtOH	140	5	82.4	37.6	32.1	13.9	16.4

[a]Reaction conditions are presented in the table along with conversion and selectivity. Reaction time was 2 h. More detailed selectivity breakdown located in Table C.1.

After conducting batch reaction experiments on catalysts with different Cu-Co ratios it was determined that 0.25Cu-2.75Co-Al had the highest activity per gram catalyst and productivity towards 1,5-PD after a 2 h reaction time. Though not the same catalyst and ratio, a similar optimal metal – metal ratio was also observed with Ni-Co-Al MMO at a lower Ni:Co ratio for the ring-opening of HMF to 1,2,6-hexanetriol.[28] To identify the active ring-opening species, THFA was chosen as a substrate. THFA was tested with the 0.25Cu-2.75Co-Al catalyst at an elevated temperature (160 °C) and 4 MPa of H_2, and almost negligible conversion was observed after 2 h (~1%). This demonstrates that THFA was essentially inactive for ring-opening with this class of catalysts, unlike Ir-ReO_x and other similar bifunctional catalysts employing precious metals.[10,17,39,40] This finding was

consistent with pathways proposing that FAL, an unsaturated cyclic ether, has a higher prevalence of ring-opening and is thermodynamically more favorable than THFA.[15,28,41,42]

Interestingly, when a small amount of Cu was added into the Co-Al matrix, there was a significant increase in activity and yield towards 1,5-PD. When a few catalysts were compared at similar conversion (above 95%) and 160 °C (Table C.2), there was no significant difference in selectivity between 3Co-Al and 0.1Cu-2.9Co-Al, but a notable difference in activity was evident. Consequently, the addition of a small amount of Cu may have primarily facilitated reduction and an increase in metallic sites, while doing little to change the adsorption conformation and reaction selectivity. In regards to the 0.1Cu-2.9Co-Al at high conversion, a yield of 44% towards 1,5-PD (62% total diols), which is the highest reported yield towards 1,5-PD using non-precious metal based catalysts.[43] Lastly, the sample with the highest Al/(Cu+Co) ratio displayed a significantly lower activity than all the other catalysts, which suggested that an excess of Al_2O_3 in the material may create fewer or perhaps less accessible metallic species for hydrogenation.

Next, a couple other solvents were chosen for investigation including isopropyl alcohol and 10 vol% H_2O in ethanol. There was not a significant difference in the reaction results between isopropyl alcohol and ethanol, just a small decrease in activity with the former solvent. However, when 10 vol% H_2O was added with ethanol, there was a much more significant decrease in activity as well as an increase in THFA selectivity. This result contrasts prior studies utilizing different bifunctional catalysts where H_2O was used as a solvent and/or was demonstrated to enhance activity.[10,20,39] One study even demonstrated that H_2O enhanced the productivity towards 1,2-PD over a Pt/CeO_2 catalyst.[20] One hypothesis for the drop in activity was the highly oxophilic nature of the catalysts after

reduction. It may be that a small amount of H_2O caused oxidation of the surface metallic species, rendering the solid a less active catalyst (fewer metallic sites) over time. Additionally, some LDH based MMOs can revert back to their LDH structures when exposed to H_2O or steam, which may have occurred during the reaction.[38] This reversibility effect may cause a loss in surface area or hydroxyl species formation, both of which could lead to lower activity.

Other conditions including temperature variation and pressure variation were tested to determine if these variables had a major effect on the ring-opening. As anticipated, as the temperature or pressure was decreased, a decrease in conversion was observed, and as temperature or pressure was increased, the opposite held true. In regards to temperature, at 120 °C, a significant increase in selectivity was observed for THFA, which suggested that ring-opening has a higher activation barrier than ring saturation, whether it be towards 1,2-PD or 1,5-PD production. In contrast, there was a decrease in THFA production at 160 °C, but with only a slight increase in ring-opening selectivity. This may be due to the large increase in other products including 2-MF, 1-POH, 2-POH. Regarding pressure variation, little difference was observed in selectivity, although activity increased at higher pressure.

It was recognized that reduction temperature plays a role in the activity of the catalysts. Multiple reduction temperatures were evaluated, and specific rates and productivities of the catalysts were determined at low conversion (below 30%). The catalyst reduction at different temperatures was carried out in a gas phase flow reactor, and an ultimate temperature of 300 °C, 400 °C, and 500 °C was chosen, with a hold for 1 h. Besides the final reduction temperature changes, the other pretreatment steps were carried out in the standard manner. When each of these reduction temperatures was evaluated,

significant changes in activity were observed, as shown in Table 4.3. The key data include specific rates at low conversions (< 30%) and the productivity towards 1,5-PD. Interestingly, the reaction rate after reduction at 300 °C was half as much as the rate at 400 °C, while the rate began to level off at 500 °C. Generally, increased reduction temperature generates more metallic species, as indicated by TPR (Figure 4.5), and could result in an increase in particle size of the metallic species, both of which affect the reactivity.

Table 4.3 – Kinetic analysis of the 0.25Cu-2.75Co-Al catalyst prepared using various reduction temperatures during the 1st pretreatment step.

Reduction Temperature	Specific Rate ($\mu mol*g_{cat}^{-1}*min^{-1}$)	$Productivity_{1,5\text{-}PD}$ ($\mu mol*g_{cat}^{-1}*min^{-1}$)
300 °C	870 ± 250	290 ± 110
400 °C	1880 ± 40	500 ± 50
500 °C	1690 ± 240	490 ± 70

Further evaluation of the ring-opening pathways was conducted utilizing FUR as the substrate to track how the series reaction progresses starting from the more saturated furanic compound. After conducting a liquid phase batch reaction with FUR as a substrate over the 0.25Cu-2.75Co-Al catalyst, the rates of the series of hydrogenation reactions could be qualitatively observed (Figure 4.2). Within 15 minutes, FUR was almost fully converted to FAL, and FAL was fully converted within ~500 min. It was clear that the rates of FAL conversion to THFA and/or diols were slower than the aldehyde hydrogenation (FUR to FAL), which further supported the proposed pathway whereby FAL was the intermediate to the diol products (exemplified in Figure 4.2)

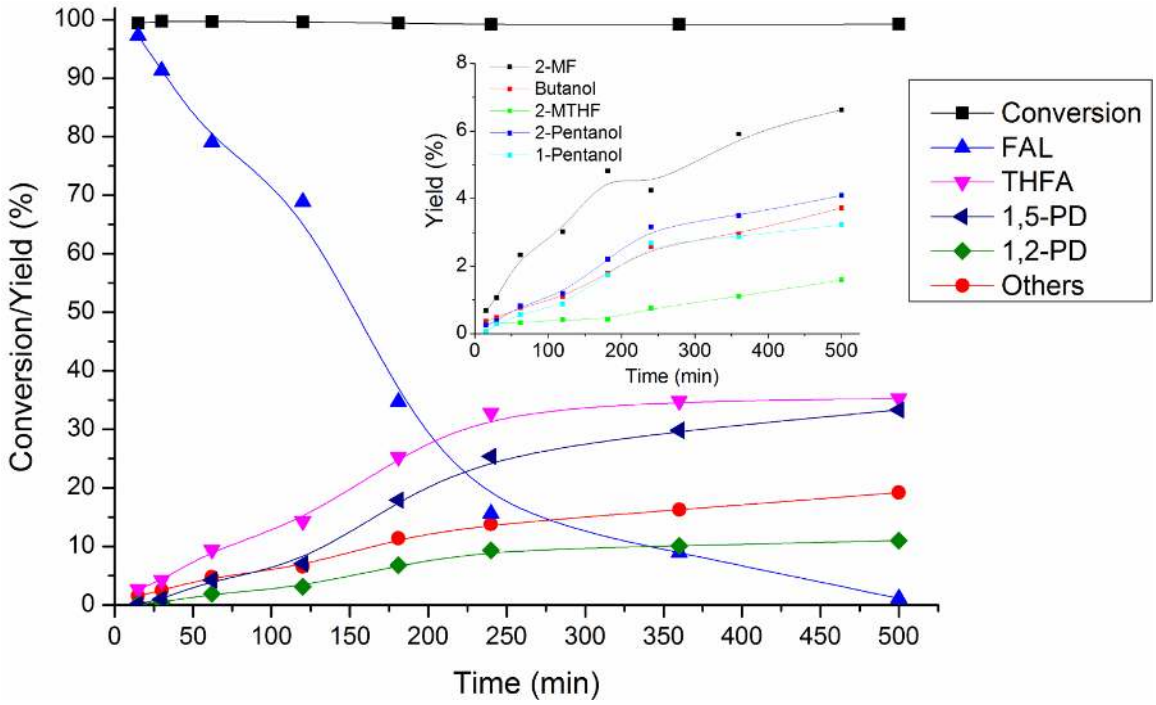

Figure 4.2 – Conversion of FUR over 0.25Cu-2.75Co-Al at 140 °C and 4 MPa of H_2

Ultimately, a yield of 1,5-PD of about 33% was achieved when FUR was utilized as the substrate, which was slightly lower than when FAL was utilized (38% yield). This very small decrease in yield may be due to small changes in substrate coverage or surface property changes when the aldehyde was introduced as the substrate. However, this approach provides a possible route to obtain diol products from the fully unsaturated furanic (FUR) in one pot without the need for expensive catalyst modifications (i.e. Pd-Ir-ReO_x/SiO_2).[13] Further experiments probing various side reactions in the pathway were conducted (Table C.3), and it was observed that the unsaturated compounds could further ring-open to their respective alcohols. The pathways displayed in Scheme 1 are consistent with the hypothesis that these catalysts do not convert the fully ring-saturated compounds into ring-opened products under the conditions employed.[31]

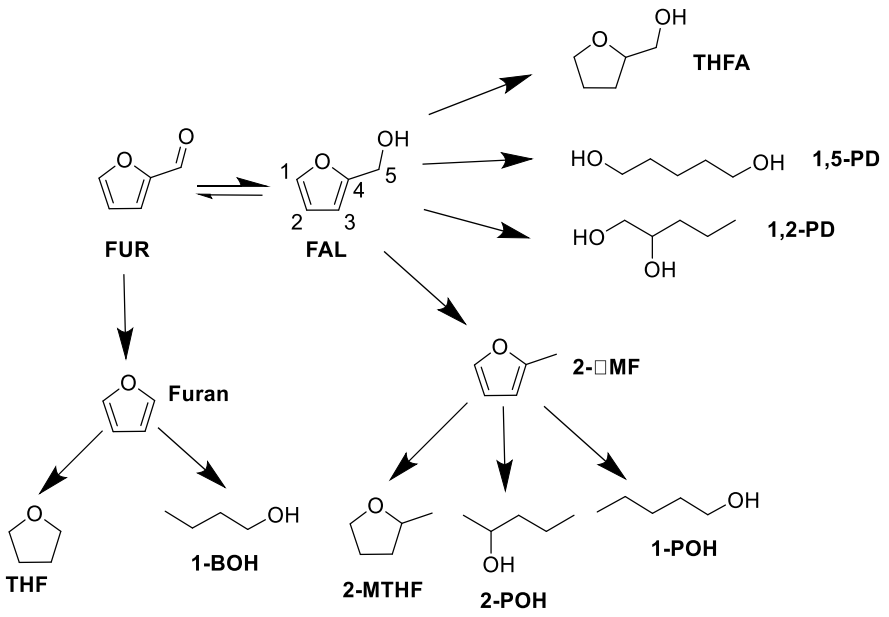

Figure 4.3 – Proposed reaction pathways for the conversion of FUR to the ring-opening products and ring saturated product.

4.3.3 XRD and TPR Experiments

To supplement the reaction data, a variety of characterization techniques before and after reduction were conducted. The XRD patterns in Figure 4.4 of the MMO materials showed very few features compared to the patterns of the uncalcined samples. After drying the LDH, the XRD patterns of these precursor materials displayed (Figure C.1) a few sharp crystalline peaks associated with the layered structure in the z-direction; however, after a high temperature treatment the layers become distorted, creating a more amorphous MMO. The lack of sharp crystalline peaks in the patterns of the calcined MMOs suggested that a dispersed and amorphous material was formed. The only visible feature was a short, broad peak at approximately 37°, which matches well with Co_3O_4 species, the major species in each catalyst. The broadness of the peaks and lack of sharp individual domains suggested a well-dispersed MMOs. Potentially a solid-solution was created with small domain sizes

of Co_3O_4, CuO, and Al_2O_3, which would increase the probability of each species interacting closely with each other.[28]

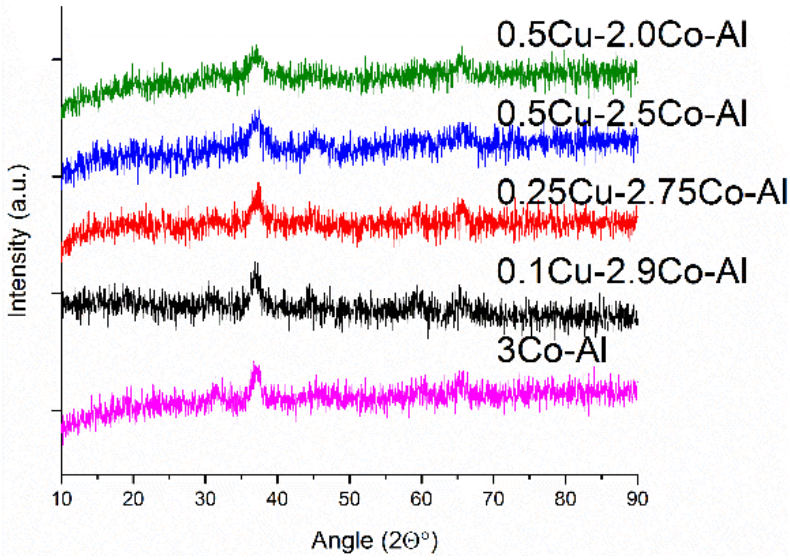

Figure 4.4 – Powder XRD patterns of each xCu-yCo-Al catalyst synthesized and were conducted after calcination and before reduction.

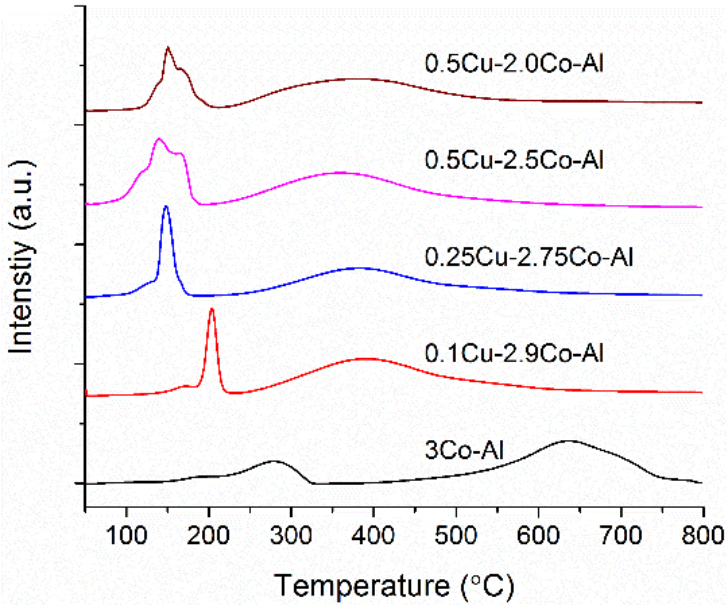

Figure 4.5 – TPR profile of each MMO material utilized in this study.

The MMO catalysts undergo a pretreatment to reduce some or all the oxides into metallic species, which were needed to dissociate H_2. Before reaction tests above were conducted, TPR was performed by flowing 10% H_2 (balance Ar) at increasing temperatures. The relation between the H_2 consumption versus temperature allowed for the evaluation of the bulk reduction properties of each pre-catalyst. The most qualitative difference in the TPR profiles was for 3Co-Al relative to the rest of the samples. Even a small addition of Cu significantly reduced the temperature where the initial uptake of H_2 took place. Furthermore, there was an emergence of a sharper peak between 150 °C - 210 °C, which indicated the significant impact Cu had on the reduction of the catalysts. Cu oxide has a higher propensity to reduce, which may result in a hydrogen spillover effect, easing the reduction of Co, similar to what has been observed in other multi- metal systems.[44,45] In all cases, there were two distinct reduction regions: low temperature, 150 °C - 250 °C (150 °C – 325 °C for 3Co-Al) and high temperature, 250 °C – 600 °C (400 °C – 750 °C for 3Co-Al). From prior literature and spectroscopic experiments that will be explained in more detail later, it was deduced that the main species after calcination were CuO, Co_3O_4, and Al_2O_3.[33,44,46] Although there was no evidence through XRD, due to the high dispersity, it may be possible for the formation of small domains of spinal structures such as $CuAl_2O_4$, $CuCo_2O_4$, and/or $CoAl_2O_4$.[46–48] From this knowledge, the low temperature peak can be assigned to the reduction of Co_3O_4 to CoO and/or CuO to Cu^0. Then the broader high temperature peak would be associated with CoO reducing to Co^0 and/or highly integrated Cu/Co oxide species reducing to the metallic state. The broad profile of the high temperature peak suggested two possibilities: (i) small amounts of spinal structures, which were more difficult to reduce, and/or (ii) the increased metal dispersion

created small metal domains, which were harder to reduce.[46,49] In general, as the Cu content increased there was a shift towards lower reduction temperatures and an increase in broadening of the 1st peak.

A second TPR profile (Figure C.2) was conducted on the catalysts after reduction and passivation. It was thought that passivation would result in oxidation of only surface species, which could then be re-reduced in H_2 at slightly lower temperatures in the batch reactor before starting the reaction. The obtained TPR profiles of the MMO materials post-passivation showed H_2 uptake starting below 150 °C, which was in the same range as the tested reaction temperature (140 °C). Based on the observed reduction behavior, the catalysts were re-reduced in the batch reactor at 180 °C in a solution of ethanol to provide all the catalysts with a common reduction experience before reaction: the bulk of the reduction completed at high temperatures in a flow reactor, and a final, low temperature reduction in situ. More explanation of the re-reduction TPR profiles is provided in the supplemental information.

4.3.4 Spectroscopic Experiments

To further the understanding of the structure of these complex MMO materials, beyond XRD and TPR, various spectroscopic experiments were conducted to provide more insight into the electronic environment of the catalysts. XAS was investigated at Argonne National Lab (ANL) after various pretreatment conditions, including reduction at various temperatures and post-passivation in 1% O_2. Due to the difficulty conducting pressurized batch reactions at ANL, the catalysts were not treated by the second reduction pretreatment on the beamline. Additionally, the high Co:Cu ratios made it extremely difficult to ascertain

quality Cu scans due to the significant energy absorption from Co species. This coupled with low Cu loadings resulted in a small edge step and low signal: noise ratio, with only qualitative information ascertained. The reader can refer to the supplemental information for the near-edge spectra of Cu, and a more detailed description of the spectra. Although it was difficult to ascertain quantitative Cu analysis, the XANES data (Figure C.17 and C.18) suggested that the Cu species may have been in a $CuAl_2O_4$ state prior to reduction due to its higher edge energy, and after reduction at various temperatures most species appeared to be Cu^0. This further supports the hypothesized high dispersion of Cu oxide species among the other metal oxides in the system.

Analyzing the Co species embedded in the catalysts through XANES helped gain information about the electronic structure of Co after reduction and passivation. A variety of standards were scanned under ambient conditions, which were then utilized to fit the spectrum of the 0.25Cu-2.75Co-Al sample after various pretreatment steps, as shown in Figure 4.6. Before reduction, the Co species mimicked Co_3O_4, which is a spinal structure with 2+ and 3+ Co species that are tetrahedrally and octahedrally coordinated, respectively. After pretreatment in pure H_2 at any temperature tested (300 ºC – 500 ºC), there was clear shift in the edge energy, indicating reduction of the Co_3O_4 to either a 2+ or metallic state.

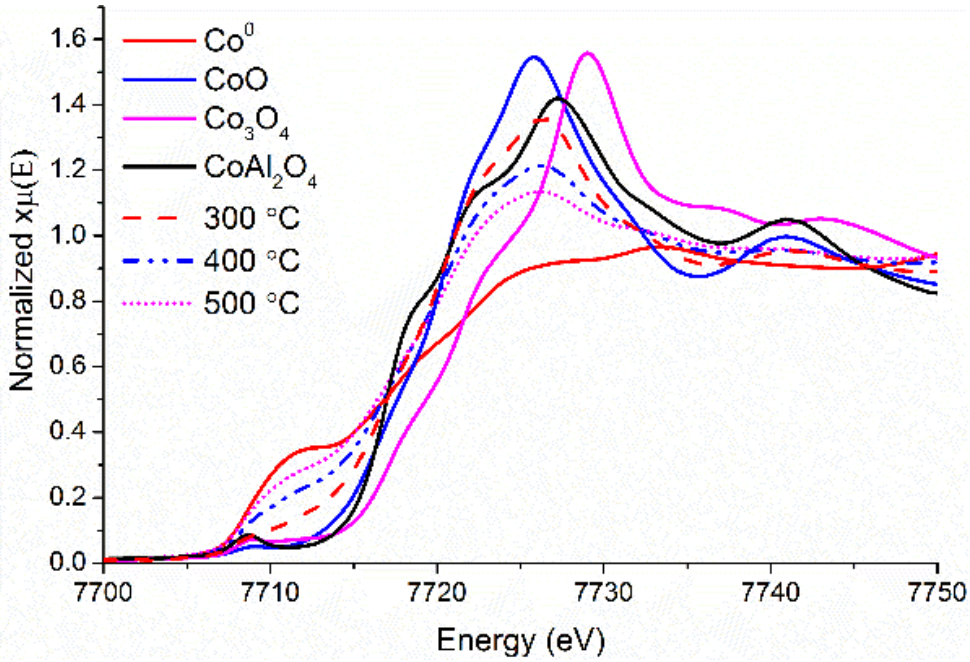

Figure 4.6 – XANES spectra of Co k-edge of known standards and the 0.25Cu-2.75Co-Al catalyst after H_2 pretreatment at 300 °C, 400 °C, and 500 °C, and subsequent passivation for 1 h in 1% O_2/N_2.

As anticipated, as the reduction temperature decreased, there was a clear increase in the white line intensity, indicating a less reduced Co species. Linear combination fitting was utilized to qualitatively discern the electronic state of the catalysts after reduction and passivation. After fitting (Figure 4.6), it was suggested that no Co_3O_4 species remained in the catalysts after reduction, and the combination Co^0, CoO, and $CoAl_2O_4$ (Co^{2+}) gave the best fitted results. It was interesting that XANES suggested the formation of a $CoAl_2O_4$ type species after reduction while there was no indication of these species prior to reduction; however, EXAFS analysis and TPR profiles suggested the possibility of high Co-O-Al interactions, which would be consistent with $CoAl_2O_4$ domains. This may be a result of fewer Co^{2+} atoms interacting with Al^{3+} before reaction, since the majority of Co species present in Co_3O_4 are octahedral Co^{3+}. However, once introduced to H_2 at low

temperatures, the Co^{3+} species begin to form Co^{2+}, which increases the probability of a cobalt aluminate species forming, especially given the high dispersion of the metal oxides in the overall matrix. The high dispersity and low Al_2O_3 loading suggested that the $CoAl_2O_4$ species that do form had small domain sizes and may not equate to a bulk aluminate material.

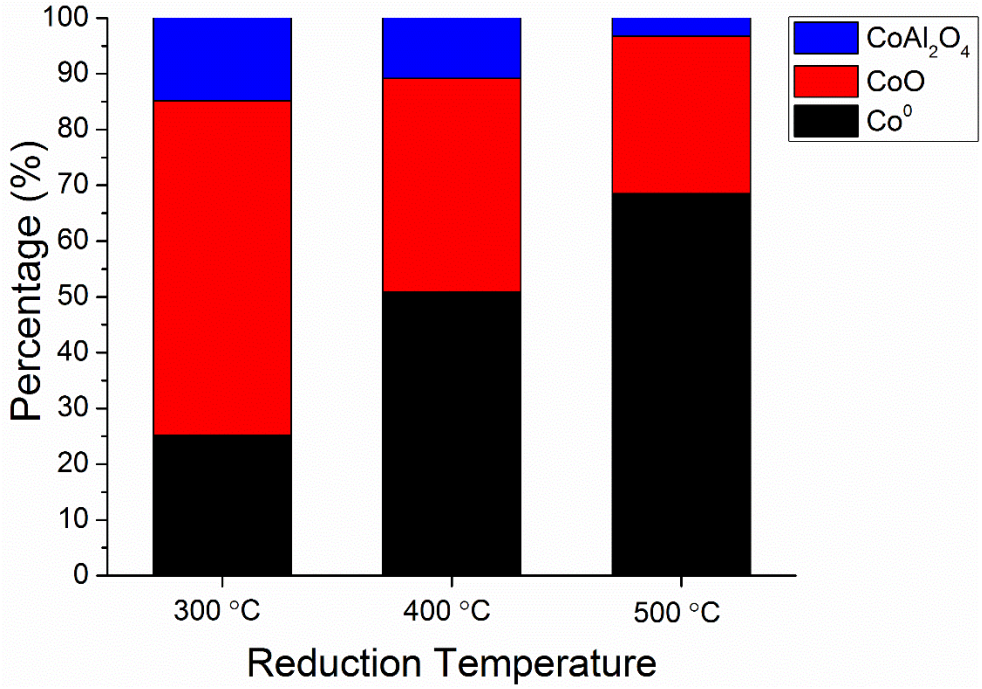

Figure 4.7 – XANES linear combinations of the 0.25Cu-2.75Co-Al material after various pretreatment conditions.

Clearly, as the reduction temperature increased the number of metallic species increased, more than doubling between 300 °C and 400 °C. Interestingly, formation of $CoAl_2O_4$ species seemed to sharply decrease at 500 °C, which may have been due to a higher degree of sintering among Co atoms reducing the amount of Co-O-Al interactions. This was evident through extended EXAFS fitting at each reduction temperature, the results of which are displayed in Table 4.4. As mentioned previously, this analysis was

done on scans conducted at room temperature to avoid adjusting the Debye-Waller factor, a variable that is a function of thermal disorder. From the XANES analysis, it was clear that Co-O and Co-Co (Cu) scattering should be included in the fitting to achieve the best fit.

Table 4.4 – EXAFS fitting of the 0.25Cu-2.75Co-Al material after pretreatment at various reduction temperatures and a passivation step[a]

Sample	Shell	CN[c]	r (Å)[d]	Δσ (10^{-3} Å^2)[e]	ΔE_0 (eV)[f]	R factor
Co Foil[b]	Co-Co	12	2.50 ± 0.01	6.4 ± 0.4	7.8 ± 0.5	0.008
Co(III) acac	Co-O	6	1.88	1.8 ± 1.1	-3.5 ± 0.6	0.013
300 °C	Co-O	3.2 ± 0.4	2.07 ± 0.01	5.5 ± 1.8	0.8 ± 1.2	0.010
	Co-Co(Cu)	2.5 ± 0.7	2.50 ± 0.01	8.5 ± 2.3	0.8 ± 1.2	
400 °C	Co-O	2.4 ± 0.4	2.02 ± 0.01	8.6 ± 2.8	-1.6 ± 0.9	0.003
	Co-Co(Cu)	3.5 ± 0.3	2.49 ± 0.01	6.3 ± 0.7	-1.6 ± 0.9	
500 °C	Co-O	1.4 ± 0.4	2.01 ± 0.02	6.3 ± 4.3	-3.7 ± 1.0	0.007
	Co-Co(Cu)	4.9 ± 0.5	2.50 ± 0.01	6.7 ± 0.8	-3.7 ± 1.0	

[a]Fitting parameters: Fourier transform range, Δk, 2.4-12.5 Å^{-1} with weighting k^2. [b]Fourier transform range, Δk, 2.7-14 Å^{-1} with weighting k^2. The R-space that was fit was 1.0-3.5 Å. Coordination number assigned from standard HCP Co^0 structure; S_0^2 (Co-Co) = 0.78 determined from Co foil fitting and S_0^2 (Co-O) = 0.69 determined from Co(III) acac. [c]Coordination number; [d]Bond distance; [e]Debye-Waller Factor; [f]Edge energy difference.

The results indicated there was an increase in the metallic Co-Co (Cu) coordination number as the reduction temperature increased, which aligned well with the XANES analysis. The rise in the coordination number could have indicated larger metallic particles due to sintering of the Co and/or agglomeration with Cu atoms. The coordination number for the metallic species was much smaller than that of bulk metallic Co, indicating that metallic nanoparticles were forming, which may be due to the Al_2O_3 acting as a

binder/support oxide well-dispersed throughout the matrix. However, particle size determination was challenging using TEM (due to low contrast between the oxide and metallic phases) or through chemisorption, making particle size validation by a complimentary technique unavailable. Another indication of strong Al interaction was demonstrated by the average bond distance of Co-O, which was found to be lower than CoO (2.13 Å) in all cases.[50] The Co-O bond distance in bulk $CoAl_2O_4$ is lower than CoO at 1.94 Å, which suggested an influence of Al on the oxide matrix, and Co^{2+} species may be in a mix of tetrahedral and octahedral coordination environment.[51] As expected, the Co-Co bond distance did not stray away from that in bulk metallic Co because of the large amounts of Co and similar atomic sizes of Co and Cu.

To further understand the catalyst's behavior after the various reduction conditions employed, XPS was utilized to analyze the surface species. While XAS is a bulk technique, XPS can allow for a better understanding of the electronic environment within a few nanometers of the surface.[52] Additionally, XPS could help validate copper's oxidation state. Lastly, the catalysts were pretreated through both reduction steps before being introduced to the spectrometer, which allowed for a better understanding the role of each pretreatment step conducted prior to reaction.

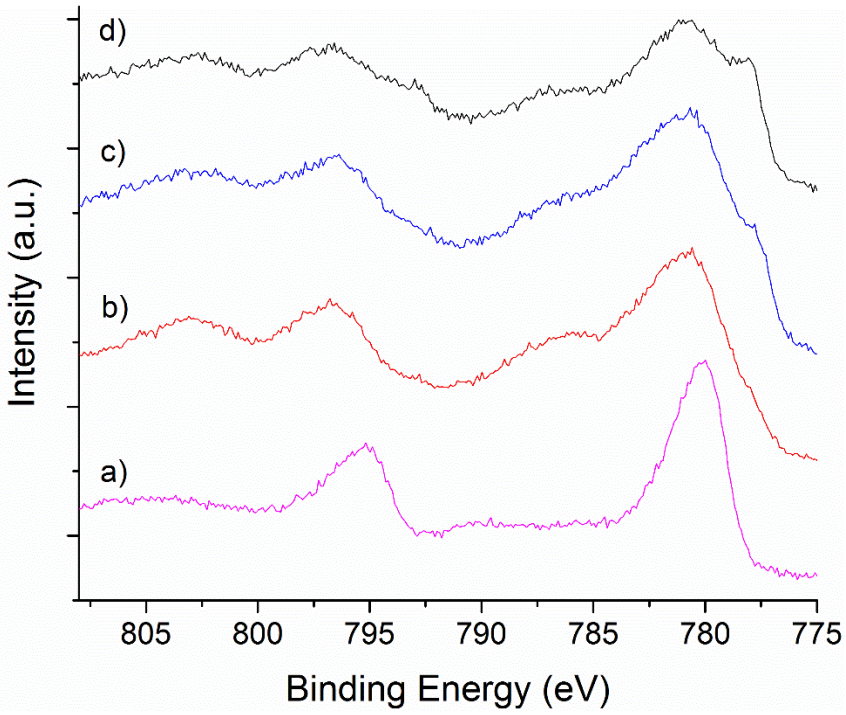

Figure 4.8 – Co 2p XPS spectra of the 0.25Cu-2.75Co-Al material after reduction in the flow reactor at various temperatures, passivation, and re-reduction in the batch reactor to 180 °C and 500 psi of H_2. A) No Reduction; b) 300 °C reduction; c) 400 °C reduction; d) 500 °C reduction

It was evident from XPS that the major metal species, Co, displayed a shift and broadening of the $2p_{3/2}$ peak (775-783 eV) after reduction at any temperature. Upon reduction, there was the evolution of a satellite peak at ~786 eV and a shoulder at about 778 eV, which were associated to the formation of Co^{2+} and Co^0, respectively.[53,54] The initial oxide material in Figure 4.8a mimicked a standard Co_3O_4 material due to its $2p_{3/2}$ peak located at ~780 eV and the lack of a major satellite peak located around 785 eV – 790 eV. This correlated well with XAS findings prior to reduction, which indicated that the major component was Co_3O_4. A clear trend was observed in regards to the shoulder located at 778 eV. As the reduction temperature increased, so did the intensity of the shoulder, which indicated an increase in the amount of metallic Co on the surface and further

corroborated the XANES analysis. It was clear that the second reduction step played a role in increasing the number of metallic sites on the surface, which can be discerned qualitatively through the increased shoulder intensity at 778 eV when comparing similar reduction temperatures (Figure 4.8 versus C.5). This provided evidence that MMO materials after the first reductive pretreatment step could undergo surface alterations during reaction, which could have affected the reaction kinetics. Consequently, this finding furthered the decision in this study to re-reduce the catalysts in situ prior to reaction.

The X-ray photoelectron spectra can be analyzed quantitatively through deconvolution to obtain percentages specific to Co oxidation states on the surface. A distinction between CoO and $CoAl_2O_4$ was not included in the fitting to simplfy the deconvolution and the two species were lumped and designated Co^{2+}. The results in Table 4.5 do complement the qualitative observations; however, interestingly, the percentage of metallic species on the surface was significantly less than the bulk species determined by XANES, even after the additional reduction. This suggested that the passivation step effectively coated the surface and potentially subsurface (range of ~10 nm), creating a barrier over the bulk metallic species. In general, XPS and XAS provided evidence that there were two types of Co species (Co^{2+} and Co^0) located on the surface and the bulk during reaction, which could create a bifunctional catalyst active for ring-opening.

Table 4.5 – Quantitative XPS analysis of Co species from various spectra displayed in Figure 4.8.

Sample	Co	Co^{2+}
300 °C	1.8 %	98.2 %
400 °C	7.2 %	92.8 %
500 °C	14.2 %	85.8 %

*Values obtained by the peak areas from $2p_{3/2}$

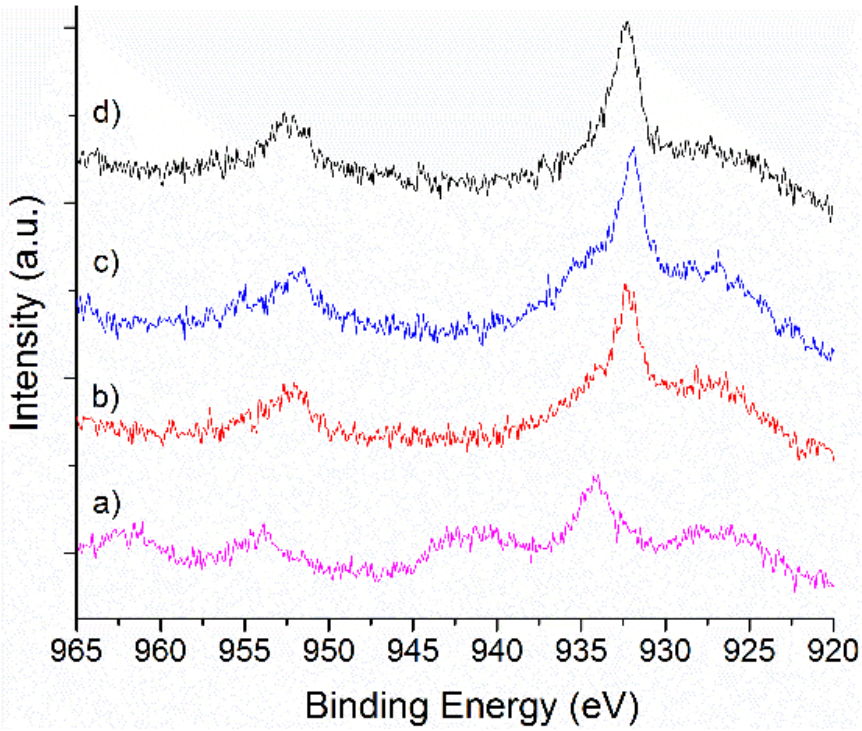

Figure 4.9 – Cu 2p XP spectra of the 0.25Cu-2.75Co-Al material after reduction in the flow reactor at various temperatures, passivation, and re-reduction in the batch reactor to 180 °C and 500 psi of H_2. A) No reduction; b) 300 °C reduction; c) 400 °C reduction; d) 500 °C reduction

Additionally, XPS could help understand the electronic environment of Cu, even though it was present at a low weight loading. Similar reduction conditions were employed as for the samples in Figure 4.8, and the Cu 2p binding energy region was analyzed (Figure 4.9). The sample prior to reduction mimicked a Cu^{2+} electronic state, based on the $2p_{3/2}$ peak centered at 934 eV and the strong satellite peak centered at 942 eV.[54,55] After the reduction pretreatments were conducted, there was a major shift to lower binding energy to approximately 932.5 eV, which was indicative of a metallic Cu^0 or Cu_2O species. It was difficult to discern between Cu^0 and Cu_2O in the 2p binding energy region, and due to the low Cu loadings, the LMM auger peak was undetectable; however, XANES analysis suggested that mainly Cu^0 was present (Figure C.18 and Table C.7). This made it more likely the change in XPS was due to the formation of Cu^0 with very minimal Cu oxide species present.

Additional XAS analysis was conducted on a few other catalysts to potentially gain insight into why the performance varied over each catalyst. It was found that both XANES linear combination (Figure C.16) and EXAFS fitting (Table C.5) were within the margin of error for each Cu-Co-Al catalyst tested. However, it was observed from TPR experiments both before and after pretreatment that varying the Cu-Co ratio alters the reducibility of the catalyst. With this observation and insight gained from varying reduction temperatures, the subtle changes in performance for each catalyst at a fixed pretreatment may have been a result of small changes in particle size or metallic/oxide ratios on the surface not observed through a bulk technique such as XAS. It is possible the 0.25Cu-2.75Co-Al contained a good balance between metallic/oxide species and particle size compared to the other catalysts tested, which resulted in the highest activity per gram.

Furthermore, for the conversion of FAL to progress either four (ring-saturation) or six (ring-opening) hydrogen atoms are necessary, which requires accessible metallic sites. The low activity per gram for 3Co-Al reduced at 400 °C and 0.25Cu-2.75Co-Al reduced at 300 °C may have been a result of the limited amount of Co^0 present in the system (Figure C.16 and Figure 4.8/Table 4.5, respectively). Once Cu was introduced into the system, there was a significant increase in metallic species present after reducing at 400 °C and above, which correlates with the increase in activity. The large amount of Co^{2+} species present may have a different functionality than the metallic sites present. From prior reports, others have suggested the presence of significant amounts of Co^{2+} may facilitate the adsorption of FAL in a more tilted mode, which enhances ring-opening.[23,28] This result was similar to the proposed mechanism of the Ni-Co-Al and Ru/MnO_x catalysts for ring-opening, where it was claimed the oxide oriented the molecule in a tilted confirmation, while the metallic sites hydrogenated the adsorbed species.[28,30] However, the Co species preferred the cleaving of C_4-O bond not the C_1-O bond of FAL, which was in contrast to Ru/MnO_x and Pt/Mg-Al catalysts.[16,30] Lastly, a fully saturated ring such as THFA or THF seems to interact less favorably than an unsaturated or partially unsaturated ring, which results in negligible ring-opening activity with the reduced Cu-Co-Al catalysts.

Ultimately, the spectroscopic experiments determined that the major species present on the surface was Co^{2+} oxide species with small amounts of Co^0 and Cu^0 phases located at or near the surface (most likely due to passivation), while the bulk structure contained more metallic species. As the reduction temperature increased, the amount of metallic species on the surface increased, while XAS results suggested an increase in the metallic particle size. The increase of metallic species on the surface may have increased the

specific rate, but as the particle sizes increased, the surface area – volume ratio decreased, resulting in the activity leveling off at 500 °C reduction.

Unfortunately, due to the complexity of the materials, pretreatments, and the mechanism behind ring-opening, it was difficult to identify and count active sites. To this end, further investigations will need to be conducted with more well-defined structures, including *in* situ FTIR, that will better elucidate the mechanism and sites required for this reaction, ultimately leading to the rational design of non-precious, multi-metal catalysts that are highly effectively in the ring-opening of furanic ring to produce value added products.

4.4 Conclusions

In this investigation, well-dispersed MMO materials were synthesized through the high temperature calcination of LDH prepared precursors. This synthesis technique allowed for highly versatile catalysts with very similar physical morphologies such as surface area and pore volume, which allowed for a useful comparison of materials. Additionally, it was suggested based on various spectroscopic and diffraction experiments that there was high metal dispersity and strong interactions between each component before reduction. The addition of Cu into the high loading Co catalysts proved to ease the reduction of the catalysts and perhaps increase the number of metallic species present on the surface. This corresponded to an increase in activity and yield of 1,5-PD, even when the smallest amount of Cu was introduced into the system. Ultimately a yield of ~44% to 1,5-PD (total diol yield of 62%) was achieved under optimized conditions with FAL as the substrate. Various spectroscopic experiments were employed throughout to gain a further

understanding of the species involved in the reactions. It was evident that both oxide and metallic species were present on the surface and in the bulk after the reduction and passivation steps had taken place before reaction. XPS suggested most of the species on the surface were Co^{2+} with small amounts of Co^0, while qualitatively the majority of the Cu species on the surface seemed to be Cu^0. This lends to the conclusion that a significant amount of cobalt oxide in a 2+ oxidation may potentially help orient the FAL on the surface to facilitate ring-opening, while the small domains of metallic Co and Cu present on the surface facilitated the hydrogenation. Additionally, a specific ratio of surface oxides and metallic species were required to tune the catalyst towards ring-opening chemistries.

4.5 References

(1) Sulmonetti, T. P.; Hu, B.; Lee, S.; Agrawal, P. K.; Jones, C. W. Reduced Cu−Co−Al mixed metal oxides for the ring-opening of furfuryl alcohol to produce renewable diols. *ACS Sustain. Chem. Eng.* **2017**, *5*, 8959-8969.

(2) Gallezot, P. Conversion of biomass to selected chemical products. *Chem. Soc. Rev.* **2012**, *41*, 1538–1558.

(3) Alonso, D. M.; Bond, J. Q.; Dumesic, J. A. Catalytic conversion of biomass to biofuels. *Green Chem.* **2010**, *12*, 1493–1513.

(4) Li, X.; Jia, P.; Wang, T. Furfural: a promising platform compound for sustainable production of C_4 and C_5 chemicals. *ACS Catal.* **2016**, *6*, 7621–7640.

(5) Nakagawa, Y.; Tamura, M.; Tomishige, K. Catalytic reduction of biomass-derived furanic compounds with hydrogen. *ACS Catal.* **2013**, *3*, 2655–2668.

(6) Liu, S.; Amada, Y.; Tamura, M.; Nakagawa, Y.; Tomishige, K. Performance and characterization of rhenium-modified Rh–Ir alloy catalyst for one-pot conversion of furfural into 1,5-pentanediol. *Catal. Sci. Technol.* **2014**, *4*, 2535–2349.

(7) Román-Leshkov, Y.; Chheda, J. N.; Dumesic, J. A. Phase modifiers promote efficient production of hydroxymethylfurfural from fructose. *Science* **2006**, *312*, 1933–1937.

(8) Lange, J.-P.; van der Heide, E.; van Buijtenen, J.; Price, R. Furfural-a promising platform for lignocellulosic biofuels. *ChemSusChem* **2012**, *5*, 150–166.

(9) Liu, C.; Wang, H.; Karim, A. M.; Sun, J.; Wang, Y. Catalytic fast pyrolysis of lignocellulosic biomass. *Chem. Soc. Rev.* **2014**, *43*, 7594–7623.

(10) Chia, M.; Pagán-Torres, Y. J.; Hibbitts, D.; Tan, Q.; Pham, H. N.; Datye, A. K.; Neurock, M.; Davis, R. J.; Dumesic, J. A. Selective hydrogenolysis of polyols and cyclic ethers over bifunctional surface sites on rhodium-rhenium catalysts. *J. Am. Chem. Soc.* **2011**, *133*, 12675–12689.

(11) Brentzel, Z. J.; Barnett, K. J.; Huang, K.; Maravelias, C. T.; Dumesic, J. A.; Huber, G. W. Chemicals from biomass : combining ring-opening tautomerization and hydrogenation reactions to produce 1,5-pentanediol from furfural. *ChemSusChem* **2017**, *10*, 1351–1355.

(12) Koso, S.; Furikado, I.; Shimao, A.; Miyazawa, T.; Kunimori, K.; Tomishige, K. Chemoselective hydrogenolysis of tetrahydrofurfuryl alcohol to 1,5-pentanediol. *Chem. Commun.* **2009**, *0*, 2035–2037.

(13) Liu, S.; Amada, Y.; Tamura, M.; Nakagawa, Y.; Tomishige, K. One-pot selective conversion of furfural into 1,5-pentanediol over a Pd-added Ir–ReO_x/SiO2 bifunctional catalyst. *Green Chem.* **2014**, *16*, 617–626.

(14) Liu, H.; Huang, Z.; Zhao, F.; Cui, F.; Li, X.; Xia, C.; Chen, J. Efficient hydrogenolysis of biomass-derived furfuryl alcohol to 1,2- and 1,5-pentanediols over a non-precious Cu–$Mg_3AlO_{4.5}$ bifunctional catalyst. *Catal. Sci. Technol.* **2015**, *6*, 668–671.

(15) Xu, W.; Wang, H.; Liu, X.; Ren, J.; Wang, Y.; Lu, G. Direct catalytic conversion of furfural to 1,5-pentanediol by hydrogenolysis of the furan ring under mild conditions over Pt/Co_2AlO_4 catalyst. *Chem. Commun.* **2011**, *47*, 3924–3926.

(16) Mizugaki, T.; Yamakawa, T.; Nagatsu, Y.; Maeno, Z.; Mitsudome, T.; Jitsukawa, K.; Kaneda, K. Direct transformation of furfural to 1,2-pentanediol using a hydrotalcite-supported platinum nanoparticle catalyst. *ACS Sustain. Chem. Eng.* **2014**, *2*, 2243–2247.

(17) Pholjaroen, B.; Li, N.; Huang, Y.; Li, L.; Wang, A.; Zhang, T. Selective hydrogenolysis of tetrahydrofurfuryl alcohol to 1,5-pentanediol over vanadium modified Ir/SiO_2 catalyst. *Catal. Today* **2015**, *245*, 93–99.

(18) Liu, H.; Huang, Z.; Kang, H.; Xia, C.; Chen, J. Selective hydrogenolysis of biomass-derived furfuryl alcohol into 1,2- and 1,5-pentanediol over highly dispersed Cu-Al_2O_3 catalysts. *Chinese J. Catal.* **2016**, *37*, 700–710.

(19) Guan, J.; Peng, G.; Cao, Q.; Mu, X. Role of MoO_3 on a rhodium catalyst in the selective hydrogenolysis of biomass-derived tetrahydrofurfuryl alcohol into 1,5-pentanediol. *J. Phys. Chem. C* **2014**, *118*, 25555–25566.

(20) Ma, R.; Wu, X.-P.; Tong, T.; Shao, Z.-J.; Wang, Y.; Liu, X.; Xia, Q.; Gong, X.-Q.

The Critical Role of Water in the Ring Opening of Furfural Alcohol to 1,2-Pentanediol. *ACS Catal.* **2017**, *7*, 333–337.

(21) Chatterjee, M.; Kawanami, H.; Ishizaka, T.; Sato, M.; Suzuki, T.; Suzuki, A. An attempt to achieve the direct hydrogenolysis of tetrahydrofurfuryl alcohol in supercritical carbon dioxide. *Catal. Sci. Technol.* **2011**, *1*, 1466–1471.

(22) Alonso, D. M.; Wettstein, S. G.; Dumesic, J. A. Bimetallic catalysts for upgrading of biomass to fuels and chemicals. *Chem. Soc. Rev.* **2012**, *41*, 8075–8098.

(23) Nakagawa, Y.; Tamura, M.; Tomishige, K. Catalytic conversions of furfural to pentanediols. *Catal. Surv. from Asia* **2015**, *19*, 249–256.

(24) Nakagawa, Y.; Mori, K.; Chen, K.; Amada, Y.; Tamura, M.; Tomishige, K. Hydrogenolysis of CO bond over Re-modified Ir catalyst in alkane solvent. *Appl. Catal. A Gen.* **2013**, *468*, 418–425.

(25) Wang, Z.; Pholjaroen, B.; Li, M.; Dong, W.; Li, N.; Wang, A.; Wang, X.; Cong, Y.; Zhang, T. Chemoselective hydrogenolysis of tetrahydrofurfuryl alcohol to 1, 5-pentanediol over Ir-MoO_x/SiO_2 catalyst. *J. Energy Chem.* **2014**, *23*, 427–434.

(26) Chia, M.; O'Neill, B. J.; Alamillo, R.; Dietrich, P. J.; Ribeiro, F. H.; Miller, J. T.; Dumesic, J. A. Bimetallic RhRe/C catalysts for the production of biomass-derived chemicals. *J. Catal.* **2013**, *308*, 226–236.

(27) Horiuchi, C. M.; Rangan, M.; Israel, B. M.; Medlin, J. W. Adsorption and Decomposition of 2 (5 H) -Furanone on Pd (111) and Pt (111): Comparison of Ring-Opening Pathways of an Unsaturated Cyclic Ester. *J. Phys. Chem. C* **2009**, *2*, 14900–14907.

(28) Yao, S.; Wang, X.; Jiang, Y.; Wu, F.; Chen, X.; Mu, X. One-Step conversion of biomass-derived 5-hydroxymethylfurfural to 1,2,6-hexanetriol over Ni–Co–Al mixed oxide catalysts under mild conditions. *ACS Sustain. Chem. Eng.* **2014**, *2*, 173–180.

(29) Xu, W.; Wang, H.; Liu, X.; Ren, J.; Wang, Y.; Lu, G. Direct catalytic conversion of furfural to 1,5-pentanediol by hydrogenolysis of the furan ring under mild conditions over Pt/Co_2AlO_4 catalyst. *Chem. Commun.* **2011**, *47*, 3924–3926.

(30) Zhang, B.; Zhu, Y.; Ding, G.; Zheng, H.; Li, Y. Selective conversion of furfuryl alcohol to 1,2-pentanediol over a Ru/MnO_x catalyst in aqueous phase. *Green Chem.* **2012**, *14*, 3402–3409.

(31) Lee, J.; Burt, S. P.; Carrero, C. A.; Alba-Rubio, A. C.; Ro, I.; O'Neill, B. J.; Kim, H. J.; Jackson, D. H. K.; Kuech, T. F.; Hermans, I.; et al. Stabilizing cobalt catalysts for aqueous-phase reactions by strong metal-support interaction. *J. Catal.* **2015**, *330*, 19–27.

(32) Götz, D.; Lucas, M.; Claus, P. C–O bond hydrogenolysis vs. C=C group hydrogenation of furfuryl alcohol: towards sustainable synthesis of 1,2-pentanediol. *React. Chem. Eng.* **2016**, *1*, 161–164.

(33) Sulmonetti, T. P.; Pang, S. H.; Taborga Claure, M.; Lee, S.; Cullen, D. A.; Agrawal, P. K.; Jones, C. W. Vapor phase hydrogenation of furfural over nickel mixed metal oxide catalysts derived from layered double hydroxides. *Appl. Catal. A Gen.* **2016**, *517*, 187–195.

(34) Sulmonetti, T. P.; Hu, B.; Ifkovits, Z.; Lee, S.; Agrawal, P. K.; Jones, C. W. Vapor phase hydrogenolysis of furanics utilizing reduced cobalt mixed metal oxide catalysts. *ChemCatChem* **2017**, *9*, 1815–1823.

(35) Taborga Claure, M.; Chai, S.-H.; Dai, S.; Unocic, K. A.; Alamgir, F. M.; Agrawal, P. K.; Jones, C. W. Tuning of higher alcohol selectivity and productivity in CO hydrogenation reactions over K/MoS_2 domains supported on mesoporous activated carbon and mixed MgAl oxide. *J. Catal.* **2015**, *324*, 88–97.

(36) Calvin, S.; Carpenter, E.; Ravel, B.; Harris, V.; Morrison, S. Multiedge refinement of extended x-ray-absorption fine structure of manganese zinc ferrite nanoparticles. *Phys. Rev. B* **2002**, *66*, 224405.

(37) Cavani, F.; Trifirò, F.; Vaccari, A. Hydrotalcite-type anionic clays: preparation, properties and applications. *Catal. Today* **1991**, *11*, 173–301.

(38) Salam, M. A.; Sufian, S.; Murugesan, T. Characterization of nano-crystalline Mg-Ni-Al hydrotalcite derived mixed oxides as hydrogen adsorbent. *Mater. Chem. Phys.* **2013**, *142*, 213–219.

(39) Koso, S.; Furikado, I.; Shimao, A.; Miyazawa, T.; Kunimori, K.; Tomishige, K. Chemoselective hydrogenolysis of tetrahydrofurfuryl alcohol to 1,5-pentanediol. *Chem. Commun.* **2009**, No. 15, 2035–2037.

(40) Koso, S.; Ueda, N.; Shinmi, Y.; Okumura, K.; Kizuka, T.; Tomishige, K. Promoting effect of Mo on the hydrogenolysis of tetrahydrofurfuryl alcohol to 1,5-pentanediol over Rh/SiO_2. *J. Catal.* **2009**, *267*, 89–92.

(41) Wan, W.; Jenness, G. R.; Xiong, K.; Vlachos, D. G.; Chen, J. G. Ring-opening reaction of furfural and tetrahydrofurfuryl alcohol on hydrogen pre-dosed Ir(111) and Co/Ir(111) surfaces. *ChemCatChem* **2017**, *9*, 1701–1707.

(42) Jenness, G. R.; Wan, W.; Chen, J. G.; Vlachos, D. G. Reaction Pathways and Intermediates in Selective Ring Opening of Biomass-Derived Heterocyclic Compounds by Iridium. *ACS Catal.* **2016**, *6*, 7002–7009.

(43) Husni, A.; Wijaya, W.; Kojima, T.; Hara, T.; Wijaya, H. W.; Kojima, T.; Hara, T.; Ichikuni, N. Synthesis of 1,5-pentanediol from the hydrogenolysis of furfuryl alcohol over Ni-Y_2O_3 composite catalyst. *ChemCatChem* **2017**, *9*, 2869–2874.

(44) Jacobs, G.; Ribeiro, M. C.; Ma, W.; Ji, Y.; Khalid, S.; Sumodjo, P. T. A.; Davis, B. H. Group 11 (Cu, Ag, Au) promotion of 15%Co/Al_2O_3 Fischer-Tropsch synthesis catalysts. *Appl. Catal. A Gen.* **2009**, *361*, 137–151.

(45) Hong, Y.; Zhang, H.; Sun, J.; Ayman, K. M.; Hensley, A. J. R.; Gu, M.; Engelhard, M. H.; McEwen, J.-S.; Wang, Y. Synergistic Catalysis between Pd and Fe in Gas Phase Hydrodeoxygenation of m -Cresol. *ACS Catal.* **2014**, *4*, 3335–3345.

(46) Sankaranarayanan, S.; Sharma, A.; Srinivasan, K. CoCuAl layered double hydroxides - efficient solid catalysts for the preparation of industrially important fatty epoxides. *Catal. Sci. Technol.* **2015**, *5*, 1187–1197.

(47) Wang, J.; Chernavskii, P. A.; Khodakov, A. Y.; Wang, Y. Structure and catalytic performance of alumina-supported copper-cobalt catalysts for carbon monoxide hydrogenation. *J. Catal.* **2012**, *286*, 51–61.

(48) Srivastava, S.; Jadeja, G. C.; Parikh, J. A versatile bi-metallic copper-cobalt catalyst for liquid phase hydrogenation of furfural to 2-methylfuran. *RSC Adv.* **2016**, *6*, 1649–1658.

(49) Dong, F.; Zhu, Y.; Zheng, H.; Zhu, Y.; Li, X.; Li, Y. Cr-free Cu-catalysts for the selective hydrogenation of biomass-derived furfural to 2-methylfuran: The synergistic effect of metal and acid sites. *J. Mol. Catal. A Chem.* **2015**, *398*, 140–148.

(50) Hu, B.; Bean Getsoian, A.; Schweitzer, N. M.; Das, U.; Kim, H.; Niklas, J.; Poluektov, O.; Curtiss, L. A.; Stair, P. C.; Miller, J. T.; et al. Selective propane dehydrogenation with single-site Co^{II} on SiO_2 by non-redox mechanism. *J. Catal.* **2015**, *322*, 24–37.

(51) Wang, L.; Chen, J.; Watanabe, H.; Xu, Y.; Tamura, M.; Nakagawa, Y.; Tomishige, K. Catalytic performance and characterization of Co-Fe bcc alloy nanoparticles prepared from hydrotalcite-like precursors in the steam gasification of biomass-derived tar. *Appl. Catal. B Environ.* **2014**, *160–161*, 701–715.

(52) Velu, S.; Suzuki, K.; Gopinath, C. S.; Yoshida, H.; Hattori, T. XPS, XANES and EXAFS investigations of $CuO/ZnO/Al_2O_3/ZrO_2$ mixed oxide catalysts. *Phys. Chem. Chem. Phys.* **2002**, *4*, 1990–1999.

(53) Biesinger, M. C.; Payne, B. P.; Grosvenor, A. P.; Lau, L. W. M.; Gerson, A. R.; Smart, R. S. C. Resolving surface chemical states in XPS analysis of first row transition metals, oxides and hydroxides: Cr, Mn, Fe, Co and Ni. *Appl. Surf. Sci.* **2011**, *257*, 2717–2730.

(54) Fierro, G.; Jacono, M. Lo; Inversi, M.; Dragone, R.; Porta, P. TPR and XPS study of cobalt – copper mixed oxide catalysts : Evidence of a strong Co–Cu interaction. *Top. Catal.* **2000**, *10*, 39–48.

(55) Biesinger, M. C.; Lau, L. W. M.; Gerson, A. R.; Smart, R. S. C. Resolving surface chemical states in XPS analysis of first row transition metals, oxides and hydroxides: Sc, Ti, V, Cu and Zn. *Appl. Surf. Sci.* **2010**, *257*, 887–898.

CHAPTER 5 WELL-DEFINED MULTI-METAL CATALYSTS FOR FURANIC RING-OPENING: SCREENING AND ALD EQUIPMENT DESIGN

Parts of this chapter are adapted from the published article, Sulmonetti, T. P.; Hu, B.; Lee, S.; Agrawal, P. K.; Jones, C. W. Reduced Cu−Co−Al mixed metal oxides for the ring-opening of furfuryl alcohol to produce renewable diols. *ACS Sustain. Chem. Eng.* **2017**, *5*, 8959-8969, with permission from American Chemical Society. DOI: 10.1021/acssuschemeng.7b01769.[1]

5.1 Introduction

As demonstrated in the above chapters, utilizing multi-metal catalysts can improve the selectivity and activity towards desired products, especially when dealing with highly oxygenated compounds such as FAL. The above investigations dealt with creating multi-metal systems derived from LDH precursors, which resulted in highly dispersed, porous, and thermally stable MMO materials, which could promote various hydrodeoxygenation chemistries after reduction. Along with these advantages, LDH materials are easy to synthesize and tune by various metal additions; however, the resulting complex structures make it difficult to fully understand the catalytic reaction mechanisms and the specific active sites produced after reduction.[2,3] The major complexities are due to the various interactions with each metal and multiple oxidation states in the system, making it problematic to ascertain active sites. Therefore, the motivation of this investigation is to stray away from hydrotalcite derived materials and create a process to synthesize

compositionally related materials that are more well-defined, multi-metal catalysts for the ring-opening of furanics.

Recent developments in catalysts synthesis, especially in the field of ALD and molecular layer deposition (MLD), have resulted in more advanced control of metal-metal or metal-support interactions. [4] ALD refers to the deposition of an inorganic substrate onto the surface via a self-limiting surface reaction, while MLD refers to the deposition of an organic or organic-inorganic hybrid substrate. In the field of metal catalysis, ALD is the prevalent method in depositing well-controlled metal precursors to create either metal/metal oxide films or nanoparticles. In general, ALD is a cyclic technique consisting of 4 basic steps: 1) exposure of the substrate surface to volatilized precursor resulting in precursor chemisorption; 2) purging of excess precursor through inert gas or vacuum; 3) exposure of the substrate to reactive gas (H_2, O_2, H_2O, etc.) resulting in reaction with adsorbed precursor; 4) purging of excess reactive gas through inert gas or vacuum.[4–7] Depending on the affinity of the metal atom and substrate the metal deposition could be through film growth or island growth (nanoparticles). A lot of parameters can be varied, such as the metal precursor, precursor temperature, substrate temperature, reactive gas utilized, etc., to achieve numerous morphologies and oxidation states of the metal particles on the surface of the substrate.

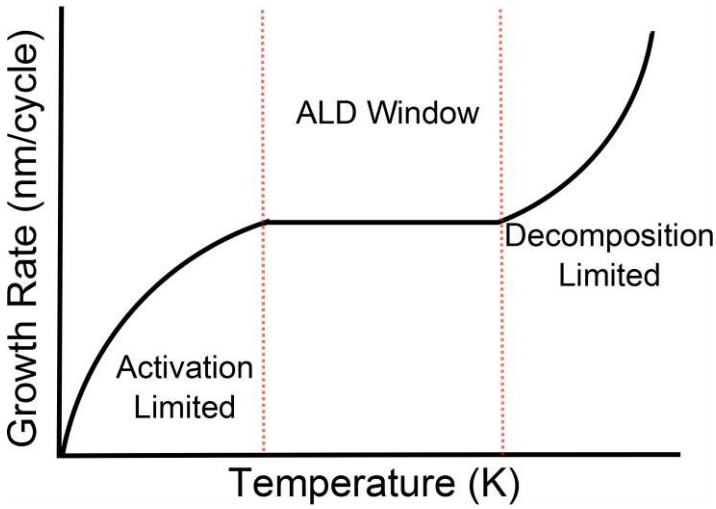

Figure 5.1 – Generalized deposition concept displaying growth rate vs substrate temperature

It is important to also distinguish ALD with chemical vapor deposition (CVD), which is a method that involves the decomposition of the precursor resulting in a non-self-limiting reaction. Figure 5.1 displays the growth rate versus substrate temperature indicating there is an optimum self-limiting growth window with constant growth rate per cycle in between activation limited growth and decomposition limited growth (CVD).[8] As a result, precursor choice and design are integral parts in conducting ALD experiments. To deposit a metal species on a substrate, the metal precursor must be volatile (contain a vapor pressure at room temperature), and have a sufficient decomposition temperature (above 200 °C), which increases the probability of a larger ALD window. Examples of precursors used in the past for base metal and precious metal deposition include bis(cyclpentadienyl)ruthenium(II), iridium(III) acetylacetonate, platinum(II) acetylacetonate, ferrocene, cobaltocene, Tris(2,2,6,6-tetramethyl-3,5-heptanedionenate)cobalt(III), copper (II) acetylacetonate, copper(II)-1,1,1,5,5,5-hexafluro-2,4-pentanedionate.[4,5,8–13]

Traditionally, ALD is used for film deposition of a metal on a flat substrate such as a circuit board or an electrode; however, depositing metal species on nanopowders introduces many more challenges, including internal diffusion through pores and uniform mixing. Many types of reactors have been constructed to investigate the deposition onto porous oxide particles such as Al_2O_3 and SiO_2.[5,14] Furthermore, some of these reactors include complex agitation systems or fluidized beds that allow for better mass transfer of the volatile precursor. However, the simplest, proven reactor configuration consists of a static bed of particles that can be heated, and the precursors must diffuse through the bed and pores to coat the surface.[5] This design is best conducted under vacuum < 1 Torr with a small catalyst bed to minimize diffusion times. The main flaw in the static bed design is scalability, but it is well suited for laboratory scale practices on the orders of 1 g or less. Gorte et al. developed a lab scale version of a static bed ALD equipment, and the equipment built in this dissertation was based on that design.[15] This system has previously been used to conduct ALD of ZrO_2 on Pd/CeO_2[16] and Pd/Al_2O_3[17] and iron oxide on Al_2O_3.[18] A more detailed discussion on the design and construction are included in the sections below.

A few ALD prepared catalysts have been studied for the conversion of furanic compounds, but due to the infancy of the technique, it has not been fully exploited for various furanic chemistries especially hydrogenolysis. One of the few examples is the coating of supported metal particles with an oxide layer to improve the stability in aqueous phase hydrogenation. Base metals, such as Cu, are more economical than precious metals, but these metals can suffer from irreversible deactivation such as sintering and leaching. Consequently, a few investigations looked into coating Cu nanoparticles with Al_2O_3 through ALD, which resulted in highly conformal alumina coatings over the metal

particles.[5,19–21] A heat treatment after ALD resulted in a porous alumina coatings, allowing for reactants to diffuse through the oxide to the metallic Cu particle. Though the ALD treated catalysts were slightly less in active than the traditional supported Cu catalysts when investigating FUR hydrogenation in liquid butanol, after catalyst regeneration it was clear that ALD had a positive impact. The ALD catalyst was able to be regenerated to its initial activity, while the non-ALD Cu catalyst continued to lose initial activity after regeneration.[19] This provides evidence that the ALD treatment hinders irreversible deactivation mechanisms such as sintering and leaching. Though not prepared through ALD, a more recent study has utilized carbon coated Pd and Cu nanoparticles to significantly enhance the stability of the catalysts when conducting liquid phase hydrogenation of FUR.[22] This study provides further evidence that utilizing an overcoat may control the stability of base metals supported on oxides.

Marshall et al. further utilized this technique by coating supported Pd nanoparticles with Al_2O_3.[23] By varying the ALD cycles the thickness of the alumina coat has been controlled, and the investigations suggest that as coating thickness increased the selectivity to furan increases, when investigating the hydrogenation of FUR in the vapor phase. This may be due to the restriction of FUR adsorbing on the step sites of Pd nanoparticles.[23] Additionally, the ALD method has been applied to a Co/TiO_2 system, where TiO_2 has been coated onto the Co supported matrix using ALD of $TiCl_4$.[24] Interestingly, these catalysts are active for the ring-opening of FAL to 1,5-PD through the same pathway as the Cu-Co-Al catalysts described in chapter 4.[24,25]

ALD prepared catalysts have many advantages, and they have become more attractive for various furanic chemistries. Therefore, the goal was to design and construct

an ALD testing system to synthesize various types of multi-metal catalysts for the selective conversion of FUR or FAL. It allowed this project to stray away from the complex MMO systems in the previous chapter; however, insight gained from the MMO catalysts provided this study with initial multi-metal combinations for specific chemistries. For example, synthesizing Cu-Co catalysts through ALD to conduct ring-opening experiments and probe the mechanism would be an initial project goal. The self-limiting ALD method would allow for the preparation of well-defined catalysts that can make it easier to understand the mechanism of FAL ring-opening. This synthesis method would reduce the complexity brought on by the co-precipitation method, and additional experiments such as *in situ* FTIR or HREELS experiments could be conducted. Consequently, this chapter lays the groundwork for constructing an ALD apparatus and conducting support screening studies on traditionally prepared catalysts.

5.2 Experimental Procedure

5.2.1 Materials and Chemicals

Furfuryl alcohol (98% purity) was purchased from Sigma Aldrich, vacuum distilled, and then stored in inert atmosphere before using in reactions. $Co(NO_3)_2 \cdot 6H_2O$ (99% purity), $Cu(NO_3)_2 \cdot 3H_2O$ (99% purity), ethanol (ACS Grade, 99.5%), and dodecane (99% purity) were purchased from Sigma Aldrich. Lastly, all other chemicals were used as is without any further purification.

Tetraethyl orthosilicate (TEOS) (99.99%), poly(ethylene glycol)-blokc-poly(propylene glycol)-block-poly(ethylene glycol) (Pluronic P-123, Mn ~5,800), citric acid (99.5%), aluminum isopropoxide (>98%), titanium ethoxide (technical grade, ~90%)

were purchased from Sigma Aldrich, and HCl (1.0N solution) was purchased from Alfa Aesar.

5.2.2 Catalysts Synthesis

5.2.2.1 Oxide Support Synthesis

The mesoporous SiO_2 support was synthesized through a templating method, and the resulting oxide is referred to as SBA-15.[26] A solution of 12 g of Pluronic P-123 (block co-polymer), 60 mL of HCl, and 318 mL of DI water were stirred in an 1000 mL Erlenmeyer flask for 3 hours. Then, 23.23 g of TEOS was added to the solution and stirred for 20 hours at 40 °C. A white precipitant was formed and then this solution was heated to 100 °C for 24 hours without stirring. After the aging, the solution was quenched by DI water, and then filtered. The precipitant was washed with approximately 1.5 L of DI water. After washing, the material was dried in an over at 75 °C overnight. The last step involved a calcination treatment with the following program: 1. ramped to 200 °C at 1.2 °C/min and soaked for 1 hour; 2. ramped to 550 °C and soaked for 12 hours.

The mesoporous Al_2O_3 material was prepared through a templating method similar to a previously reported procedure.[27] Approximately 16.02 g of Pluronic was dissolved in 400 mL of ethanol in a 1000 mL Erlenmeyer flask, and then 40.802 g of aluminium isopropoxide, 10.03 g of citric acid, and 30 mL of HCl were added into the ethanol solution. This solution was stirred vigorously for 5 hours at room temperature. Next, the ethanol was evaporated at 60 °C for 48 hours in a silicone oil bath. Finally, the resulting solid material was subjected to a calcination treatment with the following procedure: ramped to 600 °C at 1 °C/min and held for 4 hours.

The TiO_2 support was synthesized through a soft templating method similar to a previous reported method with small changes.[28] In a 100 mL beaker, 16.4 mL of HCl was added dropwise to 20.9 g of titanium(IV) ethoxide under vigorous stirring. In a 200 mL beaker, 7.595 g of Pluronic P-123 was dissolved in 82.3 mL of butanol. Next, the butanol solution was added to the Ti solution and stirred for 3 hours at room temperature. The solvent was then evaporated overnight at 60 °C. The resulting material was then placed in a calcination oven and underwent a thermal treatment: 1. ramped to 200 °C at 1.2 °C/min and soaked for 1 hour; 2. ramped to 550 °C at 1.2 °C min and held for 6 hours.

The $MgAlO_x$ support was prepared by thermally treating a LDH material. This material was prepared by Micaela Taborga and utilized for syngas conversion for higher alcohols.[29] The experimental procedure was also very similar to the outlined procedure in Chapter 2 section 2.2; however, the metal salts used were $Mg(NO_3)_2$ and $Al(NO_3)_3$, and the pH was set at 9.5 and a 48 hour aging time.

5.2.2.2 Wetness Impregnation on Various Supports

The Cu and Co nitrate salts were added into a solution equalling the pore volume of the support material. Once the salts were dissolved, the solution was added to the oxide support dropwise. After a few drops the material was vigorously stirred, and then more drops were added. This cycle was repeated until all the nitrate solution was added. Then these impregnated catalysts were placed in an oven at 60 °C overnight. The dried catalysts were then subjected to a calcination treatment at 400 °C for 4 hours with a 5 °C/min ramp rate.

5.2.2.3 ALD Prepared Catalysts

A few test ALD experiments were conducted to investigate the instrument behavior. One example test procedure is explained below in an attempt to deposit metallic Cu on TiO_2. The metal precursor was $Cu(acac)_2$ and the substrate was TiO_2. The substrate was heated to 250 °C and held under vacuum overnight to remove any adsorbates. After the desorption step, the sample was cooled to 225 °C. Then the metal precursor test tube was evacuated before heating to 140 °C. Once the whole system equilibrated (pressure: ~$1x10^{-3}$ Torr), the pulsing cycles began. One cycle consisted of the following. The vacuum valve was closed and the precursor valve was opened for 10 s, which resulted in an increase in pressure of about 0.2 Torr. After the sharp increase, the pressure began to decrease over time indicating that the precursor may be adsorbing onto the substrate. After 2 min, the system was evacuated to remove the remaining precursor. Once the pressure reached equilibrium, a pulse of H_2 was introduced into the substrate (~ 200 torr). After 5 min, the whole system was evacuated, which completed a cycle. The cycle was repeated 25 times.

5.2.3 Reaction Studies

Liquid phase batch reactions were performed in a 160 mL stainless steel Parr autoclave with a Teflon liner. The catalysts were reduced under 60 mL/min H_2 (Airgas, UHP) to 400 ˚C (unless stated otherwise) with a ramp rate of 5 °C/min, then subsequently held for 1 h. Once the reduction was completed, the bed was cooled under H_2 to room temperature. This passivation step was conducted due to the pyrophoric nature of the catalyst after reduction. For a typical reaction, 0.5 g of furfuryl alcohol, ~ 0.125 g of dodecane (internal standard), 30 mg of catalyst and 50 mL of solvent were added into the

reactor. The reactor was purged 5 times with N_2 and heated to reaction temperature under N_2 to avoid reactions during heat up. Once the reaction temperature 150 °C was achieved, the reactor was purged 5 times with H_2, and stirrer was turned to 800 RPM, which was determined to be sufficient to be free of external mass transfer limitations. As a general note, there was typically a 5 min period until the reactor temperature equilibrated at the desired value. Samples were obtained through a sampling port, and less than 300 µL were acquired for each sample to minimize reaction volume loss. The aliquots were filtered and analyzed through an Agilent 7890A GC fitted with an auto sampler. Selectivity and conversion were determined by the internal standard method, and all carbon balances closed within 5%.

5.3 Results and Discussion

5.3.1 ALD Design and Construction

As described in the introduction, there are many different types of ALD reactors that can perform the self-limiting deposition of precursors on powdered oxide materials. Many of the academic reactors constructed either utilize a fluidize bed or a packed bed, and almost all of these reactors operate under moderate to high vacuum.[5,14] One of the more established reactor designs consists of the substrate in a fixed bed under static vacuum, whereby a volatilized precursor diffuses through the reactor and deposits on the surface of the substrate.[15–18] Below, Figure 5.2 shows the schematic of a two-precursor static ALD system built at Georgia Tech.

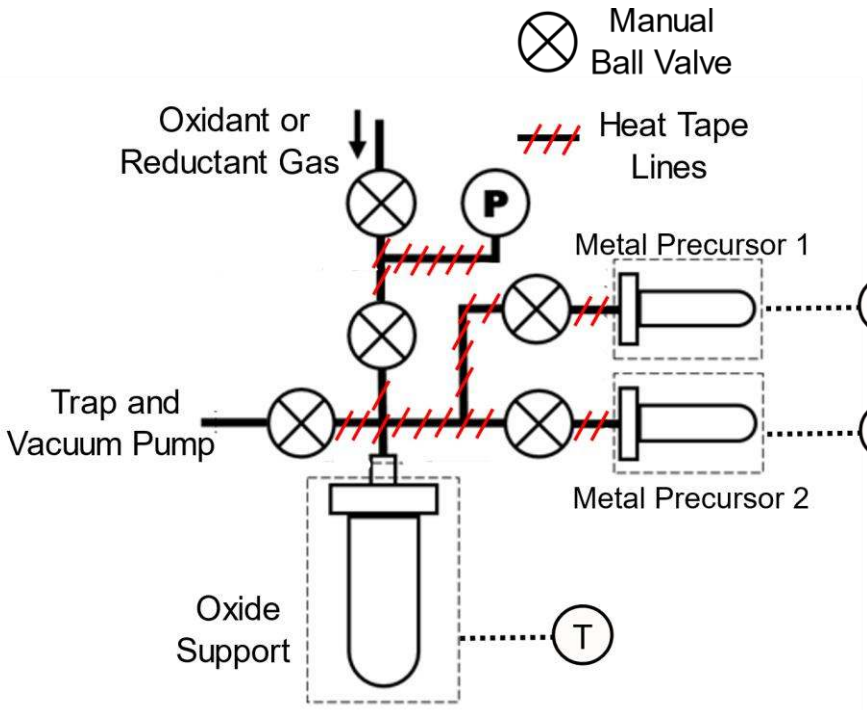

Figure 5.2 – Schematic of ALD equipment containing two precursor zones for multi-metal catalyst synthesis.

For optimum results the equipment must be able to pull vacuum on the order of $1x10^{-3}$ torr, which can allow for faster diffusion of the metal precursor from the precursor zone to the substrate. Additionally, the equipment, not including the substrate and precursor zone, must be able to sustain temperatures of 200 °C. To abide by these guidelines, the equipment was built using Swagelok® VCR, Ultra-Torr fittings, and ball valves. The precursor zones were enclosed in insulated aluminum boxes and heated utilizing a strip heater. The test tubes were connected through Swagelok® Ultra-Torr fittings to minimize leaks. A furnace that can achieve max temperatures of approximately 600 °C was utilized for the heating element of the substrate tube. To minimize the condensation of the volatile precursor in the lines, each valve and the stainless-steel lines were wrapped with heating tape and insulation and heated to temperatures at least 5 °C higher than the precursor

temperature. The reactive/inert gases were introduced through another ball valve from the top of the apparatus. A gas manifold system was created to introduce various gases, including O_2, H_2, air, and Ar, with ease and additional safety.

An attempt at depositing metallic Cu onto TiO_2 was tried, which mimicked previous studies, and is outlined in the experimental section.[12,30] $Cu(acac)_2$ was utilized as the precursor, and the reactive gas source was H_2, which would hopefully result in the deposition of metallic Cu particles. However, after conducting 25 pulses, XPS and XRD did not detect any Cu deposition even though visually the TiO_2 changed color (white to grey) post-ALD. It was possible that the amount of Cu deposited after pulsing was very small and undetectable under XRD and XPS. This does suggest the need to investigate more thoroughly the growth rate and precursor choices.

5.3.2 Screening of Various Supports

In tandem with constructing the ALD system, it was important to investigate different oxide supports for potential use in ring-opening. Since these experiments were straying away from hydrotalcite-based systems with high weight percent of reducible metals (Cu+Co ~ 75 wt %), the oxide supports may have played a larger role in the ring-opening chemistry. Consequently, synthesizing a few Cu-Co catalysts through wetness impregnation between 5-10 wt% metal was viewed to be a good starting point to avoid conducting reactions on possibly inactive catalysts. Multiple supports were synthesized including Al_2O_3, TiO_2, SiO_2 (SBA-15), and $MgAlO_x$ and impregnated with Cu and Co (Cu:Co – 1:4).

Table 5.1 – N_2 physisorption results for each support prior to metal impregnation.

Catalyst	Surface Area (m^2/g)[a]	Pore Volume (cm^3/g)	Pore Size (Å)[b]
SiO_2 (SBA-15)	933	1.04	64
Al_2O_3	197	0.50	90
$MgAlO_x$	107	0.38	195
TiO_2	38	0.09	82

[a]Brunauer-Emmett-Teller (BET) Surface Area. [b]Barett-Joyner-Halenda (BJH) Pore Size

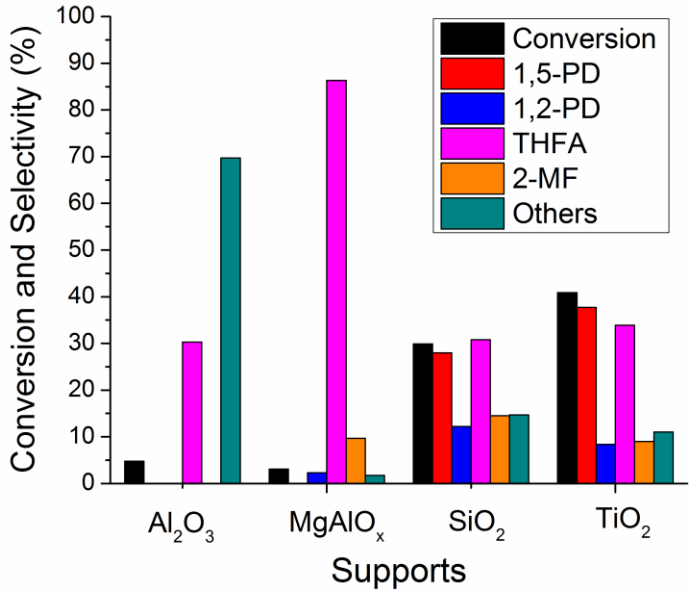

Figure 5.3 – Conversion and selectivity of FAL reaction over various 5 wt% Cu_1Co_4/Support (*Al_2O_3 support contained 10 wt% of Cu_1-Co_4). Temperature: 150 °C, H_2 pressure: 4 MPa, Time: 3 h, Catalyst: 50 mg, FAL: 500 mg, ethanol: 50 mL.

The catalysts were then reduced prior to the reaction at 400 °C for 1 hour before being charged into the batch reactor. Interestingly, the catalysts did not require a passivation step post-reduction unlike the MMO catalysts studied in Chapter 4. To this end, there was not an additional reduction step conducted in the batch reactor prior to reaction. Each catalyst was tested under similar conditions described in the experimental section, and the results are displayed in Figure 5.3. After 3 h of reaction, there were clear

distinctions between each catalyst regarding activity. Both TiO_2 and SiO_2 demonstrated the ability to convert FAL, while the other supports showed little to no conversion of FAL. The selectivity towards diols products for TiO_2 and SiO_2 was roughly 45% with 1,5-PD being the predominate diol. The other two supports displayed little to no selectivity towards diol production at low conversions. Furthermore, the Al_2O_3 produced many products that were unidentifiable, and the multiple peaks at high GC retention times suggested the formation of coupling/oligomer products. This may have been a result of a large amount of acid sites located on the surface of the Al_2O_3, which have previously shown to be active sites for humin and oligomer formation.[31] These oligomers or humins forming could have deposited on the catalyst, blocked active sites, and caused a reduction in activity.

Although selectivities between $Al_2O_3/MgAlO_x$ and SiO_2/TiO_2 cannot be compared due to the differences in conversion, it was clear that TiO_2 and SiO_2 may have more potential to use as supports for ALD synthesized catalysts for this reaction. The selectivity towards diols products for TiO_2 and SiO_2 was roughly 45%, with 1,5-PD being the predominate diol product. There were many possible hypotheses that describe why these supports lead to diol products. One possible reason for the TiO_2 activity could be a result of a strong metal-support interaction (SMSI), which caused the TiO_2 to partially reduce or partially encompass the metal particles that form after reduction. These observations were seen with different thermal treatments of a Co/TiO_2 catalyst.[25] Typically SMSI effects are not observed on SiO_2; therefore, the possible reason for a higher activity may be due to a higher dispersion of metal sites on the high surface area support. However, these hypotheses have not been validated through other characterizations. Consequently, other factors such as metal particle size, dispersion, acid/base concentration, etc. could also play

a role in the diverse activity between supports. Therefore, many other studies need to be conducted to validate the oxide support findings and then transition to ALD.

5.4 Conclusion

A static ALD equipment was designed and construction to synthesize various well-defined multi-metal catalysts for the ring-opening of FAL to diol products. The construction of this equipment was in response to the complexities that arose, including indeterminate active sites, when investigating Cu-Co-Al MMO materials for ring-opening. A versatile static ALD system was constructed and briefly tested, and the equipment can include two different precursors and utilize various reactive gases. In tandem with building the equipment, initial support screening was conducted to avoid depositing metals on a potentially inactive support. Multiple oxide supports including Al_2O_3, TiO_2, SiO_2 (SBA-15), and $MgAlO_x$ were impregnated with Cu-Co (high Co loading) using wetness impregnation. These catalysts were then tested for the liquid phase ring-opening of FAL, and TiO_2 and SiO_2 were identified as promising active supports for ring-opening (~45% diol selectivity at 150 °C). Although there could be many reasons for the changes in activity between supports, this screening study provided the benchmarks for preparing ALD catalysts with Cu-Co that will be active for the ring-opening of furanics.

5.5 References

(1) Sulmonetti, T. P.; Hu, B.; Lee, S.; Agrawal, P. K.; Jones, C. W. Reduced Cu−Co−Al mixed metal oxides for the ring-opening of furfuryl alcohol to produce renewable diols. *ACS Sustain. Chem. Eng.* **2017**, *5*, 8959-8969.

(2) Sulmonetti, T. P.; Hu, B.; Ifkovits, Z. P.; Lee, S.; Agrawal, P. K.; Jones, C. W. Vapor Phase Hydrogenolysis of Furanics Utilizing Reduced Cobalt Mixed Metal Oxide Catalysts. *ChemCatChem* **2017**, *9*, 1815–1823.

(3) Sulmonetti, T. P.; Pang, S. H.; Taborga Claure, M.; Lee, S.; Cullen, D. A.; Agrawal, P. K.; Jones, C. W. Vapor phase hydrogenation of furfural over nickel mixed metal oxide catalysts derived from layered double hydroxides. *Appl. Catal. A Gen.* **2016**, *517*, 187–195.

(4) Van Bui, H.; Grillo, F.; van Ommen, R. Atomic and molecular layer deposition: Off the beaten track. *Chem. Commun.* **2017**, *53*, 45–71.

(5) Oneill, B. J.; Jackson, D. H. K.; Lee, J.; Canlas, C.; Stair, P. C.; Marshall, C. L.; Elam, J. W.; Kuech, T. F.; Dumesic, J. A.; Huber, G. W. Catalyst design with atomic layer deposition. *ACS Catal.* **2015**, *5*, 1804–1825.

(6) George, S. M.; Ott, A. W.; Klaus, J. W. Surface chemistry for atomic layer growth. *J. Phys. Chem.* **1996**, *100*, 13121–13131.

(7) George, S. M. Atomic layer deposition: an overview. *Chem. Rev.* **2009**, *110*, 11–129.

(8) Knisley, T. J.; Kalutarage, L. C.; Winter, C. H. Precursors and chemistry for the atomic layer deposition of metallic first row transition metal films. *Coord. Chem. Rev.* **2013**, *257*, 3222–3231.

(9) Koponen, S. E.; Gordon, P. G.; Barry, S. T. Principles of precursor design for vapour deposition methods. *Polyhedron* **2016**, *108*, 59–66.

(10) Bernal Ramos, K.; Saly, M. J.; Chabal, Y. J. Precursor design and reaction mechanisms for the atomic layer deposition of metal films. *Coord. Chem. Rev.* **2013**, *257*, 3271–3281.

(11) Diskus, M.; Nilsen, O.; Fjellvåg, H. Thin films of cobalt oxide deposited on high aspect ratio supports by atomic layer deposition. *Chem. Vap. Depos.* **2011**, *17*, 135–140.

(12) Alnes, M. E.; Monakhov, E.; Fjellvåg, H.; Nilsen, O. Atomic layer deposition of copper oxide using copper(II) acetylacetonate and ozone. *Chem. Vap. Depos.* **2012**, *18*, 173–178.

(13) Dai, M.; Kwon, J.; Halls, M. D.; Gordon, R. G.; Chabal, Y. J. Surface and interface processes during atomic layer deposition of copper on silicon oxide. *Langmuir* **2010**, *26*, 3911–3917.

(14) Longrie, D.; Deduytsche, D.; Detavernier, C. Reactor concepts for atomic layer deposition on agitated particles: A review. *J. Vac. Sci. Technol.* **2014**, *32*, 10802.

(15) Yu, A. S.; Kungas, R.; Vohs, J. M.; Gorte, R. J. Modification of SOFC Cathodes by Atomic Layer Deposition. *J. Electrochem. Soc.* **2013**, *160*, F1225–F1231.

(16) Onn, T. M.; Arroyo-Ramirez, L.; Monai, M.; Oh, T. S.; Talati, M.; Fornasiero, P.;

Gorte, R. J.; Khader, M. M. Modification of Pd/CeO_2 catalyst by atomic layer deposition of ZrO_2. *Appl. Catal. B Environ.* **2016**, *197*, 280–285.

(17) Onn, T. M.; Zhang, S.; Arroyo-Ramirez, L.; Chung, Y. C.; Graham, G. W.; Pan, X.; Gorte, R. J. Improved thermal stability and methane-oxidation activity of Pd/Al_2O_3 catalysts by atomic layer deposition of ZrO_2. *ACS Catal.* **2015**, *5*, 5696–5701.

(18) Onn, T. M.; Monai, M.; Dai, S.; Arroyo-Ramirez, L.; Zhang, S.; Pan, X.; Graham, G. W.; Fornasiero, P.; Gorte, R. J. High-surface-area, iron-oxide films prepared by atomic layer deposition on γ-Al_2O_3. *Appl. Catal. A Gen.* **2017**, *534*, 70–77.

(19) O'Neill, B. J.; Jackson, D. H. K.; Crisci, A. J.; Farberow, C. A.; Shi, F.; Alba-Rubio, A. C.; Lu, J.; Dietrich, P. J.; Gu, X.; Marshall, C. L.; et al. Stabilization of copper catalysts for liquid-phase reactions by atomic layer deposition. *Angew. Chem.* **2013**, *52*, 13808–13812.

(20) Alba-Rubio, A. C.; O'Neill, B. J.; Shi, F.; Akatay, C.; Canlas, C.; Li, T.; Winans, R.; Elam, J. W.; Stach, E. A.; Voyles, P. M.; et al. Pore structure and bifunctional catalyst activity of overlayers applied by atomic layer deposition on copper nanoparticles. *ACS Catal.* **2014**, *4*, 1554–1557.

(21) Héroguel, F.; Le Monnier, B. P.; Brown, K. S.; Siu, J. C.; Luterbacher, J. S. Catalyst stabilization by stoichiometrically limited layer-by-layer overcoating in liquid media. *Appl. Catal. B Environ.* **2017**, *218*, 643–649.

(22) Pham, H. N.; Anderson, A. E.; Johnson, R. L.; Schwartz, T. J.; O'Neill, B. J.; Duan, P.; Schmidt-Rohr, K.; Dumesic, J. A.; Datye, A. K. Carbon overcoating of supported metal catalysts for improved hydrothermal stability. *ACS Catal.* **2015**, *5*, 4546–4555.

(23) Zhang, H.; Gu, X. K.; Canlas, C.; Kropf, A. J.; Aich, P.; Greeley, J. P.; Elam, J. W.; Meyers, R. J.; Dumesic, J. A.; Stair, P. C.; et al. Atomic layer deposition overcoating: Tuning catalyst selectivity for biomass conversion. *Angew. Chem.* **2014**, *53*, 12132–12136.

(24) Lee, J.; Jackson, D.; Li, T.; Winans, R. E.; Dumesic, J.; Kuech, T.; Huber, G. Enhanced stability of cobalt catalysts by atomic layer deposition for aqueous-phase reactions. *Energy Environ. Sci.* **2014**, *7*, 1657–1660.

(25) Lee, J.; Burt, S. P.; Carrero, C. A.; Alba-Rubio, A. C.; Ro, I.; O'Neill, B. J.; Kim, H. J.; Jackson, D. H. K.; Kuech, T. F.; Hermans, I.; et al. Stabilizing cobalt catalysts for aqueous-phase reactions by strong metal-support interaction. *J. Catal.* **2015**, *330*, 19–27.

(26) Zhao, D.; Feng, J.; Huo, Q.; Melosh, N.; Fredrickson, G. H.; Chmelka, B. F.; Stucky, G. D. Triblock copolymer syntheses of mesoporous silica with periodic 50 to 300 angstrom pores. *Science.* **1998**, *279*, 548–552.

(27) Yuan, Q.; Yin, A.-X.; Luo, C.; Sun, L.-D.; Zhang, Y.-W.; Duan, W.-T.; Liu, H.-C.; Yan, C.-H. Facile synthesis for ordered mesoporous gamma-aluminas with high thermal stability. *J. Am. Chem. Soc.* **2008**, *130*, 3465–3472.

(28) Choi, S. Y.; Mamak, M.; Coombs, N.; Chopra, N.; Ozin, G. a. Thermally stable two-dimensional hexagonal mesoporous nanocrystalline anatase, meso-nc-TiO_2: Bulk and crack-free thin film Morphologies. *Adv. Funct. Mater.* **2004**, *14*, 335–344.

(29) Taborga Claure, M.; Lee, L. C.; Goh, J. W.; Gelbaum, L. T.; Agrawal, P. K.; Jones, C. W. Assessing C_3–C_4 alcohol synthesis pathways over a MgAl oxide supported K/MoS_2 catalyst via $^{13}C_2$-ethanol and $^{13}C_2$-ethylene co-feeds. *J. Mol. Catal. A Chem.* **2016**, *423*, 224–232.

(30) Gordon, P. G.; Kurek, a.; Barry, S. T. Trends in copper precursor development for CVD and ALD applications. *ECS J. Solid State Sci. Technol.* **2015**, *4*, N3188–N3197.

(31) Nakagawa, Y.; Tamura, M.; Tomishige, K. Catalytic reduction of biomass-derived furanic compounds with hydrogen. *ACS Catal.* **2013**, *3*, 2655–2668.

CHAPTER 6 SUMMARY AND FUTURE DIRECTION

6.1 Summary

A summary of this dissertation with the major findings is presented below along with possible future directions.

6.1.1 Chapter 1: Introduction and Motivation

Prior art on furanic conversion demonstrates that single metal catalysts typically suffer from selectively or actively producing value-added products; however, the inclusion of an additional metal has shown promise in developing more efficient and potentially more economical reaction processes for generating products from biomass derivatives. Therefore, it is important to continue to investigate multi-metal catalyst platforms. MMOs derived from LDHs are presented as a potential route in creating active multi-metal catalysts for furanic compound conversion. Few studies have tried to exploit these catalysts promising properties including high dispersion, high porosity, high thermal stability, and tunability. Consequently, it is determined that investigating various MMO catalysts is a potential opportunity for creating active and selective catalysts for furanic conversion.

6.1.2 Chapter 2: Hydrogenation Utilizing Ni Based MMOs

Screening of multiple Ni based MMO catalysts derived from LDH materials was conducted, and upon reduction these catalysts were demonstrated to be active for the vapor phase hydrogenation of FUR to FAL and THFA. More specifically, a variety of Ni-Mg-Al and Ni-Co-Al catalysts with varying Ni:Mg and Ni:Co ratios were synthesized and

evaluated through multiple characterization techniques as well as in a vapor phase flow reactor. It was determined that varying between Ni-Mg-Al and Ni-Co-Al catalysts did not have a significant impact on hydrogenation selectivities at high conversion (>90%). The catalysts obtained approximately 75%-85% selectivity towards FAL and THFA combined, although the Co containing catalysts displayed the highest activity per gram and per site (measured by CO adsorption). Further investigation of the reduced Ni-Co catalysts using STEM and EELS suggested the formation of bimetallic particles, which facilitated the increase in activity. This study broadened our understanding of the structure of MMO materials after reduction, including both the reaction performance and the electronic environment.

6.1.3 Chapter 3: Hydrogenolysis Utilizing Co-Fe Based MMOs

Co-Fe-Al MMOs derived from LDH materials were evaluated for the side-chain hydrogenolysis of FAL to 2-MF in a vapor phase flow reactor. MMO materials with various Co:Fe:Al ratios were synthesized, along with a Co-Al and Co-Fe MMO materials. After *in situ* reduction, all catalysts except Co-Fe were active and selective for the production of 2-MF; moreover, the Fe addition in the Co-Al matrix displayed a positive impact on both selectivity and activity (60% → 82%: 2-MF selectivity). *In situ* spectroscopic experiments were used to determine the electronic and coordination environment of both reducible species in the Co-Fe-Al matrix. *In situ* XAS suggested that the Fe was well-dispersed after reduction and integrates itself in the Co lattice creating an alloy. This electronic interaction may have resulted in the enhancement of 2-MF production.

6.1.4 Chapter 4: Ring-Opening Utilizing Cu-Co Based MMOs

Building off past MMO studies, Cu-Co-Al MMOs derived from LDH materials were synthesized and then tested for ring-opening activity towards diols from furanics. It was demonstrated by multiple techniques that even small amounts of Cu significantly reduced the temperature at which the oxide matrix uptakes H_2, resulting in an increase in metallic species compared to the base Co-Al case. Although the Cu may have not resulted in a change of furanic adsorption, it increased activity more than 20x at high conversion due to increase surface metallic species. The reaction pathways were investigated, and it was determined that the unsaturated or partial saturated furanic molecules (FAL, 2-MF, and furan) was active for ring-opening instead of fully saturated molecules (THFA, 2-MTHF, and THF). Ultimately, a yield of about 44% towards 1,5-PD was obtained (total diol yield of 62%) at 160 °C and 4 MPa of H_2, which was the highest reported yield towards 1,5-PD using non-precious metals at the time of publication.

6.1.5 Chapter 5: Development of ALD Equipment for Furanic Conversion

Though reduced MMOs were recognized in this dissertation as effective catalysts for various furanic chemistries, there were many limitations in the characterization of the active sites or size of metal particles in these materials. This sparked the idea to create well-defined multi-metal systems by other methods such as ALD, while still utilizing similar multi-metal combinations. This method will help synthesize well-controlled multi-metal systems by varying metal precursors, deposition temperatures, and reactant gases. In this chapter, a home built ALD system was designed and constructed. Along with the construction of the ALD instrument, multiple supports impregnated with Cu-Co (wetness

impregnation synthesis) were tested for the ring-opening of FAL including TiO_2, Mg-Al oxide, Al_2O_3, and SiO_2. The results indicated that the metal domains on the TiO_2 and SBA-15 were active for ring-opening of FAL, while the other two supports were hardly active for FAL conversion. Through there may be many other factors that resulted in this finding, the screening study indicated the possibility of an active Cu-Co catalyst supported on an oxide such as TiO_2 and SiO_2.

6.2 Future Directions

6.2.1 Screening ALD Prepared Multi-Metal Catalysts for Ring-Opening

Chapter 5 gave a brief introduction to a new direction in catalytic furanic conversion, which involves designing and synthesizing well-defined multi-metal catalysts through ALD. Utilizing concepts gained in the MMO studies, ALD can help tune the catalyst structure and electronic state more precisely, allowing for increased ability to probe the mechanism behind ring-opening. Previously, support screening was conducted to determine which oxide support(s) would be a good candidate to investigate ring-opening with ALD-derived catalysts (SBA-15 and TiO_2). Additionally, validation studies were conducted on the ALD instrument, which shows promise in creating well-defined systems. However, there is much work to be done to complete this investigation.

It is important to determine optimum ALD conditions for both Cu and Co precursors. Cu has been widely studied in the ALD literature while depositing Co onto an oxide support is lacking throughout literature.[1,2] It is crucial to determine the temperature range where growth occurs and to evaluate the growth rate per cycle. After those factors are assessed, then different multi-metal catalysts can be synthesized through the controlled ALD

method. This study requires the synthesis of a variety of morphologies by changing the metal precursor doping order onto the oxide support. Each of these materials would be tested catalytically, and through other characterization techniques to create detailed structure-reactivity relationships. Ultimately, such studies will shed new light on the active sites for ring-opening of unsaturated furanics.

6.2.2 Ring-Opening of HMF Utilizing Reduced MMOs

Chapter 4 of this thesis described a process where reduced Cu-Co-Al MMO materials could ring-open FAL to mostly 1,5-PD, which was a useful diol for poly(ester) production. Though this is a promising route to make diols from renewable resources using non-precious metals, this reaction has not been applied to HMF, which may be able to produce 1,6-hexanediol (1,6-HD). 1,6-HD is an important value-added chemical since it is a precursor to making caprolactam, a monomer for nylon 6,6 production.[3] A few studies have investigated the ring-opening of HMF including an exploration of a reduced Ni-Co-Al material that shows high yields towards 1,2,6-hexanetriol, but produces insignificant amounts of 1,6-HD.[4] Additionally, as described in the introduction, Rh-Re/SiO_2 and a solid acid catalyst are utilized for the ring-opening of HMF and additional hydrogenolysis to create 1,6-HD.[3,5] Other literature reports include a two bed liquid phase flow reactor containing Pd/SiO_2 and Ir-ReO_x/SiO_2 where HMF is saturated by Pd and then subsequently is ring-opened by Ir-Re.[6] Lastly, a Pd/ZrP catalyst in a solution of formic acid, which acted as the hydrogen source, has achieved a yield of 44% at 140 °C.[7]

The above examples are the only investigations that have displayed promising yields towards 1,6-HD, which is possibly due to the extra complications associated with a more

reactive, oxygenated compound and a possible need for a multistep process.[8] To this end, I propose that multi-metal MMOs similar to those in chapter 4, be investigated for this reaction. The goal is to design a single catalyst or single catalytic process that ring-opens HMF (or its derivatives) to 1,2,6-hexanetriol, which subsequently undergoes selective hydrogenolysis to create 1,6-HD. This may require further alteration of the current MMO materials or alterations in the reaction conditions, such as including a solid acid catalyst along with the MMO materials.

6.2.3 Tandem Reaction: Coupled Furanics and Subsequent HDO

The goal of this direction would be to combine the findings in this dissertation, associated with hydrogenation and ring-opening on bifunctional catalysts, with supplementary chemistry. Aldol condensation is a well-studied reaction, and furfural-acetone coupling through aldol condensation is an emerging approach for chain extension to prepare drop-in fuels from biomass.[9,10] Dumesic et al. has demonstrated the ability to convert sugars into liquid alkanes in a four-step process that included aldol condensation of furans.[11] In their study, the Mg-Al MMOs derived from LDH materials facilitates aldol condensation, and the Pt/SiO_2-Al_2O_3 bifunctional catalyst conducts the hydrodeoxygenation. A few other studies have examined the chemistries of hydrodeoxygenation and furfural coupling. In terms of aldol condensation, Faba et al. has determined that the key catalyst parameter is the strength and type of the basic sites, and showed that a Mg-Zr mixed oxide produced the optimal amount of C_{13} products compared to Mg-Al and Ca-Zr metal oxides.[10] Further studies have shown that the addition of Pd modified the surface of the MMO, and significantly minimized catalyst deactivation with some decrease in C_{13} selectivity.[12,13] In regards to hydrodeoxygenation of coupled

products, a two-step process has been developed, which includes ring-opening using acetic acid and subsequent hydrodeoxygenation using Pd/C, H_2, $La(OTf)_3$, and acetic acid.[14] Very recently, Pt supported on various acidic supports has allowed researchers to observe ring-opening of the saturated condensate without using acetic acid. Pt metal dispersion along with strong acidity of the support played a key role in the alkane production, but also led to significant carbon deposition.[15]

To this end, I suggest the use of MMOs derived from LDH materials to facilitate both aldol condensation and ring-opening/hydrodeoxygenation. Along with the potential for bifunctional catalysts, the synthesis method produces highly porous materials; therefore, the large adducts created in these reactions will have little diffusion restrictions. This objective is divided into the following two sections: 1. designing a MMO for aldol condensation, and 2. designing a MMO for hydrodeoxygenation. Ultimately, one can conduct either a one-pot or continuous flow reaction process to create alkanes from FUR without the use of precious metals.

6.2.4 MOF-derived Catalysts for Furanic Conversion

Though much of this dissertation discusses the benefits of MMOs for furanic conversion and possible future direction in the MMO field, it is also critical to investigate other catalytic materials for these reactions in hopes to increase activity and selectivity. Embedding metal particles in a carbon matrix through the degradation of MOFs has been an increasingly attractive synthesis route for making catalytically active materials.[16] Unfortunately, most MOFs, without any posttreatment, tend to suffer from poor thermal, chemical stability, and water stability, which poses many challenges when converting

biomass directed compounds; however, MOFs typically benefit with high surface area, high tunability, and high metal site density.[17] Therefore, degrading the MOF crystal structure through a thermal posttreatment may increase stability while maintaining the MOF-derived benefits such as porosity, tunability, and site density. For example, pyrolyzing a MOF material in inert atmosphere will typically degrade the MOF crystal structure, leaving behind metal particles surrounded by carbon support/binder. This concept mimics the way MMOs are derived from LDHs, where a thermal treatment (reducing atmosphere) is conducted to yield well-dispersed metallic particles surrounded by an oxide support/binder (i.e. Al_2O_3). Subsequently, pyrolysis of MOFs can yield a thermally stable, highly porous, and chemical stable material with well-dispersed metal particles (oxide or metallic).

If these pyrolyzed materials are introduced to a reducing environment, metallic particles typically arise[16,17], which can result in an active catalyst for furanic hydrogenation or hydrogenolysis. To the best of our knowledge, there have been a few published studies on using MOFs as catalysts for furanic conversion, but no published research on utilizing pyrolyzed MOFs for furanic conversion.[16,17] Therefore, this task requires designing future experiments to probe how these materials will behave during hydrogenation reactions of FUR or FAL. The initial work includes screening several monometallic and bimetallic combinations such as Cu/C, Ni/C, Co/C, Fe/C, and their bimetallic mixtures, all derived from the same MOF. In the vapor phase, target product molecules include 2-MF or cyclopentanone, while in the liquid phase, the target molecules include 1,5-PD and/or 1,2-PD. After various screening tests, it is beneficial to conduct characterization studies into the catalyst's electronic environment and morphology. Key questions to answer include:

does each metal in the post-treated MOF interact (i.e. alloying)? What effect does pyrolysis temperature and/or reduction temperature have on particle size and/or distribution? Can a bifunctional catalyst be synthesized (i.e. metallic – oxide)? Lastly, can the changes in parameters and metals correlate to reactivity and selectivity?

6.3 References

(1) Knisley, T. J.; Kalutarage, L. C.; Winter, C. H. Precursors and chemistry for the atomic layer deposition of metallic first row transition metal films. *Coord. Chem. Rev.* **2013**, *257*, 3222–3231.

(2) Gordon, P. G.; Kurek, a.; Barry, S. T. Trends in copper precursor development for CVD and ALD applications. *ECS J. Solid State Sci. Technol.* **2015**, *4*, N3188–N3197.

(3) Buntara, T.; Noel, S.; Phua, P. H.; Melián-Cabrera, I.; de Vries, J. G.; Heeres, H. J. Caprolactam from renewable resources: catalytic conversion of 5-hydroxymethylfurfural into caprolactone. *Angew. Chem.* **2011**, *50*, 7083–7087.

(4) Yao, S.; Wang, X.; Jiang, Y.; Wu, F.; Chen, X.; Mu, X. One-Step conversion of biomass-derived 5-hydroxymethylfurfural to 1,2,6-hexanetriol over Ni–Co–Al mixed oxide catalysts under mild conditions. *ACS Sustain. Chem. Eng.* **2014**, *2*, 173–180.

(5) Buntara, T.; Noel, S.; Phua, P. H.; Melián-Cabrera, I.; Vries, J. G.; Heeres, H. J. From 5-Hydroxymethylfurfural (HMF) to Polymer Precursors: Catalyst Screening Studies on the Conversion of 1,2,6-hexanetriol to 1,6-hexanediol. *Top. Catal.* **2012**, *55*, 612–619.

(6) Xiao, B.; Zheng, M.; Li, X.; Pang, J.; Sun, R.; Wang, H.; Pan, X.; Wang, A.-Q.; Wang, X.; Zhang, T. Synthesis of 1,6-hexanediol from HMF over double-layered catalysts of Pd/SiO_2+Ir-ReO_x/SiO2 in a fixed-bed reactor. *Green Chem.* **2015**.

(7) Tuteja, J.; Choudhary, H.; Nishimura, S.; Ebitani, K. Direct synthesis of 1,6-hexanediol from HMF over a heterogeneous Pd/ZrP catalyst using formic acid as hydrogen source. *ChemSusChem* **2014**, *7*, 96–100.

(8) Tang, X.; Wei, J.; Ding, N.; Sun, Y.; Zeng, X.; Hu, L.; Liu, S.; Lei, T.; Lin, L. Chemoselective hydrogenation of biomass derived 5-hydroxymethylfurfural to diols: Key intermediates for sustainable chemicals, materials and fuels. *Renew. Sustain. Energy Rev.* **2017**, *77*, 287–296.

(9) Lange, J.-P.; van der Heide, E.; van Buijtenen, J.; Price, R. Furfural-a promising

platform for lignocellulosic biofuels. *ChemSusChem* **2012**, *5*, 150–166.

(10) Faba, L.; Díaz, E.; Ordóñez, S. Aqueous-phase furfural-acetone aldol condensation over basic mixed oxides. *Appl. Catal. B Environ.* **2012**, *113–114*, 201–211.

(11) Huber, G. W.; Chheda, J. N.; Barrett, C. J.; Dumesic, J. A. Production of liquid alkanes by aqueous-phase processing of biomass-derived carbohydrates. *Science* **2005**, *308*, 1446–1450.

(12) Faba, L.; Díaz, E.; Ordóñez, S. Improvement of the stability of basic mixed oxides used as catalysts for aldol condensation of bio-derived compounds by palladium addition. *Biomass and Bioenergy* **2013**, *56*, 592–599.

(13) Faba, L.; Díaz, E.; Ordóñez, S. Performance of bifunctional Pd/M_xN_yO (M=Mg, Ca; N=Zr, Al) catalysts for aldolization–hydrogenation of furfural–acetone mixtures. *Catal. Today* **2011**, *164*, 451–456.

(14) Sutton, A. D.; Waldie, F. D.; Wu, R.; Schlaf, M.; Silks, L. a P.; Gordon, J. C. The hydrodeoxygenation of bioderived furans into alkanes. *Nat. Chem.* **2013**, *5*, 428–432.

(15) Faba, L.; Díaz, E.; Ordóñez, S. Role of the support on the performance and stability of Pt-based catalysts for furfural–acetone adduct hydrodeoxygenation. *Catal. Sci. Technol.* **2015**, *5*, 1473–1484.

(16) Zhao, S.-N.; Song, X.-Z.; Song, S.-Y.; Zhang, H. Highly efficient heterogeneous catalytic materials derived from metal-organic framework supports/precursors. *Coord. Chem. Rev.* **2017**, *337*, 80–96.

(17) Janiak, C.; Herbst, A. MOF catalysts in biomass upgrading towards value-added fine chemicals. *CrystEngComm* **2016**, *19*, 4092–4117.

APPENDIX A SUPPORTING INFORMATION FOR CHAPTER 2

A.1 Additional XRD Patterns

LDH materials were synthesized, filtered and dried materials were characterized through powder XRD to verify the creation of these materials (Figure A.1). The most distinguishable peaks are the (003) and (006) reflections at approximately 12.5° and 23°, which correspond to the vertical stacking of the layers.[1]

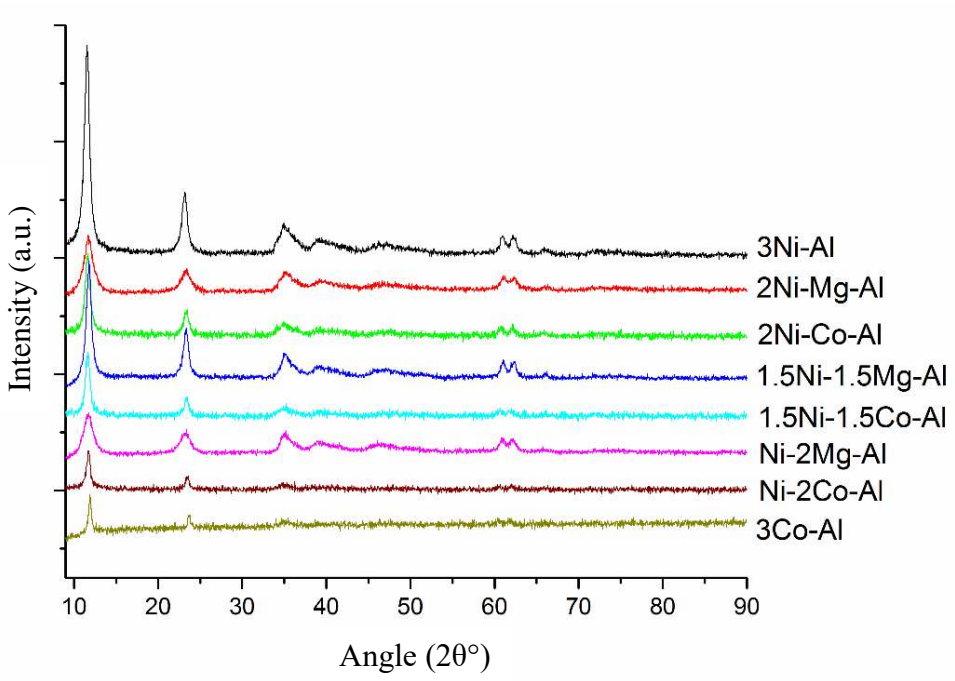

Figure A.1 – XRD Patterns of filtered and dried LDH materials.

Figure A.2 displays potential diffraction peaks for each of the potential oxides present in the MMOs synthesized. It can clearly be seen that many contain overlapping peaks that making assigning peaks in the calcined MMOs in Figure 2.1 very difficult.

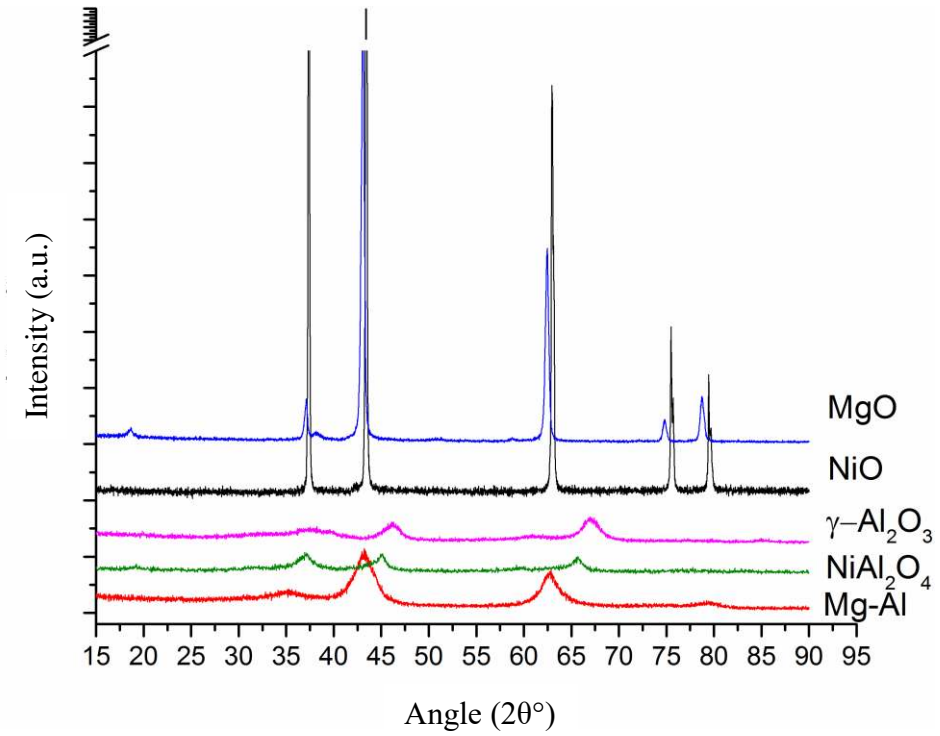

Figure A.2 – XRD Patterns of known references to compare.

A.2 Temperature Programmed Reduction

The table below (Table A.1) displays the hydrogen uptake values and peak temperatures for each of the catalysts used in the catalysts used in this study. Each of the Co containing catalysts have two peaks, which are distinguished in the table.

Table A.1 – Hydrogen uptake and peak temperatures obtained by temperature programmed reduction.

Catalyst	Peak 1		Peak 2		At 500 °C
	Uptake (µmol/g)	Peak Temperature (°C)	Uptake (µmol/g)	Peak Temperature (°C)	Total Uptake (µmol/g)
2Ni-Al	11060	509	-	-	4820
1.9Ni-Mg-Al	7750	548	-	-	2790
1.3Ni-0.5Co-Al	1140	201	9070	546	4270
1.4Ni-1.4Mg-Al	4920	673	-	-	1404
1.1Ni-0.8Co-Al	1620	216	9290	575	4870
0.9Ni-1.9Mg-Al	3320	665	-	-	560
0.7Ni-1.1Co-Al	2250	242	9290	630	4034
Co-Al	2350	279	9180	636	2920

A.3 Reaction Data

Time on stream data for the high conversion testing related to Table 2.2 are shown below in Figure A.3. Each contain two runs to display reproducibility in the experiments. Minor conversion/selectivity discrepancies can be attributed to error within weighing out catalysts. Error was included in the activity per gram calculations in Table 2.2.

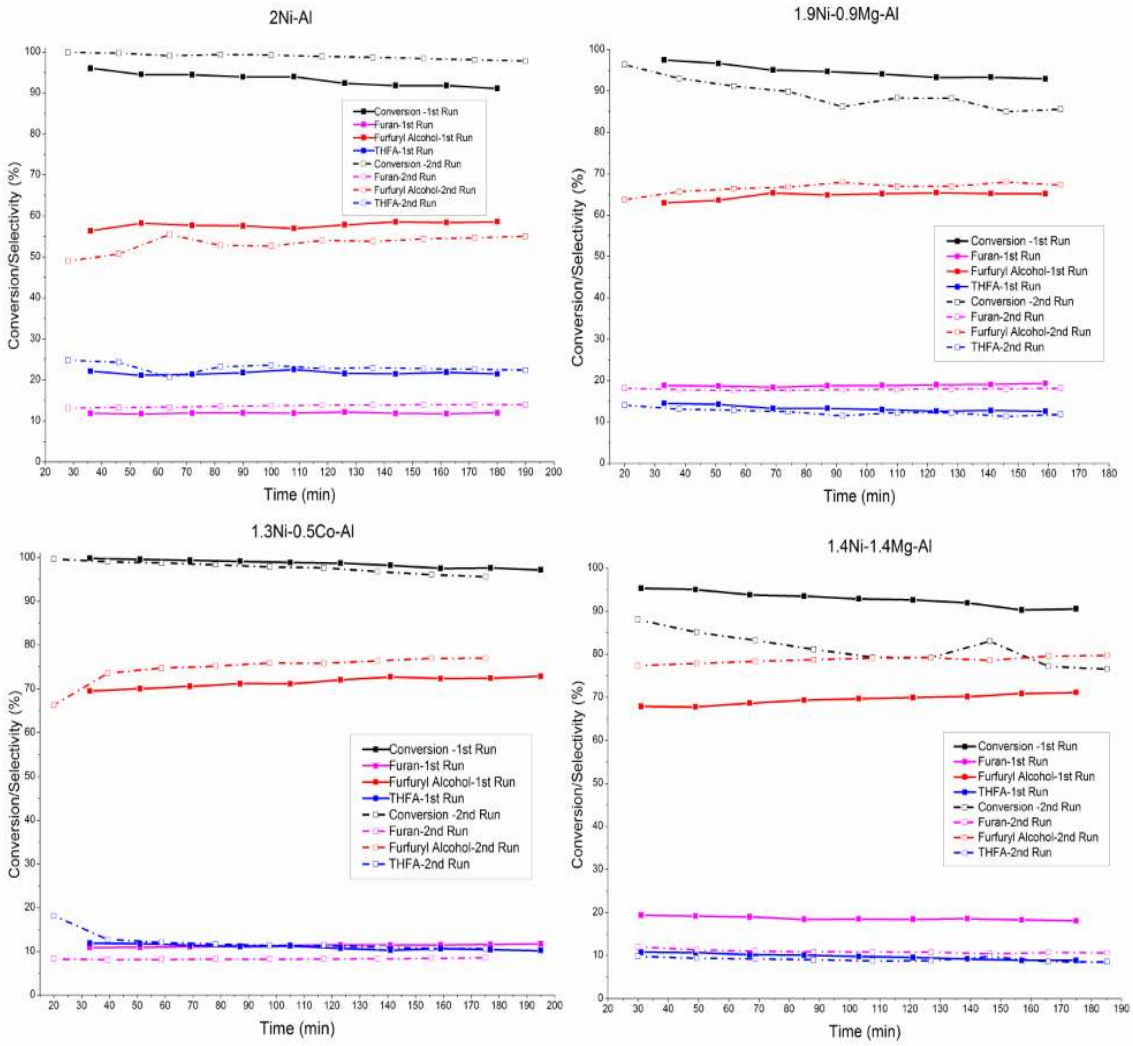

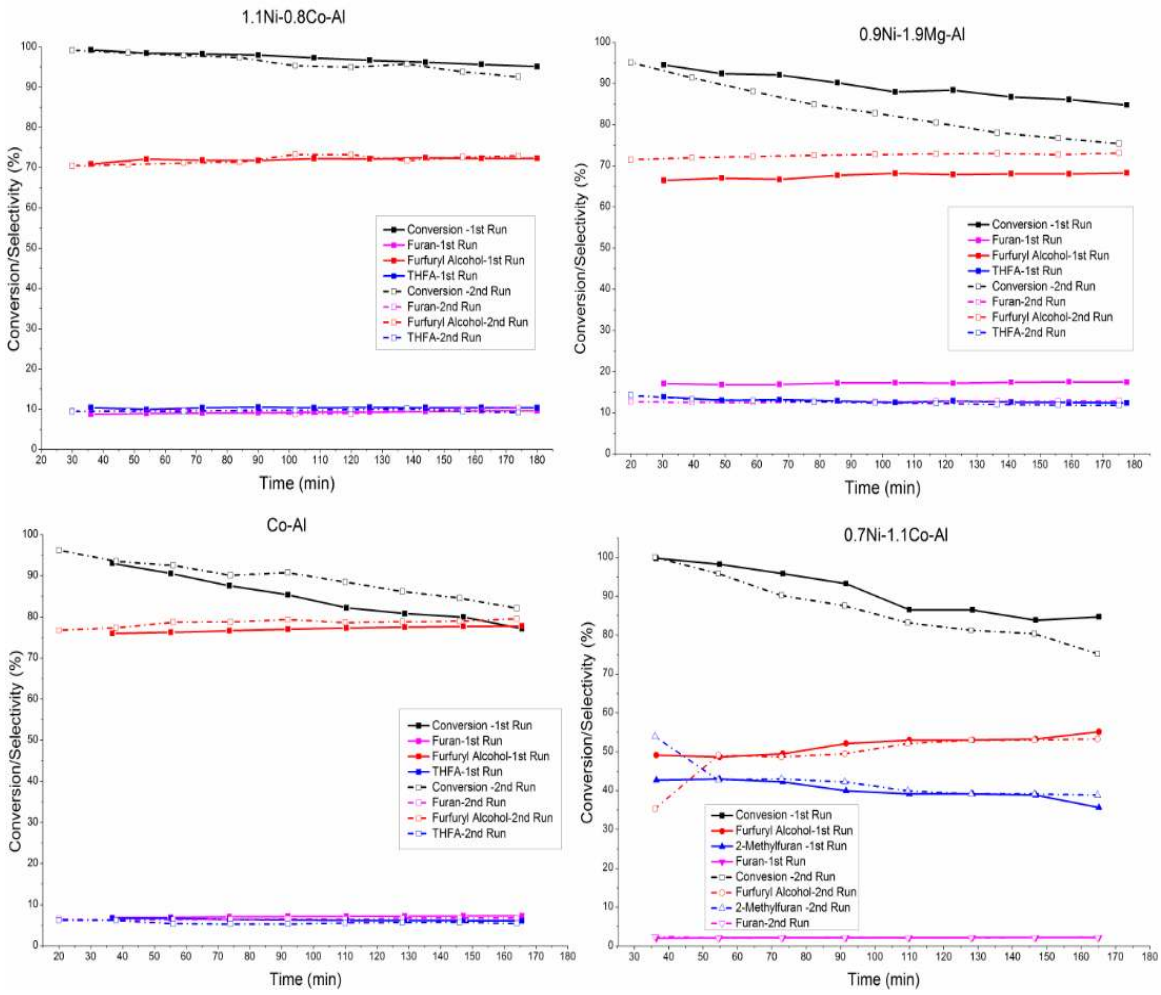

Figure A.3 – Conversion and major product selectivities vs time on stream for multiple runs of each catalyst.

A.4 Post-reaction TGA

Post-reaction TGA was conducted on several catalysts to analyze carbon deposition after reaction. Figure A.4 shows the mass loss and differential scanning calorimetry (DSC) curves for 1.1Ni-0.8Co-Al, 1.4Ni-1.4Mg-Al, and Co-Al. All graphs display a single exothermic peak which can be attributed to both oxidation of metallic species and small amounts of carbon. The increase in mass can be attributed to metal oxidation, since the catalysts were only passivated at room temperature. However, there is not significant overall weight loss suggesting minimal carbon deposition on the catalysts after three hours of reacting. There is not clear evidence of carbon deposition suggesting that GC error and minor unidentified products are the major contributing factors to the small discrepancy in the carbon balance.

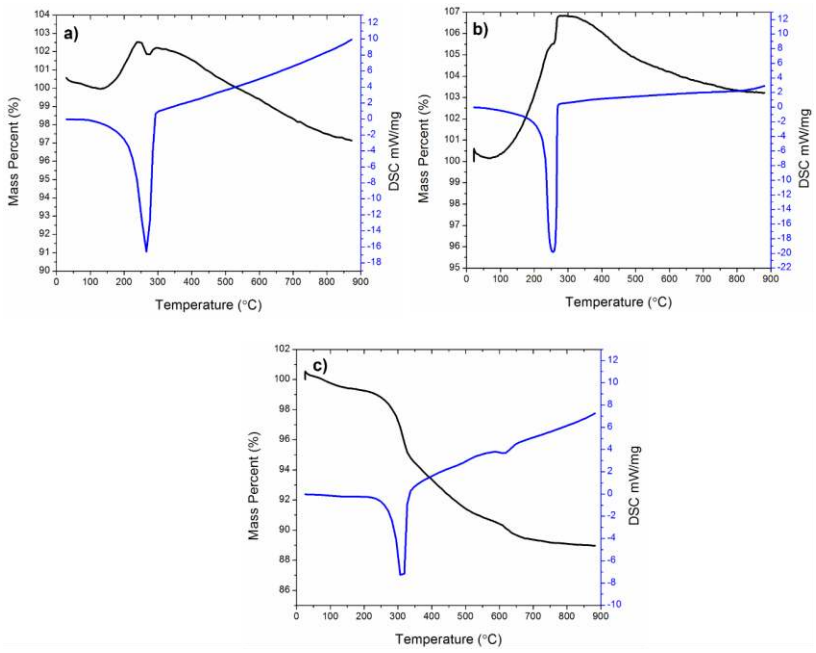

Figure A.4 – Ramp rate 10 °C/min. a) 1.1Ni-0.8Co-Al post-reaction mass change and DSC vs temperature. b) Co-Al post-reaction mass change and DSC vs temperature. c) 1.4Ni-0.4Mg-Al post-reaction mass change and DSC vs temperature.

A.5 CO Adsorption Data

The CO pulse chemisorption experimental procedure is described in the experimental section of the report. 1.5 sites per CO molecule was used to calculate the number of sites per gram of catalyst. These results were then used to calculate apparent activity, written as site-time-yields (STYs), as shown in Table 2.3. Additionally, CO adsorption was conducted on unreduced samples, and no adsorption was seen on the 2Ni-Al or the 1.4Ni-1.4Mg-Al. However, approximately 57 μmol/g_{cat} was observed on the unreduced 1.1Ni-0.8Co-Al catalysts, which suggests that on Co oxide species there may be some adsorption of CO. This may slightly inflate the calculated number of sites of the reduced sample. This small adsorption was not factored into the reduced CO adsorption calculations.

Table A.2 – CO pulse chemisorption results conducted at 30 °C.

Catalyst	CO Adsorption (μmol/g_{cat})	Calculated Sites (μmol$_{sites}$/g_{cat})	Metallic Surface Area (m^2/g_{cat})	Dispersion (%)	Particle Size (nm)
1.4Ni-1.4Mg-Al	243±5	365±8	14.2±0.3	5.4±0.1	18.4±0.4
1.1Ni-0.8Co-Al	174±16	261±24	10.3±0.9	2.7±0.2	37.1±3.1
2Ni-Al	184±14	276±21	10.8±0.8	2.7±0.2	36.6±2.6
0.7Ni-1.1Co-Al	166±18	248±27	9.7±1.1	3.7±0.4	27.0±3.0
1.9Ni-Mg-Al	354±3	530±5	20.7±0.2	7.9±0.01	12.6±0.1

$$\textbf{Metallic Surface Area (MSA)}\left(\frac{m^2}{g}\right) = \frac{1.5 * Q_A}{N_A * S_A}$$

$$\textbf{Particle Size (nm)} = \frac{6}{MSA * \rho}$$

$$\textbf{Dispersion} = \frac{1}{\textbf{Particle Size}}$$

$$Q_A = \textbf{Quantity Adsorbed}\left(\frac{mol}{g}\right)$$

$$N_A = Avogadro's\ Number$$

$$S_A = Surface\ atoms\ per\ area\ (m^{-2})$$

$$\rho = metal\ density$$

A.6 Derivatives of XAS Data Ni k-edge

The XANES data can be further analyzed though the plotting the derivative of norm(E) as a function of energy. The Ni foil reference is shown in the plot, as well, for comparison to the pure metallic state.

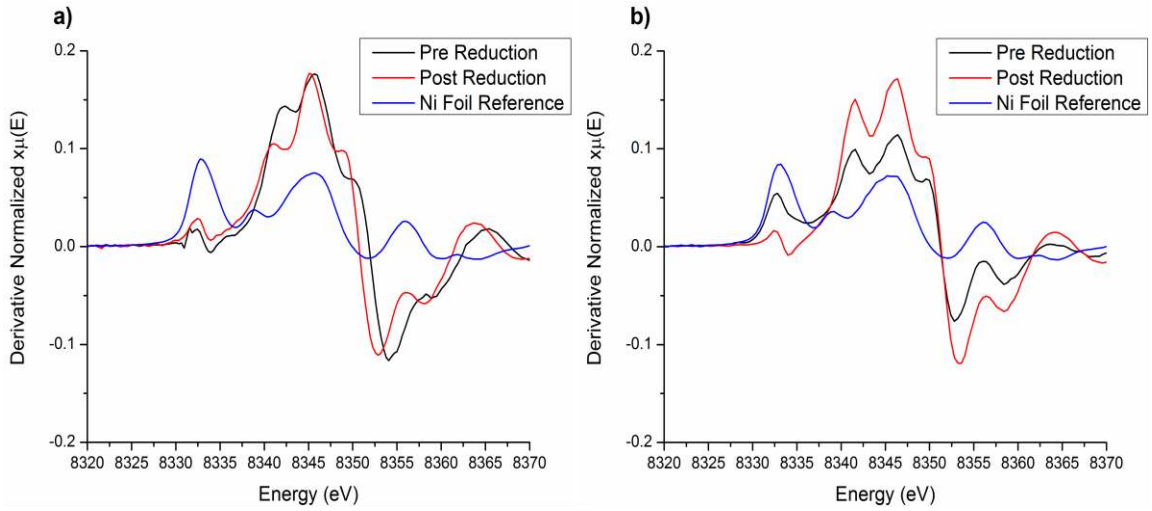

Figure A.5 – Derivative of norm(E) of XANES data from Figure 2.6. a) 1.1Ni-0.8Co-Al pre- and post-reduction compared to Ni foil. b) 1.4Ni-1.4Mg-Al pre- and post-reduction compared to Ni foil.

A.7 Additional XPS Spectra

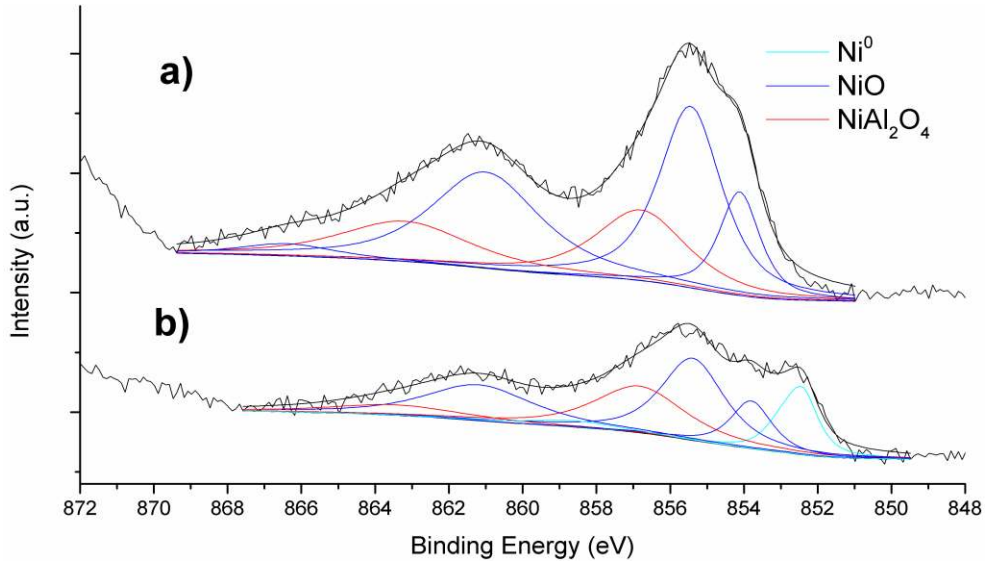

Figure A.6 – XPS spectra in the Ni $2p^{3/2}$ binding energy region of pre- and post-reduction samples of 1.1Ni-0.8Co-Al. a) pre-reduction; b) post-reduction.

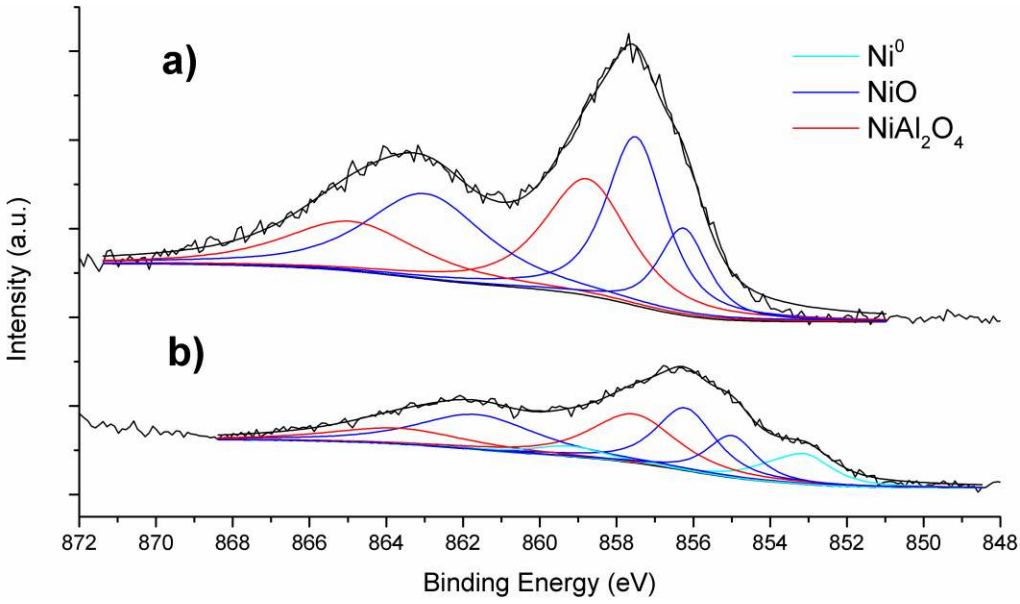

Figure A.7 – XPS spectra in the Ni $2p^{3/2}$ binding energy region of pre- and post-reduction samples of 1.4Ni-1.4Mg-Al. a) pre-reduction; b) post-reduction.

The XP spectrum of the 1.4Ni-1.4Mg-Al sample showed significant shifts in the peak fitting binding energies due to the strong interaction of the MgO and NiO/Ni. MgO is more electronegative than Co or Ni, causing a decrease in the electron density of Ni, causing a shift in the binding energies. Once reduced, the electron density increased, causing an overall shift in the peaks.[2] To address this issue, each peak was shifted by the same amount between pre- and post-reduction, within ±0.2eV.

Table A.3 – Co XPS peak fitting parameters for the 1.1Ni-0.8Co-Al sample, both pre- and post-reduction (Refer to Figure 2.8).

Pre-reduction		**Post-reduction**	
Position (eV)	**FWHM (eV)**	**Position (eV)**	**FWHM (eV)**
	Co		
-	-	775.8	2.35
-	-	778.1	1.45
	CoO		
780.8	2.50	780.9	2.74
782.9	3.00	783.0	3.00
786.7	4.30	786.5	4.25
	Co_3O_4		
779.55	1.57	779.6	1.54
780.7	1.73	780.7	1.73
782.1	2.45	782.1	2.54
785	2.39	-	-
789.2	2.86	-	-

Table A.4 – Ni XPS peak fitting parameters for the 1.1Ni-0.8Co-Al sample, both pre- and post-reduction (Refer to Figure A.6).

Pre-reduction		Post-reduction	
Position (eV)	**FWHM (eV)**	**Position (eV)**	**FWHM (eV)**
		Ni	
-	-	852.5	1.05
-	-	858.6	2.71
		NiO	
854.1	1.32	853.8	1.31
855.5	2.03	855.4	2.03
861	3.50	861.2	3.50
866.4	3.04	-	-
		$NiAl_2O_4$	
856.8	2.92	856.8	2.92
863.2	4.22	863.4	4.22

Table A.5 – Ni peak fitting parameters for the 1.4Ni-1.4Mg-Al sample, both pre- and post-reduction (Refer to Figure A.7).

Pre-reduction		Post-reduction	
Position (eV)	**FWHM (eV)**	**Position (eV)**	**FWHM (eV)**
		Ni	
-	-	853.1	1.72
		NiO	
856.3	1.52	855.0	1.52
857.5	1.84	856.2	1.84
862.9	3.72	861.6	3.72
		$NiAl_2O_4$	
858.8	2.66	857.6	2.66
864.9	4.16	863.7	4.16

A.8 Additional STEM Images

EELS spectrum was taken from the image presented in Figure A.8. It can be seen that the EELS data displays both peaks from Co and Ni at that resolution. This supports the idea of well mixed alloys once the material is reduced

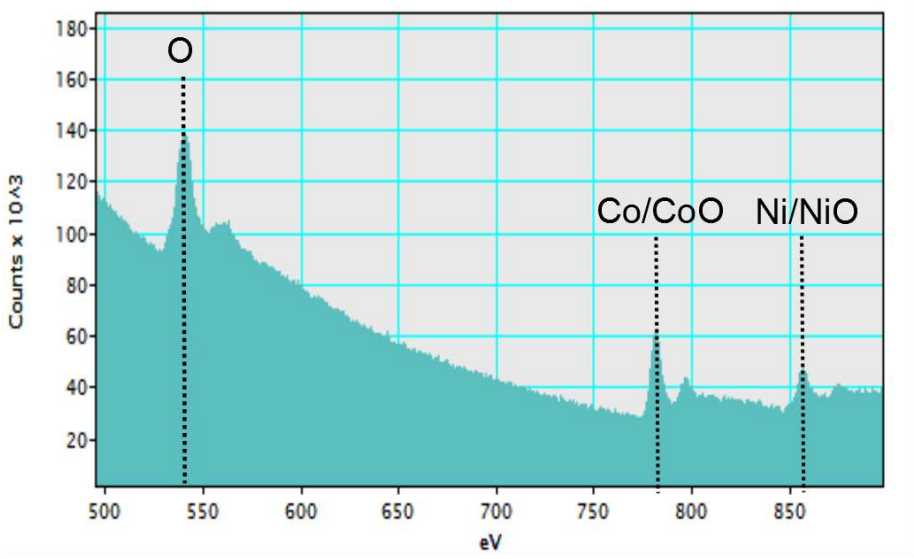

Figure A.8 – Electron Energy Loss Spectrum of Figure 2.9 STEM image.

Additional STEM imaging along with EDS spectra are shown below in Figures A.9 and A.10. The EDS spectra displayed high mixing of each of the species before and after reduction. There was no clear separation of species or specific oxide/metallic domains.

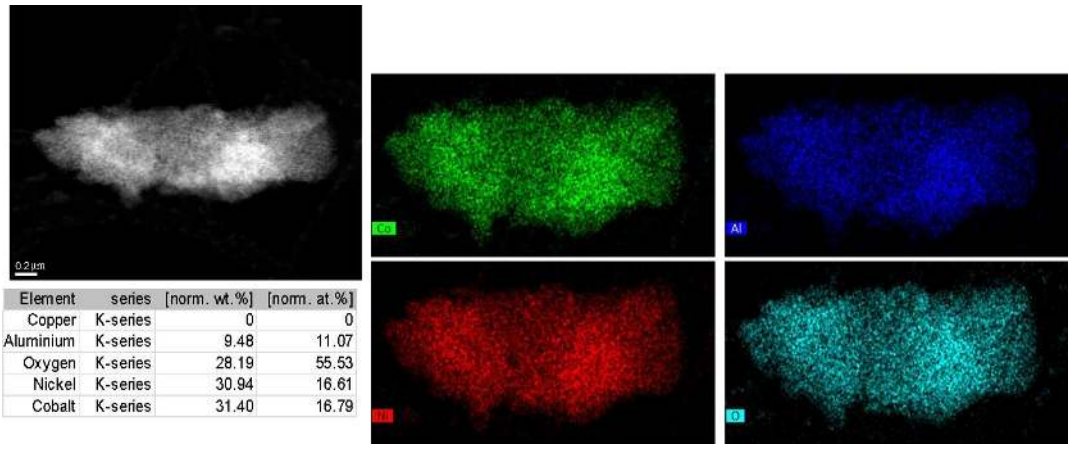

Element	series	[norm. wt.%]	[norm. at.%]
Copper	K-series	0	0
Aluminium	K-series	9.48	11.07
Oxygen	K-series	28.19	55.53
Nickel	K-series	30.94	16.61
Cobalt	K-series	31.40	16.79

Figure A.9 – STEM image and EDS spectra of each species present in the unreduced 1.1Ni-0.8Co-Al catalysts. The inset table displays the quantification of each species from EDS analysis

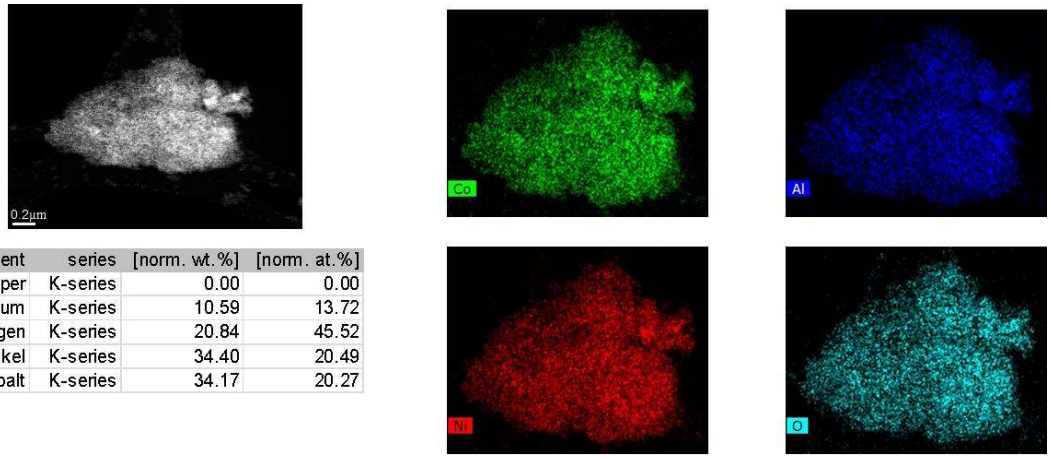

Element	series	[norm. wt.%]	[norm. at.%]
Copper	K-series	0.00	0.00
Aluminium	K-series	10.59	13.72
Oxygen	K-series	20.84	45.52
Nickel	K-series	34.40	20.49
Cobalt	K-series	34.17	20.27

Figure A.10 – STEM image and EDS spectra of each species present in the reduced 1.1Ni-0.8Co-Al catalysts. The inset table displays the quantification of each species from EDS analysis

A.9 References

(1) Cavani, F.; Trifirò, F.; Vaccari, A. Hydrotalcite-type anionic clays: preparation, properties and applications. *Catal. Today* **1991**, *11*, 173–301.

(2) Guittet, M. J.; Crocombette, J. P.; Gautier-Soyer, M. Bonding and XPS chemical shifts in $ZrSiO_4$ versus SiO_2 and ZrO_2: Charge transfer and electrostatic effects. *Phys. Rev. B* **2001**, *63*, 125117.

APPENDIX B SUPPORTING INFORMATION FOR CHAPTER 3

B.1 Additional Physical Characterizations

The N_2 physisorption plots are displayed in Figure B.1, and show a clear hysteresis started approximately at 0.75 P/P_0. The analysis of the N_2 physisorption are displayed in Table 3.1.

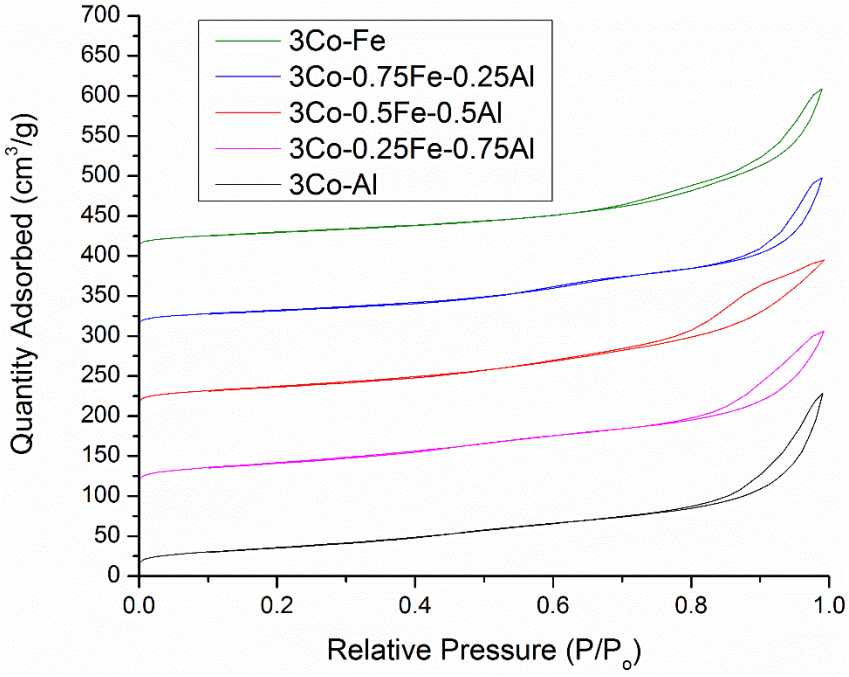

Figure B.1 – N_2 physisorption isotherms of the catalytic materials post-calcination utilized in this study. The catalysts are arbitrarily offset from 0 to display clearly. The $P/P_0 = 0$ offset of each catalysts were 100 cm^3/g except 3Co-Al has no offset.

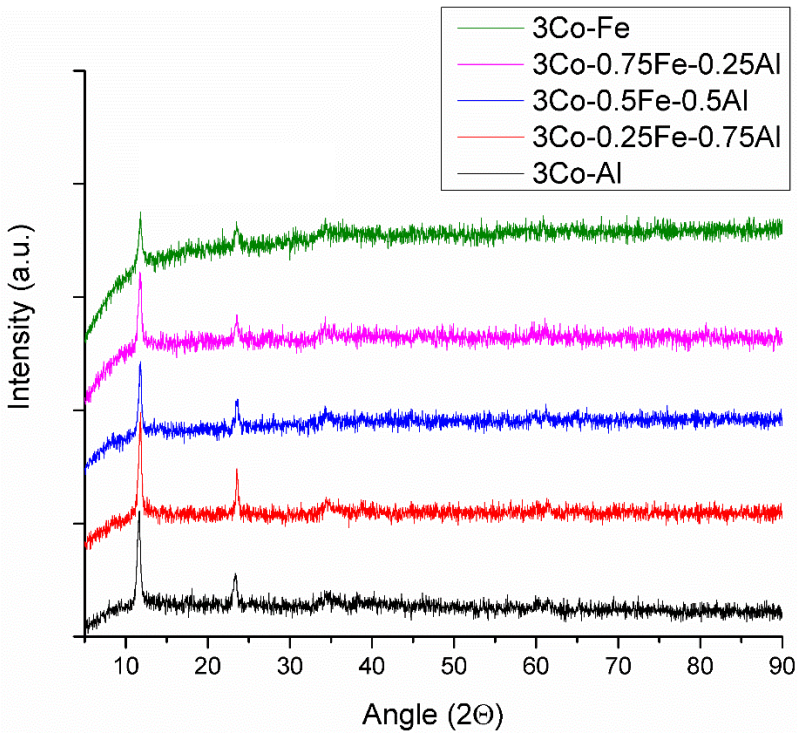

Figure B.2 – XRD patterns of each catalyst after filtration and drying and before calcination. The patterns have a y-axis offset to display each clearly.

The XRD patterns of the uncalcined catalysts displayed above mimic similar LDH patterns in the literature.[1] The first two peaks are indicative of an LDH material, which refers to the diffraction of the (003) and (006) planes. Other peaks associated to LDH materials are present, but at lower much lower intensity. The lack of intensity of the XRD patterns indicate small domain sizes, which may result in small domain sizes after calcination.

B.2 Additional Reaction Data

Calculations were made to assess the potential for mass transfer (internal and external) and heat transfer limitations of the system. Internal mass transfer was analyzed by using the Weisz-Prater Criterion shown in the equation below.[2] Due to the significantly lower concentration of FAL than H_2, our calculations were based on FAL parameters.

$$WPN = \frac{-R_{obs} * L^2}{D_{eff} * C_A}$$

The concentration of FAL in the system, C_A, was 0.0015 mmol/mL, and the particle radius, L, was 0.005 cm (mesh size 270-400). We used Knudsen diffusivity for D_{eff} as a conservative estimate since our pore sizes were approximately 10 nm, which was calculated to be 0.0205 cm^2/s.[3] Lastly, the rate observed, R_{obs}, used was at low conversions (~13%) for 3Co-0.25Fe-0.75Al, since it was the highest rate (0.081 mmol/(s*g_{cat})). The conservative estimate for the WPN number is calculated to be 0.07, which was much below 1. From this conservative calculation is was assumed that internal mass transfer limitations were negligible. Additionally, Figure B.3 displays various particle sizes tested at lower conversion. The experiments suggest that particle sizes under 50 µm do not display significant external mass transfer effects. If particle sizes above 90 µm were used, it is possible that mass transfer effects would need to be considered.

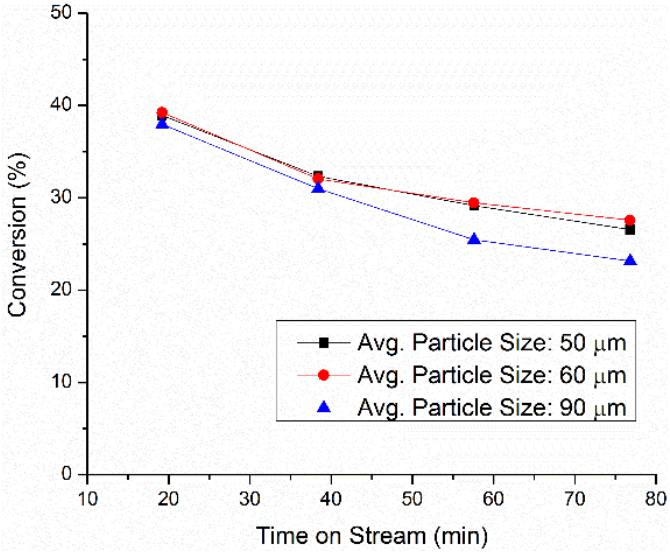

Figure B.3 – Conversion of FAL vs. time on stream for 3Co-0.25Fe-0.75Al with various particle sizes.

External mass transfer limitations were assessed by the Mears criterion, which is displayed below.[4]

$$M_{ext} = -\frac{R_{obs} * p_b * L * n}{k_c * C_A}$$

The Re was calculated with U as the superficial gas velocity (0.0315 m/s), R is the pellet radius (5 x 10^{-5} m), and ν is the kinematic viscosity at approximately 200 °C (1.34 x 10^{-4} m^2/s). The Re is two orders of magnitude less than 1 (0.024), which suggests the mass transfer coefficient can be estimated by $Sh = \frac{k_c * 2R}{D_e} = 2$.[5] The effective diffusivity in this equation is for the bulk diffusivity of the H_2-FAL mixture, which was estimated to be 6.3 x 10^{-5} m^2/s.[5] With those values, the mass transfer coefficient was calculated to be ca. 1.26 m/s. The density of the catalyst bed, p_b, was estimated as the density of SiC since it makes up a majority of the catalyst bed with a porosity, φ, of 0.3 (p_b= (1-φ)*3220 kg/m^3 = 2254 kg/m^3). Lastly the reaction order, n, with respect to FAL was approximated to be 1. With these estimates, the Mears criterion for external mass transfer is approximately 0.048, which is order of magnitude lower than the 0.15 criterion.

Heat transfer limitations was also probed by the Mears criterion, which is shown in the equation below.[5]

$$M_{heat} = \frac{-R_{obs} * p_b * L * E_a * (-\Delta H_{rxn})}{R_g * h * T^2}$$

The main reaction was hydrogenation of FUR to FAL, which has a heat of reaction, ΔH_{rxn}, of approximately -167 kJ/mol.[5] The apparent activation energy, E_a, was approximated by using a value from prior literature that utilized Cu-Fe for hydrogenolysis

of furfuryl alcohol, 31.2 kJ/mol.[6] Since the Re was less than 1, we can estimate the heat transfer coefficient by the Nusselt number correlation, $Nu = \frac{h*2R}{k_t} = 2.$[5] The thermal conductivity, k_t, can be estimated using H_2 at approximately 150 °C (0.19 W/(m*K)). The heat transfer coefficient is estimated to be 1.81 x 10^3 W/(m^2*K). With the above estimates and a gas constant, R_g, of 8.314 x 10^{-3} kJ/(mol*K), the Mears criterion for heat transfer is approximately 1.61 x 10^{-5}. This approximation is significantly lower than the criteria of 0.15, which suggests negligible heat transfer limitations.

Table B.1 – Conversion and selectivity of products of various catalysts tested in Figure 3.3

Catal.	Conv.	2-MF	2-MTHF	Furan	2-PONE	1-BOL	THFA	Hydro-carbon	Others[a]
3Co-Al	26.4 ± 2.4	53.2 ± 1.6	7.6 ± 0.2	6.5 ± 0.2	1.6 ± 0.1	5.3 ± 0.1	7.9 ± 0.8	6.6 ± 0.5	11.3 ± 0.3
3Co-0.25Fe-0.75Al	90.7 ± 3.1	83.2 ± 0.8	3.0 ± 0.1	2.1 ± 0.1	3.9 ± 0.1	1.5 ± 0.1	0.8 ± 0.1	2.9 ± 0.1	2.7 ± 0.1
3Co-0.5Fe-0.5Al	56.3 ± 1.9	82.6± 0.4	3.1 ± 0.1	2.2 ± 0.1	3.1 ± 0.1	0.6 ± 0.1	1.5 ± 0.4	3.2 ± 0.1	2.8 ± 0.1
3Co-0.75Fe-0.25Al	48.7 ± 0.3	83.4± 0.2	3.2 ± 0.1	2.4 ± 0.1	3.2 ± 0.1	0.7 ± 0.1	1.4 ± 0.1	2.9 ± 0.1	2.6 ± 0.1

Reaction parameters: W/F (gcat*h*mol^{-1}) = 3.63, 180 °C, 1 atm, and FAL conc = 0.0015 mmol/mL; Reaction data taken at about 40 min on stream for data associated to Figure 3.3; [a]Others include products that were typically under 1% selectivity including furfural, 1-pentanol, 2-pentanol, 1-butanal, and 1,2-PD.

Table B.2 – Conversion and selectivity of products of various catalysts tested in Figure 3.5

W/F (g_{cat}*h*mol^{-1})	Conv.	2-MF	2-MTHF	Furan	2-PONE	1-BOL	THFA	Hydro-carbon	Others[a]
5.45	98.2 ± 0.1	83.2 ± 0.1	3.1 ± 0.2	2.0 ± 0.2	3.8 ± 0.2	1.7 ± 0.1	0.5 ± 0.2	3.0 ± 0.4	2.6 ± 0.3
3.63	90.7 ± 3.1	83.2 ± 0.8	3.0 ± 0.1	2.1 ± 0.1	3.9 ± 0.1	1.5 ± 0.1	0.8 ± 0.1	2.9 ± 0.1	2.7 ± 0.3
2.27	62.3 ± 2.9	84.0 ± 0.5	3.2 ± 0.1	2.2 ± 0.1	3.5 ± 0.1	1.2 ± 0.1	1.5 ± 0.4	2.4 ± 0.1	2.3 ± 0.3
0.91	29.0 ± 1.3	82.5± 0.8	3.5 ± 0.1	3.3 ± 0.2	3.6 ± 0.1	0.8 ± 0.1	2.4 ± 0.1	2.8 ± 0.4	3.6 ± 0.2
0.38	12.9 ± 0.7	73.9 ± 2.2	3.4 ± 0.1	5.9 ± 0.4	3.7 ± 0.1	0.1 ± 0.1	5.6 ± 0.3	3.9 ± 0.4	7.5 ± 0.5

Reaction parameters: 180 °C, 1 atm, and FAL conc = 0.0015 mmol/mL; Reaction data taken at about 40 min on stream for data associated to Figure 3.5; [a]Others include products that were typically under 1% selectivity including fufural, 1-pentanol, 2-pentanol, 1-butanal, and 1,2-PD.

The reaction data shown in Table B.1 and B.2 display a more comprehensive list of each product observed at a single point from experiments given in Figure 3.3 and Figure 3.5. The error was derived from conducting reactions multiple times, which demonstrates the reproducibility of the results within a few percentage points.

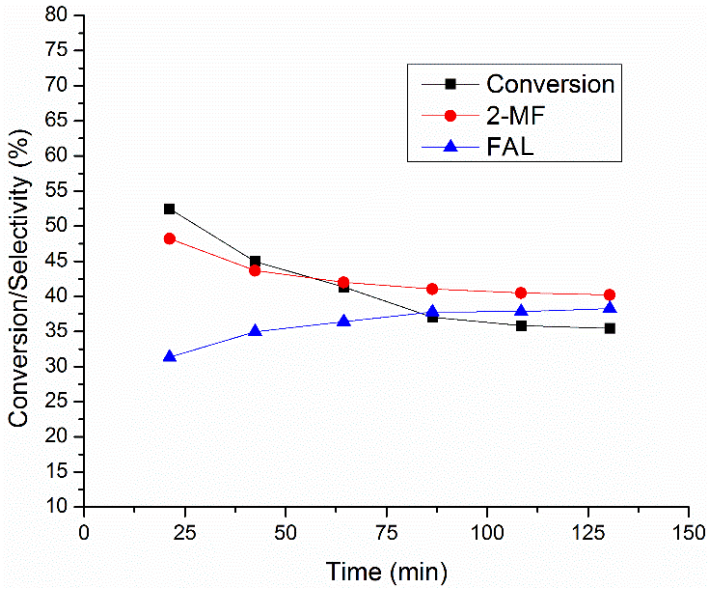

Figure B.4 – Conversion and selectivity (2-MF and FAL) vs. time on stream for FUR reaction displayed in Table 3.2; Reaction conditions: 180 °C and 1 atm, W/F (g_{cat}*h*mol^{-1}) = 3.63, substrate: FUR.

In the above figure, time on stream data of the FUR reaction with W/F = 3.63, which summarizes the deactivation and change in selectivity overtime. The plot only displays selectivities towards the two main products: FAL and 2-MF. Clearly, deactivation of the catalysts was observed and FUR conversion decreased by about 15% with a little over two hours on stream. This about the same amount of conversion loss compared to each 3Co-xFe-yAl catalyst when FAL was utilized as the substrate (15-20% decrease). Additionally, it was observed that selectivities of FAL and 2-MF increase and decrease, respectively, as time progresses. This clearly indicates that deactivation does not only effect FUR conversion, but also, FAL conversion, since it is an intermediate to 2-MF.

B.3 Additional Spectroscopic Experiments and Data

B.3.1 XPS data

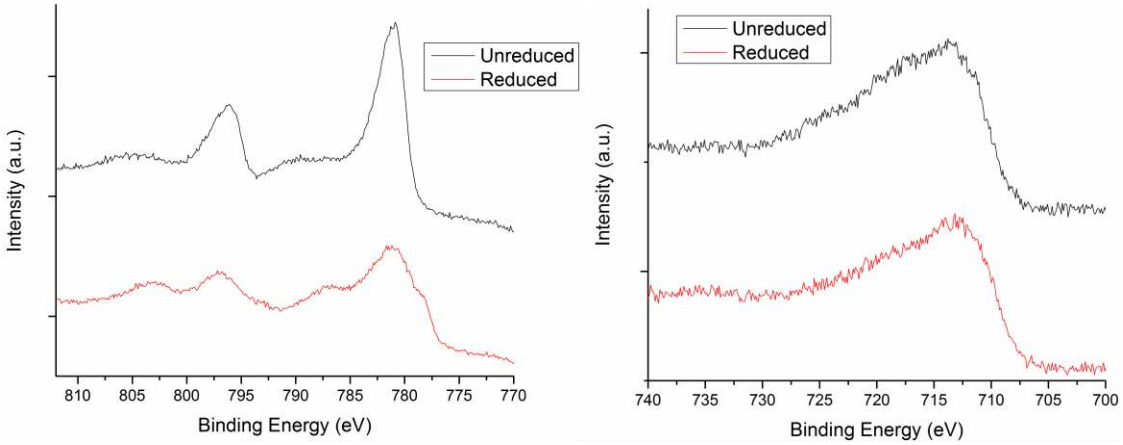

Figure B.5 – XPS of the 3Co-0.25Fe-0.75 sample before and after reduction/passivation. Co species of the reduced and unreduced sample (right). Fe species of the reduced and unreduced sample (left).

The above XPS spectra above depict the electronic environment on the surface before and after reduction and a 1 h passivation in 1% O_2/N_2. Despite indication of the reduction of Co oxide species, there is little indication of Fe species reduction. The lack of observed Fe reduction may indicate the limitations of *ex situ* characterization due to the requirement of passivation after reduction. Unfortunately, passivation was required for these materials due to their pyrophoric nature post-reduction. This resulted in the need for various other *in situ* characterization techniques including *in situ* XAS.

B.3.2 XAS Data

The XAS data below display the XANES analysis of each active catalyst before and after reduction. It becomes evident that the pretreatment process significantly reduces the

Co species to almost pure metallic species; however, the Fe species may exhibit a mix between FeO and metallic Fe.

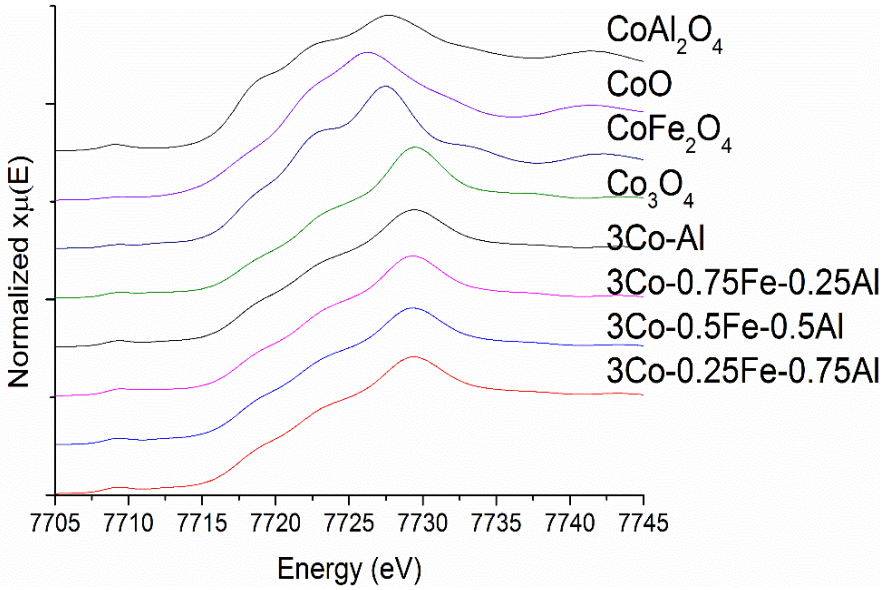

Figure B.6 – XANES spectrum of Co k-edge for various Co-Fe-Al oxides before reduction and post-calcination; Also displayed are some standards used.

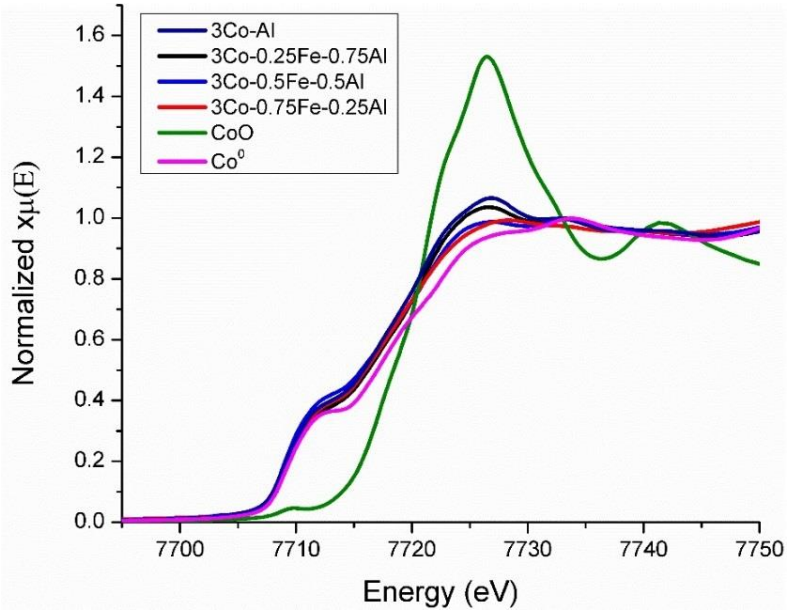

Figure B.7 – Normalized XANES spectrum of Co k-edge of each 3Co-xFe-yAl after reduction at 500 °C; Also displayed with some standards used.

Table B.3: XANES analysis of Co k-edge for each catalyst and standard.

Catalyst	Edge Energy (eV)
CoO	7717.0
Co Foil	7709.0
3Co-Al	7708.8
3Co-0.25Fe-0.75Al	7708.8
3Co-0.5Fe-0.5Al	7708.9
3Co-0.75Fe-0.25Al	7709.0

[a]Edge Energy was determined by the 1st major derivative peak

Each catalyst displayed an edge energy that mimics Co foil indicating that a majority of Co species were in the metallic Co phase. Linear combinations to obtain a qualitative amount of each species was not possible due to the complexity of the catalysts. Also, it was indicated that reduced Fe may have interactions with Co, which could cause small changes in the XANES spectra that could not be represented in any of the standards brought.

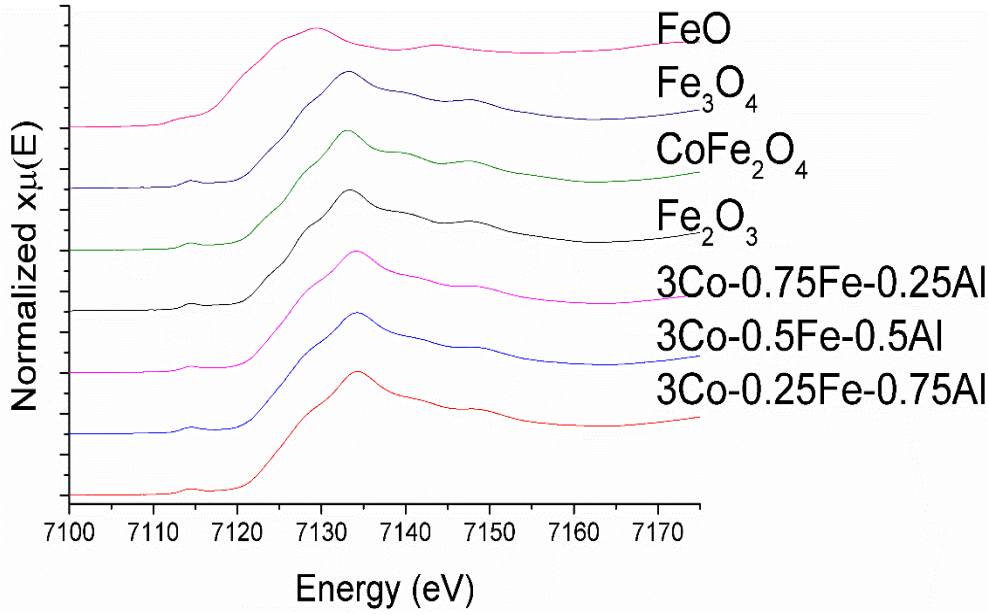

Figure B.8 – Normalized XANES spectrum of Fe k-edge collected before reduction for each catalyst before reduction and post-calcination; Also displayed with some standards used.

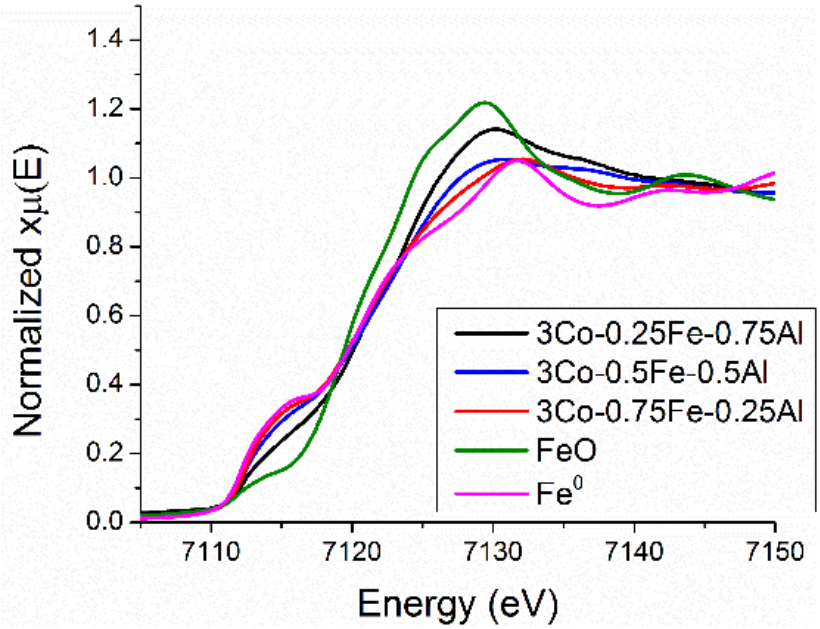

Figure B.9 – Normalized XANES spectrum of Fe k-edge of each 3Co-xFe-yAl after reduction at 500 °C; Also displayed with some standards used.

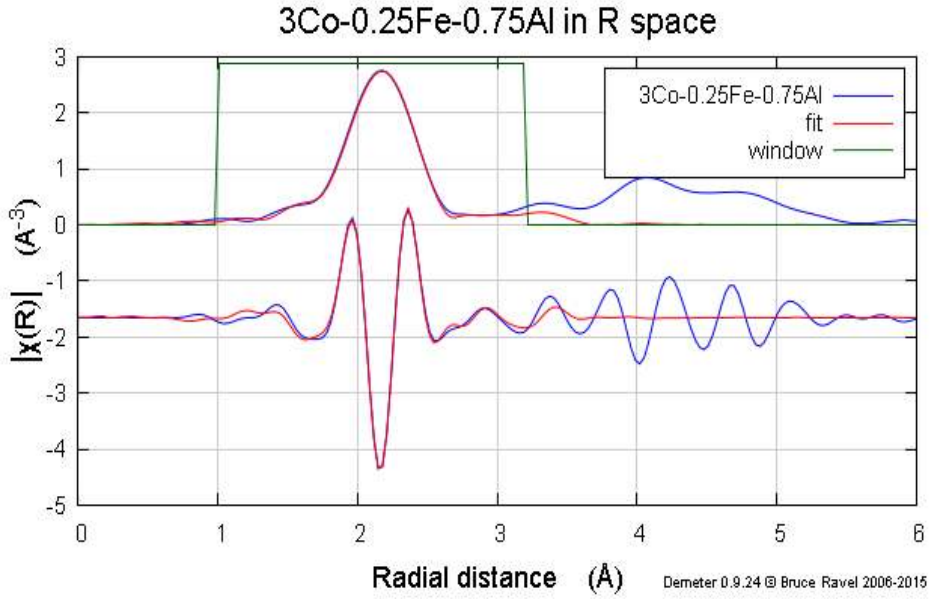

Figure B.10 – Fourier transformed EXAFS of Co k-edge of 500 °C reduced 3Co-0.25Fe-0.75Al catalysts at k weight, k^2. This demonstrates an example fit conducted on the catalysts.

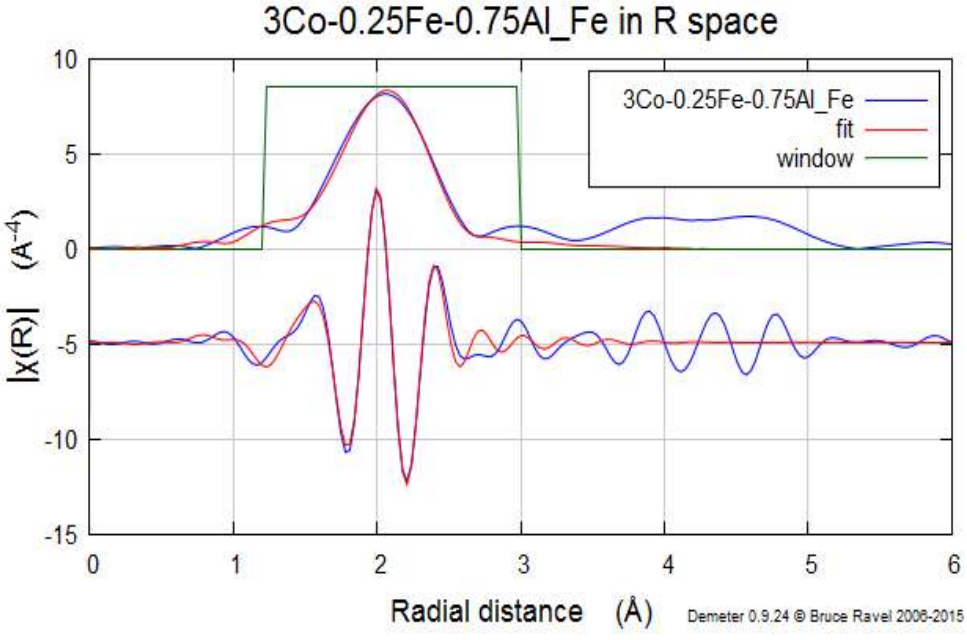

Figure B.11 – Fourier transformed EXAFS of Fe k-edge of 500 °C reduced 3Co-0.25Fe-0.75Al catalysts at k weight, k^2. This demonstrates an example fit conducted on the catalysts.

The above plots, Figures B.10 and B.11, exemplify the fitting conducted on the Fourier transformed EXAFS data. The two above figures give an example of the fitting window and visual indication of the wellness-of-fit for both the Co and Fe species.

B.4 Post-reaction TGA

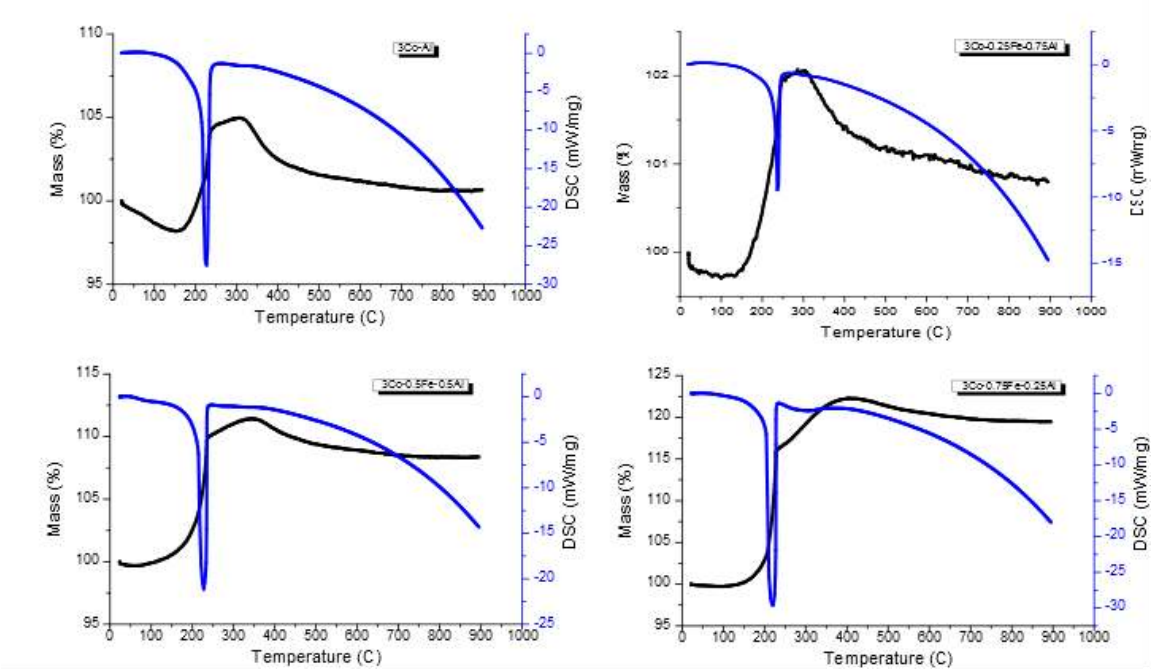

Figure B.12 – TGA/DSC profiles of catalysts post-reaction when FAL is fed for approximately 180 min. Top-left: 3Co-Al, Top-right: 3Co-0.25Fe-0.75Al, Bottom-left: 3Co-0.5Fe-0.5Al, Bottom-right: 3Co-0.75Fe-0.25Al.

Post-reaction TGA analysis of the catalysts after reaction and passivation indicate very little if any indication of carbon deposition. All the catalysts demonstrate an increase in weight due to the full oxidation of each reduced species in air; however, after oxidation, there is very little weight loss, less than 5% up to 900 °C. This supports the hypothesis that deactivation does not come from carbon deposition, but more likely metal oxidation and/or CO poisoning.

B.5 References

(1) Cavani, F.; Trifirò, F.; Vaccari, A. Hydrotalcite-type anionic clays: preparation, properties and applications. *Catal. Today* **1991**, *11*, 173–301.

(2) Weisz, P. B.; Prater, C. D. Weisz-Prater Criteria. *Adv. Catal.* **1954**, *6*, 143.

(3) Smith, J. M. *Chemical Engineering Kinetics*; McGraw-Hill Co., 1970.

(4) Mohagheghi, M.; Bakeri, G.; Saeedizad, M. Study of the effects of external and internal diffusion on the propane dehydrogenation reaction over Pt-Sn/Al2O3 catalyst. *Chem. Eng. Technol.* **2007**, *30*, 1721–1725.

(5) Lee, W.-S.; Wang, Z.; Zheng, W.; Vlachos, D. G.; Bhan, A. Vapor phase hydrodeoxygenation of furfural to 2-methylfuran on molybdenum carbide catalysts. *Catal. Sci. Technol.* **2014**, *4*, 2340–2352.

(6) Sheng, H.; Lobo, R. F. Iron-promotion of silica-supported copper catalysts for furfural hydrodeoxygenation. *ChemCatChem* **2016**, *8*, 3402–3408.

APPENDIX C SUPPORTING INFORMATION FOR CHAPTER 4

C.1 Additional Physical Characterizations

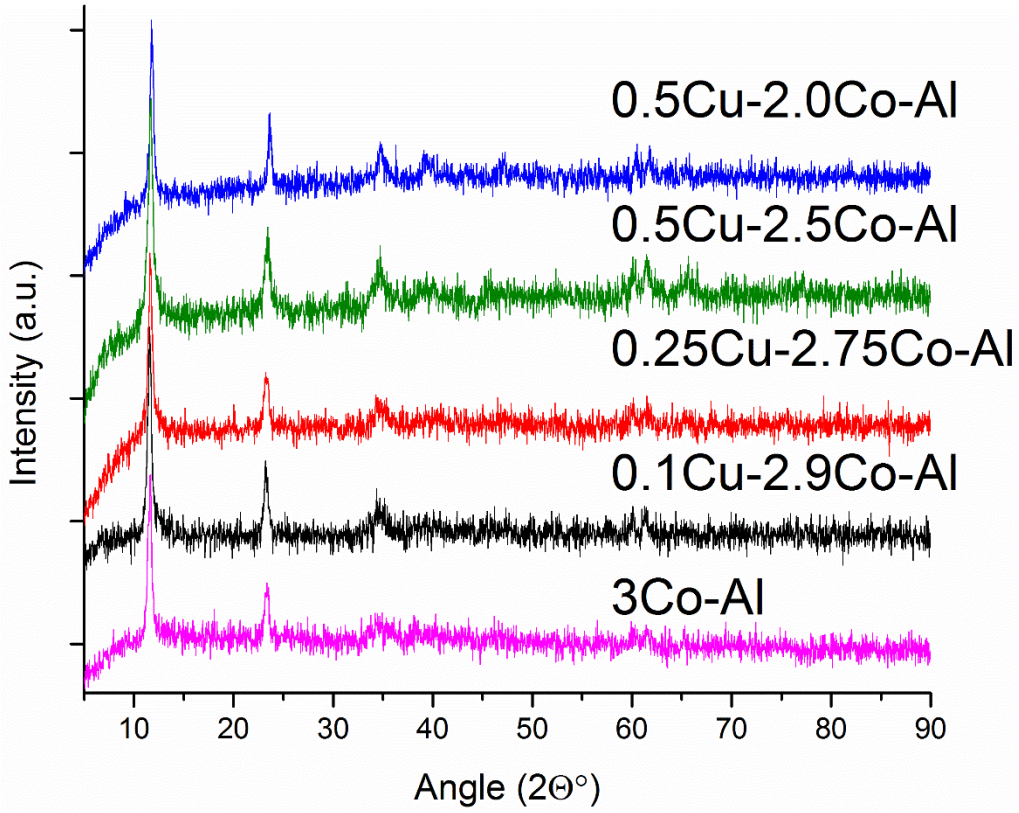

Figure C.1 – XRD patterns of each catalyst after filtration and drying and before calcination. The patterns have a y-axis offset to display each clearly.

The XRD patterns of the uncalcined pre-catalysts displayed above mimic similar LDH patterns in the literature.[1] The first two peaks are indicative of an LDH material, which refers to the diffraction of the (003) and (006) planes. Other peaks associated to LDH materials are present, but at much lower intensity. The lack of intensity of the XRD patterns indicate small domain sizes, which may result in small domain sizes after calcination.

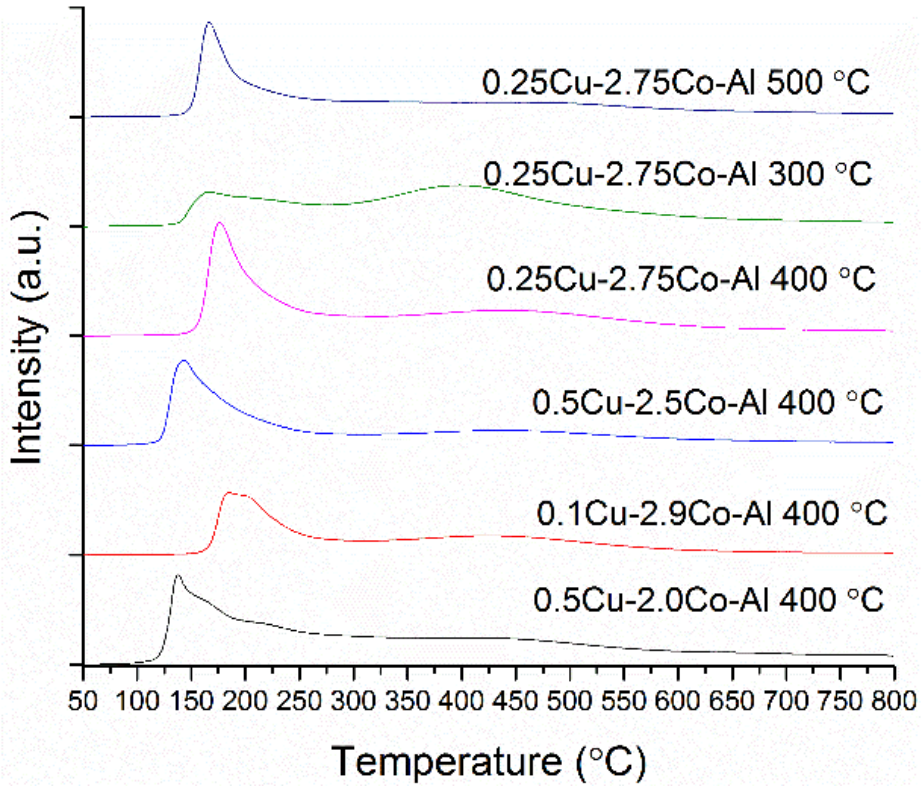

Figure C.2 – TPR profile of the catalysts after reduction and passivation. The reduction temperature is indicated after the catalyst name.

TPR was performed on each catalyst after reduction at 400 °C and 1 h of room temperature passivation, and additionally, multiple reduction temperatures were investigated for the 0.25Cu-2.75Co-Al catalysts to complement the reduction temperature study. As expected, the reduction for all the reduced/passivated catalysts begin at a lower temperature than the oxide samples post-calcination. Interestingly, most of the samples displayed a similar two-step reduction of the post-calcination samples, which suggested that the post-reduction samples contained strong metal interactions with Al_2O_3 species, possibly a species like $CoAl_2O_4$ and $CuAl_2O_4$.

Additionally, the second reduction peak seems to diminish after being treated at higher reduction temperatures, which supported XANES and EXAFS analysis that

suggested there was an increase in metallic Co particle size and percentage of metallic species.

C.2 Additional Reaction Data

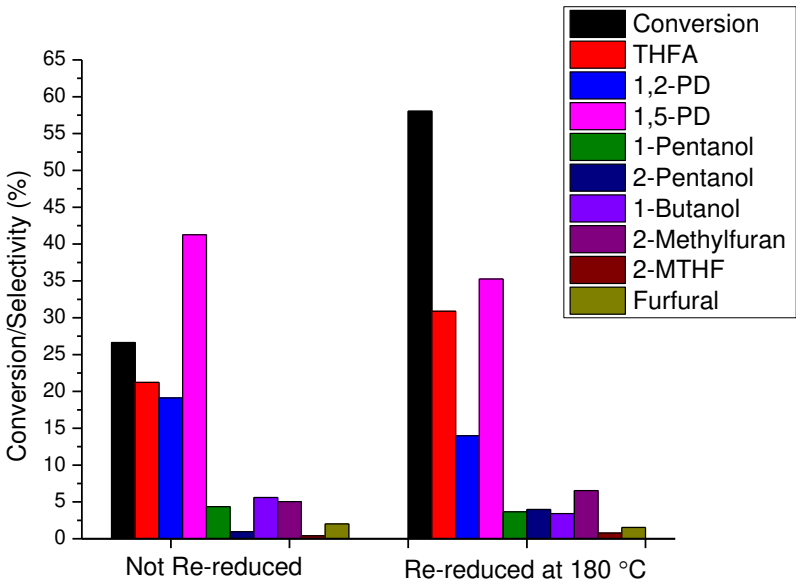

Figure C.3 – Temperature: 140 °C, Pressure: 4 MPa of H_2, Reaction time: 1 h, 0.25Cu-2.75Co-Al/Furfuryl Alcohol/Solvent: 25 mg/500 mg/ 50 mL.

The above figure indicated the significant impact that occurs when the catalyst goes through a second, in situ reduction after being reduced at 400 °C for 1 h and passivated at room temperature for 1 h in 1% O_2. It was evident that the conversion increased after being re-reduced in the batch reactor prior to conducting the reaction. Additionally, there was an increase in THFA selectivity and a decrease in the ring-opening product selectivity; however, the yield towards ring-opening after 1 h compared to the single-phase reduction catalysts was significantly enhanced. Also, it was likely that the sample without re-reduction was reducing during reaction, which made it very difficult to determine specific

rates. Consequently, the experiments presented in the manuscript include the *in situ* reduction step in every case.

Table C.1 – Conversion and selectivity to products of various catalysts tested in Table 4.2

Entry	Conv.	1,5-PD	THFA	1,2-PD	2-POH	1-POH	1-BOH	2-MF	2-MTHF	FUR
1	12.2 ± 2.6	31.1 ± 2.1	35.6 ± 3.4	9.6 ± 1.1	2.1 ± 0.4	2.6 ± 0.1	6.5 ± 0.1	6.1 ± 1.3	3.6 ± 1.1	2.7 ± 0.9
2	41.0 ± 0.8	39.5 ± 1.3	25.2 ± 0.4	17.9 ± 1.0	2.7 ± 0.4	2.2 ± 0.2	5.3 ± 0.5	4.3 ± 1.0	1.4 ± 0.2	1.5 ± 0.9
3	69.5 ± 3.6	36.6 ± 0.1	29.6 ± 0.1	14.1 ± 0.4	4.3 ± 0.1	3.0 ± 0.1	3.8 ± 0.2	6.3 ± 0.6	1.2 ± 0.2	1.2 ± 0.1
4	53.4 ± 0.7	32.2 ± 1.4	32.2 ± 1.5	13.2 ± 0.2	3.8 ± 0.3	2.4 ± 0.3	3.8 ± 0.1	9.9 ± 0.8	1.1 ± 0.1	1.3 ± 0.1
5	16.1 ± 1.7	30.4 ± 0.8	29.6 ± 0.1	22.2 ± 0.4	2.7 ± 0.1	0.5 ± 0.3	5.9 ± 0.1	4.9 ± 0.2	2.8 ± 0.1	1.0 ± 1.2
6	52.0 ± 4.6	32.3 ± 1.9	31.0 ± 3.7	15.4 ± 1.2	2.8 ± 0.6	1.3 ± 0.3	4.0 ± 0.2	8.7 ± 0.5	2.3 ± 0.2	1.4 ± 0.3
7	50.1 ± 3.6	35.5 ± 3.1	40.7 ± 3.4	10.1 ± 1.1	2.9 ± 0.1	1.7 ± 0.2	3.0 ± 0.2	4.1 ± 1.2	0.9 ± 0.2	1.1 ± 0.1
8	37.0 ± 0.1	24.0 ± 3.7	57.0 ± 4.3	8.3 ± 0.8	2.0 ± 0.1	0.9 ± 0.1	2.5 ± 0.1	3.3 ± 0.2	1.2 ± 0.1	0.7 ± 0.2
9	98.7 ± 0.3	42.7 ± 1.6	15.1 ± 0.2	15.5 ± 0.9	6.7 ± 0.2	4.6 ± 0.2	4.6 ± 0.1	7.8 ± 1.1	1.5 ± 0.1	1.1 ± 0.3
10	55.2 ± 0.9	36.5 ± 1.7	26.2 ± 3.5	15.0 ± 1.2	4.5 ± 0.1	3.2 ± 0.1	4.4 ± 0.5	7.8 ± 0.1	1.0 ± 0.3	1.5 ± 0.1
11	80.8 ± 2.3	37.7 ± 0.2	33.5 ± 1.9	13.5 ± 0.5	3.9 ± 0.2	2.8 ± 0.2	3.2 ± 0.2	3.5 ± 1.1	0.9 ± 0.1	0.9 ± 0.2

Reaction parameters: Reaction time of 2 h, Catalyst/Furfuryl Alcohol/Solvent: 15 mg/500 mg/ 50 mL. This data is representative of the average and error achieved from at least 2 runs. Table 4.2 in the main text displays just 1 run. 2-MTHF: 2-methyltetrahydrofuran.

The reaction data shown in Table C.1 give a comprehensive list of each product observed at a single point from experiments given in Table 4.2. The error was derived from conducting reactions twice, which demonstrates the level of reproducibility of the results to be within a few percentage points.

Table C.2 – Reaction conditions, conversion, and selectivity of additional reactions with FAL

Entry	Catal.	Catal. Amount (mg)	Temp. (°C)	Pressure (MPa)	Time (h)	Conv. (%)	1,5-PD (%)	THFA (%)	1,2-PD (%)	Others (%)
1	3Co-Al	15	140	4	5	21.0	33.7	34.8	10.2	21.3
2	3Co-Al	100	140	4	3	32.2	40.9	28.6	14.6	15.9
3	0.1Cu-2.9Co-Al	15	140	4	3	55.1	39.0	25.9	16.1	19.0
4	0.1Cu-2.9Co-Al	15	160	4	2	97.8	44.7	13.0	18.9	23.4
5	3Co-Al	125	160	4	5	96.8	48.2	14.0	18.0	19.8

Reaction Conditions: 500 mg of FAL, 50 mL of EtOH, reduction pretreatment and procedure described in experimental section.

Table C.3 – Reaction conditions, conversion, and selectivity utilizing other substrates

Entry	Catalyst	Catal. Amount (mg)	Substrate	Pressure (MPa)	Time (h)	Conv. (%)	2-POH (%)	1-POH (%)	2-MTHF (%)	Others [b] (%)
1[a]	0.1Cu-2.9Co-Al	30	2-MF	4	2	42.4	17.9	7.9	69.5	4.6
2	0.1Cu-2.9Co-Al	30	1,2-PD	4	2	<1.0	0.0	0.0	0.0	0.0
3	0.1Cu-2.9Co-Al	30	1,5-PD	4	2	<1.0	0.0	0.0	0.0	0.0
4[a]	0.1Cu-2.9Co-Al	30	2-MTHF	4	2	<1.0	0.0	0.0	0.0	0.0
						Conv. (%)	**1-BOH (%)**	**THF (%)**	**Others[b] (%)**	
5[a]	0.1Cu-2.9Co-Al	30	Furan	4	2	97.9	26.4	70.7	2.9	
6[a]	0.1Cu-2.9Co-Al	30	THF	4	2	<1.0	0.0	-	0.0	

Reaction Conditions: 500 mg of substrate, 50 mL of EtOH, reduction pretreatment and procedure described in experimental section. [a] Reactions were heated in H_2 to reaction temperature and the samples were acquired at R.T. after rapid cooling to minimize substrate loss due to high vapor pressures. [b] Others: unknown carbon species

The reactions above were additional experiments conducted to validate claims throughout the study. The experiments described in Table C.2 were conducted to compare some of the catalysts at similar levels of conversion. An attempt to increase the conversion of 3Co-Al by increasing time and catalyst amount were tried, and it suggested an increase in conversion, increased selectivity towards diols slightly. This was not seen when the time of reaction increased with 0.1Cu-2.9Co-Al. To obtain a higher diol yield, the reaction temperature was set to 160 °C, and a comparative analysis was done between 95%-99% conversion. This analysis supported the claim that Cu may not have had a significant influence on adsorption conformation, which is hypothesized to affect the formation of diol products, but only facilitated reduction of the Co oxide species. Ultimately, this led to a drastic increase in activity possibly due to the more metallic species present on the surface and in the bulk.

The experiments presented in Table C.3 demonstrate the reactivity and selectivity of different substrates other than FUR, FAL, and THFA, which helps elucidate the pathways. The data suggest that the diol products do not undergo further reaction/hydrogenolysis to pentanol products; however, they suggest that 2-MF was the intermediate to the pentanol products while furan was the intermediate to 1-butanol. Additionally, it was observed that under the conditions employed, furan was highly reactive compared to the other substrates (2-MF and FAL) and it produced both 1-butanol and THF.

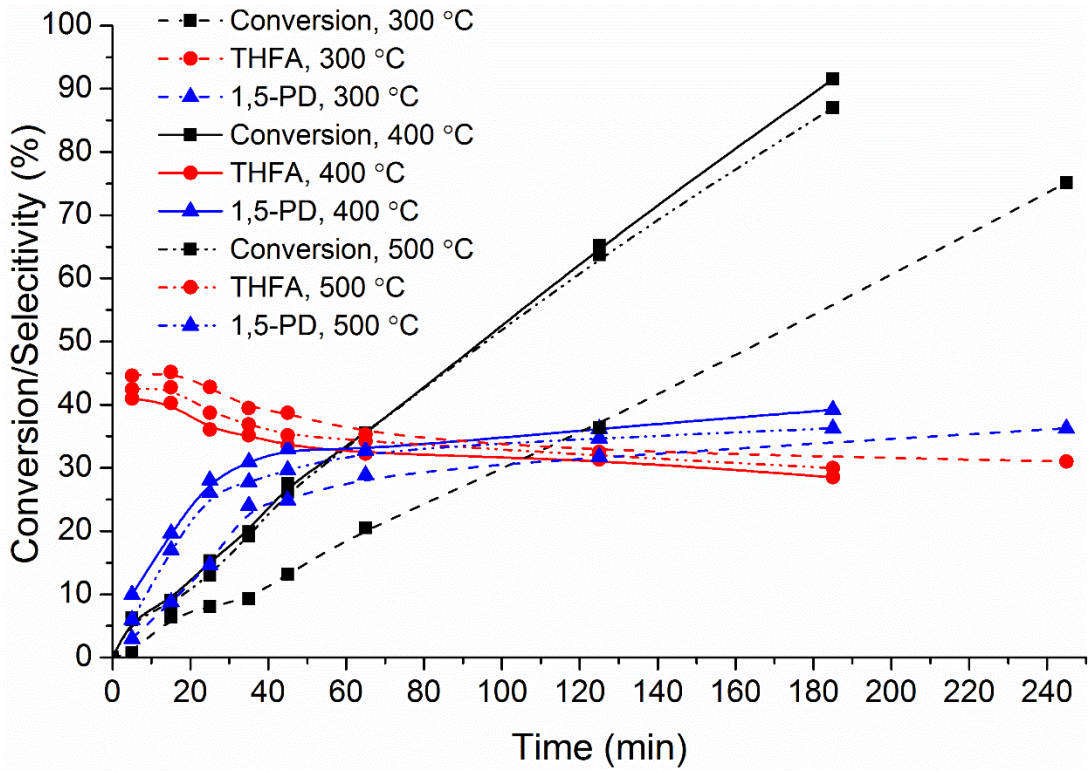

Figure C.4 – Conversion of FAL time on stream data for 0.25Cu-2.75Co-Al after different pretreatment temperatures. The data displayed include conversion and selectivity towards to the two major products (THFA and 1,5-PD).

The figure above displays the conversion and selectivities (THFA and 1,5-PD) over the time of reaction utilizing different reduction temperatures. Specific activities were determined utilizing the data points between 0-30% conversion.

C.3 Additional XPS Data

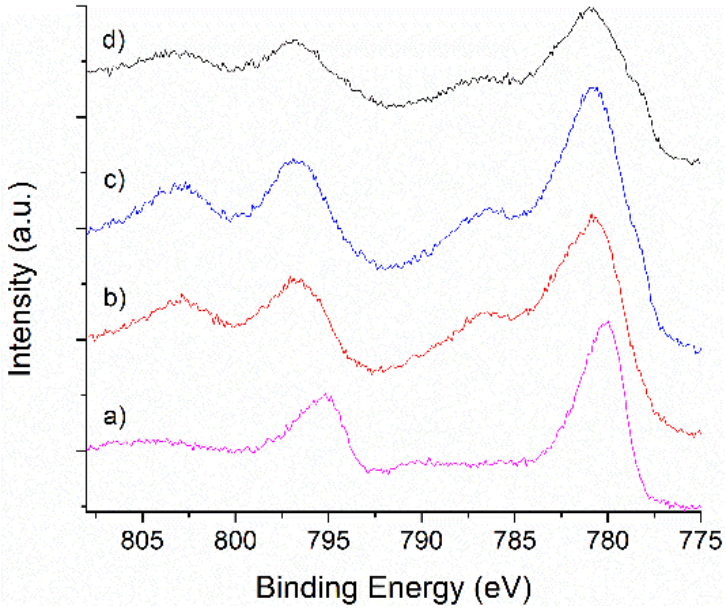

Figure C.5 – Co XPS spectra, 2p, of 0.25Cu-2.75Co-Al after reduction in a flow reactor and passivation. A) No reduction; b) 300 °C reduction; c) 400 °C reduction; d) 500 °C reduction.

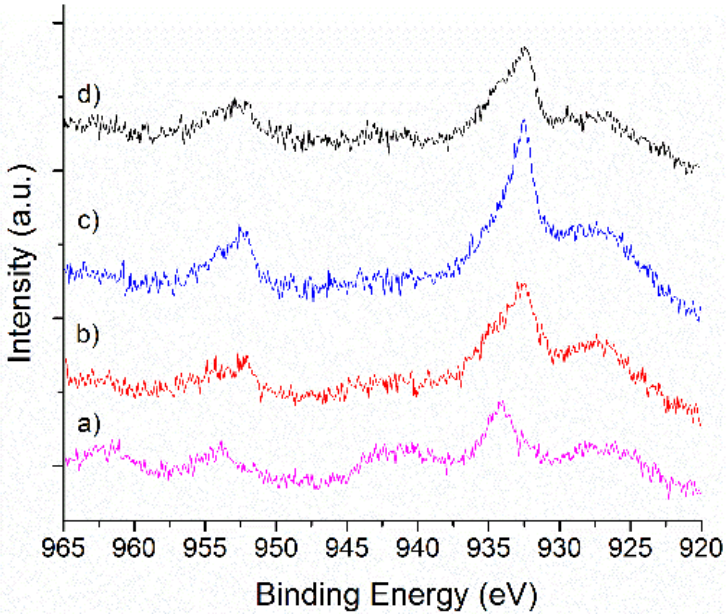

Figure C.6 – Cu XP spectra, 2p, of 0.25Cu-2.75Co-Al after reduction in flow reactor and passivation. A) No reduction; b) 300 °C reduction; c) 400 °C reduction; d) 500 °C reduction.

The above XPS spectra (Figure C.5 and C.6) were analyzed after the first reduction step and passivation. Qualitatively, the Co $2p_{3/2}$ displayed both CoO and Co^0 features after reduction, as indicated by the emergence of a shoulder around 778 eV and a satelite peak around 785 eV. It was clear in the Co spectra that after the second reduction step (Figure 4.8) in the batch reactor the shoulder at 778 eV became more prominent, indicating that more metallic species were present on the surface. This suggested that the second reduction step does alter the catalyst. The fitting displayed in Figure C.7 was conducted by fitting both the $2p_{3/2}$ and $2p_{1/2}$ modes with specific area constraints ($1/2*2p_{3/2}$ area ~ $2p_{1/2}$ area) and binding energy constraints, within error.[2,3]

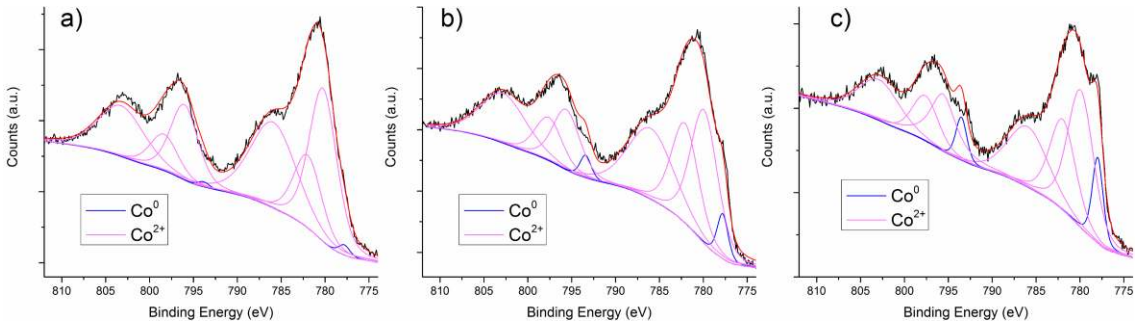

Figure C.7 – Deconvolution of XPS Spectra of Co species for 0.25Cu-2.75Co-Al catalyst displayed in Figure 4.8. These catalysts have been reduced at their respective temperature for 1 h, passivated at room temperature for 1 h in 1% O_2, and re-reduced in the batch reactor to 180 °C. a) 300 °C reduction; b) 400 °C reduction; c) 500 °C reduction.

Table C.4 – Peak fitting data for Figure C.7 for various reduction temperatures conducted after fully pretreatment (Flow reduction, passivation, and batch reactor reduction).

SPECIES	300 °C			400 °C			500 °C		
$2p_{3/2}$	B.E. (eV)	Area	FWHM (eV)	B.E. (eV)	Area	FWHM (eV)	B.E. (eV)	Area	FWHM (eV)
Co^0	777.8	1317	1.5	777.8	6600	1.5	778.0	9499	1.5
Co^{2+}	780.2	48831	3.7	779.9	48060	3.6	779.9	34557	3.5
Co^{2+}	782.0	23241	3.7	782.1	36002	3.6	782.0	22801	3.5
Co^{2+} satellite	785.9	44833	6.1	786.0	42809	6.1	786.0	23693	5.4
$2p_{1/2}$	B.E. (eV)	Area	FWHM (eV)	B.E. (eV)	Area	FWHM (eV)	B.E. (eV)	Area	FWHM (eV)
Co^0	793.9	658	1.5	793.4	3300	1.5	793.5	4749	1.5
Co^{2+}	796.1	24485	3.7	795.6	21806	3.6	795.6	17278	3.5
Co^{2+}	798.4	11620	3.7	797.6	15632	3.6	797.6	11400	3.5
Co^{2+} satellite	803.2	26503	6.1	802.8	30050	6.1	802.9	15945	5.4

C.4 Additional Co XAS Data

The XAS data below display the XANES analysis of each active catalyst before and after reduction as well as after a 1 h passivation step in 1% O_2. The catalysts that were tested include 0.1Cu-2.9Co-Al, 0.25Cu-2.75Co-Al, 0.5Cu-2.0Co-Al, and 3Co-Al.

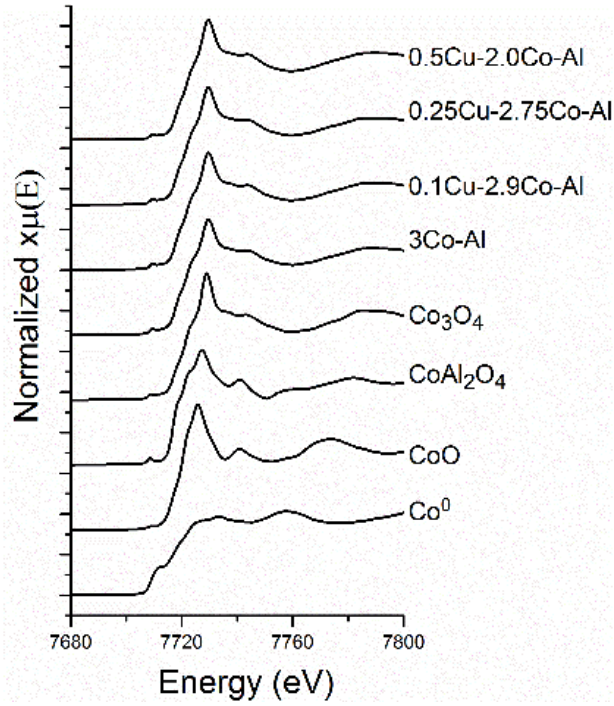

Figure C.8 – XANES spectra of the Co K-edge after calcination and prior to any reduction.

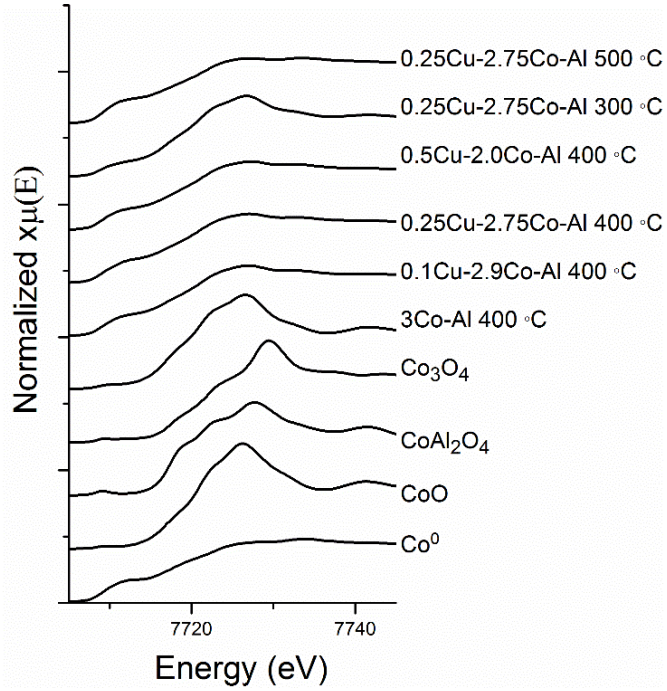

Figure C.9 – XANES spectra of the Co k-edge for various Cu-Co-Al oxides; Also displayed are some standards used. Post-reduction and prior to passivation.

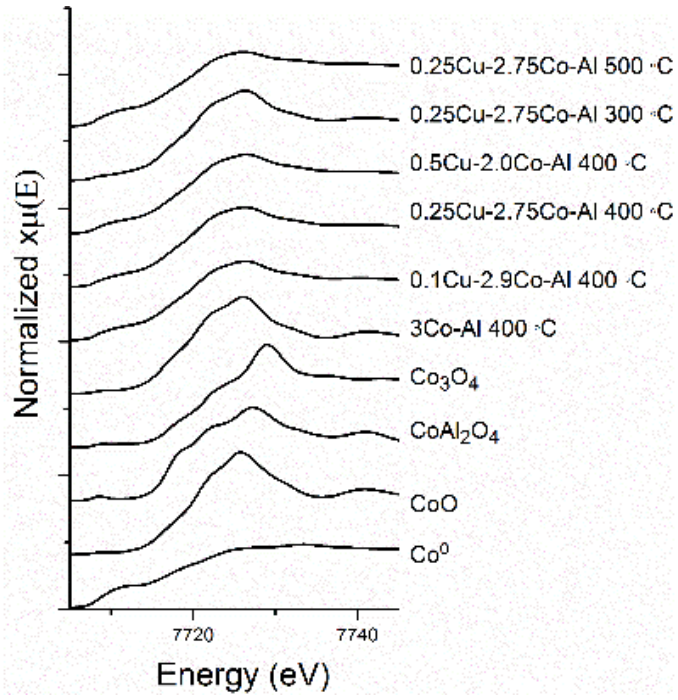

Figure C.10 – XANES spectra of the Co k-edge for various Cu-Co-Al oxides; Also displayed are some standards used. Post-passivation.

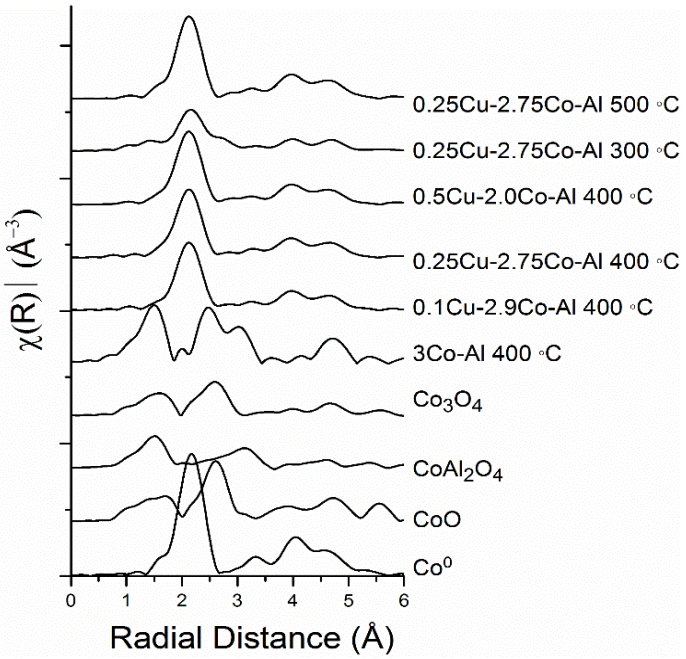

Figure C.31 – Normalized EXAFS spectra of the Co k-edge collected before reduction for each catalyst; displayed with some standards used. Post-reduction and prior to passivation.

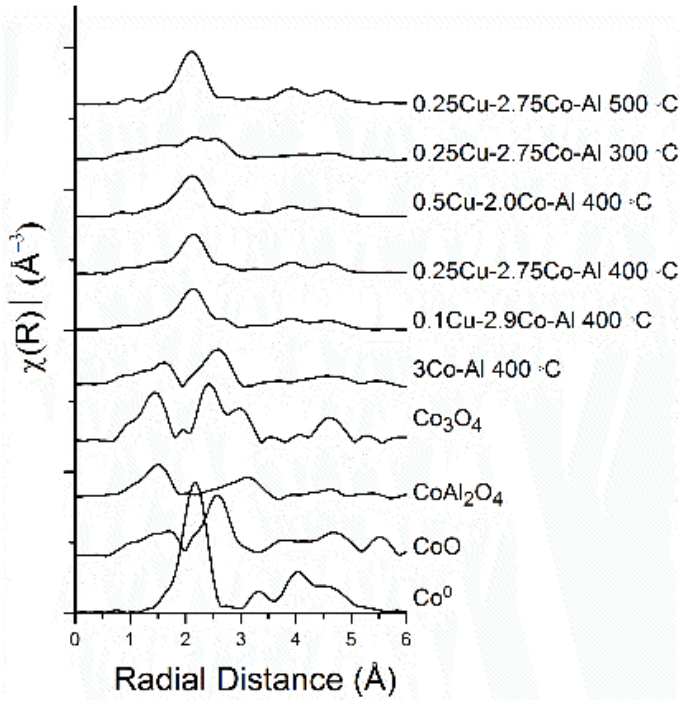

Figure C.12: Normalized EXAFS spectra of the Co k-edge collected before reduction for each catalyst; Also displayed with some standards used. Post-passivation.

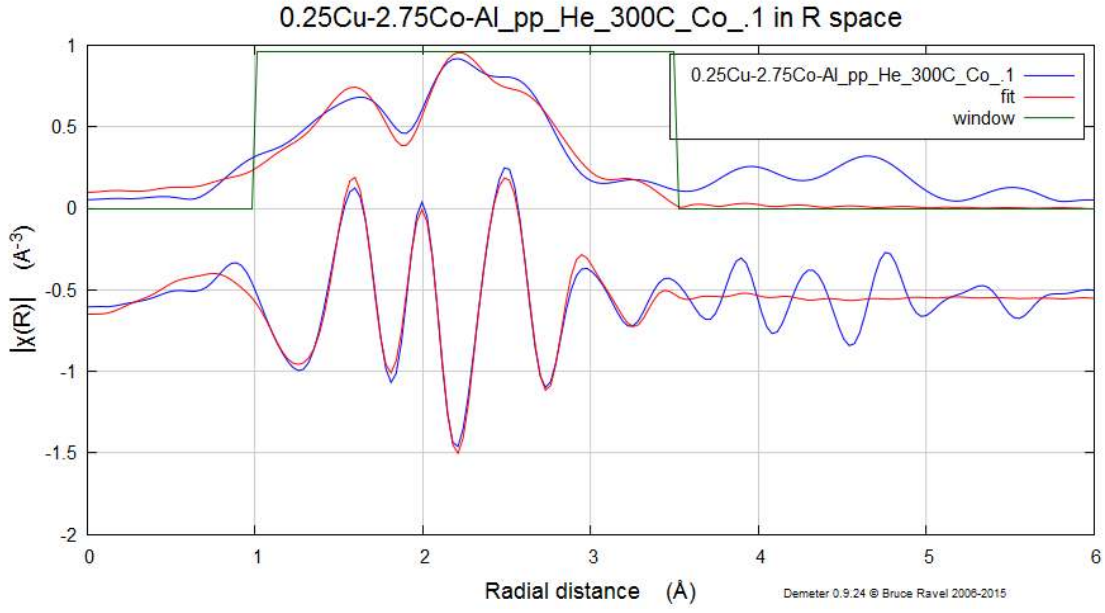

Figure C.13: Fourier transformed EXAFS of the Co k-edge of reduced (300 °C) 0.25Cu-2.75Co-0.75Al catalysts at k weight of k^2. This demonstrates an example fit conducted on the catalysts. Post-passivation.

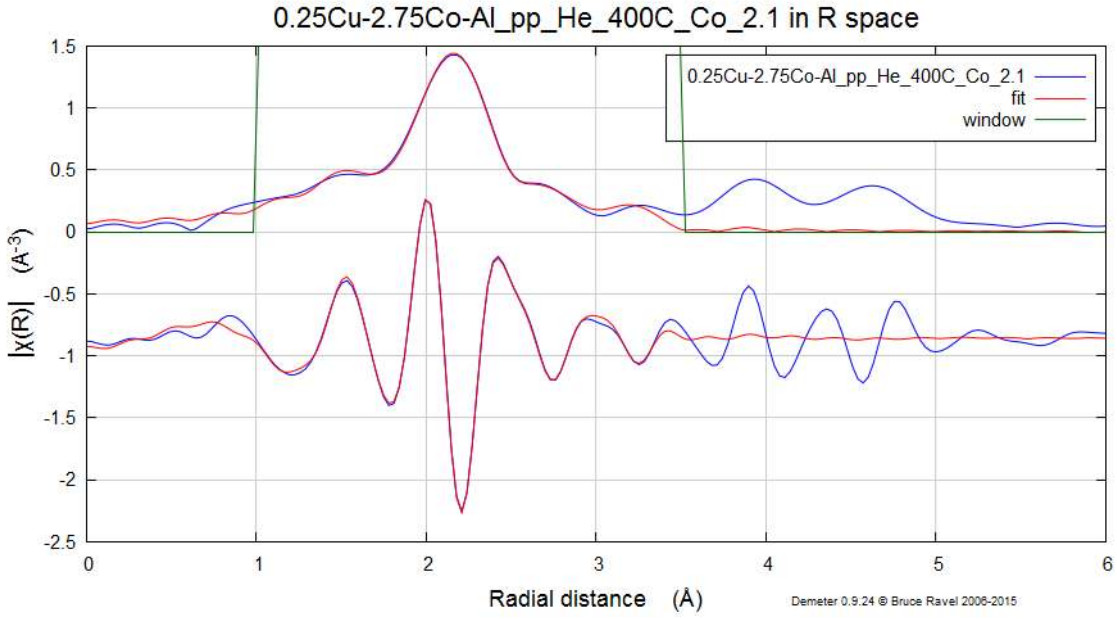

Figure C.44: Fourier transformed EXAFS of the Co k-edge of reduced (400 °C) 0.25Cu-2.75Co-0.75Al catalysts at k weight of k^2. This demonstrates an example fit conducted on the catalysts. Post-passivation.

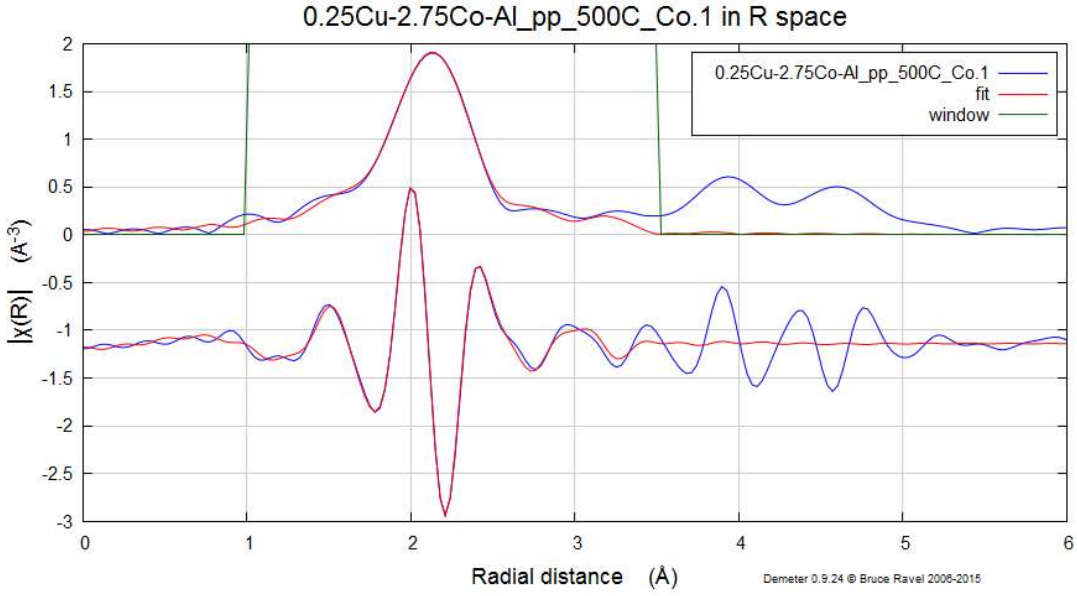

Figure C.55: Fourier transformed EXAFS of the Co k-edge of reduced (500 °C) 0.25Cu-2.75Co-0.75Al catalysts at k weight of k^2. This demonstrates an example fit conducted on the catalysts. Post-passivation.

The above plots, Figures C.13-C.15, exemplify the fitting conducted on the Fourier transformed EXAFS data using Artemis.[4] The two above figures give an example of the fitting window and visual indication of the wellness-of-fit for the Co species.

Table C.5: EXAFS results for the analysis of the Co k-edge post-reduction.[a]

Sample	Shell	CN	r (Å)	Δσ (10^{-3} Å^2)	ΔE_0 (eV)	R factor
Co Foil[b]	Co-Co	12	2.50 ± 0.01	6.4 ± 0.4	7.8 ± 0.5	0.008
Co(III) acac	Co-O	6	1.88	1.8 ± 1.1	-3.5 ± 0.6	0.013
0.1Cu-2.9Co-Al	Co-Co(Cu)	3.4 ± 0.4	2.48 ± 0.01	6.0 ± 0.9	-4.4 ± 0.9	0.007
	Co-O	2.1 ± 0.4	2.01 ± 0.02	7.9 ± 3.0	-4.4 ± 0.9	
0.25Cu-2.75Co-Al	Co-Co(Cu)	3.6 ± 0.3	2.49 ± 0.01	6.5 ± 0.7	-1.7 ± 1.0	0.003
	Co-O	2.4 ± 0.4	2.03 ± 0.01	8.7 ± 2.9	-1.7 ± 1.0	
0.5Cu-2.0Co-Al	Co-Co(Cu)	4.0 ± 0.6	2.49 ± 0.01	7.1 ± 1.1	-4.6 ± 1.1	0.008
	Co-O	2.2 ± 0.5	2.03 ± 0.01	8.3 ± 3.4	-4.6 ± 1.1	

[a]Fitting parameters: Fourier transform range, Δk, 2.4-12.5 Å^{-1} with weighting k^2. [b]Fourier transform range, Δk, 2.7-14 Å^{-1} with weighting k^2. The R-space that was fit was 1.0-3.5 Å. Coordination number assigned from standard HCP Co^0 structure; S_0^2 (Co-Co) = 0.78 determined from Co foil fitting and S_0^2 (Co-O) = 0.69 determined from Co(III) acac.

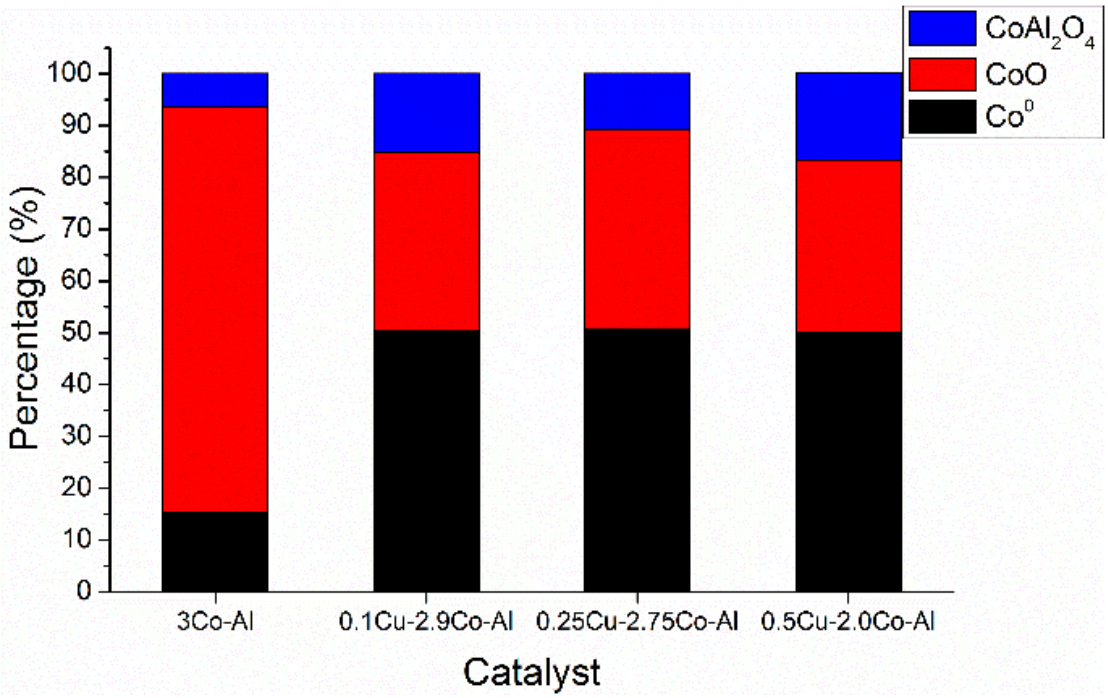

Figure C.6 – XANES linear combinations of the catalysts after pretreatment (reduction at 400 °C for an h and passivation for 1 h). Related to Figure C.10.

C.5 Additional Cu XAS Data

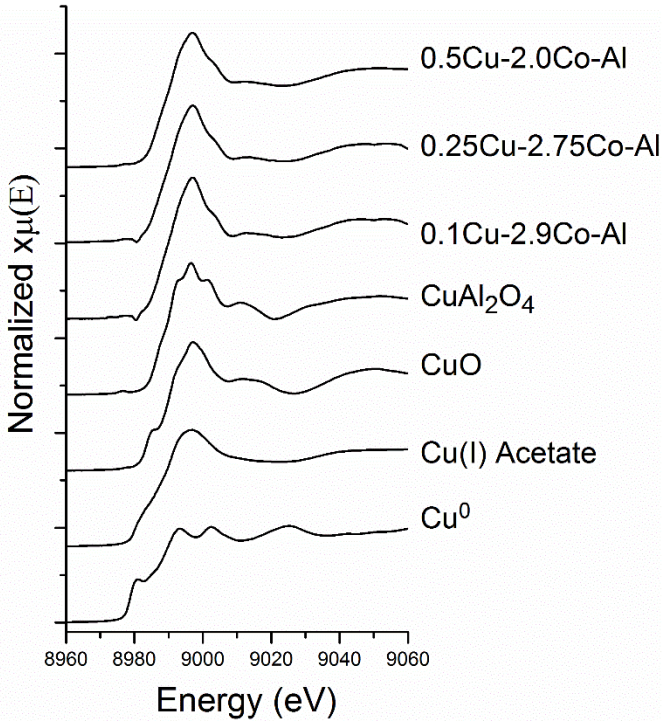

Figure C.17: XANES of the Cu K-edge post-calcination and prior to any reduction.

Table C.6: Edge Energy of the Cu K-edge from Figure C.17.

Sample	Edge Energy (eV)[1]
0.5Cu-2.0Co-Al	8986.5
0.25Cu-2.75Co-Al	8986.3
0.1Cu-2.9Co-Al	8986.9
Cu^0	8979.0
Cu(I) Acetate	8980.1
CuO	8983.5
$CuAl_2O_4$	8986.5

[1]Edge Energy was determined by the 1st major derivative peak

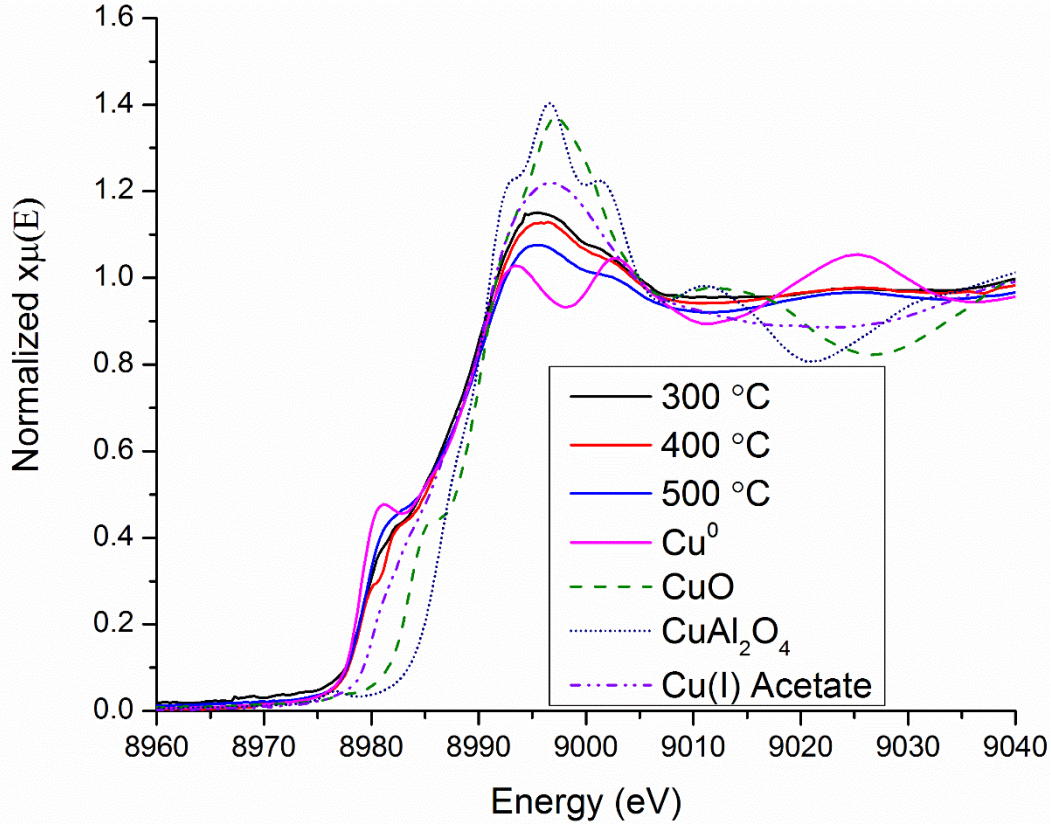

Figure C.18: XANES spectra of the Cu k-edge for 0.25Cu-2.75Co-Al oxides pretreated at different reduction temperatures and with a room temperature passivation for 1 h; Also displayed are some standards used.

Table C.7: Edge Energy of Cu K-edge from Figure C.18

Sample	Edge Energy (eV)[1]
0.25Cu-2.75Co-Al 300 °C	8978.9
0.25Cu-2.75Co-Al 400 °C	8978.9
0.25Cu-2.75Co-Al 500 °C	8978.6
Cu^0	8979.0
Cu(I) Acetate	8980.1
CuO	8983.5
$CuAl_2O_4$	8986.5

[1]Edge Energy was determined by the 1st major derivative peak

From the above Figure C.18 and Table C.7 it seemed that qualitatively the Cu species was almost fully reduced even after passivation. This complements the analysis conducted with XPS. Additionally, before reduction the edge energy analysis mimicked more closely to $CuAl_2O_4$ standard brought to ANL. Unfortunately, $CuCo_2O_4$ was not analyzed by XAS, but it was possible this spinal may mimic the edge energy of the copper aluminate spinal. This suggested the Cu was highly dispersed among the metal oxides especially Al_2O_3.

C.6 References

(1) Cavani, F.; Trifirò, F.; Vaccari, A. Hydrotalcite-type anionic clays: preparation, properties and applications. *Catal. Today* **1991**, *11*, 173–301.

(2) Biesinger, M. C.; Payne, B. P.; Grosvenor, A. P.; Lau, L. W. M.; Gerson, A. R.; Smart, R. S. C. Resolving surface chemical states in XPS analysis of first row transition metals, oxides and hydroxides: Cr, Mn, Fe, Co and Ni. *Appl. Surf. Sci.* **2011**, *257*, 2717–2730.

(3) Biesinger, M. C.; Payne, B. P.; Lau, L. W. M.; Gerson, A.; Smart, R. S. C. X-ray photoelectron spectroscopic chemical state quantification of mixed nickel metal, oxide and hydroxide systems. *Surf. Interface Anal.* **2009**, *41*, 324–332.

(4) Calvin, S.; Carpenter, E.; Ravel, B.; Harris, V.; Morrison, S. Multiedge refinement of extended x-ray-absorption fine structure of manganese zinc ferrite nanoparticles. *Phys. Rev. B* **2002**, *66*, 224405.